Electroabsorption in semi-insulating materials

McGinnity, T. M.

ELECTROABSORPTION IN SEMI-INSULATING MATERIALS

A thesis presented by
T. M. McGinnity
to the University of
Durham in application
for the degree of
Doctor of Philosophy

Durham 1979

ACKNOWLEDGEMENTS

I gratefully acknowledge the assistance of the large number of people who have helped make this thesis possible. In particular I would like to thank my supervisor, Prof. G. G. Roberts, for his constant advice and encouragement. In addition, I gratefully acknowledge the assistance of the Imperial Chemical Industries and the Royal Signals and Radar Establishment for the provision of samples; the University of Durham and the New University of Ulster (where the research was started) for the provision of research facilities; the technical and secretarial staff in the relevant departments of the above institutions for their assistance and co-operation; the Northern Ireland Department of Education for the provision of a research scholarship. I also gratefully acknowledge the patience of Miss. R. McGinnity who struggled through my handwriting to type this thesis.

Finally, I am deeply indebted to my wife, without whose constant support, patience and encouragement this thesis would never have been written.

ABSTRACT

The electroabsorption properties of a number of semi-insulating materials including indium phosphide, gallium arsenide and Langmuir/Blodgett thin films of anthracene are reported. Single crystals of InP:Cr, InP:Fe and GaAs:Cr were subjected to large electric fields at a variety of temperatures and the resulting small changes upon the optical absorption spectra were carefully recorded. Prior to the performance of the electroabsorption measurements, the specimens were examined using such techniques as ac. and dc. conductivity, photoconductivity and zero-field optical absorption. Electroabsorption measurements were performed as a function both of the frequency and magnitude of the applied electric field. In addition, the presence of odd harmonics in the electroabsorption signal was examined. A correlation between the existence of frequency dependent effects and the specimens' photoconductivity was found. The electroabsorption spectra were analyzed within the context of the one-electron Franz-Keldysh theory, thus allowing the reduced effective masses of InP:Fe, InP:Cr and GaAs:Cr to be calculated. These values are in good agreement with published data for pure material.

The lightly substituted anthracene Langmuir films were also examined using ac. and dc. conductivity techniques. In addition, data are reported concerning the fluorescent, electroluminescent and photoconductive properties of the specimens. The electroabsorption spectra for these materials is interpreted in terms of the quadratic Stark effect. An analysis of these data leads to a value of 36 $\mathring{A}^3$ for the average static polarizability change of a C4 anthracene film in the vicinity of the first singlet state absorption.

CONTENTS

PAGE

PAGE

PAGE

INTRODUCTION

Electroabsorption is a particular branch of the family of experimental techniques known as modulation spectroscopy. The technique involves the application of large electric fields to a specimen and the measurement of the small resultant changes in the sample's optical transmission. The method has a wide range of applications. Its principal use is in providing valuable information concerning band structure and phonon spectra. However, it has also been applied to a study of band-tailing effects in solids and as a sensitive test of the reproducibility of thin film properties. More recently the technique has been used in the study of impurity state symmetry. In molecular crystals electroabsorption studies have been performed with a view to the determination of static polarizability changes.

While the electroabsorption technique is a powerful experimental tool, it also has practical device applications. Recent papers have demonstrated the use of the electroabsorption mechanism to make light intensity modulators with extinction ratios up to 20 dB. Proposals have also been made that the electroabsorption effect can be applied in an integrated emitter/modulator, a multiple-section photodetector in which each section only responds to selectively absorbed optical wavelengths, and a variable bandpass optical filter.

In this thesis, the electroabsorption technique is applied to the study of some semi-insulating materials, namely gallium arsenide, indium phosphide and some novel Langmuir/Blodgett thin films of anthracene. The principal aims of the study are to use the technique to obtain values for the reduced effective masses in doped indium phosphide and gallium arsenide, and to investigate the Stark effect in the anthracene Langmuir films. However, the influence of certain experimental complications are also examined. These influences, such

as non-uniform field distributions, space charge injection, photo-carrier effects, are often present and frequently ignored in electro-absorption studies. In particular, measurements are usually performed at a fixed frequency, a procedure which may result in an incorrect interpretation of experimental data. Another effect which is often present, though not noticed, is the existence of harmonics in the electroabsorption signal. These topics are also investigated in this thesis. In order to better understand these effects, additional data are obtained from ac. and dc. conductivity, capacitance, and photoconductivity measurements.

Chapter I of the thesis is devoted to a brief review of optical absorption in solids. This is followed in Chapter II with a summary of current electroabsorption theory. A decription of the exper-imental equipment needed to record the data is presented in Chapter III. In Chapter IV an introduction to the properties of InP and GaAs is presented, and the results of experiments performed on these materials are given in Chapter V. Electroabsorption and related data obtained on the Langmuir films of anthracene are presented and discussed in Chapter VI. The thesis concludes in Chapter VII with a summary of the information obtained in the study and some suggestions for further work.

CHAPTER I

OPTICAL ABSORPTION IN SOLIDS

1.1 Introduction

One of the simplest methods of probing the band structure of a semiconductor or semi-insulator is to measure the absorption coefficient as a function of photon energy. The underlying principle which connects the optical properties of a solid with its electronic structure is that the absorption or emission of radiation is accompanied by the transfer of an electron from one state to another.

Of greatest relevance to the present work is the absorption at the fundamental bandgap Eg between the conduction and valence bands. A number of different optical transitions are possible, depending on the particular shape of the bands of the solid in question. These may be listed as direct allowed, direct forbidden and indirect transitions. A summary of these processes and related topics will now be presented.

1.2 Direct Transitions

Direct transitions are said to occur when an electron in the valence band is transferred to the conduction band without a change in momentum; that is, these transitions are vertical in k-space. This process is illustrated in Figure 1.1, where an energy band diagram for InSb is displayed. It is evident from the diagram that direct transitions occur when the maximum of the valence band and the minimum of the conduction band appear at the same point in k-space. For direct transitions the onset of strong absorption occurs at $h\nu = Eg$, and the absorption coefficient α rises very rapidly with increasing photon energy. This is shown very clearly

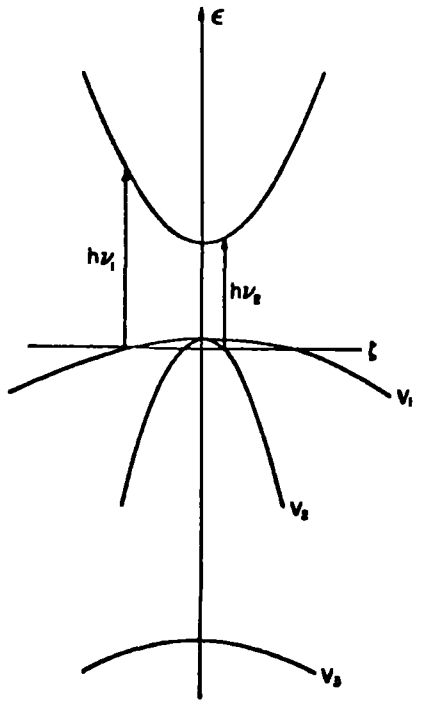

Fig. 1.1 Schematic diagram of energy bands of indium antimonide.

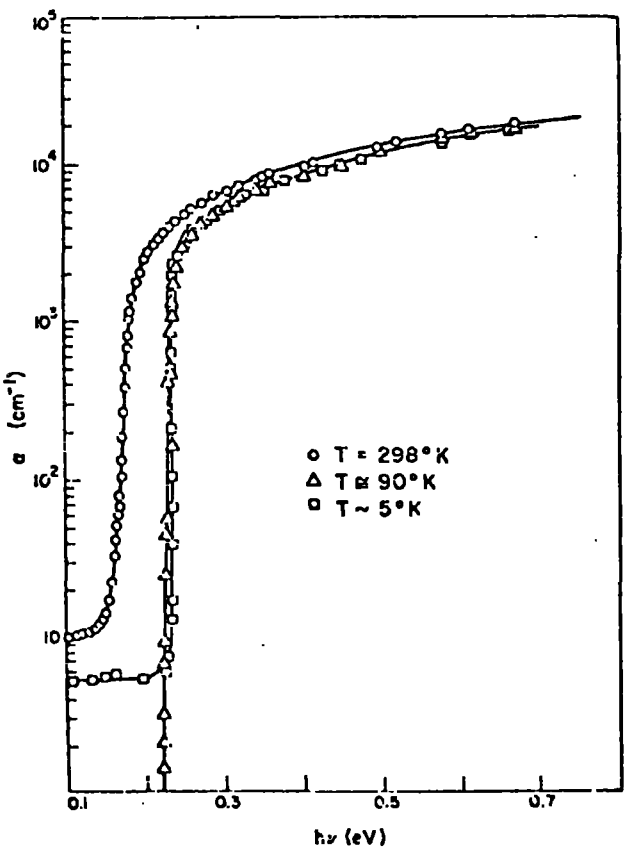

Fig. 1.2 Absorption edge of pure InSb.(1)

in Figure 1.2, where a graph of the absorption coefficient of InSb is drawn. One can see that α rises over several orders of magnitude in a small range of energy. No change in momentum occurs in this type of transition, since the momentum of the photon may be neglected. Direct absorption edges are found in a large number of materials, such as GaAs, CdTe, and InP.

1.2.1 Transition Matrix Elements

It is a relatively simple matter to calculate the dependence of the absorption coefficient α upon photon energy. For a given photon energy $h\nu$, α is proportional to the transition probability $P_{mo}(t)$ between the initial state o and the final state m. It is also proportional to the density of electrons in the initial state and the density of available final sites. From 1st order perturbation theory we may write:-

$$P_{mo}(t) = \frac{\left|H_{mo}\right|^2 \sin^2\left[\frac{1}{2}(\omega-\omega_o)t\right]}{\hbar^2(\omega-\omega_{mo})^2} \qquad (1)$$

where H_{mo} is the matrix element of the perturbation given by

$$\left|H_{mo}\right|^2 = \frac{2e^2 I(\nu)\left|\underline{p}_{mo}\right|^2}{3m_o^2 n \varepsilon_o c \omega^2} \qquad (2)$$

In this expression, $\hbar\omega_{mo}$ is the energy separation of the two levels, m_o is the free electron mass, and $\omega = 2\pi\nu$, where ν is the frequency of the incident radiation $I(\nu)$. The term $\left|p_{mo}\right|^2$ is the square of the momentum matrix element given by:-

$$\left|\underline{p}_{mo}\right|^2 = \left|(p_x)_{mo}\right|^2 + \left|(p_y)_{mo}\right|^2 + \left|(p_z)_{mo}\right|^2 \qquad (3)$$

where n is the refractive index, and ε_o the dielectric constant of the material. It is easily shown that $\left|p_{mo}\right|$ vanishes unless the

transitions are vertical in k-space, that is

$\underline{k}_c = \underline{k}_v$.

1.2.2 Evaluation of the Absorption Coefficient

In order to obtain a quantitative value for the transition, it is necessary to integrate equation (1) over all pairs of energy states in the crystal with energy separations close to $\hbar\omega_{mo}$. The result is:-

$$P_{cv}(t) = \frac{2e^2 I(\nu)\, \rho(\omega_{mo})}{3m_o^2 n \varepsilon_o c \hbar \omega^2} \left|\underline{p}_{mo}\right|^2 \int_o^\infty \frac{\sin^2\left[\frac{1}{2}(\omega-\omega_{mo})t\right]}{(\omega-\omega_{mo})^2}\, d\omega_{mo} \qquad (4)$$

where $\rho(\omega_{mo})\hbar\Delta\omega_{mo}$ is the number of energy-level pairs having separations in the range $\hbar\omega_{mo}$ to $\hbar\omega_{mo} + \hbar\Delta\omega_{mo}$. For reasonable times the integral has the value $\pi t/2$ so that we may write the absorption coefficient as:-

$$\alpha = \frac{e^2 \left|\underline{p}_{mo}\right|^2 \rho(\omega_{mo})}{6m_o^2 n \varepsilon_o c\, V\nu} \qquad (5)$$

where V is the volume of the crystal. This is a general expression and may be simplified if we assume parabolic E-k curves centred at k = 0. In this case we have:-

$$h\nu = E_g + \hbar^2 k^2 / 2m_r \qquad (6)$$

where m_r is the reduced mass given by:-

$$1/m_r = 1/m_e + 1/m_h \tag{7}$$

From (7) we can derive an expression for the joint density of states so that:-

$$\rho(h\nu) = 4\pi V(2m_r)^{3/2}(h\nu - E_g)^{1/2}/h^3 \tag{8}$$

The final expression for the absorption coefficient may then be written as:-

$$\alpha = A(h\nu - E_g)^{\frac{1}{2}}$$

with

$$A = \frac{2\pi e^2(2m_r)^{3/2}\left|p_{mo}\right|^2}{3m_o^2 n\varepsilon_o ch^3\nu} \tag{9}$$

"A" varies very gradually with photon energy for allowed transitions. In zinc-blende type semiconductors, it is necessary to include in "A" a term allowing for the fourfold degeneracy of the valence band.

It is possible to obtain an estimate for the momentum matrix element $\left|p_{mo}\right|$ using Kane's [2] k.p perturbation theory. Using this theory it can be shown that:-

$$A \approx \frac{3.38 \times 10^7}{n}(m_e/m_o)^{1/2}(E_g/h\nu)eV^{-1/2}m^{-1} \tag{10}$$

This expression is in reasonable agreement with the observed magnitudes of the direct absorption edges in the III-V compounds.

It is usual to plot α^2 versus photon energy in situations where direct transitions are expected. A straight line then confirms the presence of a direct gap material. This is the case in Figure 1.3, where a graph of the absorption coefficient of InAs above 10^3 cm^{-1} is displayed. The intercept on the energy axis gives the energy gap Eg as 0.355eV, in approximate agreement with the date of Spitzer and Fan [4]. In direct bandgap materials the absorption coefficient usually rises to a shoulder at around 10^4 cm^{-1}, thereafter increasing at a much slower rate.

1.2.3 Direct Forbidden Transitions

In some materials the matrix element $|p_{mo}|$ vanishes at $k = k_o$ due to the relative symmetry of the wavefunctions. In this case, the transitions are forbidden at $k = 0$ but are allowed for $k \neq 0$, since away from the $k = 0$ position the wavefunctions are modified by interactions between bands. It may be shown that for forbidden direct transitions the absorption coefficient takes the form:-

$$\alpha = A'(h\nu - E_g)^{3/2}$$

where A' is given by

$$A' = \frac{8\pi^3 e^2 (2m_r)^{3/2}}{3m_o^2 n \varepsilon_o c h^5 \nu} \left| \frac{\partial |\underline{p}_{mo}(\underline{k})|}{\partial k} \right|^2_{k=0} \qquad (11)$$

Examples of symmetry forbidden transitions occur in the case of transitions between the three valence bands in Ge [5] and in other semiconductors having the zinc-blende structure. The absorption requires the presence of holes and is therefore only seen in p-type material. This type of absorption has also been observed in InAs [6],

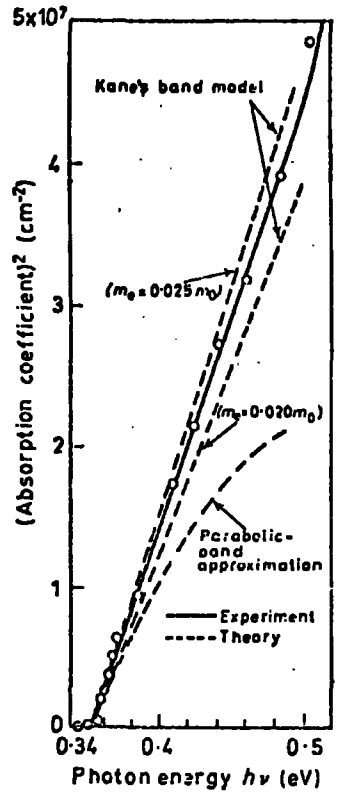

Fig. 1.3 Energy dependence of the absorption coefficient of InAs above 10^3 cm^{-1}. (3)

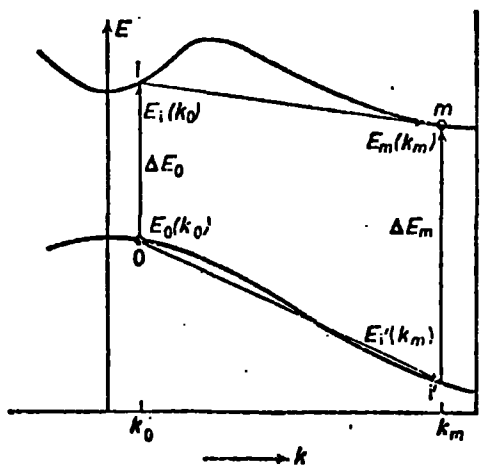

Fig. 1.4 The shape of the E-k curves in many indirect gap materials.

AlSb [7] and GaAs [8].

1.3 Indirect Transitions

Indirect transitions are said to occur when an electron in a valence band is transferred to a conduction band state which has a different $\underset{\sim}{k}$ vector. As a consequence of this change in momentum, these transitions are only possible if phonons participate in the process. Two possibilities need to be considered, namely, phonon emission and phonon absorption. Indirect transitions are most likely to occur when the band structure of the material is such that the minimum of the conduction band and the valence band maximum do not occur at the same point in k-space.

This situation is illustrated in Figure 1.4 where a form of the E-k curves common to many indirect gap materials is shown. With reference to 2nd order perturbation theory, it is found that an electron in the valence band at E_o (k_o) may make a transition to the lowest conduction band states at E_m (k_m) by means of two possible processes. It may transfer either by the short lived intermediate state i, or the equally transient i' state. If we consider the first process it can be shown that the transition probability $P_{mv}(t)$, relating to transfers between various valence band states to a conduction band state m, may be expressed as:-

$$P_{mv}(t) = \frac{4\left|H_{io}\right|^2\left|H_{mi}^{\pm}\right|^2}{\hbar^4(\omega_{io}-\omega)^2} \times \rho_v(E_v)\int_0^{\infty}\frac{\sin^2\left[\frac{1}{2}(\omega_{mo}-\omega\pm\omega_p)t\right]}{(\omega_{mo}-\omega\pm\omega_p)^2}\,d(\hbar\omega_{mo}) \qquad (12)$$

in a similar manner to equation (1) for direct transitions, where

H_{io} is the optical matrix element and H_{mi} the matrix element for electron-phonon interaction. In this expression $\hbar\omega$ is the photon energy, $\hbar\omega_p$ the phonon energy E_p, and $h\omega_{io}$ the width of the forbidden gap at the valence band maximum. ρ_v is the density of valence band states per unit energy interval.

For reasonable times equation (12) reduces to:-

$$P_{mv}(t) = \frac{2\pi \left| H_{io} \right|^2 \left| H_{mi}^{\pm} \right|^2}{\hbar \left(\Delta E_o - h\nu \right)^2} \rho_v(E_v)\, t \qquad (13)$$

where $\Delta E_o = h\omega_{io}$. On summing over all possible conduction band states, the net transition rate becomes:-

$$\frac{P_{cv}(t)}{t} = \frac{2\pi \left| H_{io} \right|^2 \left| H_{mi}^{\pm} \right|^2}{\hbar^2 \left(\Delta E_o - h\nu \right)^2}$$

$$\times \int_0^{E'} \rho_c(E_c)\, \rho_v(E_c - h\nu \pm E_p)\, dE_c \qquad (14)$$

where $E' = h\nu + E_p - E_g$ for phonon absorption and

$E' = h\nu - E_p - E_g$ for phonon emission. For parabolic bands with the valence band maximum at $k = 0$, we may write for the density of states:-

$$\rho_c(E_c) = V M 4\pi (2m_c)^{3/2} E_c^{1/2} / h^3$$

$$\rho_v(E_v) = V 4\pi (2m_v)^{3/2} (E_g - E_v)^{1/2} / h^3 \qquad (15)$$

where m_c is a density of states effective mass, m_v the valence band

mass and V the volume of the crystal. M is an integer inserted to allow for more than one equivalent conduction band minima.

The matrix element for electron-phonon interaction may be written in the form:-

$$\left|H_{mi}^{-}\right|^2 = B_c\left[\left(e^{E_p/kT} - 1\right)^{-1}\right] \Big/ V \quad ..(16)$$ for phonon

absorption and for phonon emission,

$$\left|H_{mi}^{+}\right|^2 = \frac{B_c}{V}\left[\frac{1}{e^{E_p/kT} - 1} + 1\right] \quad (17)$$

B_c is a constant referring to the phonon scattering process for electrons in the conduction band. The optical matrix element $\left|H_{io}\right|$ is the same as that given in equation (2) for direct transitions.

On evaluation of the integral in equation (14), and substitution for $\left|H_{io}\right|^2$ and $\left|H_{mi}^{\pm}\right|^2$, the absorption coefficient α may be obtained from:-

$$\alpha = \hbar\omega P_{cv}(t) \;/\; I(\nu)Vt \quad (18)$$

giving

$$\alpha = \frac{C(h\nu + E_p - E_g)^2}{\exp(E_p/kT)-1} + \frac{C(h\nu - E_p - E_g)^2}{1-\exp(-E_p/kT)} \quad (19)$$

where the first term refers to phonon absorption and the second to phonon emission.

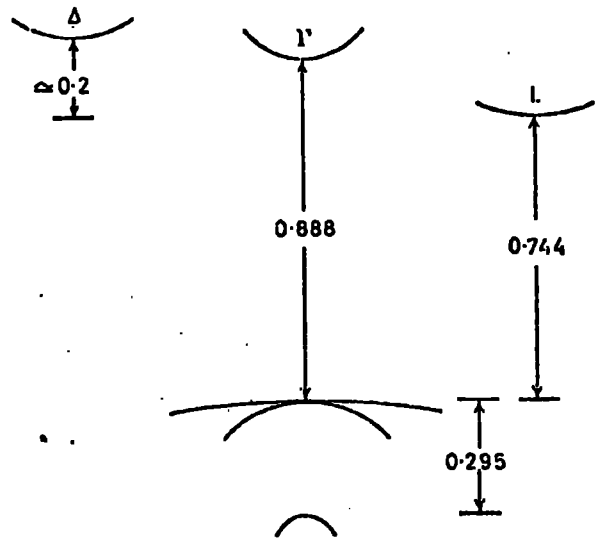

Fig. 1.5 Energy band structure of Ge at 4.2°K (eV).

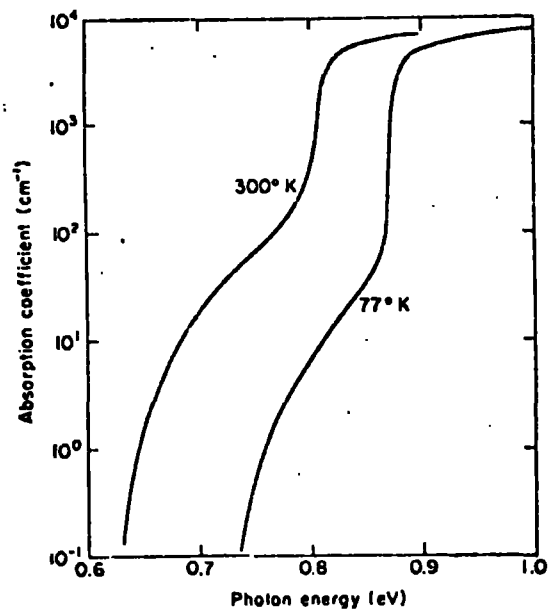

Fig. 1.6 Spectral dependence of the absorption coefficient for Ge. (10)

When the appropriate vertical transition (0 to i, or i' to m) is not allowed as described in section 1.2.3, the corresponding indirect transition is also termed forbidden and the expression for the absorption coefficient takes the form:-

$$\alpha = C'(h\nu \pm E_p - E_g)^3 \qquad (20)$$

A large number of important semiconductors (including Si, Ge and GaP) exhibit indirect absorption edges. Figure 1.5 shows the band structure of Ge. It is evident that Ge has a band structure with features very similar to those shown in Figure 1.4. Accordingly one would expect the optical properties of this material to exhibit an indirect absorption edge, and this is indeed found. Figure 1.6 shows the absorption coefficient of a Ge crystal at two different temperatures. The area of the curve below the "knee" may be fitted to an expression of the form given in equation (19), indicating the presence of an indirect absorption edge.

As for the case of a direct edge, it is possible to obtain more information on the transition type involved by plotting α^n versus photon energy, where n is indicative of the transition in question. For example Figure 1.7 shows an analysis of the data contained in Figure 1.6. In this case, a graph of $\alpha^{\frac{1}{2}}$ versus energy has two branches one corresponding to phonon emission, the other to phonon absorption. Such a diagram enables one to obtain information concerning the size of the indirect energy gap and the energy of the phonon involved. Denoting the intersections of the two branches in Figure 1.7 with the energy axis by E_1 and E_2, the indirect bandgap is:-

$$E_g = (E_1 + E_2)/2 \qquad (21)$$

with the phonon energy equal to

$$E_p = (E_2 - E_1)/2 \text{ for } E_2 > E_1 \qquad (22)$$

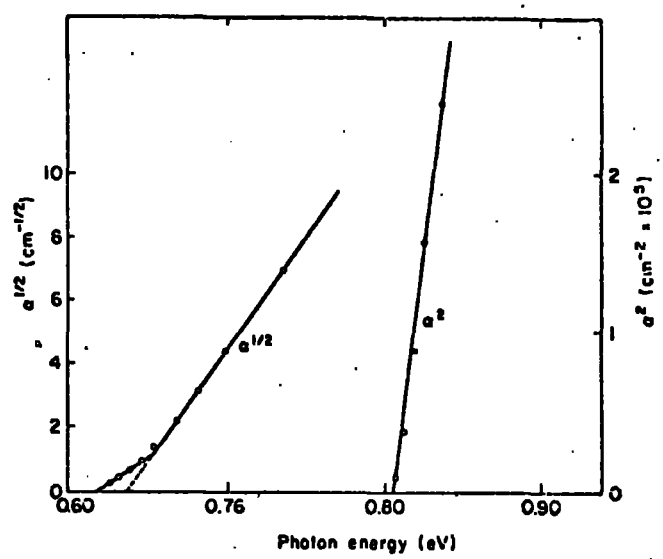

Fig. 1.7 Analysis of the data of Fig. 1.6 in terms of direct and indirect transitions.(10

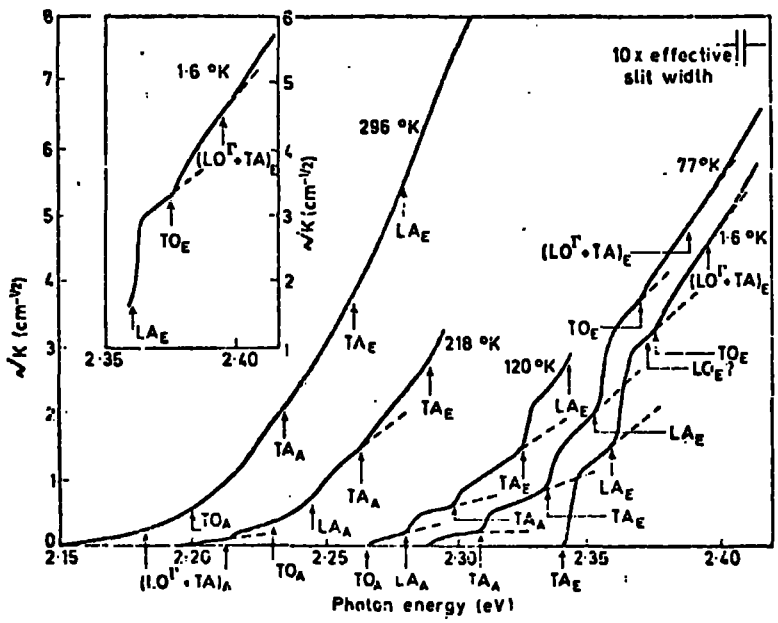

Fig. 1.8 The absorption edge of GaP at a number of temperatures. (11)

The above treatment has been restricted to a consideration of single phonon processes. It must be recognised, however, that indirect absorption may well include the participation of more than one phonon. A limiting condition at all times is that momentum must be conserved for the complete process. Despite the fact that the probability of this occurring is somewhat smaller, transitions of this type have been observed in GaP, as shown in Figure 1.8.

The values of α obtained from indirect edges are usually less than 100 cm^{-1}. A point worth noting is that although the matrix elements for indirect transitions are usually smaller than for the direct case, the number of possible sites for indirect transitions is larger. The net result is that indirect transitions contribute more to the total absorption than might be expected.

1.4 Absorption due to Excitons

When an electron is excited from the valence band to the conduction band of a semiconductor due to the absorption of a photon of energy $h\nu$, there exists the possibility of an interaction occurring between the photo-excited electron and the hole remaining in the valence band. In the theories of optical absorption presented previously, this Coulomb interaction between the electron-hole pair has been neglected. In some materials, particularly pure materials, this procedure is not entirely valid, since, for these materials, the interaction can lead to the formation of bound states in a hydrogenic orbit. This excited state is referred to as an exciton and has an energy of formation less than E_g.

The theoretical description of exciton states in a solid is a many-body problem and cannot be solved without making many simplifying assumptions. Depending on the material, one of two basic approximations is normally applied. If the atoms in the solid interact weakly, such as in ionic or molecular crystals, the electronic excitation can be considered to be essentially localized in space, covering at most a few lattice sites. Nevertheless, it is possible for the excitation to

propagate through the crystal, and provide a means for the transfer of energy. This approach to the theory of excitons was first proposed by Frenkel [12]. The Frenkel approximation regards the exciton as being essentially atomic or molecular in nature, including the crystal only as a small perturbation on the atomic or molecular energy levels.

In contrast, in semiconductors, the interaction between individual atoms is quite strong and the excitation can no longer be considered localized. In this case, the localized model due to Frenkel is completely inadequate. Instead, a model proposed by Wannier[13] which regards the exciton as a bound electron-hole pair, is found to be more appropriate.

This electron-hole pair may be considered to be a hydrogenic atom modified by the dielectric constant of the solid, and also by the effective masses of the electron and hole.

The brief treatment to follow concentrates on Wannier excitons. A discussion of optical absorption by Frenkel excitons is included in section 1.5.

Elliott [14], Knox [15] and Dimmock [16] have made detailed calculations on the effect of Wannier excitons on the optical absorption edge. The results of their calculations show that the energy of formation of an exciton in a bound state is given by:-

$$E = E_g + \hbar^2 \underline{k}^2/2 (m_e + m_h) - R/l^2 \qquad (23)$$

where l is a quantum integer. R is known as the exciton Rydberg, that is:-

$$R = m_r e^4 / 8 \varepsilon_o^2 \varepsilon^2 h^2 \qquad (24)$$

where ε is the static dielectric constant and m_r the reduced mass of the electron-hole pair. If we now consider direct transitions in the

presence of excitons, we find a series of absorption peaks occurs at energies given by:-

$$h\nu = E_g - R/l^2 \qquad (25)$$

The intensity of each line falls off as l^{-3}, according to Elliott [14]. For photon energies such that $h\nu \gg E_g$ it may be shown that:-

$$\alpha = \pi A R^{\frac{1}{2}} e^{\pi\gamma} / \sinh \pi\gamma \qquad (26)$$

where

$$\gamma = \left[R/(h\nu - E_g)\right]^{\frac{1}{2}}$$

and A is as defined in equation (9). The Coulomb interaction becomes negligible at very large values of $h\nu$, where $\gamma \rightarrow 0$.

Excitonic effects in absorption have been observed in a number of semiconductors. Sturge [17] has measured excitonic absorption spectra in GaAs, while Turner et al [18] have done the same for InP. Excitonic effects have also been reported for GaSb [19] and representative curves for this material are shown in Figure 1.9. As in most semiconductors, where the exciton binding energy R for the l = 1 state is of the order of 2-4meV, only one peak is observed even at low temperatures. The magnitudes and spectral widths of the discrete lines are influenced predominantly by thermal broadening. This explains why the exciton peak is almost invisible at room temperature in most materials. Exciton lifetimes can also be reduced by scattering at defects or impurities with a resultant further broadening of the peak. The Coulomb field between the electron and the hole may also be screened by the presence of free carriers. At high carrier densities, when the screening length becomes comparable with the separation of the electron-hole pair, excitonic effects are very much reduced.

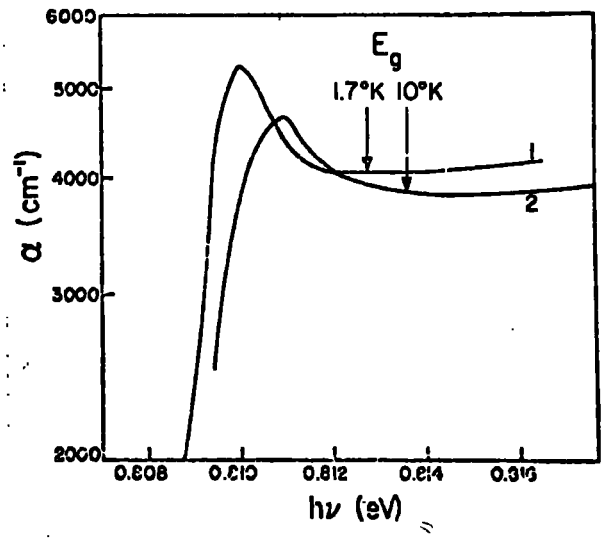

Fig. 1.9

The effect of temperature on the exciton peak in GaSb (1) T = 1.7K (2) T = 10K.(19

1.5 Optical Absorption Processes in Organic Molecular Crystals

The absorption spectra of molecular crystals are in general more complicated than those of inorganic crystals, which are covalently bonded, such as germanium, or ionically bonded, like the alkali halides. For the latter, the absorption spectrum is interpretable essentially as a transition from a valence band to a conduction band, with the onset of steep absorption at the energy gap Eg. Such an interpretation is generally impossible in molecular crystals where the bonding is by weak van der Waals forces. Instead the absorption spectra are more directly related to the spectra of the isolated molecules, with various perturbations introduced by the crystal. Accordingly, the following discussion concentrates primarily on free molecular transitions, with a brief summary of the main effects of the crystalline lattice.

1.5.1 Vibronic States

The total energy E_t of a molecule in its electronic ground state, excluding translational and nuclear energy, may be expressed as:-

$$E_t = E_e + E_v + E_r \qquad (27)$$

where E_e is the electronic energy, E_v the vibrational energy, and E_r the rotational energy. In an equivalent manner, the total energy of a molecule in an excited state may be written:-

$$E_t' = E_e' + E_v' + E_r' \qquad (28)$$

If an absorption transition is defined by:-

$$\Delta E_x = E_x' - E_x$$

where x = t, e, v or r; then we find $\Delta E_r \simeq 10\ cm^{-1}$, $\Delta E_v \simeq 1000\ cm^{-1}$

and $\Delta E_e \simeq 30{,}000\ cm^{-1}$. Transitions involving ΔE_r yield the rotational spectrum, and occur in the far infrared region. Transitions involving ΔE_v and ΔE_r yield the vibrational and vibrational-rotational spectra, which occur in the near infrared area. Those involving ΔE_e and ΔE_v give the electronic and electronic-vibrational spectra, appearing in the visible and ultraviolet region. These latter transitions involving both electronic and vibrational energy are known as vibronic transitions. Each electronic absorption ΔE_e gives rise to an absorption band system, each band of which corresponds to a different value of ΔE_v.

Consider a molecule in which only one vibrational mode is dominant, so that it approximates to an harmonic oscillator. If the energy of the fundamental vibrational mode in the ground state is E_{1v} then:-

$$E_t = E_e + (n+\tfrac{1}{2})\, E_{1v} \qquad (29)$$

where n = 0, 1, 2 ... is the vibrational quantum number. If the energy of the fundamental vibrational mode in the excited state is E'_{uv} then:-

$$E_t' = E_e' + (n+\tfrac{1}{2})\, E'_{uv} \qquad (30)$$

where n = 0, 1, 2 .... The transitions constituting the main electronic absorption spectrum are:-

$$\Delta E_t = (E_e' - E_e) + n\, E'_{uv} + \tfrac{1}{2}(E'_{uv} - E_{1v}) \approx (E_e' - E_e) + n\, E'_{uv} \qquad (31)$$

since $E'_{uv} \simeq E_{1v}$. The lowest energy vibronic transition in a given band system (n = 0) is the 0-0 transition. A transition to the n^{th} vibrational level is the 0-n vibronic transition. An illustration of vibronic absorption levels is given in Figure 1.10.

The following simple notation for the electronic states is often

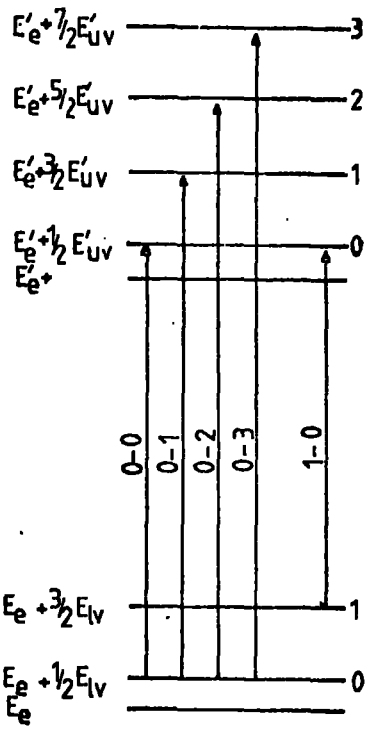

Fig. 1.10 Vibronic absorption levels.

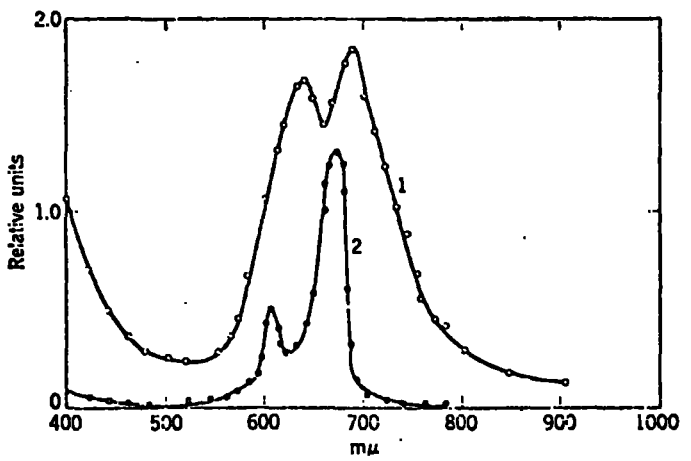

Fig. 1.11 Optical absorption spectra for Mg - phthalocyanine. (20)
(1) Sublimed film
(2) Solution in acetone

found.

S_0 - ground singlet state
S_1 - first excited singlet
S_p - higher excited singlet ($p>1$)
T_1 - first excited triplet
T_q - higher excited triplet

In general $S_0 - S_1$ and $S_0 - S_p$ absorptions are spin allowed, and correspond to the main electronic absorption spectrum, whereas the $S_0 - T_1$ and $S_0 - T_q$ transitions are spin forbidden, but may be observed with intense light sources.

There are several effects of the crystalline environment on the absorption spectra. It has been recognised for a long time that a general shift in frequency of the bands occurs. As an illustration, Figure 1.11 shows the frequency shift of a Mg-phthalocyanine sample on going from a solution in acetone to a sublimed film. Another effect is that the degeneracy present in the free molecule is removed, and that the selection rules may be relaxed to allow the appearance of "forbidden" transitions in the spectrum. In addition there is a multiplication of allowed transitions due to resonance between molecules, and a loss of rotational fine structure. However, a detailed discussion of these points is beyond the scope of this text.

1.5.2 Exciton States in Molecular Crystals

In section 1.4, excitons were categorised into two main types, namely, the delocalized Wannier exciton, generally suitable for semiconducting materials, and the localized Frenkel exciton, which is more appropriate to ionic and organic solids. Frenkel's exciton theory was first applied to molecular crystals by Davydov [21, 22]. Many aromatic crystals such as naphthalene and anthracene are comprised of two groups of translationally inequivalent molecules. If ψ_a and ψ_b are the wavefunctions of these molecules, the factor

group wavefunctions of the unit cell are:-

$$\psi_{\alpha} = (\psi_a + \psi_b)/\sqrt{2} \qquad (32)$$

and

$$\psi_{\beta} = (\psi_a - \psi_b)/\sqrt{2} \qquad (33)$$

These functions correspond to two exciton states, originating from the two inequivalent sites in the unit cell. Thus in a molecular crystal, with two molecules per unit cell, each excited state in the molecule produces two exciton states in the crystal. The energy separation between these states, known as the Davydov splitting factor, corresponds to the interaction energy of the molecule with translationally inequivalent molecules. The energy transitions to the exciton states are of the form:-

$$E_c = E_o + A \pm B \qquad (34)$$

where E_o is the corresponding energy transition in an isolated molecule; A is the spectral shift parameter, and 2B is the Davydov splitting factor.

The magnitude of the Davydov splitting depends on the transition moment of the transition and may vary between 20,000 cm^{-1} and 10 cm^{-1}, depending also on the extinction coefficient. When the intensity of a band system is distributed over a number of vibronic levels, the splittings are lower than they would otherwise be. Table 1.1. gives the Davydov splitting for p-transitions in crystalline anthracene. For a detailed theory of exciton absorption spectra of aromatic crystals, the reader is referred to McClure [23], Wolf [24] or Craig and Walmsley [25].

	p(0-0)		p(0-1)		p(0-2)	
	2B	P	2B	P	2B	P
Expt.	220	-	150	-	40	-
Expt.	190	-	140	-	80	-
Expt.	230	5	140	4.5	80	3
Theory	207	3.5	102	2.5	54	1.9
Theory	228	-	105	-	59	-

Table 1.1 Davydov splitting factors 2B and polarization ratios P of p-transitions in crystalline anthracene.

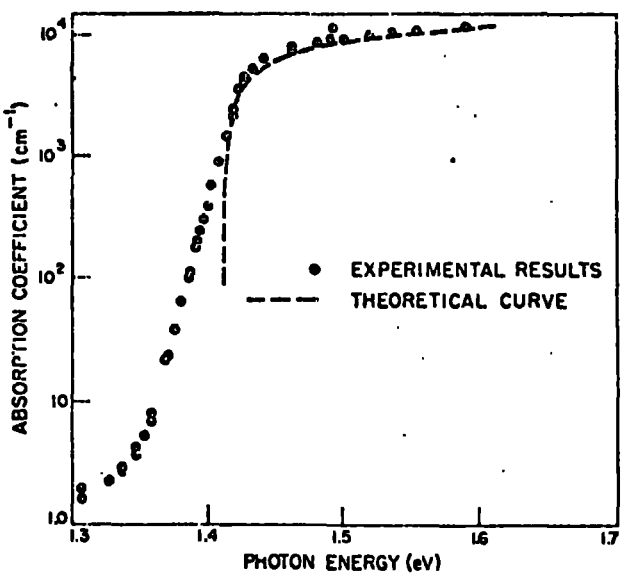

Fig. 1.12 Room temperature absorption edge of GaAs. (26)

1.6 Exponential Absorption Edges

In section 1.2, it was stated that for momentum conserving transitions between parabolic bands the absorption coefficient takes the form:-

$$(\alpha h\nu) = A(h\nu - E_g)^{\frac{1}{2}} \qquad (35)$$

Consequently, for direct transitions, zero absorption below E_g is expected, followed by a steeply rising edge. In practice, however, one often finds an exponentially increasing absorption coefficient, where α obeys the general relationship:-

$$\alpha = \alpha_0 \exp \beta\omega \qquad (36)$$

with $\omega = h\nu$, and β a constant of the material. This type of absorption edge is found, for example, in GaAs and InP for $\alpha \leqslant 10^4$ cm^{-1}, and in a number of other materials such as CdS and CdSe. As an illustration, Figure 1.12 shows the exponential absorption edge of GaAs at room temperature.

Several attempts have been made to explain the exponential dependence of absorption coefficient on energy. The most satisfactory explanations suggest that, depending on the situation, the effect is due either to the existence of impurity band tails or internal microfields within the specimen. These will be briefly referred to in turn.

When the concentration of shallow impurities in a semiconductor reaches a sufficiently high level, a density of states tail is formed which extends from the conduction or valence band into the forbidden gap. Stern and Dixon [27] have suggested that the minimum density of

impurities at which overlap occurs is given by:-

$$N_m \simeq 3\times10^{23} \quad (m^*/m_o\varepsilon) \quad cm^{-3}.$$

where ε is the dielectric constant and m^* the effective mass for carriers in the main band. For donors, in GaAs, this corresponds to about 10^{16} cm^{-3}. Figure 1.13 illustrates the mechanism of absorption due to tails of states. This diagram shows parabolic bands for a degenerate p-type semiconductor, with an exponential tail of states extending into the forbidden gap. The density of the states at energy E is given by:-

$$N_f = N_o e^{E/E_o} \tag{37}$$

where E_o is an empirical parameter. Assuming that the matrix element for the transition is independent of the photon energy, and that the transitions are allowed from momentum considerations, we may write for α:-

$$\alpha = -Ae^{h\nu/E_o} (E_o)^{3/2} \int_{(h\nu+\xi_p)/E_o}^{\xi_p/E_o} x^{1/2} e^{-x} dx \tag{38}$$

where $x = h\nu - E/E_o$, and ξ_p is the Fermi level. If $h\nu \gg E_o$ we find:-

$$\alpha(h\nu) = A (E_o)^{3/2} e^{h\nu/E_o} \cdot const. \tag{39}$$

giving the observed exponential energy dependence. The quantity E_o may be correlated with the impurity concentration as shown in Figure 1.14. The effect of the band tails is usually masked in absorption by the Burnstein/Moss shift due to free carriers. However, the effect is clearly noticed in compensated materials, where the tail states are depleted. Pankove [28] has studied band tailing effects in GaAs and has concluded that there is a definite correlation between the impurity

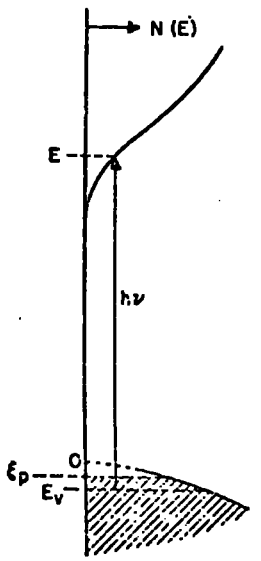

Fig. 1.13 Illustration of the absorption mechanism probing tails of states in a p-type semiconductor. The valence band tail is assumed to be empty and is therefore omitted.

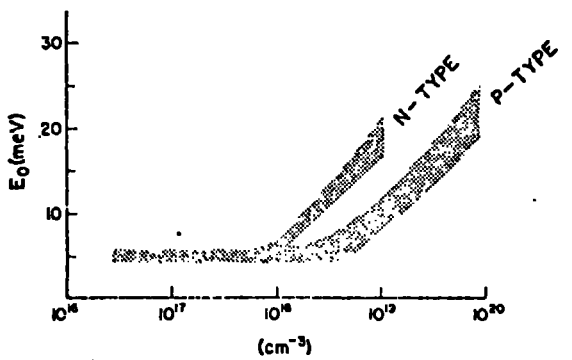

Fig. 1.14 Effect of increasing carrier concentration on the parameter E_0. (28)

state density and the absorption edge shape.

In contrast to the above approach, Redfield [29] attributes the broadening of the absorption edge to the electric fields of charged defects such as phonons, impurities and dislocations; he suggested that these fields could be as high as 10^5 V/cm. The effect of these fields is essentially an internal analogue of the Franz/Keldysh effect, [30, 31] whereby an electric field acting on a material produces an exponential shift of the absorption edge to lower energies. (The Franz/Keldysh effect will be discussed in detail in Chapter II). The origin of these internal fields has been the subject of work by a number of authors [32, 33]. Recently Dow and Redfield [34] have extended and improved upon Redfield's original work. Their latest approach unifies Redfield's original theory and the work of Dexter [35] and raises the possibility that virtually all exponential absorption edges may be due to electric field ionization of an exciton.

Some materials, such as CdS, display a definite temperature dependence of the slope of the exponential absorption edge, such that the various absorption curves at different temperatures combine at a focal point. For these materials, the absorption coefficient may be expressed as:-

$$\alpha = \alpha_o \exp \frac{\gamma'(\hbar\omega - \varepsilon'_o)}{kT} \qquad (40)$$

where T is the absolute temperature. ε'_o is then the focal point mentioned above, with each isotherm having a slope equal to γ'/kT. This empirical expression is known as the Urbach rule, after Urbach [36] who first proposed it to explain data on the alkali halides. The Urbach rule is found to be applicable to a number of materials, such as the alkali halides, CdS and trigonal selenium. Figure 1.15 illustrates this behaviour for a trigonal selenium specimen. At present the most satisfactory explanation of the Urbach rule is to be found in the Dow/Redfield theory.

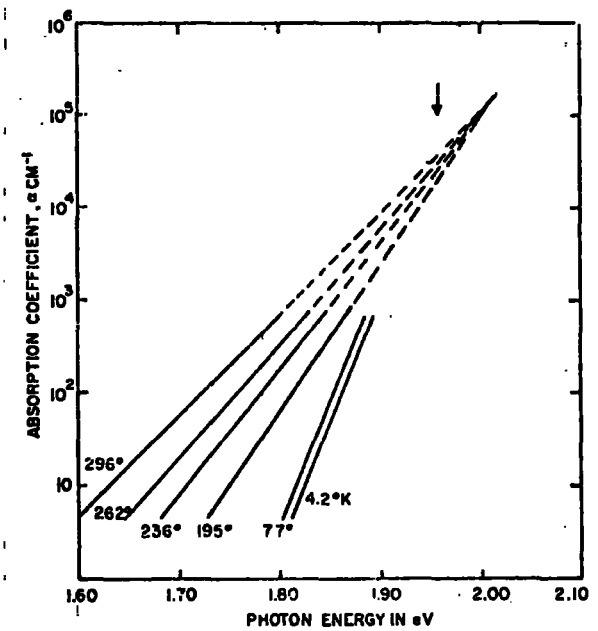

Fig. 1.15 Spectral dependence of the absorption coefficient of trigonal Se for light polarized with the E vector perpendicular to the c axis. The arrow gives the position of the exciton peak at 20 K. (37)

1.7 Polarization Effects in Absorption

In some materials, the use of polarized light in the optical absorption experiment enables one to obtain extra information concerning the solid's band structure. This is because the selection rules for optical absorption may vary, depending on the direction of the electric field vector of the incident radiation. A good example of this behaviour is CdS, whose absorption curve is displayed in Figure 1.16. It is evident from the diagram that, irrespective of the temperature, the absorption for light parallel to the c axis occurs at a higher energy. This situation may be understood with reference to Figure 1.17, which shows the band structure of CdS. The selection rules for this material are such that transitions from both the V_1 and V_2 valence bands are allowed for light polarized perpendicular to the c axis of the crystal but only transitions from the V_2 band are allowed for light polarized parallel to the c axis. The use of polarized light in this instance enables one to obtain the separation of the V_1 and V_2 valence bands.

1.8 Temperature Dependence of the Energy Gap

As the temperature of a semiconductor increases, the lattice expands and the oscillations of the atoms about their equilibrium positions increase. A major result of this is that the magnitude of the energy gap Eg will vary with temperature. A decrease in temperature results in an increase in energy gap for most materials, although the converse is true for the lead chalcogenides.

Table 1.2 gives the position and temperature dependence of the energy gaps of some III - V compounds. Since the shape of the absorption edge may vary as the temperature changes, the data are presented for $\alpha = 10\ cm^{-1}$.

The temperature dependence of the energy gap involves two contributions, namely, thermal dilatation of the lattice, and

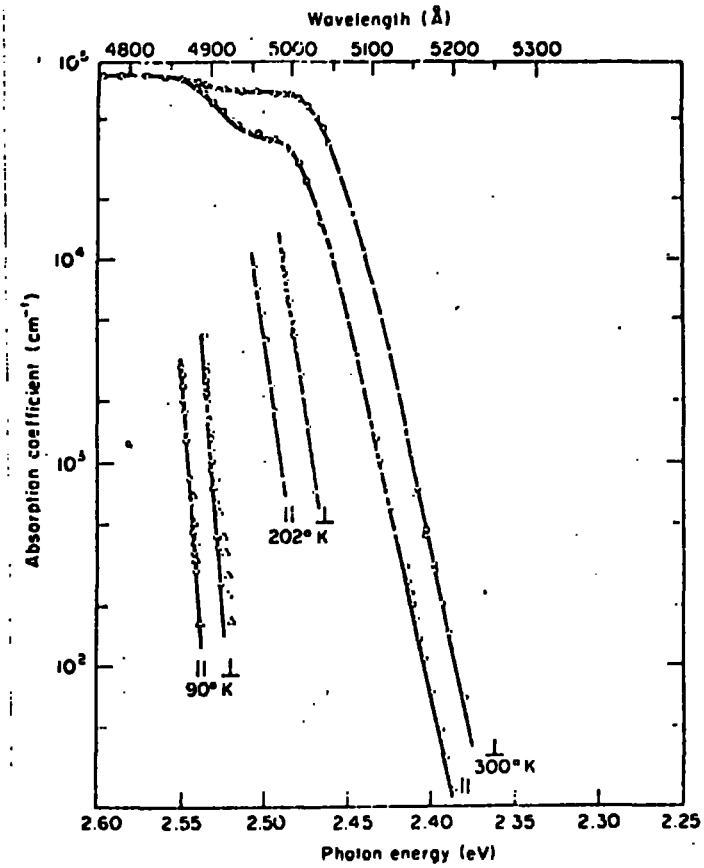

Fig. 1.16 Polarization dependence of the absorption coefficient of CdS at 300 and 90 K.(38)

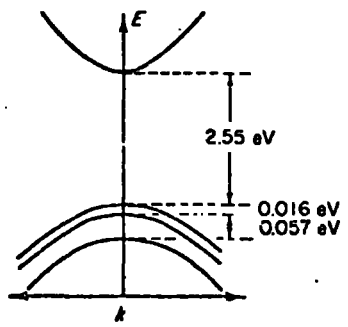

Fig. 1.17

Energy band diagram E(k) versus k near the conduction and valence band extrema in CdS.

electron-phonon interactions. The expression for the temperature coefficient of the energy gap at constant pressure is:-

$$\left(\partial E_g / \partial T\right)_p = \left(\partial E_g / \partial T\right)_V - (\beta / \chi)\left(\partial E_g / \partial P\right)_T \qquad (41)$$

where the first term arises from electron-phonon interactions and the second is the result of thermal expansion of the lattice. β is the coefficient of volume expansion, and χ the volume compressibility. Typically, twenty-five per cent of the total temperature dependence is due to the latter term. Bardeen and Shockley [40] and Shockley [41] have carried out an investigation of the lattice dilatation term and have suggested that, at high temperatures, a linear dependence of energy gap on temperature should be observed. This is in agreement with the result of Varshni [42] who fitted the energy gaps of a number of semiconductors to the relation:-

$$Eg(T) = Eg(o) - \frac{\alpha' T^2}{T + \theta} \qquad (42)$$

where α' and θ are constants of the material. For many materials, θ is found to be approximately equal to the Debye temperature at 0 K. Panish and Casey [43] have found that the energy gaps of GaAs and GaP fit the above equation over a wide range. As an illustration of the expected behaviour, Figure 1.18 shows the variation of the energy gap of a Ge crystal over a large temperature range. It is evident that the graph is linear at higher temperatures, in agreement with equation (42).

1.9 Absorption by Localized Impurities and Defects

The optical absorption spectrum of a semiconductor may be modified by the presence of impurities, defects, or charge complexes in the solid. This topic was briefly mentioned in section 1.6, in the context of exponential absorption edges. The intensity of this additional absorption is related, not only to the concentration of

	Photon energy for $\alpha = 10\ cm^{-1}$ (300°K) (eV)	Temperature dependence (eV K^{-1})	Extrapolation to 0 K (eV)
InSb	0.16	-2.9×10^{-4}	0.25
InAs	0.33	-3.5	0.44
InP	1.29	-4.5	1.42
GaSb	0.67	-4.3	0.80
GaAs	1.39	-4.3	1.52
GaP	2.24	-5.4	2.40
AlSb	1.63	-4.1	1.75

Table 1.2 Temperature dependence of the absorption edge in some III-V compounds.

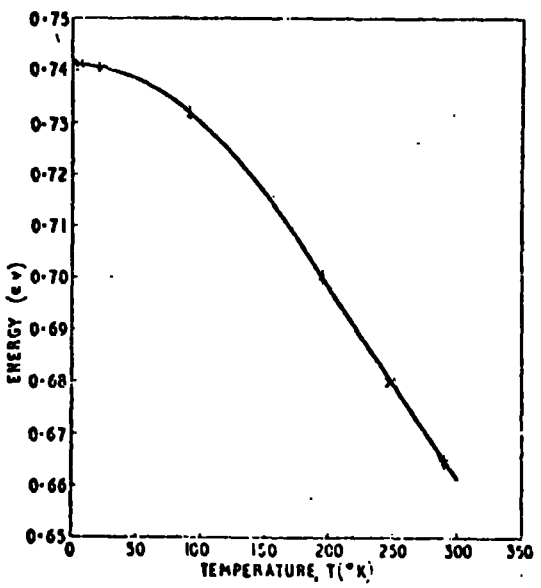

Fig. 1.18 Variation of the bandgap of Ge with temperature. (44)

impurities or defects, but also to the centre's charge state and capture cross-section. If the impurities are neutral, with charge carriers residing in the ground state, the only optical transitions possible are due either to transfers from the ground state to an excited state of the impurity, or to ionizing transitions in which the carriers are excited to a main band.

A good example of a transition from a neutral donor to a conduction band is illustrated in Figure 1.19, where the absorption spectrum of a boron doped silicon sample is shown. Absorption peaks are obtained for excitations to the states n = 1, 2, 3 .... The decrease of the absorption coefficient beyond the broad peak of Figure 1.19 is due to a decrease in the transition probability away from the bottom of the conduction band.

Deep transitions are also possible, between the valence band and the donor level, or an acceptor level and the conduction band. In these cases, the donor or acceptor must be ionized for the transitions to occur.

Eagles [46], Calloway [47] and Duke [48] have calculated an expression for absorption due to transitions from an ionized acceptor to the conduction band. Their analysis which is based upon the use of hydrogenic wave functions, leads to:-

$$\alpha = \frac{N_1 A_1 (h\nu - E_g + E_A)^{\frac{1}{2}}}{\left[1 + 2m_e a^{*2}(h\nu - E_g + E_A)/\hbar^2\right]^4} \qquad (43)$$

for direct transitions. A somewhat similar expression is obtained for transitions between a single valence level and a donor level. In the above expression N_1 is the density of ionized acceptors, E_A the ionization energy, and A_1 is given by:-

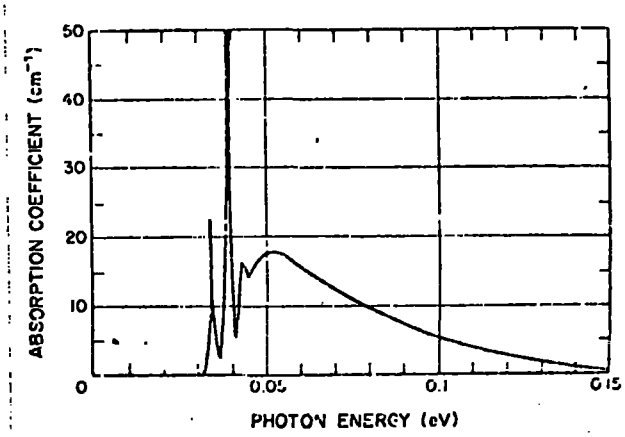

Fig. 1.19

Absorption spectrum of a boron-doped silicon specimen as a function of photon energy. (45)

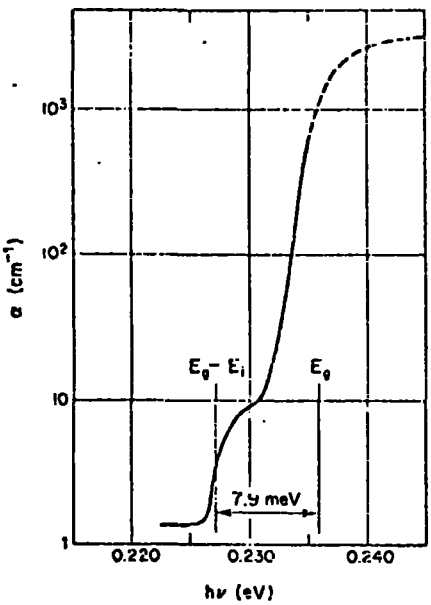

Fig. 1.20 Absorption by impurities in InSb at a temperature of 10 K. (19)

$$A_1 = \frac{256\pi^2 e^2 a^{*3} |p_{mo}|^2 (2m_e)^{3/2}}{3m_o^2 n \varepsilon_o c h^3 \nu} \qquad (44)$$

where a^* is the modified Bohr radius, p_{mo} the momentum matrix element between the main bands, m_e is the electron mass and ε_o the dielectric constant. In practice, the absorption due to shallow impurities is seldom resolved from the background absorption due to tails of states. However, when E_A is large compared to the width of the absorption edge, the impurity can contribute a definite step in the absorption spectrum. A good example of this is shown in Figure 1.20 where the absorption by zinc or cadmium in InSb is displayed. Assuming an energy gap of 0.236eV at 10°K, an ionization energy of 7.9 meV is found.

For indirect transitions the analysis is considerably more intricate. The photon energy at which an absorption takes place in this case is modified by the absorption or emission of a phonon, creating a pair of impurity spectra for each phonon energy.

1.10 Summary

In this brief review, the dominant optical transitions occurring in both inorganic and organic materials have been discussed. For the inorganic materials, some general expressions have been quoted for direct, indirect and forbidden transitions, and these are summarized in Table 1.3. Also shown is the expression for an exponential absorption edge. In addition to the above topics, the effect of excitons, temperature and polarized light on the optical spectra have also been examined. However, a number of topics such as free carrier and lattice absorption have been omitted, since they are of no direct relevance to the present work.

In the next chapter, the effects of large electric fields on the optical absorption properties of solids will be examined.

DIRECT TRANSITION	$\alpha\ E_p \propto (E_p - E_G)^m$ where $m = \frac{1}{2}$ holds for allowed transitions and $m = \frac{3}{2}$ holds for forbidden transitions
INDIRECT TRANSITION	$\alpha\ E_p \propto \frac{(E_p + E_{Pn} - E_G)^m}{\exp \frac{E_{Pn}}{kT} - 1} + \frac{(E_p - E_{Pn} - E_G)^m}{1 - \exp - \frac{E_{Pn}}{kT}}$ where $m = 2$ holds for allowed transition and $m = 3$ holds for forbidden transition
'SPECTRAL' URBACH RULE	$\alpha = \alpha_o \exp \frac{Y'[E_p - E_o]}{kT}$ where α_o, Y' and E_o are constants.

Table 1.3 Absorption edge mechanisms in semiconductors, ignoring excitonic effects.

CHAPTER II

ELECTROABSORPTION THEORY

2.1 Introduction

The electroabsorption technique may be defined as the application of large electric fields to materials, and the measurement of the resulting changes in optical transmission. The analysis of electroabsorption data is usually based upon two phenomena, namely the Franz/Keldysh effect and the Stark effect. In the interests of clarity, we will discuss the two effects in separate sections. It should, however, be borne in mind that in the majority of electroabsorption experiments both effects will be present. The magnitude of each effect will vary, depending on the material in question, and indeed the spectral area which one is investigating.

All the early electroabsorption theories were based upon models which totally neglected the Coulomb interaction between the electron-hole pair. These "one-electron" theories are discussed in section 2.2. As the quality of experimental data improved, it became obvious that the neglect of the electron-hole interaction was inadvisable in some cases. Accordingly, theories of electroabsorption including the Coulombic interaction began to appear about 1967. These theories are reviewed in section 2.4 of this chapter. The Stark effect is discussed in section 2.5, and its application to molecular crystals is reviewed in section 2.6. The chapter concludes with a discussion of impurity electroabsorption.

2.2 The Franz/Keldysh Effect

Franz [1] and Keldysh [2] were the first to consider

theoretically the effect of an electric field on the fundamental absorption edge of a semiconductor. The primary prediction of these authors was that in the presence of a high electric field, the optical absorption edge broadens and shifts towards lower energies. That is, a tail region (exponential in shape) is added to the absorption edge. This phenomenum is widely referred to as the Franz/Keldysh effect. The finite absorption for $h\nu < Eg$ is considered to be the result of a photon assisted tunnelling process.

The main conclusions of Keldysh's paper will now be summarized. In the absence of an electric field, the total probability of absorption of a photon $\hbar\omega$ per unit time per unit volume may be expressed as:-

$$W(\omega) = \left(\frac{e}{m}\right)^2 \frac{2\pi\hbar}{\omega} \int \left| \underline{\underline{eM}}_{vc}(\underline{p}) \right|^2 \delta\left\{\mathcal{E}_c(\underline{p}) - \mathcal{E}_v(\underline{p}) - \hbar\omega\right\} \frac{d^3p}{(2\pi\hbar)^3} \qquad (1)$$

where

$$\underline{M}_{vc}(\underline{p}) = \int \psi_c(\underline{p},\underline{r})\, \nabla\, \psi_v(\underline{p},\underline{r}) d\tau \qquad (2)$$

and the other symbols have their usual meanings. For a symmetry allowed transition, (direct edge), this may be simplified to:-

$$W(\omega) = \frac{1}{\pi}\frac{e^2}{\hbar c}\frac{c}{\omega}\left[\frac{m_1 m_2 m_3}{m^3}\,\frac{2(\hbar\omega-\varepsilon_o)}{m}\right]^{\frac{1}{2}} \left| \underline{\underline{eM}}_{vc}(\underline{p}_m) \right|^2 \qquad (3)$$

where m_i^{-1} is the principal value of the tensor m_{ik}^{-1}.

When an electric field is applied to the crystal expression (1)

no longer contains delta functions and therefore, absorption of photons with energy less than ω_o is possible. In this case, the total probability of absorption may be written as:-

$$W(\omega) = \frac{e^2}{\hbar c}\frac{c}{\omega}\left(\frac{m_1 m_2 m_3}{m^3}\,\frac{2(\varepsilon_o - h\omega)}{m}\right)^{\frac{1}{2}} \frac{(e\hbar E)^2}{m_{\parallel}\,(\varepsilon_o - h\omega)^3}\left|\underline{\underline{eM}}_{vc}(\underline{p}_m)\right|^2$$

$$X \exp\left\{-\frac{4(2m_{\parallel})^{\frac{1}{2}}}{3e\hbar E}(\varepsilon_o - h\omega)^{3/2}\right\} \qquad (4)$$

with

$$m_{11}^{-1} = \sum_i \mathrm{Cos}^2\,\gamma_i/m_i \qquad (5)$$

Here m_i^{-1} are the diagonal terms of the tensor m_{ik}^{-1} and γ_i are the angles between the field and the principal axis of m_{ik}^{-1}.

The above expression indicates the formation of an exponential-type tail in the long wavelength region. Comparison of expressions (3) and (4) illustrates further that there is a shift of the absorption edge towards the red, such that:-

$$\Delta\omega_E = \frac{1}{\hbar}\left[(eEd)^2\frac{\hbar^2}{m_{\parallel}\,d^2}\right]^{1/3} \qquad (6)$$

For a direct absorption edge, the field dependence of the change in the absorption coefficient is thus given by:-

$$\Delta\alpha = \text{constant} \times E^{0.33} \qquad (7)$$

Later workers have found that for direct forbidden transitions, the change in absorption should be dependent on $E^{1.0}$, whereas, for indirect transitions, it is proportional to $E^{1.33}$.

Physically, one may understand the Franz/Keldysh effect as follows. The application of a large electric field causes the energy bands to tilt in real space, as shown in Figure 2.1(a). The band edges, however, remain parallel and separated vertically by the energy gap Eg. The wavefunctions of the conduction and valence band states will now have exponentially decaying tails extending into the forbidden gap, corresponding to negative potential energy. This raises the possibility that an electron may tunnel some distance Δx into the forbidden gap and then, by absorbing a photon of energy $h\upsilon < Eg$, be transferred to the conduction band, thereby giving rise to field-induced absorption for energies $<Eg$. The tunnelling process is similar to that proposed by Zener [3] in 1933. The effect of an electric field on a typical direct edge is illustrated in Figure 2.1(b).

2.2.1 Extension of Original Theories

The original theories of Franz and Keldysh have subsequently been greatly extended. Two alternative approaches have been developed. In 1963 Callaway [4] was able to produce expressions for transition rates in optical absorption in the presence of an electric field. This author used the results of Adams [5], Kane [6], Argyres [7] and Houston [8] to calculate the mixing of Bloch functions under an applied field. A direct result of the application of an electric field is that states are mixed along the field direction in k-space.

An alternative method of tackling the problem was given by Tharmalingham [9]. He based his calculations on the results of the work of Dresselhaus [10] and Elliott [11] on excitons. Discarding the electron-hole interaction, Tharmalingham evaluated the effect of a uniform electric field on the probability of producing an electron-hole pair. If one neglects the Coulombic interaction, the solution to the effective mass Schrodinger equation may be expressed in terms of Airy functions. Since the characteristics of Airy functions were well known, Tharmalingham

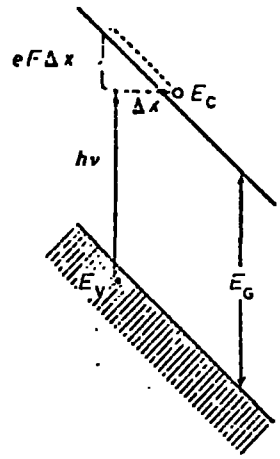

Fig. 2.1 (a)

Energy band diagram illustrating absorption in the presence of an electric field.

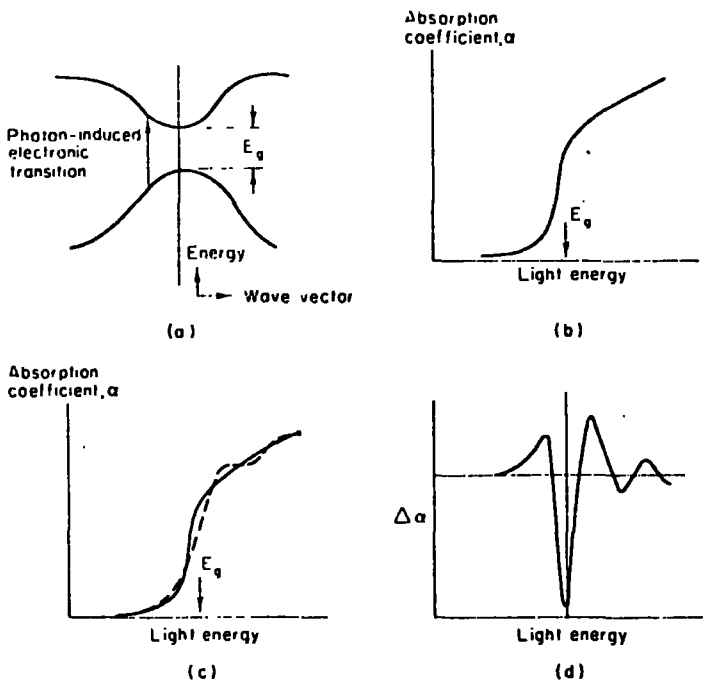

Fig. 2.1 (b) Typical electroabsorption spectrum and its correlation with band structure:-(a) semiconductor band diagram (b) absorption edge (c) finite and zero-field absorption (d) electroabsorption spectra.

was able to postulate that, as well as the field induced exponential tail in the absorption, a series of oscillations in the absorption coefficient would arise above the energy gap. Callaway [12] in 1964, extended his original treatment and confirmed that oscillations should indeed occur above the energy gap. The oscillations were explained by Callaway as being due to Stark splitting of the band states in the presence of the electric field. The Stark effect will be discussed in some detail in section 2.5, so it will suffice at this point to say that the phenomenon is the electrical analogue of the Zeeman effect, whereby in the presence of an electric field, discrete levels may be broadened or split into a number of components. The theory of Stark splitting of the continuum of states into a series of discrete levels has been given by Wannier [13]. The oscillations are assumed to be due to a series of transitions between the field induced discrete states. A more complete discussion of the oscillatory part of the electroabsorption spectrum will be given in section 2.4.

Aspnes [14][15] in 1966 and 1967 expanded the above mentioned theories to include all four types of critical point, rather than simply an M_0 absorption edge. Critical points are defined as regions of the energy band structure in k-space where the conduction and valence bands are parallel, that is where:-

$$\nabla k \, (E_c - E_v) = 0 \qquad (8)$$

There are four types of critical point, namely:-

M_0: m_1^*, m_2^*, m_3^* all positive

M_1: m_1^*, m_2^* positive, m_3^* negative

M_2: m_1^*, m_2^* negative, m_3^* positive

M_3: m_1^*, m_2^*, m_3^* all negative

m^* is the reduced effective mass of an electron-hole pair, that is,

$$1/m_i^* = 1/m_{ei}^* + 1/m_{hi}^* \qquad i = 1, 2, 3 \tag{9}$$

Figure 2.2 summarizes the main conclusions of Aspnes paper. ε_2 is the imaginary part of the dielectric constant and is related to the absorption coefficient by:-

$$\varepsilon_2 \propto al \propto/\hbar\omega \tag{10}$$

ε_1 is the real part of the dielectric constant. Philips [16] also considered the effect of electric fields on all four types of critical point and came to somewhat similar results.

In an attempt to consolidate electroabsorption theory, Aspnes, Handler and Blossey [17] demonstrated that the method of Callaway and that of Tharmalingham come to the same effective conclusion. In their paper they produced an expression for the imaginary dielectric constant ε_2 in the presence of a field F, namely:-

$$\varepsilon_2 = \sum_{\underline{k}\, n'n} C_{n'n}(\underline{k}) \frac{1}{|\hbar\Omega|} A_i \left[\frac{E_{n'n}(\underline{k}) - \hbar\omega}{\hbar\omega}\right] \tag{11}$$

where

$$C_{n'n}(\underline{k}) = \frac{4\pi^2 e^2}{m^2\omega^2} \frac{2}{(2\pi)^3} \left|\hat{\varepsilon} \cdot P_{n'n}(k)\right|^2 \tag{12}$$

with

$$\hbar\Omega = \left[\frac{\hbar^2 F^2}{8m^*}\right]^{1/3} \tag{13}$$

and

$$P_{n'n}(k) = dr\, \psi^*_{kn'}(r) \frac{\hbar}{2} \nabla \psi_{kn}(r) \tag{14}$$

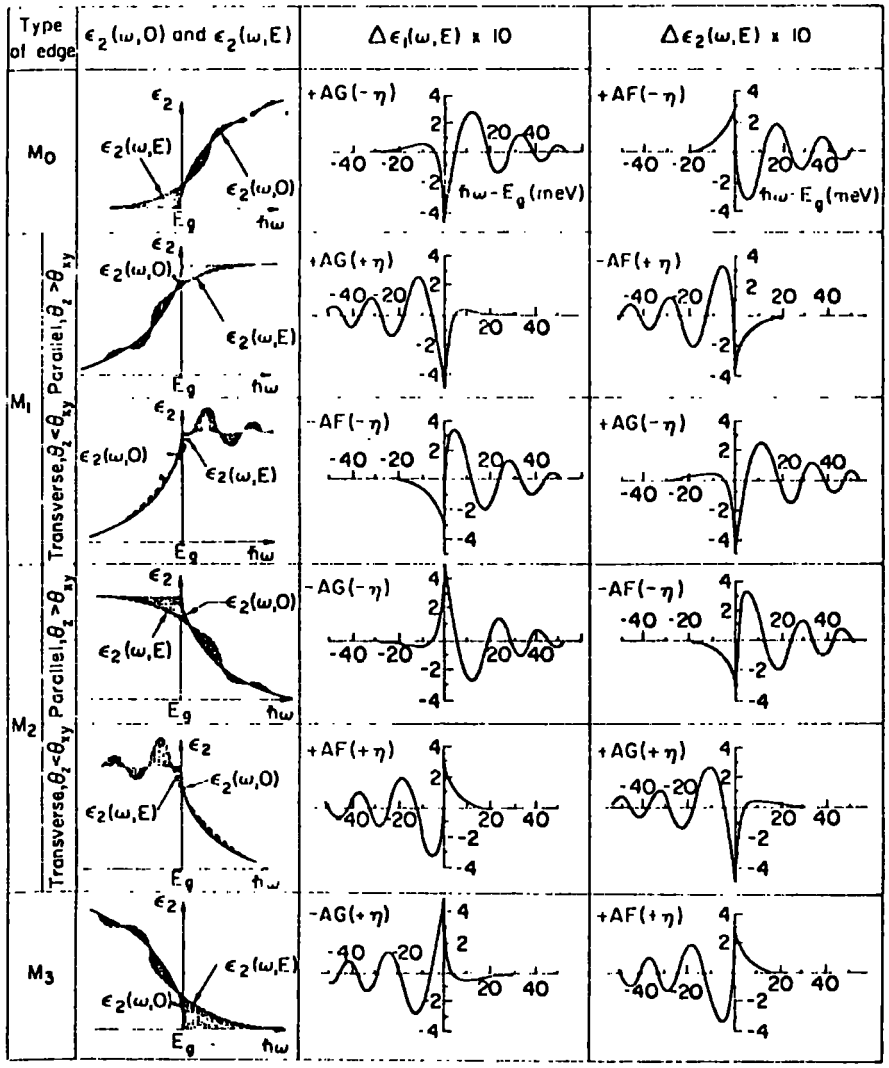

Fig. 2.2 Effects of the electric field on the dielectric constant near critical points neglecting electron-hole interaction. $\Delta\mathcal{E}_1$ and $\Delta\mathcal{E}_2$ are calculated assuming $\hbar\Theta$= 10 meV, E_g = 0.8 eV and B = 1. Also $\eta = (\hbar\omega - E_g)/\hbar\Theta$ $A = (B \times \Theta^{\frac{1}{2}})/\omega^2$, and $\Theta = (eF)^{\frac{2}{3}}/2m^*\hbar^{\frac{1}{3}}$. Here E_g is the bandgap, F the applied field and m^* the reduced effective mass. (37)

In these expressions A_i is the Airy function, m^* the reduced effective mass and F the applied field.

The formula for ε_2 in the absence of an electric field has been found to be:-

$$\varepsilon_2 = \sum_{\underline{k}} \sum_{n' \; n} C_{n'n}(k) \, \partial(E_{n'n}(k) - h\omega) \qquad (15)$$

On inspecting the two equations for ε_2, it may be seen that the result of the application of the electric field is to substitute the Airy function for the energy conserving delta function. Figure 2.3 shows in more detail the type of electroabsorption data predicted by these early theories for an M_0 edge. One can see that for this type of edge an exponential tail in α is expected below Eg, with oscillations above Eg.

2.2.2 Indirect Absorption Edges

As a logical sequence to the work of Tharmalingham and Callaway on direct transitions, Penchina [18] considered the effect of an electric field on an indirect absorption edge. This work was consolidated in the same year by papers from Fritsche [19], Chester and Fritsche [20] and Yacoby [21]. Taking the direct transition theory as his starting point, Penchina estimated the scattering by phonons in terms of an extra sum over the centre of mass wave vector. The net result in the electroabsorption spectra is a series of peaks related to phonon emission or absorption. A good example of an indirect gap electroabsorption spectra is provided in Figure 2.4 for silicon [22]. For these data, which were obtained on a p-n-n^+ junction, the authors noted that the limiting factor in the observation of structure was the overlapping of the various processes. Nevertheless, several phonon peaks were identified and are noted in the diagram.

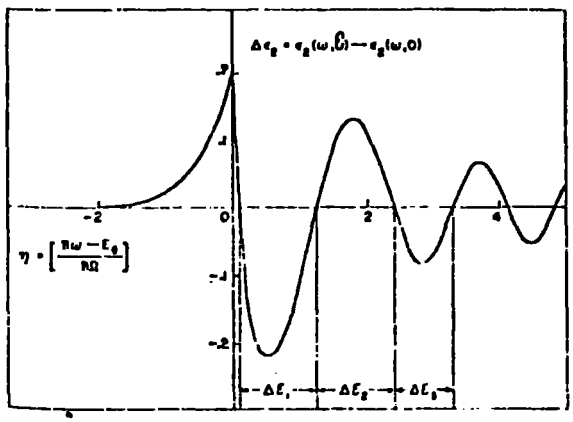

Fig. 2.3 The change in the imaginary part of the dielectric constant $\Delta\varepsilon_2$ as a function of η, where η is as defined in Fig. 2.2. (37)

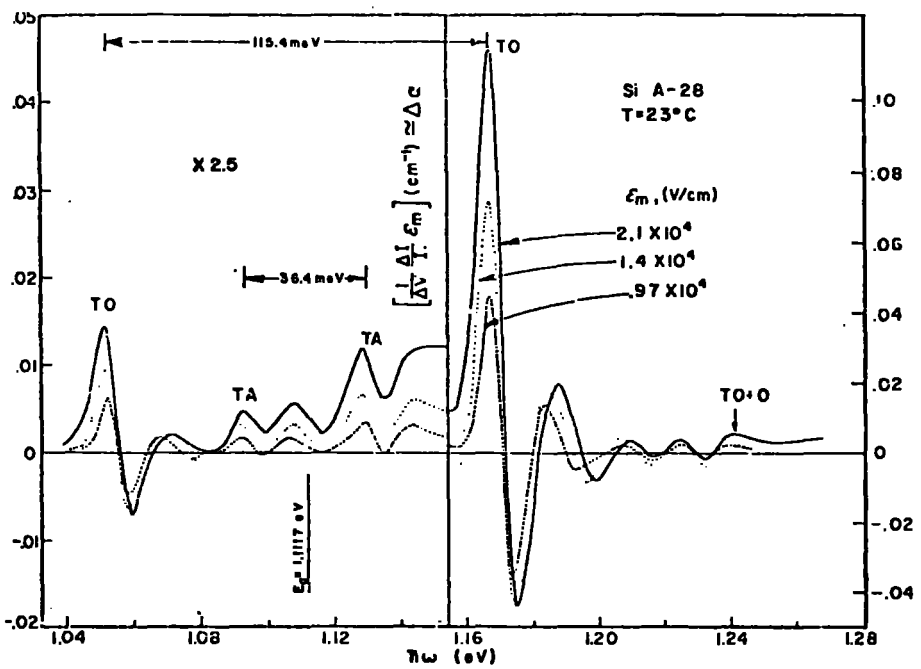

Fig. 2.4 Electric field induced absorption at the indirect edge of Si for three different electric fields at T = 23° C. TO is the transverse optical phonon, TA the transverse accoustical phonon and O is the optical phonon with zero momentum. (22)

2.2.3 Exponential Absorption Edges

The theories described previously have dealt with the transformation of a direct absorption edge into an exponential type edge due to the electric field. However, as pointed out in section 1.6, many materials exhibit an exponential type absorption edge, even in the absence of an external field. The origin of such an absorption edge was discussed previously. In his original paper, Franz examined the effect of an electric field on an exponential type absorption edge and found that over low values of α, the theoretical expressions could be greatly simplified. For an absorption edge obeying the relationship

$$\alpha = \alpha_o e^{-\beta E/kT} \tag{16}$$

Franz found that the change in absorption, $\Delta\alpha$, could be expressed as:-

$$\Delta\alpha = \alpha\beta^3\hbar^2F^2/24m^*_e \tag{17}$$

where β is the logarithmic slope of the absorption edge, F is the applied field and m^* is the reduced effective mass. This expression is valid for low values of α, irrespective of the cause of the original absorption edge. It assumes, however, that in the presence of the electric field, the edge retains its original slope β. It is clear from the above equation that for materials which exhibit exponential type absorption edges, electroabsorption provides a means of measuring the reduced effective mass m^*. Since it is extremely difficult to measure effective masses in doped materials, this represents an important use of the electroabsorption experiment. The quadratic dependence of $\Delta\alpha$ on field in these cases is evident from the above equation. This is significantly different from the

0.33 field dependence expected for direct edges. Gutsche and Lange [23] have found a quadratic field dependence in CdS and CdSe single crystals, and using the above equation have determined the effective mass along a number of crystallographic directions.

2.2.4 Summary of Main Conclusions of "One-Electron" Theories

It is essential to note that all the theories mentioned up to the present have been formulated within the context of the one-electron model, that is without the electron-hole interaction. A summary of the various conclusions of these theories is presented in tables 2.1(a) and 2.1(b). The main predictions are that the first peak in the electroabsorption spectra should occur at, or very near, the energy gap Eg, as shown in Figure 2.3. In addition, the relative amplitude of the various peaks should increase in a fixed ratio, while the magnitude of those above Eg should decay slowly with energy. Furthermore, the distance between peak heights should be dependent upon electric field as $F^{\frac{2}{3}}$. The second part of the table gives the field dependence of the change in absorption coefficient α for a number of different absorption mechanisms. It is interesting to note that if m is the exponent in the spectral dependence of the zero field absorption mechanism and n the exponent in the field dependence of the electroabsorption peak, then:-

$$3n = 2m \qquad (18)$$

In section 2.4, some of the deficiencies of these theories will be exposed. However, before doing so, it is worth examining the results of the early experimental work in electroabsorption.

2.3 Review of Early Experimental Papers

The earliest experimental verification of the theoretical predictions of Franz and Keldysh was recorded in 1960, by Williams [24] on CdS. An example of Williams' data is shown in Figure 2.5, together with an illustration of how the crystal was mounted. This observation

(i) Energy gap at (or near) 1st positive peak i.e. $\eta = \frac{E_P - E_G}{h\Omega} = 0$
(ii) Field dependences of amplitude of peaks in $\Delta\alpha$ summarized in Table 2.1(b)
(iii) Relative amplitude of various peaks should increase in a fixed ratio.
(iv) $\Delta\alpha(E_P,F) = \alpha(E_P,F) - \alpha(E_P,0)$ $= \frac{K\mu}{\omega(E_G-\omega)} \exp \frac{4}{3} \frac{(2\mu)^{\frac{1}{2}}(E_G-\omega)^{\frac{3}{2}}}{\hbar \epsilon F}$ for energies below the band gap $E_P \equiv h\omega$
(v) Amplitude of the peaks on the high energy side should decrease slowly with η.
(vi) Distance between peak heights should increase as $F^{\frac{2}{3}}$.

(a)

TYPE OF TRANSITION	$\alpha(E_P)$	MAJOR PEAK AMPLITUDE $\Delta\alpha \propto F^n$
DIRECT ALLOWED	$(E_P - E_G)^{\frac{1}{2}}$	$n = 0.33$
DIRECT FORBIDDEN	$(E_P - E_G)^{\frac{3}{2}}$	$n = 1.00$
INDIRECT	$(E_P - E_G \pm E_{Pn})^2$	$n = 1.33$

(b)

Table 2.1 (a&b) Theoretical predictions of the one-electron electroabsorption theories.

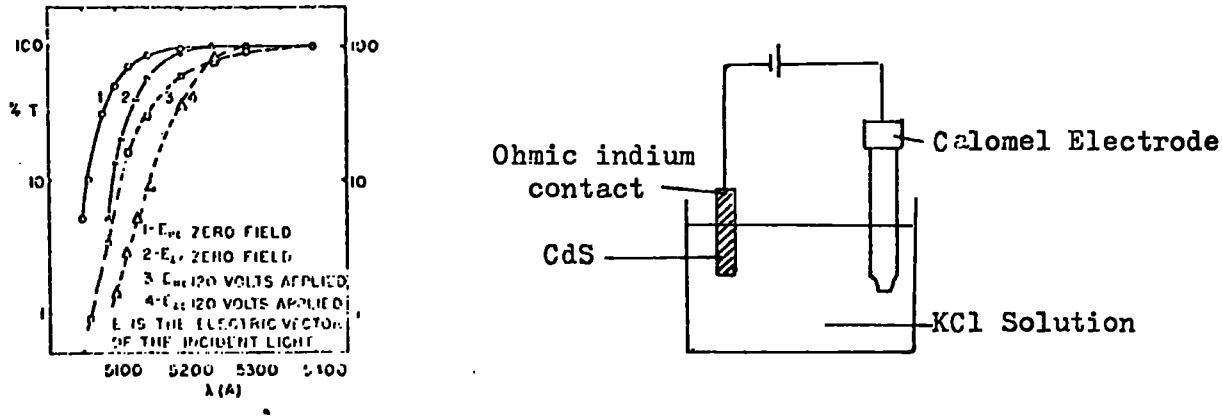

Fig. 2.5 Percentage transmission for light of various wavelengths through a CdS crystal. The way in which the crystal was mounted is shown on the right. (24)

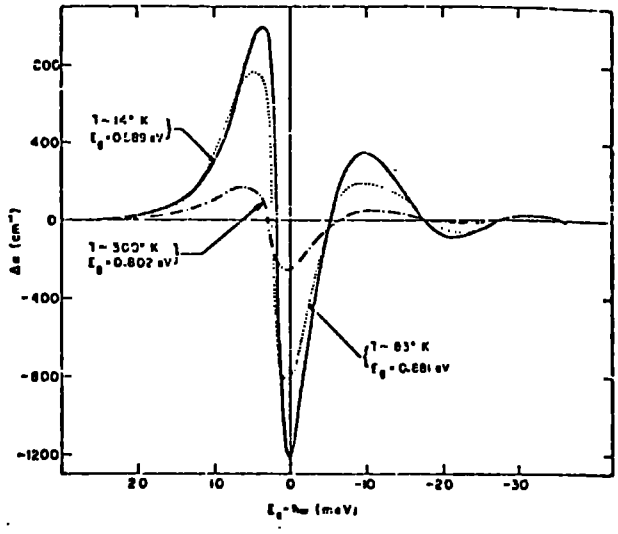

Fig. 2.6 Field-induced change in the absorption coefficient of germanium near its direct edge for an electric field of 10^4 V/cm, at three different temperatures. (37)

was followed in 1962 by Moss [25], who measured the effective mass for GaAs using the electroabsorption technique. The interest generated by these results stimulated a great deal of experimental work in this field. At the Paris Semiconductor Conference in 1964, Chester and Wendland [26] described their results on silicon, while Frova and Handler [27][28] produced data on germanium. The latter group of authors used a back-biased p-n junction to sustain the high fields. Rees [29] in 1967 observed the oscillations above the band gap in gallium arsenide, as predicted by Tharmalingham and Callaway. By 1968 published data were available on the effect of electric fields on the absorption edges of CdS [30], GaAs [25], S_i [31], CdTe [32], GaP [33] and a few other materials [34, 35].

Attempts were made by experimentalists and theoreticians to fit the above data to the one-electron theories mentioned in section 2.2, with varying degrees of success. Discrepancies between theory and experiment were initially blamed on non-uniform field distributions, band non-parabolicities and certain other experimental factors. However, by about 1966, it was generally accepted that, for certain materials and spectral regions, experimental factors could not explain the observed deviation of the results from theory. In that year, Hamakawa et al [36] suggested that excitonic effects were the dominant cause of discrepancy between theory and experiment. In 1968 he and his co-workers demonstrated that only one of the six possible predictions of single-particle electroabsorption theory could be verified experimentally, using Ge [37]. An example of Hamakawa's data is displayed in Figure 2.6. The figure shows the field-induced change in the absorption coefficient of germanium near its direct edge. We note that the energy gap Eg falls, not at the first positive peak as predicted by single-particle electroabsorption theory, but at the centre of the first negative peak. A further discrepancy was found in the field dependence of the peak magnitudes. Instead of the expected field dependence of $F^{\frac{1}{3}}$, the observed dependences were $\frac{3}{4}$, $\frac{5}{4}$ and $\frac{3}{4}$ respectively. Other deviations from theory were also noted. The inadequacy of single-particle electroabsorption theory to explain additional data on CdS [38] was similarly attributed to excitonic

effects.

The following section of this thesis discusses attempts to incorporate Coulombic effects in electroabsorption theory.

2.4 Excitonic Effects In Electroabsorption

As mentioned in section 1.4, excitons have generally been categorized into two types, Frenkel [39] or Wannier [40]. This section is restricted to a discussion of electric field effects on Wannier excitons, since very little information exists on electric field effects on Frenkel excitons.

Wannier first suggested his non-localized exciton theory in 1937. The theory was greatly improved by Dresselhaus [41], who introduced effective masses into Wannier's treatment. Optical absorption by Wannier excitons was calculated by Elliott [42], using the results of the improved theory. As mentioned in section 1.4, the Wannier exciton may be considered as an electron-hole pair, bound together by a Coulomb potential. We may define the bound states of this electron-hole pair by:-

$$E_n = E_g - R/n^2 \qquad (19)$$

These states occur in the forbidden band-gap of semiconductors and insulators. In this equation Eg is the energy gap, R the effective Rydberg, and n an integer. We may define the effective Rydberg as

$$R = 13.6\ (m^*/m_o^2)\ \text{eV} \qquad (20)$$

In this equation, m is the rest mass of the electron, m^* is the reduced mass of the electron-hole pair, and ε_o is the static dielectric constant of the material. It is also possible to define an effective Bohr radius as:-

$$a_o = \hbar^2 \varepsilon_o / m e^{*2} \qquad (21)$$

Using a_o and R it is possible to specify an ionization field E_i, where E_i is the field required to ionize the ground state of the exciton. E_i is simply given by:-

$$E_i = R/ea_o \qquad (22)$$

2.4.1 Numerical Calculations

The first calculations of the effect of an electric field on Wannier excitons were performed for the Stark effect in hydrogen [43]. (This is discussed in section 2.5). First and second order perturbation theory were used in these calculations. This approach is evidently valid for hydrogen, since the ionization field is very high ($\simeq 10^9$ V/cm), and accordingly any externally applied field will only produce a small modification to the energy levels of the system. However, if we consider the case where the externally applied field is of the order of, or greater than, the ionization field, we see that this approach is invalid. In this case, the externally applied field must be treated on an equivalent basis to the Coulombic field. The value of E_i varies greatly between materials. Table 2.2 gives some examples. In many materials it is possible to apply fields in excess of 10^5 V/cm before breakdown occurs. From a glance at table 2.2, we can see that for many of the materials listed, fields of that order would be greater than the ionization field E_i.

In 1966, Duke and Alferieff [44] treated a simplified model of optical absorption by excitons in an external field. The approach of these authors was to assume that the Coulombic potential is zero outside a given critical radius, and to assume the external field is zero inside this radius. (Figure 2.7 shows the Coulombic potential well with and without an applied field). Unfortunately, the model of Duke and Alferieff predicted incorrect Stark shifts of the exciton lines with electric field, despite the apparently reasonable nature of the approximation.

The approach of Duke and Alferieff was subsequently improved by

Material	Energy gap (eV) E_g	Effective Rydberg energy (eV) R^a	Ionization field R/ea(V/cm) $\mathcal{E}_i$
PbI_2	2.55	0.073	4.6×10^5
Ge	0.80	0.0014	5.5×10^2
GaAs	1.41	0.0051	5.7×10^3
GaSb	0.813	0.0018	1.0×10^3
InP	1.29	0.0065	7.8×10^3
InAs	0.360	0.0018	7.0×10^2
InSb	0.2357	0.0005	7.6×10^1
AlSb	1.6	0.0075	1.2×10^4
CdS	2.5831	0.0294	1.4×10^5
CdSe	1.8415	0.0157	6.0×10^4
CdTe	1.606	0.0100	3.1×10^4
ZnS	3.9115	0.0401	2.0×10^5
ZnSe	2.818	0.0190	7.5×10^4
ZnTe	2.301	0.0130	4.7×10^4

Table 2.2 Energy gaps, Rydberg energies and Ionization fields for several semiconductors.

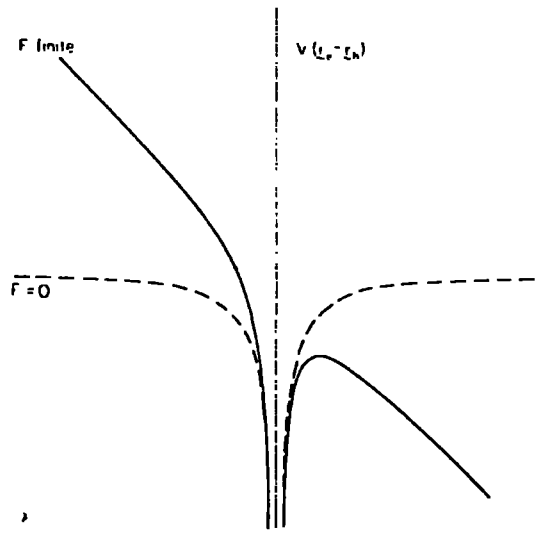

Fig. 2.7 The Coulomb potential for both zero and finite electric fields.

Ralph [45] and Dow and Redfield [46][47], who numerically integrated the effective mass differential equation. Unfortunately, the results of these workers do not show the electric field induced oscillations in the continuum density of states. An alternative approach to the problem was suggested by Enderlein [48] who attempted to solve the equations using a Green's function method. However, the calculations of Enderlein are only valid in the limit of weak electron-hole binding [47]. Blossey [49] was the first to calculate the effect of an electric field on the higher bound exciton levels, and succeeded in obtaining the electric field induced oscillations in the continuum density of states. His derivation therefore, represents the most detailed computation to date. The main conclusions of the numerical computations are now presented.

2.4.2 Results of Numerical Calculations

The main conclusions of the numerical calculations are as follows:

1. In the region below the absorption edge, the logarithm of the absorption coefficient should be linearly dependent on photon energy.

2. The energy position of the exciton ground state should vary with field in the manner shown in Figure 2.8. In agreement with perturbation theory, the ground state shifts to lower energies for fields less than 0.85 F_i. However for $F \geq 0.85\ F_i$ the ground state begins to tunnel out of the potential well, and accordingly, shifts towards higher energies.

3. Again in accordance with perturbation theory, other bound states are split and broadened according to their degeneracies. For higher fields, these levels will be blurred into the continuum. This occurs earlier for these levels since they have lower binding energies.

4. As a result of the quenching and broadening of the exciton

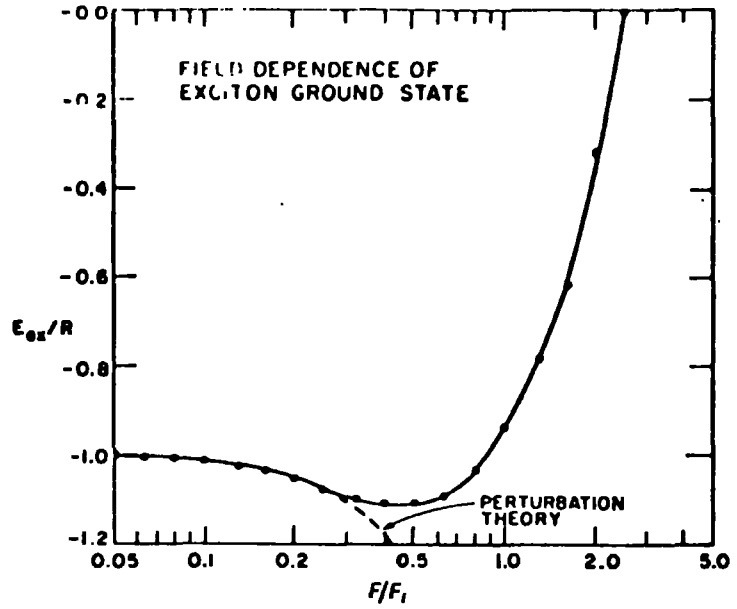

Fig. 2.8 Electric field dependence of the exciton ground state energy for a hydrogenic model. The position is measured in units of the exciton Rydberg from the continuum. The electric field is in units of the ionization field Fi.

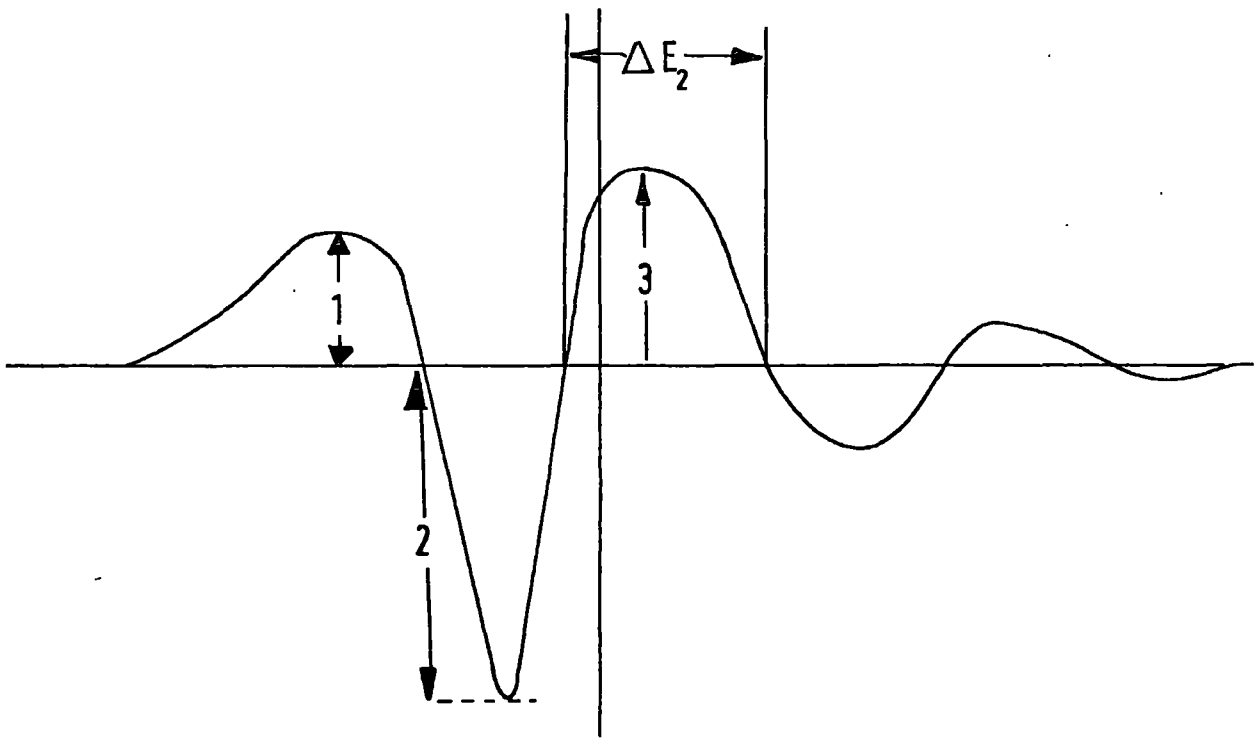

Fig. 2.9 Definition of quantities discussed in section 2.4.2.

ground state, peaks of the form shown in Figure 2.9 occur. The magnitude of peaks 1 and 3 will be dependent on the degree of quenching and broadening, and accordingly may increase or decrease with applied field. The negative peak (2) should never decrease with applied field, since this peak is related to the degree of ionization of the exciton.

5. For low fields, that is, $F/F_i < 0.5$, the energy position of the negative peak (2) should occur at Eg-R. Note that for non-excitonic electroabsorption theory, the first positive peak should occur at Eg.

6. The separation ΔE_2 in Figure 2.9 should increase as $(F/F_i)^{\frac{2}{3}}$, and be independent of temperature.

7. Finally, for fields in excess of the ionization field, the external electric field begins to dominate the Coulombic field, so the inclusion of the Coulombic interaction has a negligible effect.

2.4.3 Typical Data

A good example of a material in which excitonic effects are crucial in electroabsorption is PbI_2. This material has been studied by several authors [50, 51] who have detected a number of exciton absorption lines in the zero field spectra of the fundamental absorption edge. Perov [52] et al in their electroabsorption studies on this material found that the free electron-hole electroabsorption theory was not capable of explaining their results. Figure 2.10 shows the absorption spectra of this material with and without an applied field. It is evident that the exciton ground state (A), is clearly quenched and broadened. The type of electroabsorption spectrum found in this material is shown in Figure 2.11, where $\Delta\alpha$ is plotted as a function of photon energy.

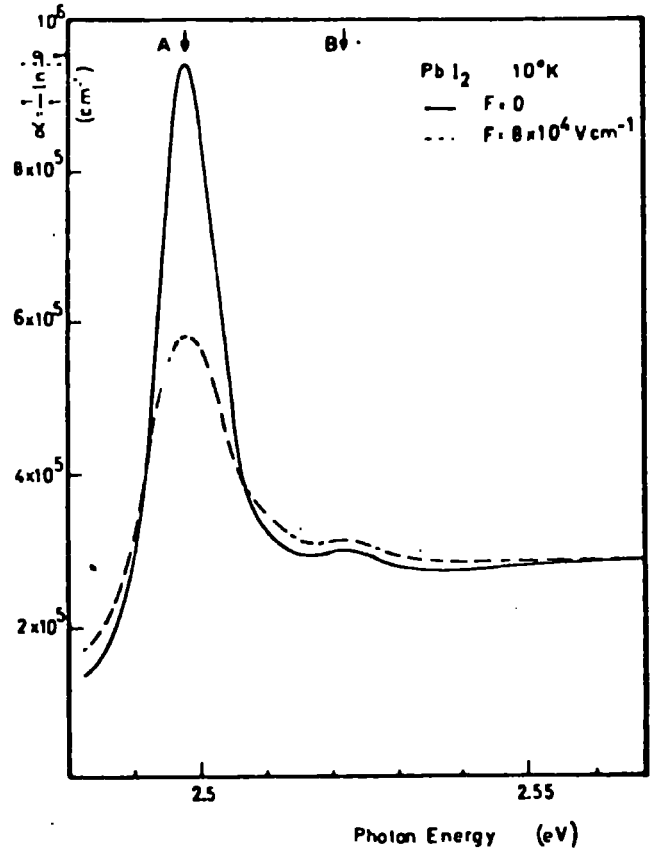

Fig. 2.10

Absorption spectrum of the exciton at the fundamental absorption edge of PbI_2. (53)

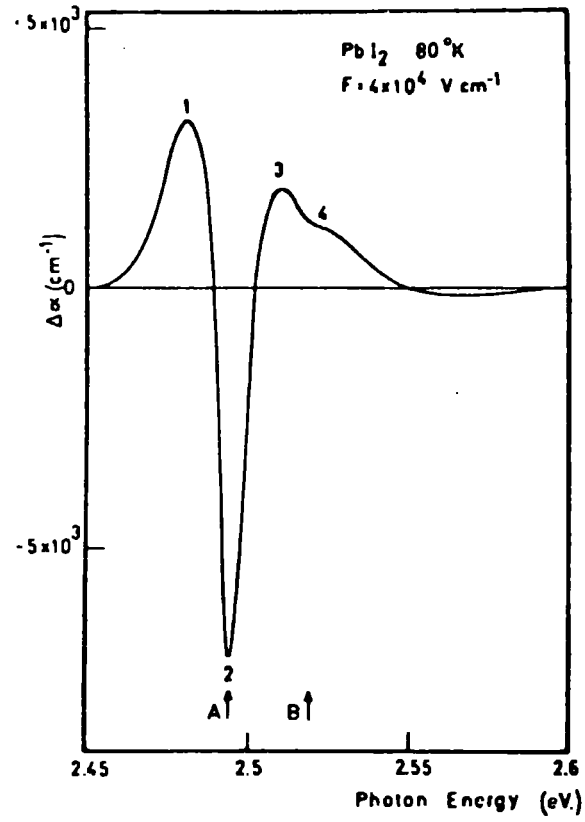

Fig. 2.11

Electroabsorption spectrum of the exciton of PbI_2 at 80 K and F = 4 x 10^4 V/cm. (53)

The similarity between these results and the theoretical curves shown in Figure 2.9 is obvious. These data are typical of the high field regime, that is, fields of the order of the ionization field F_i. In Figure 2.12 a theoretical fit to the experimental shifts of the exciton ground state with field is shown. The data have been corrected for the anisotropy of the lattice [53]. Although the agreement in the region of the Stark effect is poor the ground state does begin to tunnel out of the potential well at high fields in a similar manner to that shown in Figure 2.8.

The above effects, and others which we have not discussed, are consistent with interpretation by means of the excitonic electroabsorption theory. For PbI_2 the agreement is not surprising since the exciton is clearly visible in the zero-field spectrum. Blossey however, concludes that the exciton peak need not be observable in the absorption spectra for Coulombic effects to be important in the electroabsorption spectra, and in particular to affect the period and magnitude of the electric field induced oscillations.

In addition to the above-mentioned excitonic effects, Handler et al [54] have proposed that it is necessary to account for the degeneracy of light and heavy hole bands. These authors observed destructive interference in the oscillations in GaAs due to contributions from the light and heavy hole bands.

2.5 The Stark Effect

Despite the fact that the splitting of spectral lines in a magnetic field was first performed in 1897, by Zeeman, some sixteen years passed before Stark [55] and Surdo [56], working independently, demonstrated that a similar effect would be observed on placing a spectral source in an electric field. Stark showed that the lines of the Balmer series of hydrogen, when excited in an electric field of 10^5 V/cm, split into a number of components. It is probable that the Stark effect would have been observed much earlier, were it not

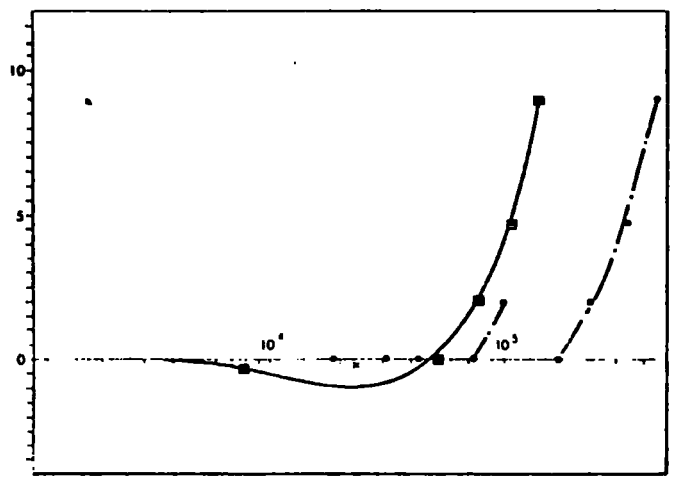

Fig. 2.12 Theoretical fit including anisotropy, to experimentally measured shifts at the ground state of the exciton in PbI_2. (53)

for the difficulty in maintaining such high fields in a discharge tube.

In comparison to the Stark effect in hydrogen, the effect of an electric field on the optical properties of molecular crystals is extremely complicated. The vast majority of experimental and theoretical work in this field has been carried out on inorganic solids where the Franz/Keldysh effect dominates. As discussed in the earlier sections of this chapter, the Franz/Keldysh effect is considered to be a band phenomenon, as opposed to the Stark effect which acts on the electronic levels of the constituent elements of the solid. Experimentally the Franz/Keldysh effect received more attention since in inorganic solids the effect is larger than the Stark effect by about an order of magnitude at least. The Stark effect therefore, only contributes significantly to the observed electroabsorption spectra when the Franz/Keldysh effect is small and when excitonic effects are present. This situation is usually realised when the valence and conduction bands of the solid are very narrow, a condition normally satisfied for organic molecular solids.

2.5.1 The First-Order Stark Effect In Hydrogen

It is quite informative to briefly review the Stark effect in hydrogen. This is probably the simplest system in which to examine the Stark effect. For a more detailed treatment the reader is referred to Pauling and Wilson [57] or Schiff [58].

The application of an electric field to a material may usually be considered to result in a small perturbation of the energy levels, provided that the magnitude of the external field is small, relative to the appropriate ionization field of the sample in question. For hydrogen, for fields up to 10^8 V/cm this is indeed the case, and the resulting quantum mechanical problem may be treated by the well known perturbation theory.

For the hydrogen atom, the unperturbed Hamiltonian may be written as:-

$$H = \frac{-\hbar^2 \nabla^2}{2m} - \frac{e^2}{4\pi \varepsilon_o r} \qquad (23)$$

which has eigenfunctions of the type:-

$$R_{n\,l}(r)\, P_l^{|m|}(\cos\theta)\, e^{im\phi} \qquad (24)$$

The perturbation is:-

$$H' = -e\mathcal{E}z = -e\mathcal{E}r\cos\theta \qquad (25)$$

The perturbation is thus an odd function of the co-ordinates, so the energy change in the ground state is zero.

The first excited state is however, four-fold degenerate. The perturbed states may be written as superpositions of eigenstates of the unperturbed Hamiltonian, and these are eigenstates of m_z (the z component of angular momentum). Accordingly, the matrix of m_z is diagonal. Since the perturbation is proportional to z, which commutes with m_z, we may write:-

$$H' m_z - m_z H' = 0$$

or in terms of a typical element of a commutator matrix:-

$$H'_{rs} = 0 \quad \text{unless} \quad (m_z)_r = (m_z)_s$$

This means that the elements of H' which do not vanish must all refer to states with the same m values. The first excited state has four degenerate components (2,0,0), (2,1,1), (2,1,0) and (2,1,-1). Of these only two have the same m-value, so the matrix must be a 2 x 2 matrix corresponding to these states. Since the diagonal elements of this

matrix vanish, we only consider the off diagonal elements, which are easily shown to be equal to $3_e \mathscr{E} a_o$. Hence the H' matrix becomes:-

$$\begin{bmatrix} 0 & 3e\mathscr{E}a_o \\ 3e\mathscr{E}a_o & 0 \end{bmatrix} \tag{28}$$

giving

$$\lambda^2 = (3e\mathscr{E}a_o)^2 \tag{29}$$

or $\lambda = \pm 3_e\mathscr{E}a_o$ where λ is the energy change due to the perturbation.

The eigenvectors are therefore

$$\frac{1}{\sqrt{2}}\begin{bmatrix} 1 \\ 1 \end{bmatrix} \quad \text{and} \quad \frac{1}{\sqrt{2}}\begin{bmatrix} 1 \\ -1 \end{bmatrix} \tag{30}$$

giving the linear combination of eigenstates as:-

$$\psi_+ = \frac{1}{\sqrt{2}} \left\{ \psi_{210} + \psi_{200} \right\} \tag{31}$$

and

$$\psi_- = \frac{1}{\sqrt{2}} \left\{ \psi_{210} - \psi_{200} \right\} \tag{32}$$

Hence we obtain a symmetric splitting of the energy level, that is,

ψ_+ —— $l = 1,0 \quad m = 0$

$\psi_{2,1,1}$ and $\psi_{2,1,-1}$ —— $l = 1 \quad m = \pm 1$

ψ_- —— $l = 1,0 \quad m = 0$

A somewhat similar analysis holds for the second excited state, which is ninefold degenerate. The electric field reduces this degeneracy to a quintuplet. The splitting of levels of the hydrogen atom in an electric field is shown in Figure 2.13.

In the above discussion, we have simply considered the effect of the electric field to a first approximation. However, if the effect of the field on a particular level is zero to a first approximation, it is often necessary to proceed to a more detailed analysis. The procedure is then known as second order perturbation theory, and in relation to the Stark effect, we obtain the first order Stark effect and the second order Stark effect respectively. We shall now proceed to give a very brief analysis of the second order Stark effect in hydrogen.

2.5.2 The Second-Order Stark Effect In Hydrogen

Although the hydrogen atom exhibits no first order Stark effect in the ground state, there does exist a second order effect. If we write:-

$H_o\psi_o = W_o\psi_o$ as the unperturbed system and

$H_o\psi_1 + H'\psi_o = W_o\psi_1 + W_1\psi_o$ as the first order perturbation, then

$H_o\psi_2 + H_1\psi_1 = W_o\psi_2 + W_1\psi_1 + W_2\psi_o$ is the second order effect.

We have expressed $H' = -e\mathcal{E}_z$, so

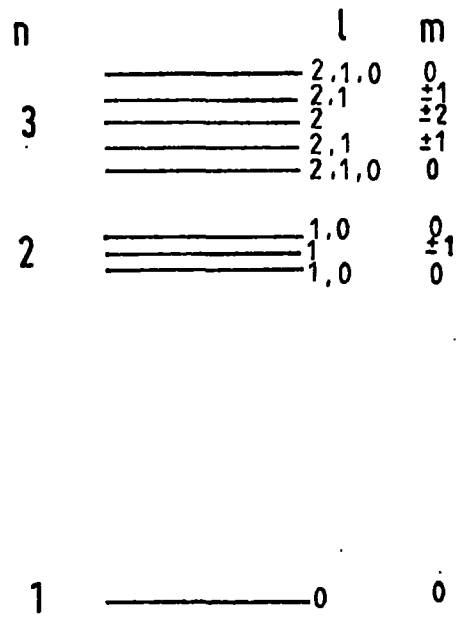

Fig. 2.13 Stark splitting of the three lowest states of the hydrogen atom.

$$W_2 = e^2\mathcal{E}^2 \sum_{n \neq k} \frac{|z_{kn}|^2}{E_k - E_n} \qquad (33)$$

It is convenient to define an atomic polarizability α by:-

$$W_2 = -\tfrac{1}{2}\,\alpha\,\mathcal{E}^2. \qquad (34)$$

For the ground state k = 1, so

$$\alpha = 2e^2 \sum_{n>1} \frac{|z_{1n}|^2}{E_k - E_1} \qquad (35)$$

It is also customary to define an oscillator strength f_n for the transition $1 \longrightarrow n$ by:-

$$f_n = 2m/\hbar^2 \,(E_n - E_1)\,|z_{1n}|^2 \qquad (36)$$

giving

$$\alpha = \frac{e^2\hbar^2}{m} \sum_{n>1} \frac{f_n}{(E_n - E_1)^2} = \frac{e^2}{m} \sum_{n>1} \frac{f_n}{W_{n1}^2} \qquad (37)$$

It is fairly easy to show that

$$\sum_n f_n = 1 \qquad (38)$$

An approximate estimate of the polarizability may be obtained if we assume that the oscillator strength for the transition $1 \longrightarrow 2$ is strongly dominant. Then from equations (33) and (36) we may write:-

$$\alpha \simeq \frac{e^2\hbar^2}{m} \left\{ \frac{1}{(E_2 - E_1)^2} \right\} \qquad (39)$$

However since

$$E_2 - E_1 = {}^{1}/_{4\pi\varepsilon_o} \cdot (3e^2/8a_o) \qquad (40)$$

we have

$$\frac{a}{4\pi\varepsilon_o} \simeq 7a_o^3 \qquad (41)$$

This means that the energy change due to the field is:-

$$W_2 = -\tfrac{1}{2}\mathcal{E}^2(7a_o^3 4\pi\varepsilon_o) \qquad (42)$$

This represents a unidirectional shift of the transition to lower energies.

2.5.3 Classical Interpretation Of The Stark Effect

A more classical consideration of the Stark effect would lead us to write the following expression for the interaction energy of a hydrogen-like atom in an electric field:-

$$\Delta W = A\mathcal{E} + B\mathcal{E}^2 + C\mathcal{E}^3 \qquad (43)$$

Once again ΔW is the shift of the energy levels in an electric field $\mathcal{E}$. The coefficients A, B, C have been calculated by Epstein [59], Van Vleck [60], Schrodinger [61] and others to be:-

$$A = 6.42 \times 10^{-5}$$
$$B = 5.22 \times 10^{-16}$$
$$C = 1.53 \times 10^{-25}$$

if the field is expressed in V/cm.

Obviously the first term in equation (43) relates to the first-order Stark effect, the second to the second-order Stark effect and

so on. The first term results in a symmetrical splitting of the energy levels about the field-free position, whereas the second term is a unidirectional shift. In classical terms we may say that only those states which exhibit a permanent dipole moment will show the first-order Stark effect. In contrast however, any state will exhibit a polarizability α, and accordingly the second-order shift is always present. This concept of dipole moments and polarizability will be extremely useful in the next section, which deals with the effect of an electric field on optical absorption in molecular crystals.

2.6 The Stark Effect In Molecular Crystals

The interaction of an electric field with a molecular crystal causes spectral effects which can usually be readily related to important parameters of the charge distribution. In view of the fact that the quantum mechanical equations for the effect of the electric field on the optical properties of molecular crystals are insoluble analytically, it is convenient to discuss the problem in terms of dipole moments and polarizabilities, as briefly mentioned at the end of the last section. This approach lends itself to a more physical understanding of the situation. The interpretation of the field-induced spectral changes along these lines can often lead to new knowledge of molecular dipole and higher moments of the charge distribution, polarizabilities of excited electronic states, and parameters describing intermolecular interactions in crystals. While a significant volume of information is available concerning ground state charge distributions, not nearly the same amount of data have been accumulated for higher electronic states. The data obtained from electric field studies on the optical properties of molecular crystals are badly needed, both as a testing ground for the theory and to help rationalize the chemistry of excited states.

2.6.1 Linear Stark Splitting

As for the hydrogen atom, a change in potential energy arises

when a molecule is placed in an electric field. This change may be written as:-

$$V(F_1) = -\int_0^{F_x} m_x \, dF_x = -\mu F_x \cos\theta - \tfrac{1}{2} a_{xx} F_x^2 + \ldots\ldots \qquad (44)$$

Here m_x is the component of the dipole moment in the presence of the electric field F_x, μ is the permanent dipole moment such that:-

$$m_x = \mu\cos\theta + a_{xx}F_x \qquad (45)$$

We assume that μ makes an angle θ with the electric field, and is one of the six independent components of the polarizability. The term $\mu F_x \cos\theta$ is the linear Stark effect, while $\frac{1}{2} a_{xx} F_x^2$ is the quadratic Stark effect. It is useful to consider a system in which we assume a model crystal of N non-interacting molecules per unit cell. In practice this approximation is partly achieved by having a dilute mixed crystal which has the molecule of interest, the guest, dispersed randomly throughout a host of known structure. In Figure 2.14, we show the various possible guest orientations for the case of two molecules per unit cell, two interpenetrating translational sublattices A and B, and each host molecule assumed to be centrosymmetric. The labels A_α, A_β, B_α, B_β correspond to four possible guest dipole orientations. The host lattice is assumed to be non-polar. In the presence of an electric field, several effects occur. Neglecting the polarizability term, the change in energy per molecule is given by $-\mu_o F_1 \cos\theta$, where μ_o is the ground state dipole moment, and θ the angle between μ_o and the field F_1. An immediate effect of the field is thus to lower the energy of molecules of type A_α and B_α, and to raise the energy of molecules A_β and B_β. Hence the ground state of the total system is split, as in Figure 2.15. In a similar manner an excited state would be split by $2\mu_e F_1 |\cos\theta|$, with μ_e the excited state dipole moment. An optical spectrum of the mixed crystal in the field would show a splitting of:-

$$\Delta E = 2F_1(\mu_e - \mu_o)|\cos\theta| \qquad (46)$$

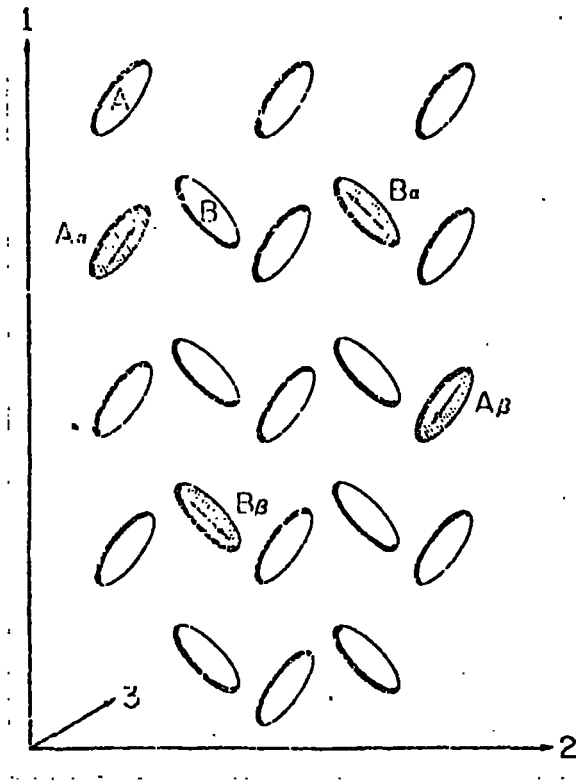

Fig. 2.14 Orientation of molecules in a model molecular crystal. (74)

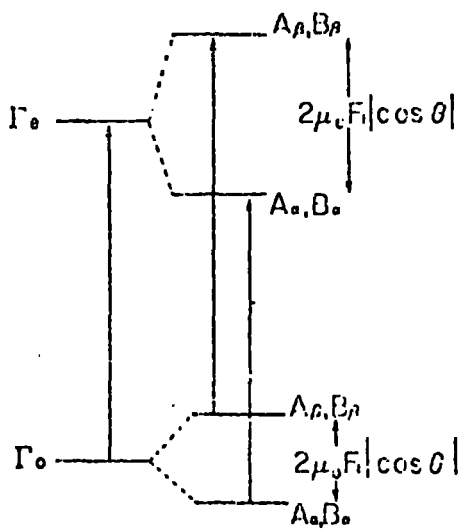

Fig. 2.15 Model energy level diagram for oriented polar molecules of a crystal in an electric field. A non-polarizable lattice is assumed. (74)

Thus in a similar manner to the hydrogenic atom, we obtain a linear Stark effect for a transition between any two states which have:-

$$\Delta\mu = (\mu_e - \mu_o) \neq 0 \qquad (47)$$

As an example, Figure 2.16 shows the Stark splitting of the lowest singlet state origin of p-Benzoquinone.

2.6.2 Static Polarizability Change

For neat molecular crystals there occurs a resonance interaction between the molecules and it is unreasonable to assume that the observed spectroscopic transitions indicate states of isolated molecules. In this case, Frenkel excitonic effects would also have to be included in the theory. A further complication is that dipolar molecules quite often form centrosymmetric crystals, and as a result the crystal state will have zero dipole moment, even though the component molecules are strongly polar. A general rule is that crystals having non-polar space groups will not exhibit a first order Stark effect. However, as in the case of the hydrogen atom, the induced dipole moment will lead to a quadratic Stark effect, resulting in a red shift of the absorption line. The qualitative relationship between the observed change in absorbance ΔA, and the differences in static polarizability may be obtained from the theory developed by Liptay and coworkers [62], namely:-

$$\Delta A = (\tfrac{1}{3}\delta a_x + \delta a_y + \delta a_z)\,(L)\,E^2 A'/5 \qquad (48)$$

where L is the Lorentz correction (as discussed below) δa_x is the difference in static polarizability along the direction of the transient moment and A' is the derivative of the absorbance with respect to energy. This equation neglects the reaction field of the solute molecules.

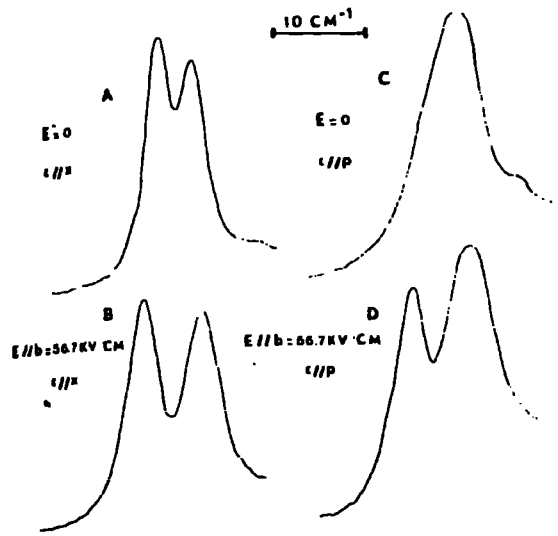

Fig. 2.16 The polarized absorption spectrum at 20060 cm^{-1} of the lowest singlet state origin in PBQ-h_4. The effect of an electric field on the spectra is shown in (c) and (d). (87)

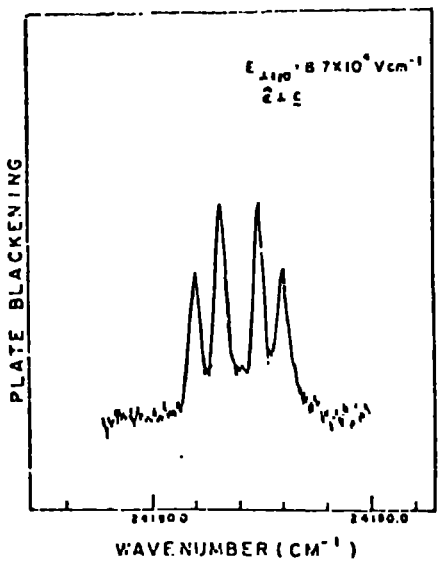

Fig. 2.17 Effect of an electric field on the absorption spectrum of a benzophenone crystal at 4.2 K. The electric field is perpendicular to the 110 crystal plane. At zero field only a single line is observed at the centre of the pattern. (74)

2.6.3 Lorentz Field Approximation

In order to determine the dipole moment change $\Delta\mu$ or the polarizability change $\Delta\alpha$ it is necessary to know the local field F_1 for this may be considerably different from the applied external field. To this end, a number of assumptions are often made. For example, it is assumed that the field is uniform over each molecule, and that the fluctuations in the field due to the non-uniformity of the electronic distribution around a given molecule may be neglected. Furthermore, each polar molecule is regarded as a point dipole, and each polarizable molecule as a point induced dipole. For mixed crystals, the guest and host polarizabilities are assumed to be identical. Then we may describe the effective field F_1 as the average field in the crystal. An approximation which is often made is to treat the local field by an empirical Lorentz field approximation. Recently several authors have questioned the validity of this and other approximations. Udagawa and Hanson [63] have pointed out that the apparent change in the dipole moment, between the ground state and the first excited state of parafluoraniline isolated in a durene host crystal, determined by this method, is about 100% larger than the value reported for the molecule in the vapour phase. In general, we may write $F_1 = L_1 E_1$ where E_1 is the externally applied field and L_1 is a constant of the material to be calculated. Calculations of L_1 are extremely difficult however. In order to assess the accuracy of molecular parameters determined from Stark effect measurements, Chen and Hanson [64, 65] have developed a more rigorous theory for the Stark effect of a guest molecule in a host molecular crystal. Specific calculations were performed within the context of the point dipole approximation for one molecule per unit cell. This analysis was later extended to two or more molecules per unit cell, and the relevant quantities calculated for durene and naphthalene crystals [65]. Problems however still exist due to the lack of knowledge on the ground and excited state polarizabilities. A somewhat similar analysis has been performed by Dunmur and Munn [66], who treated the specific case of azulene, again within the point dipole approximation. In general, the application of these more exact theories to electroabsorption data

is not possible due to lack of information on effective polarizabilities and local field tensors.

2.6.4 Symmetry Analysis By Electroabsorption

We stated above that centrosymmetric crystals do not, in general, show a linear Stark splitting. Although this provides a convenient method of distinguishing between centrosymmetric and non-centrosymmetric crystals, it is not the only information on crystal structure to be obtained from Stark effect measurements. An important relationship also exists between the number of components into which a spectral line is split and the number of molecules per unit cell. The number of components depends on the field direction, and if this is chosen as a symmetry axis, the observed number of peaks will be reduced. Figure 2.17 shows the spectrum of a benzophenone crystal [67], in which four lines are clearly visible. For any field direction, four is the maximum number of lines. Three mutually perpendicular directions exist for which only two lines are seen. Using these results it is possible to specify D_2 symmetry for the group interchanging the molecules in the unit cell. The complete analysis of this situation is available in reference [67].

2.6.5 Shape Of Electroabsorption Curves

In a typical electroabsorption experiment, one measures the fractional change in the transmission of the sample due to the applied field. Since the first-order Stark effect results in a symmetrical splitting of a spectral line, the measured $\Delta I/I$ will have the shape of a 2nd derivative curve of the zero field spectrum. In contrast, the quadratic Stark effect results in a unidirectional shift of an electronic level, producing a first derivative trace of the field-free spectrum. In terms of the change in transmission, we may write:-

$$\frac{\Delta I}{I} = \frac{1.15}{hc}\left[\frac{V^2}{d\sqrt{2}}\right]\left[\frac{\xi+2}{3}\right]^2 \cdot \Delta a\left[D + \lambda\frac{dD}{d\lambda}\right]\lambda \qquad (49)$$

for the quadratic case. Here V is the applied voltage, d the sample thickness, ε the static dielectric constant and D the optical density. The term:-

$$\left[\frac{\varepsilon + 2}{3}\right]^2$$

is the Lorentz field approximation. The limitations of this type of approach have been discussed in section 2.6.3. For the linear Stark effect case, the observed splitting in λ can readily be correlated with the approximate theoretical expression, that is:-

$$\Delta S = 2\Delta\mu E.L \qquad (50)$$

where ΔS is the observed splitting, $\Delta\mu$ the dipole moment change, and L the Lorentz field approximation.

2.6.6 Summary Of Electroabsorption Effects In Molecular Crystals

The main features of the Stark effect in molecular crystals may be summarized as follows:-

1. In general, crystals with polar space groups will exhibit a first-order Stark effect, leading to a symmetrical splitting of a crystal state. This is usually recognised in electro-absorption spectra as a 2nd derivative of the zero-field absorption curve.

2. By varying the direction in which the electric field is applied to a crystal, it may be possible to obtain additional information on the crystal symmetry.

3. Crystals having non-polar space groups may still exhibit a second-order Stark effect, leading to a unidirectional shift of an absorption line. This process may be recognised in electroabsorption spectra as a 1st derivative of the zero-field absorption curve.

2.7 Recent Electroabsorption Experiments Using Molecular Crystals

The volume of work performed on the Stark effect in molecular crystals is quite small, mainly due to the experimental difficulty in measuring extremely small changes in transmission. In 1961, Platt [68] suggested that the absorption spectra of certain dyes could be shifted by the application of an electric field, and in the following year Powers [69] produced results of a study of the Stark effect in a methyl red dye, dissolved in a polystyrene matrix. Again in 1963, Powers [70] demonstrated the effect of an electric field on a phenol blue dye. Very little new data were then produced until 1968 when Hochstrasser [71] suggested that the splitting of spectral lines in an electric field would give useful information on dipole moment changes, with which to compare theory and experiment. Since then the interest in the topic has rapidly gained momentum. Blinov et al [72] discussed the Stark effect in phthalocyanine and showed that their data was consistent with a red shift due to the field, as expected for non-polar molecules. Mathies and Albrecht [73] produced data on the $^1A_{1g} - {}^1B_{2u}$ transition in benzene. Subsequently, Hochstrasser [74], in a review article, discussed the possible benefits of further research into the Stark effect in molecular crystals. This article was rapidly followed with data on p-benzoquinone [75], tetracene [76] and hexatriene [77]. Blinov et al [78] in 1974 produced further results for tetracene and perylene films. Figure 2.18 reproduces data obtained by these latter workers on an evaporated tetracene film. The electroabsorption curve is a good first derivative of the zero-field absorption spectra. Roberts et al [79] have studied the quadratic Stark effect in evaporated anthracene films and have found a correlation between the heights of the observed peaks and the temperature of the substrate during deposition of the film. With reference to Figure 2.19, the height of peak A was found to reach a maximum when the substrate temperature was below $-100^{\circ}C$ during deposition. This experiment thus indicates the sensitivity of the electroabsorption technique.

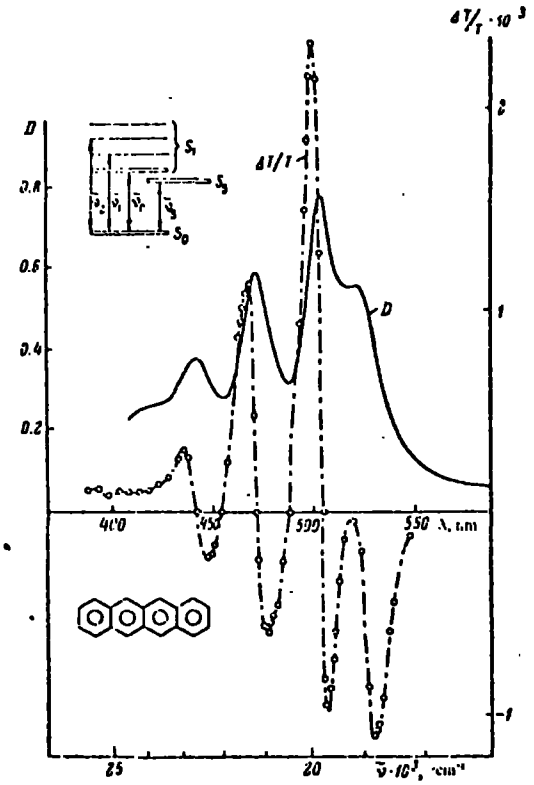

Fig. 2.18 Optical density and the Stark effect spectrum $\Delta T/T$ of a 0.14 μm thick tetracene film as a function of photon energy. The formula of the molecule is given in the lower corner. (78)

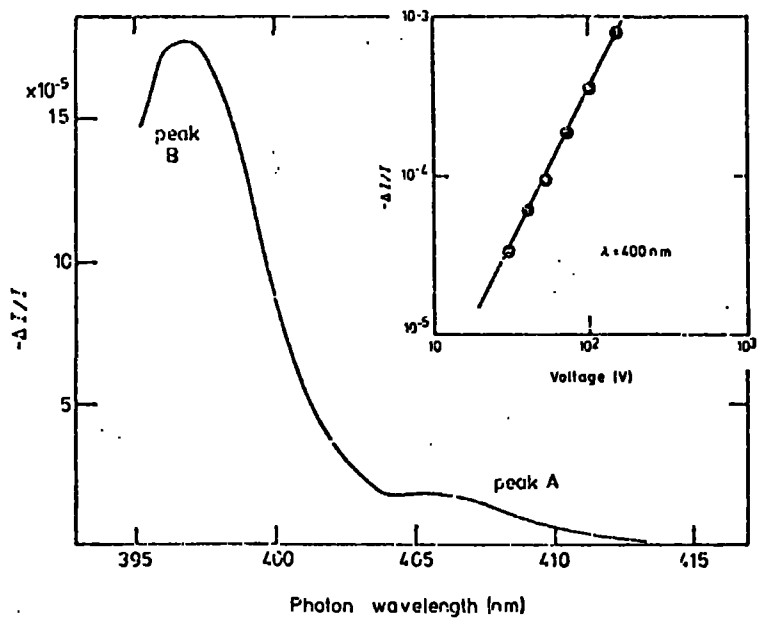

Fig. 2.19 The fractional change in transmission as a function of photon energy for an anthracene film evaporated onto a substrate held at -20°C. The inset shows the field dependence of $\Delta I/I$ at a wavelength of λ = 400 nm. (79)

The most recent papers have concentrated on the theoretical interpretation of Stark effect data, particularly a more exact expression for the local field [63-66].

2.8 The Stark Effect In Impurity Levels In Inorganic Solids

The Stark effect in inorganic solids has been discussed previously with relation to electric field effects on Wannier excitons. It is worth noting however, that many of the conclusions of the preceding sections on the Stark effect in molecular crystals may be applied equally well to inorganic crystals with deep impurities or localized defects. This is a topic which has been receiving increasing attention in recent years, and is possibly one of the more exciting areas of modulation spectroscopy. The first work in this area was performed on colour centres in alkali halide crystals. Figure 2.20 shows the change in absorption of an F centre in K Br [80]. As with molecular crystals, first and second derivative curves are obtained for defects with and without inversion symmetry respectively. Although the alkali halides have received most attention in the area of impurity electroabsorption, in recent years the work has gradually extended to other materials as well, such as semiconductors. Jonath et al [81] have carried out a detailed study of impurities and defects in GaAs:O. An example of their data is shown in Figure 2.21. As one can see, the electric field perturbation produces a wealth of peaks, which may possibly be correlated with data obtained using other methods of investigation. Unfortunately, our knowledge of localised defects in compound semiconductors is less advanced than in alkali halides, and often the experimental results cannot be interpreted in terms of known defects and clearly resolved phenomena. This is the case for the study performed by Jonath et al. These authors observed linear and quadratic effects which they tentatively explained in terms of dipole defects by substitutional impurities of Si or C (at the Ga lattice site), bounded to an interstitial oxygen atom. The possible orientations of these fixed dipoles were determined by the polarization dependence of the observed electroabsorption signal.

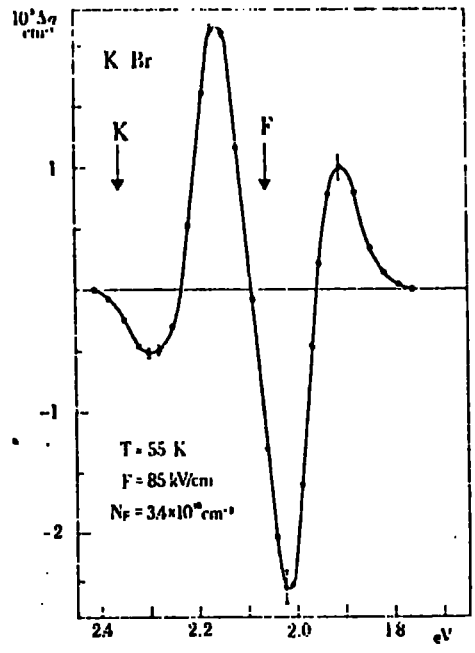

Fig. 2.20 Electroabsorption spectrum of the F-centre in K Br. (80)

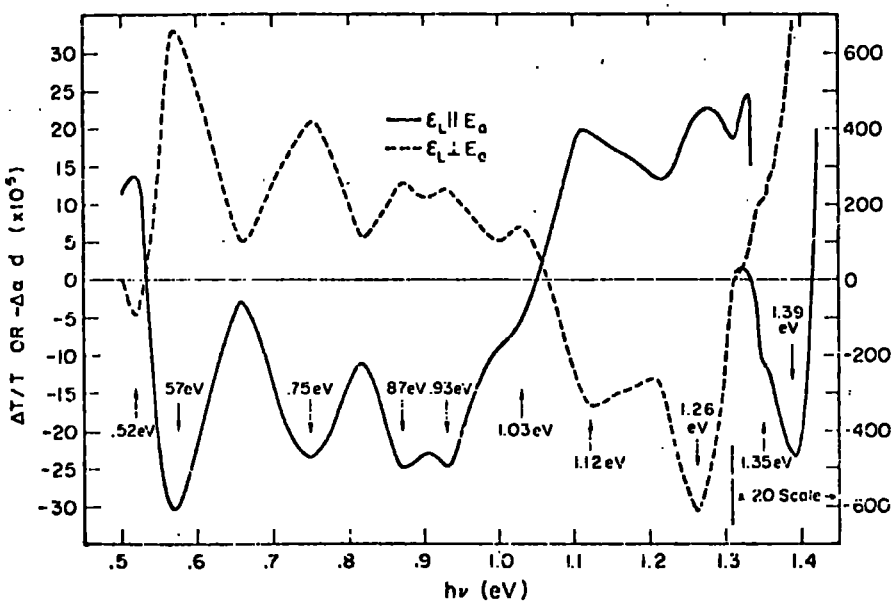

Fig. 2.21

Electroabsorption of GaAs:O as a function of photon energy. V = 64V, f = 255Hz. (81)

The properties of a substitutional deep impurity in Wurtzite-type crystals have been thoroughly studied by Boyn and Gardawsky [82,83]. The centre investigated by these authors was a substitutional transition metal impurity such as N_2^{2+} or Co^{2+}. These impurities are inversion symmetrical but the lattice site in Cds or CdSe does not possess inversion symmetry and therefore the centre does exhibit a linear Stark effect. Bower [84] has measured electroabsorption in GaP:N, and recently Neu et al [85] have measured the Stark effect of impurities and defects in CdTe:Cl. There is no doubt that these studies now form an important area of electroabsorption spectroscopy. A brief review of this topic has recently been given by Lüty [86].

2.9 Summary Of Electroabsorption Theory

To conclude this chapter we now summarize the main conclusions of electroabsorption theory. These are as follows;

1. In inorganic materials, the Franz/Keldysh effect usually dominates the observed electroabsorption spectrum, with a resulting "red shift" on the low energy side of the spectrum.

2. Oscillations above the edge in the electroabsorption spectrum can result from field-induced Stark ladders in the continuum, and from the Stark effect on excitons.

3. In materials which display an exponential type absorption edge, it is possible to obtain a value for the effective mass from the electroabsorption data, provided that excitonic effects may be neglected.

4. The "one-electron" electroabsorption theories predict that the amplitude of the electroabsorption peaks will be proportional to F^n. For direct allowed, direct forbidden and indirect transitions, n takes the value

0.33, 1.0, and 1.33 respectively. For exponential absorption edges n is equal to 2.0. The situation for the excitonic electroabsorption theories is more complicated, and depends on the ratio of the external field to the ionization field.

5. Inorganic materials, specifically molecular crystals, usually exhibit a linear or quadratic Stark effect.

6. A linear Stark effect may be observed if the transition in question involves a net change in dipole moment.

7. Quadratic Stark effects are always present, but are small, and manifest themselves as a first derivative curve.

8. Apart from electroabsorption effects at critical points, inorganic materials may also exhibit Stark effects due to localized impurities or defects. The theory in this case needs to be modified due to the presence of several competing processes.

CHAPTER III

EXPERIMENTAL DETAILS

3.1 In chapters five and six of this thesis, results will be presented describing the effect of high electric fields on the optical properties of several semi-insulating materials. Chapter five will include results for semi-insulating gallium arsenide and indium phosphide, while chapter six will present data obtained on Langmuir films of anthracene. Before doing so, however, we present here a description of the experimental equipment used to obtain those results.

While the main objective of this work was to study the electroabsorption properties of solids, several ancillary experiments were also performed. These included ac. and dc. conductivity and capacitance measurements. A description of the apparatus used in these experiments is also included.

Experiments were carried out on both organic and inorganic materials, whose sample preparation varied considerably. A discussion of this topic is thus left until the respective chapters.

3.2 Electroabsorption Equipment

The changes produced by the application of a large electric field to a material are generally extremely small. Usually, one would expect to measure a change of one part in 10^4 for fields of 10^4V/cm at the absorption edge of crystalline solids, such as cadmium sulphide, where effective masses are less than the free electron mass. In these materials one would expect the Franz/Keldysh effect to dominate the electroabsorption spectra. However, for the Stark effect one needs to apply fields of 10^5-10^6V/cm before a change of this magnitude would be expected to occur. The

detection of such small changes requires the use of extremely sensitive equipment. In any electroabsorption system, one aims therefore, for as high a transmitted light intensity as possible, together with high electric fields, good resolution and the highest achievable signal to noise ratio.

3.2.1 Optical System

In order to achieve the dual aim of high resolution and low radiation losses, the optical system was based on the Hilger/Watt D 331 double monochromator. This instrument is capable of resolving the 3610.5 - 3612.8 Å cadmium doublet while its short path length ensured very little radiation losses. Two gratings were available for the monochromator, one blazed at 1.0 μm, the other at 0.5 μm.

The wavelength of the emitted radiation could be varied either manually or by means of a small electric motor used to rotate the grating. A number of different motor speeds were available from one revolution in two hours, to one revolution per minute. The input and output slit widths could be adjusted between .004 and 3.0 mm.

The optical source used in the experiment was an Atlas 24V, 250 watt projector bulb. These bulbs have a nominal life of 50 hours, but by operating them at slightly less than 24V and by cooling with compressed air, the lifetime could be greatly extended. The bulbs were powered from the stabilized mains supply, stepped down with a Variac. The lamp was allowed to stabilize for more than 90 minutes before measurements were commenced.

Light transmitted by the sample was detected either by a photomultiplier or an infra-red detector, depending on the spectral area of interest. Care was taken to make sure that only light passing through the electrodes was recorded. For

the indium phosphide and gallium arsenide samples use was made of an EMI 9659B photomultiplier with an extended S20 response. A high voltage was applied to the photomultiplier using a Brandenburg photomultiplier power supply model 472 R. An RCA C31034 tube was also occasionally used. Both these photomultipliers have a cut-off at approximately 9300 Å. However, by running the tubes at the maximum permitted voltage, it was found possible to collect data up to the 1 μm area. Figure 3.1 shows the quantum efficiency of an S20 type photomultiplier tube. As one can see the response in the range 8000 - 10,000 Å is extremely small, falling below 1% for the area above 8500 Å. This indicates one of the major problems encountered in the work on the III-V materials, namely extremely low detector sensitivities, resulting in very noisy signals. The problem of extracting the signal from the noise will be discussed in section 3.2.4.

A Mullard RPY 35 Indium Antimonide infra-red detector was also available. This device was suitable for the 1-5 μm range. The detector was operated at 77K, and was cooled using liquid nitrogen transferred by means of a Rank automatic cooling head, type ZX 6481. In practice, however, this device was only used to look for impurity absorption or electroabsorption in the 1-2 μm range, since in the spectral range below 1 μm the photomultipliers were found to be more useful.

The Langmuir films of anthracene were studied using the 0.5 μm grating together with an EMI 9558 photomultiplier with a quartz window, giving an extended ultra-violet response.

Extreme care was taken to eliminate second order effects from the gratings. Unwanted orders were eliminated by means of a set of Optics Technology bandpass filters. It was found that even though these filters transmitted less than 0.05% below their cut-off, unwanted orders could still be detected due to the fact that maximum voltages were applied to the

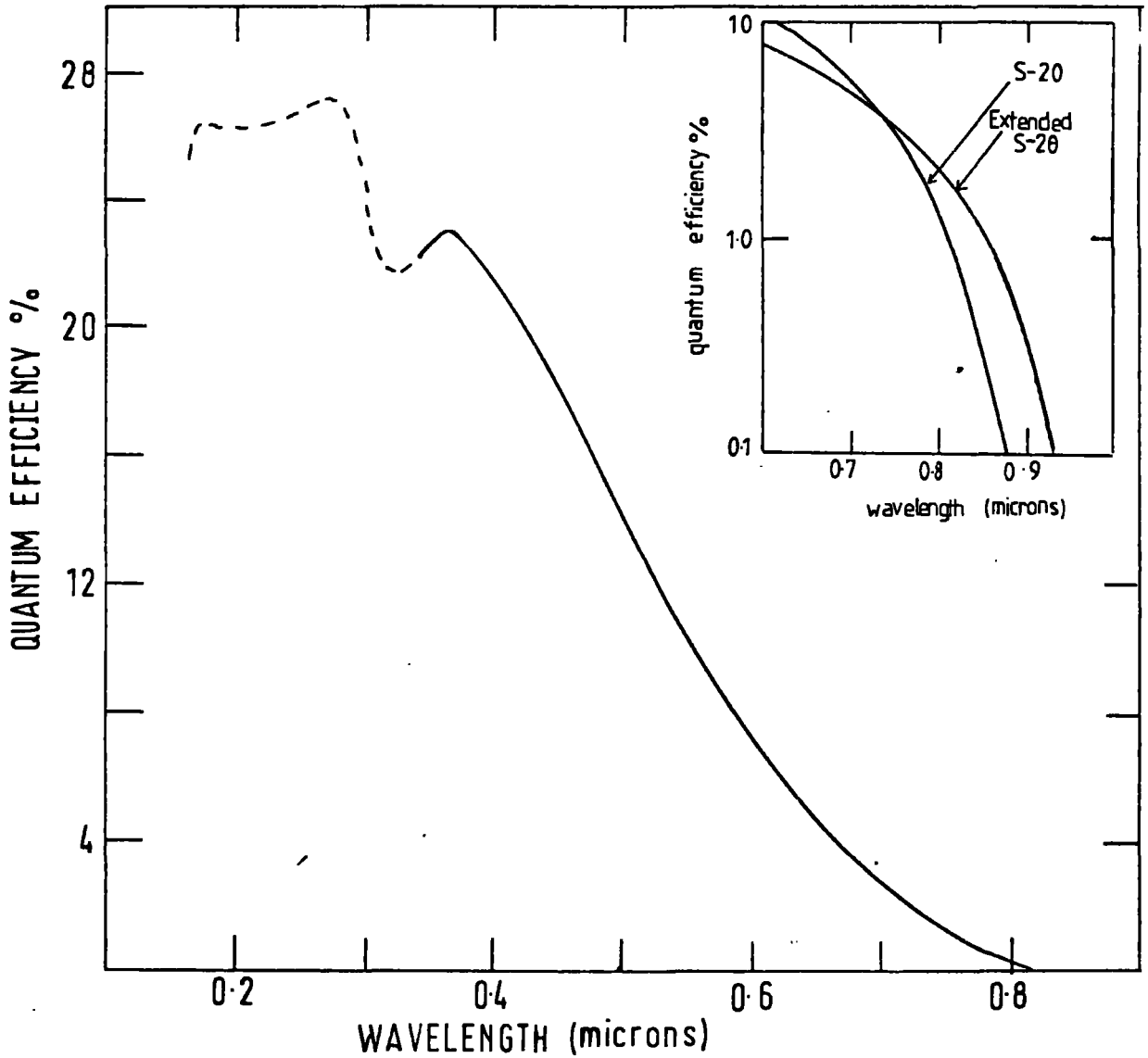

Fig. 3.1 Quantum efficiency of an S 20 photomultiplier tube.

photomultipliers. It was found necessary therefore, to use a series of filters to produce the correct spectral purity.

A schematic of the complete optical system is shown in Figure 3.2. Light from the source was focussed on the entrance slit of the monochromator using quartz lens. The light passed by the monochromator was transmitted through the sample to either a photomultiplier or an infra-red cell. The signal from the photomultiplier was taken to a load resistor, and thence to the detection system.

3.2.2 Sample Chamber

The samples were mounted in an Oxford Instruments CF 104 continuous flow cryostat. This equipment was capable of being operated between 315K and 4K. In practice, however, the cryostat was only used down to 77K.

The cryostat consisted of a centrally positioned cold finger, surrounded by a radiation shield. Around the radiation shield was the outer wall of the cryostat. A 30 watt heater was positioned in good thermal contact with a heat exchanger block and the cold finger. Liquid nitrogen was continually drawn through this heat exchanger block from an external dewar by means of a pump. The temperature of the sample was controlled by adjusting the liquid nitrogen flow rate and by varying the voltage applied to the heater. Automatic temperature control could be achieved by using an Oxford Instruments DTC 2 digital temperature controller. This instrument controlled the output to the heater depending on the difference between the measured and set temperature. Using this equipment, temperature stability of $\pm$ 0.1K could be achieved.

The actual temperature measuring device was a carbon linear temperature sensor attached in close proximity to the cold finger. Samples were mounted directly onto the cold finger. Good thermal

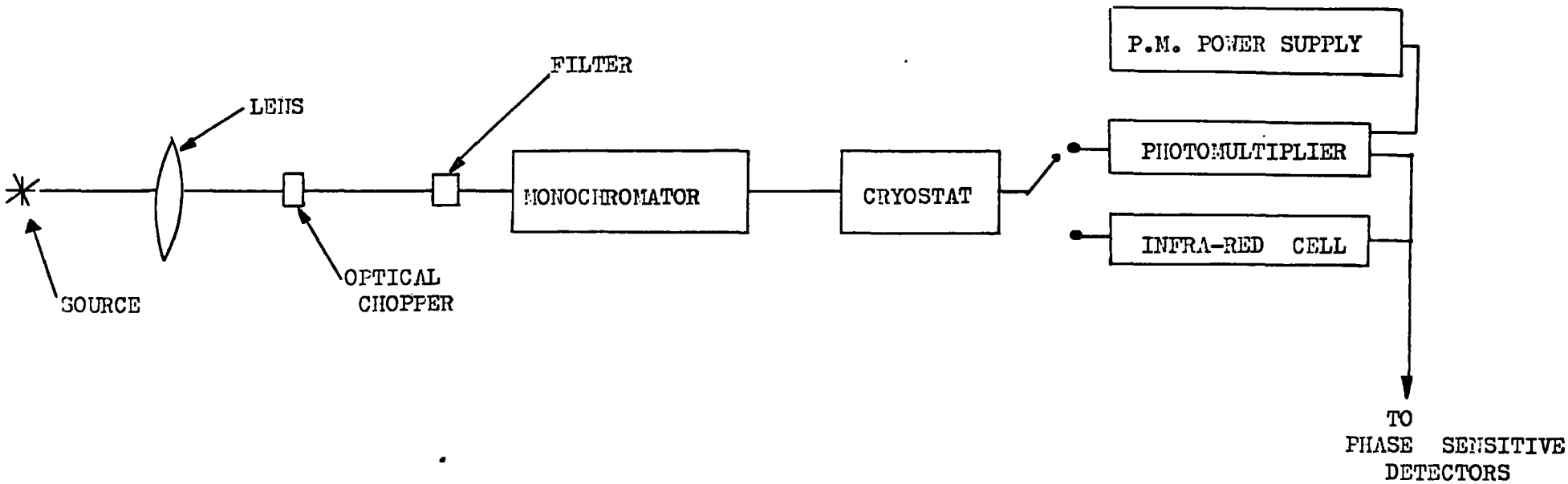

Fig. 3.2 Schematic diagram illustrating the optical system.

contact was ensured by using G.E. varnish to mount the samples.

To prevent water vapour condensing on the sample, and to provide good thermal insulation, the sample chamber was evacuated to a pressure of 10^{-6} torr using an Edwards 3" diffusion pump. The sample chamber was equipped with Spectrosil windows. In order to eliminate stray light, the cryostat was attached directly to the monochromator on one side, and to the photomultiplier on the other. A schematic of the inside of the cryostat is shown in Figure 3.3.

3.2.3 Pulse Generation System

In the early electroabsorption work, experimentalists applied high dc. fields to their samples in order to obtain a measurable change in transmission. However, with the advent of lock-in amplifiers, ac. fields have become the norm. Although it is preferable to apply square-wave modulation to the sample, sinusoidal waveforms are often more convenient. The difficulty with sinusoidal waveforms is that the observed electroabsorption signal is a composite of the changes produced by the various magnitudes of voltage in the sinusoidal pulse, dominated of course, by the peak. It is difficult therefore, to estimate the average voltage applied to the sample, since the transmission changes are in general a non-linear function of voltage. However, it is not easy to obtain undistorted high-voltage square-wave pulses above approximately 2 KHz, so above that frequency sinusoidal voltages must be applied to the samples. In chapter five, we will demonstrate that it is occasionally necessary to work at frequencies greater than 2 KHz.

In addition to the symmetrical pulse shapes mentioned above, it is useful to be able to apply to the sample voltage pulses which are unidirectional (i.e. from zero to a positive voltage only) or to superimpose a small dc. bias on a large ac. signal. It is also convenient to have a small rest period between positive and

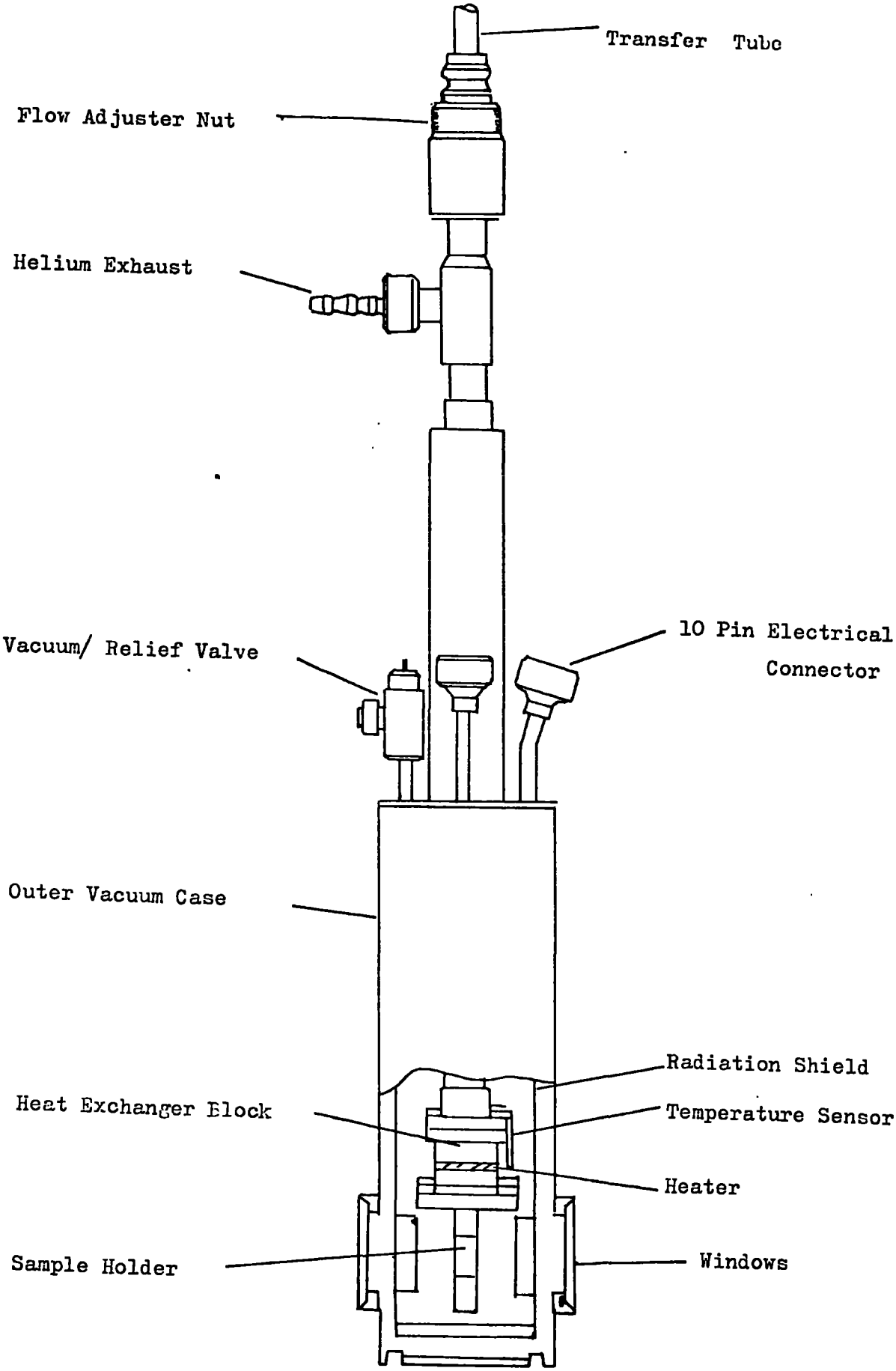

Fig. 3.3 Schematic of the inside of the CF104 cryostat.

negative going pulses. The advantages of having a variety of voltage pulse shapes to apply to the samples are discussed in detail in chapter five and appendix one.

Bearing in mind the above point, our pulse generation system was designed to be as flexible as possible. A diagram of the equipment used is shown in Figure 3.4. The square-wave generation system was based on an Advance pulse generator, model PG 511, and a Keithley 240A high voltage power supply. Low voltage pulses from the pulse generator were fed to the grid of a high-voltage triode valve, with the high voltage from the Keithley being applied between the cathode and anode. The high voltage output from the valve was thus modulated by the small modulation voltage applied to the grid. Positive and negative transgressions of this voltage were obtained by capacitively coupling the valve to the sample. Unidirectional positive pulses were obtained by using dc. coupling. A delay between the positive going pulse and the negative going pulse could be obtained by inserting a delay unit between the pulse generator and the triode.

The frequency of the voltage applied to the sample could be varied at the pulse generator. This unit also enabled the mark-space ratio of the pulses to be varied. The square-wave pulses employed had extremely fast rise and fall times. To ensure that the full voltage appeared across the sample, the capacitor formed by the cell had to be charged fairly rapidly, and accordingly the unit was built to withstand currents up to 10 mA. The unit was capable of supplying 550V peak-to-peak voltage, or 1100 volts in the unidirectional case. The system could be operated between 1.0 Hz and 10 KHz. In practice however, deterioration of the pulse shape was noticed at approximately 2 KHz, becoming serious at 5 KHz. Accordingly square-wave modulation was not used above 2 KHz to prevent introducing errors into the numerical results.

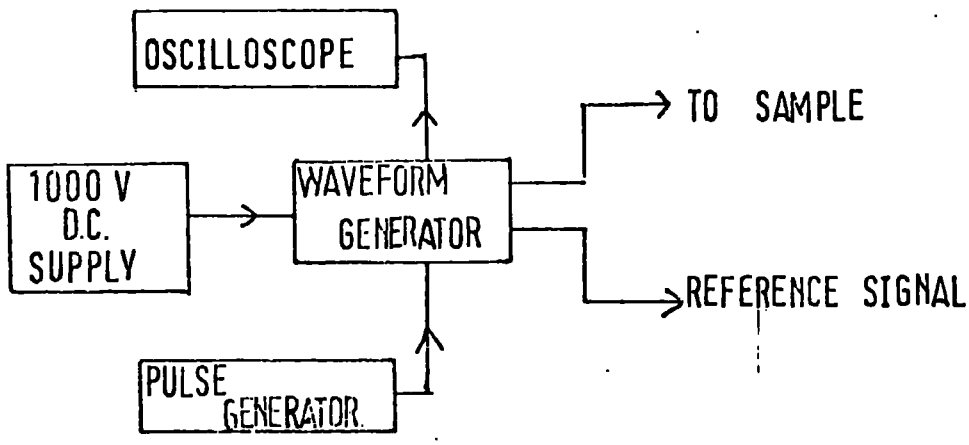

Fig. 3.4 The pulse generation system for the electroabsorption studies.

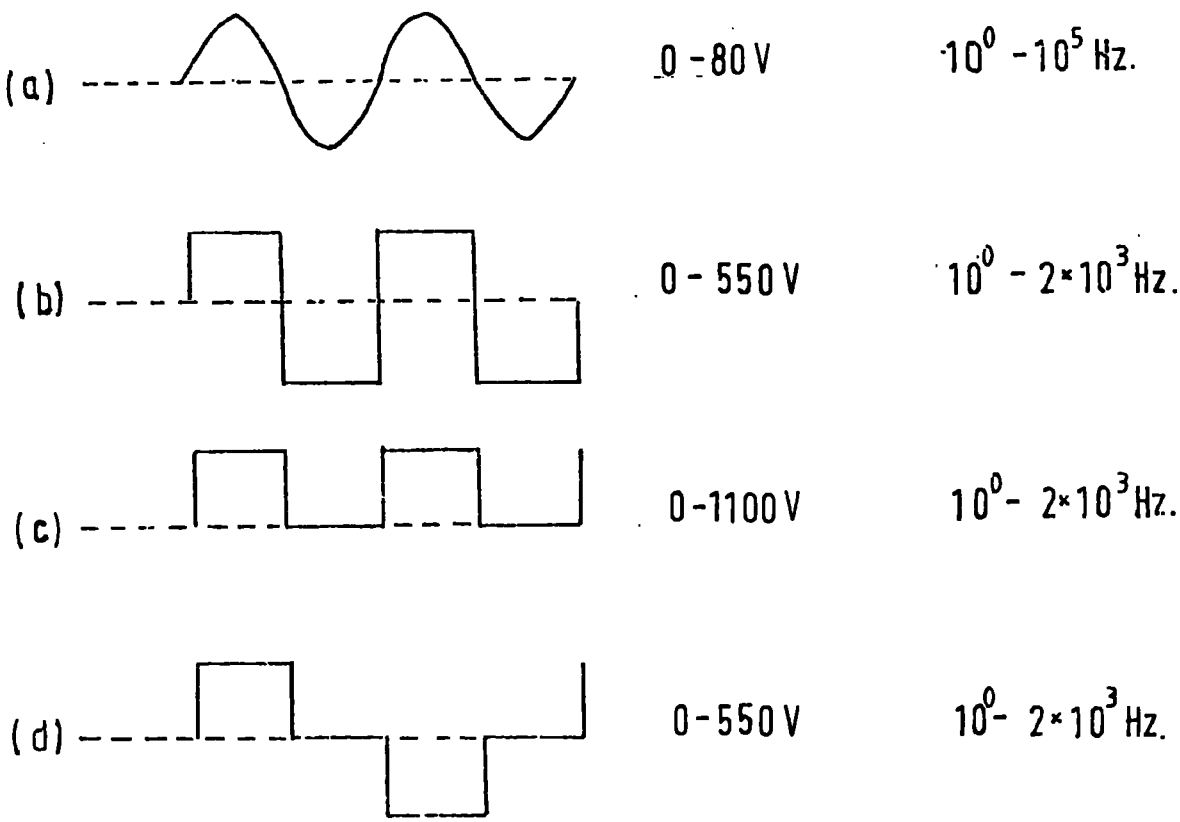

Fig. 3.5 Available pulse shapes together with voltage and frequency ranges.

Sinusoidal voltages up to 80V peak-to-peak could be applied using an Advance low frequency oscillator model HIE. This unit could be operated at frequencies up to 50 KHz.

A dc. voltage could be superimposed on the above mentioned waveforms by incorporating an extra 0-200V power supply. The ac. voltage could thus be made to oscillate about a positive or negative level as required.

The various pulse shapes available for the electroabsorption equipment are shown in Figure 3.5, together with the respective voltage and frequency ranges.

3.2.4 Detection System

As mentioned previously, the magnitude of the change in transmission observed in electroabsorption experiments is in general very small. Accordingly one uses lock-in amplifier techniques to detect the signal and improve the signal to noise ratio.

The detection apparatus used in this work was based on the Brookdeal system of lock-in amplifiers. A schematic of the equipment is shown in Figure 3.6. The signal from the photo-multiplier contains two ac. signals. The first signal is due to the modulation of the incident light beam by the optical chopper at 400 Hz, while the second is due to the much smaller periodic change in transmission due to the effect of the electric field on the absorption of the sample. The signal from the photo-multiplier is fed to two Brookdeal 9501 lock-in amplifiers, one of which is referenced at the frequency of the optical chopper, namely 400 Hz, the other at twice the frequency of the applied field. This second phase-sensitive detector is referenced at twice the frequency of the modulating field since the change in transmission is independent of the sign of the field. (This is an idealized case and deviations from this behaviour are

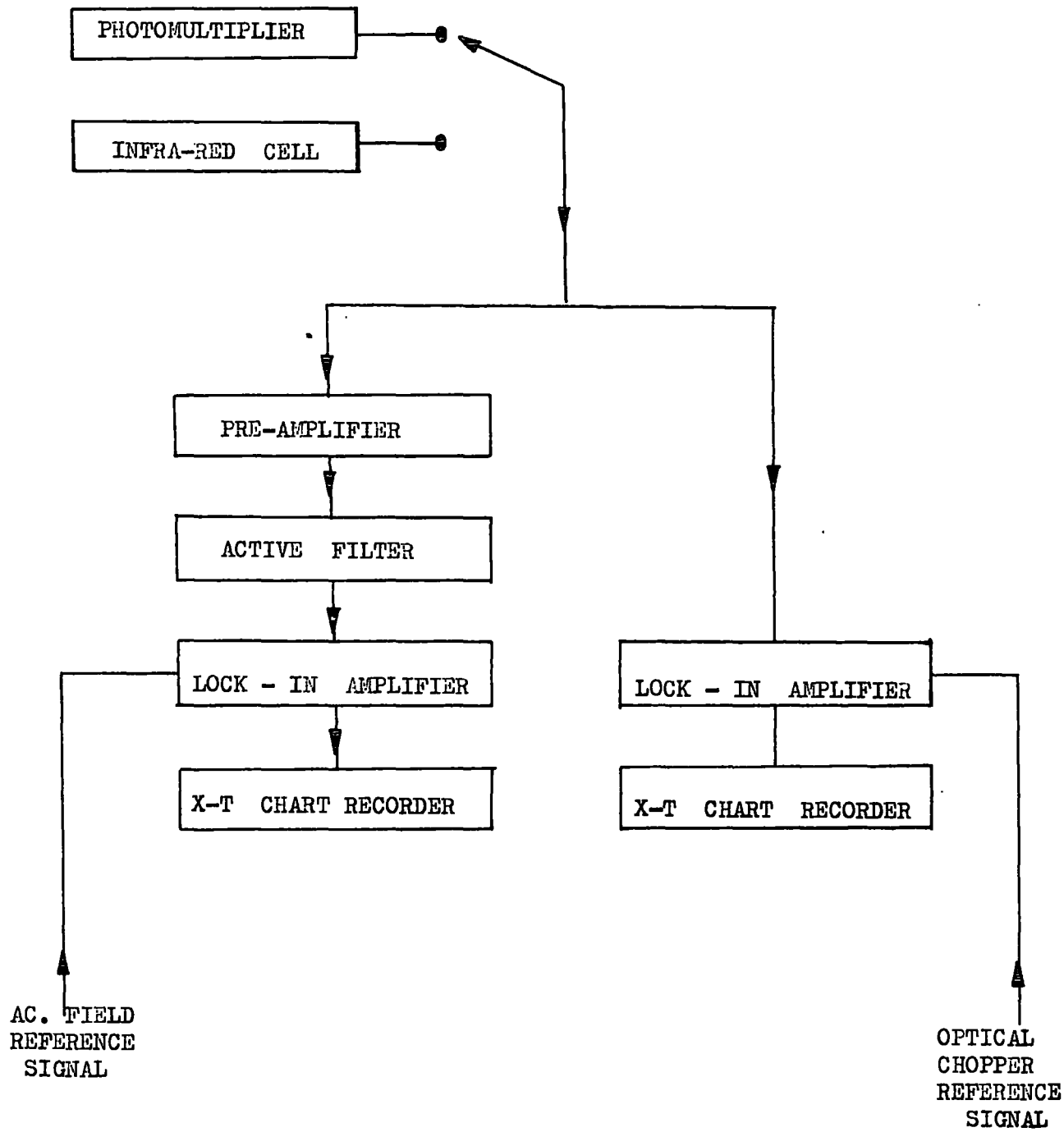

Fig. 3.6 Schematic of the detection system.

often observed. This point is discussed further in chapter five). The Brookdeal 9501 phase sensitive detector conveniently contains a facility for reference frequency doubling. It is important that the frequency of the electric field is sufficiently far away from the frequency of the optical chopper for interference between the two signals to be avoided. If the electroabsorption measurement is to be performed at approximately the same frequency as the optical chopper, then the zero field transmission, I, must be determined subsequently, or if the transmitted light is high, the dc. signal from the photomultiplier (with the optical chopper off) can be connected directly to a chart recorder.

The lock-in amplifier which handles the small signal due to the electric field incorporates a Brookdeal 5004 preamplifier, in order to make the signal easier to handle. This equipment, however, also amplifies any noise present in the signal, so a Brookdeal 5011F active filter is used to improve the signal to noise ratio. This filter may be operated either in notch mode, in order to exclude a particular noise frequency, or in bandpass, in which case a narrow band of frequencies centred on the reference frequency is passed. These two units are plug-in accessories to the 9501 lock-in amplifier but are shown seperately in the diagram for clarity.

After passing through the active filter the signal is passed to the lock-in amplifier proper. After maximizing the signal by varying the reference phase angle, the signal is rectified and an output is taken to a Bryans 28000 x/t chart recorder. A similar procedure is adopted for the signal passed to the other lock-in amplifier, except that this system does not incorporate a preamplifier or an active filter.

Two signals are thus measured, namely ΔI the change in transmission due to the field, and I, the zero field transmission. By means of the motorized drive on the monochromator, one may measure these two quantities as a function of wavelength, thereby obtaining an electroabsorption spectrum. In practice the scan was always made

very slowly since, due to the noise on the signals, time constants of 100 seconds were often used. Typical scan rates in our experiments were 250 Å - 500 Å per hour. Another stringent requirement is that the phase angle required to maximize the signal must be constant with wavelength before a scanned measurement may be performed. If this condition is not met, a point by point measurement needs to be performed, adjusting the phase at each point.

It is easily shown that the two quantities ΔI, I, are related to $\Delta\alpha$, the change in absorption coefficient by

$$\Delta\alpha = -\frac{1}{d} \cdot \frac{\Delta I}{I} \cdot \left\{ \frac{1 - R^2 e^{-2\alpha d}}{1 + R^2 e^{-2\alpha d}} \right\} \qquad (1)$$

where d is the thickness of the sample and R is the reflection coefficient.

3.2.5 Electrical Noise

The above description of the experimental procedure fails to illustrate the difficulties inherent in electroabsorption measurements. In practice the light transmitted by the sample is extremely small, leading to signals buried in noise. Great care was taken to reduce the noise level as far as possible by using low-noise cable, careful positioning of equipment and the utilization of filters. However, since the photomultipliers often had to be run at the maximum permitted voltage, this contributed a considerable level of photomultiplier shot noise. In the best of cases photon shot noise predominated, leading to signal to noise ratios proportional to $I^{\frac{1}{2}}$. Although the use of strong light sources is suggested by this, there is a practical limit to the intensity of source one can conveniently use.

3.3 Zero Field Absorption Equipment

The equipment described in section 3.2 was also used to measure the zero field absorption coefficient. The incident light was once again modulated by the 400 cps. optical chopper. After passing through the sample the transmitted light, I, was detected by the photomultiplier and the signal fed into the lock-in amplifier. Only one lock-in amplifier was used in this case, as no electric field was being applied.

In order to measure the incident light intensity, Io, the cryostat could be turned through 90^{o} so that the sample was moved out of the light beam. The light in this case passed through an aperture identical in size to that over which the sample was mounted, and travelled exactly the same path length before detection. Since the equipment available was a single beam instrument this measurement was recorded subsequent to the measurement of I. To reduce errors from this procedure the source was allowed to stabilize for 90 minutes before the measurements and each run was performed in approximately 15 minutes. The III - V materials were investigated using the 1.0 μm grating while this was changed to 0.5 μm for the Langmuir films.

The two recorded signals I and Io are related to the absorption coefficient α by the equation:

$$I = \frac{I_o e^{-\alpha d}(1 - R)^2}{1 - R^2 e^{-2\alpha d}} \qquad (2)$$

In our experiments the term $R^2 e^{-2\alpha d}$ was always negligible and was ignored. The value for the reflection coefficient R was taken from published data. The small changes in R over the energy range of interest were neglected.

Measurement of absorption coefficient α at various wavelengths were thus plotted for several temperatures, that is 295K, 175K and 77K.

3.4 DC. Conductivity Measurements

The dc. conductivities of all the samples investigated by the electroabsorption method were determined, both at room temperature and as a function of temperature. Two different cryostats were used for these measurements, one for the inorganic materials, the other for the organic samples.

The apparatus used to measure the conductivities of the inorganic samples is indicated in Figure 3.7. It consisted of a stainless steel gas exchange cryostat, mounted firmly on a supporting rack. The cryostat was evacuated to a pressure of 10^{-3} torr using an Edwards ES 330 rotary pump, to prevent water vapour condensing on the samples. Helium exchange gas was passed down a hollow metal tube to the bottom of the chamber, and allowed to permeate out slowly through a valve positioned at the top of the cryostat. The rate of flow could be adjusted accurately by a needle valve. The temperature of the sample was controlled by varying the temperature of the helium gas flowing past it. This was accomplished by balancing the cooling effect of a jacket of liquid nitrogen, surrounding the outside of the cryostat, with a 150 watt circular heater, surrounding the area in which the sample was positioned. The liquid nitrogen was contained in a glass dewar, which could be raised or lowered around the steel cryostat as required. The dewar had two walls, with the adjoining space evacuated to provide good thermal insulation. It was built into a box for safety reasons, and ease of handling.

The power supplied to the heater was controlled by a Eurotherm temperature controller, using a feedback system. The temperature of the sample was measured by means of a copper-constantan thermocouple placed very close to the sample. A room temperature reference junction compensation circuit was contained in the Eurotherm. The voltage supplied to the heater was varied automatically by the Eurotherm depending on the difference between the set and measured temperatures. Using this system,

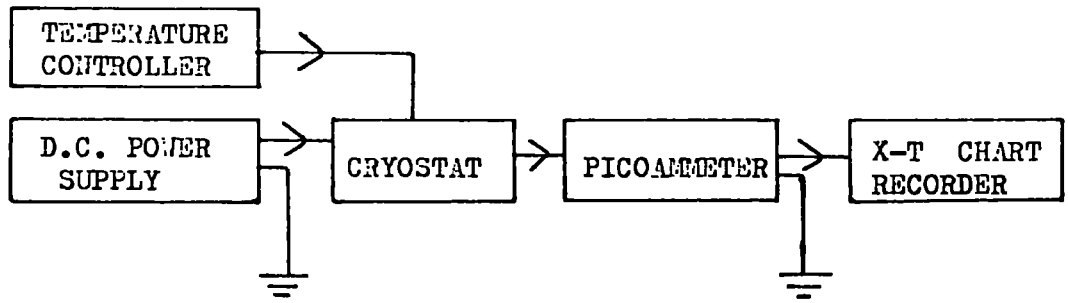

Fig. 3.7 Schematic of the dc. conductivity measurement system.

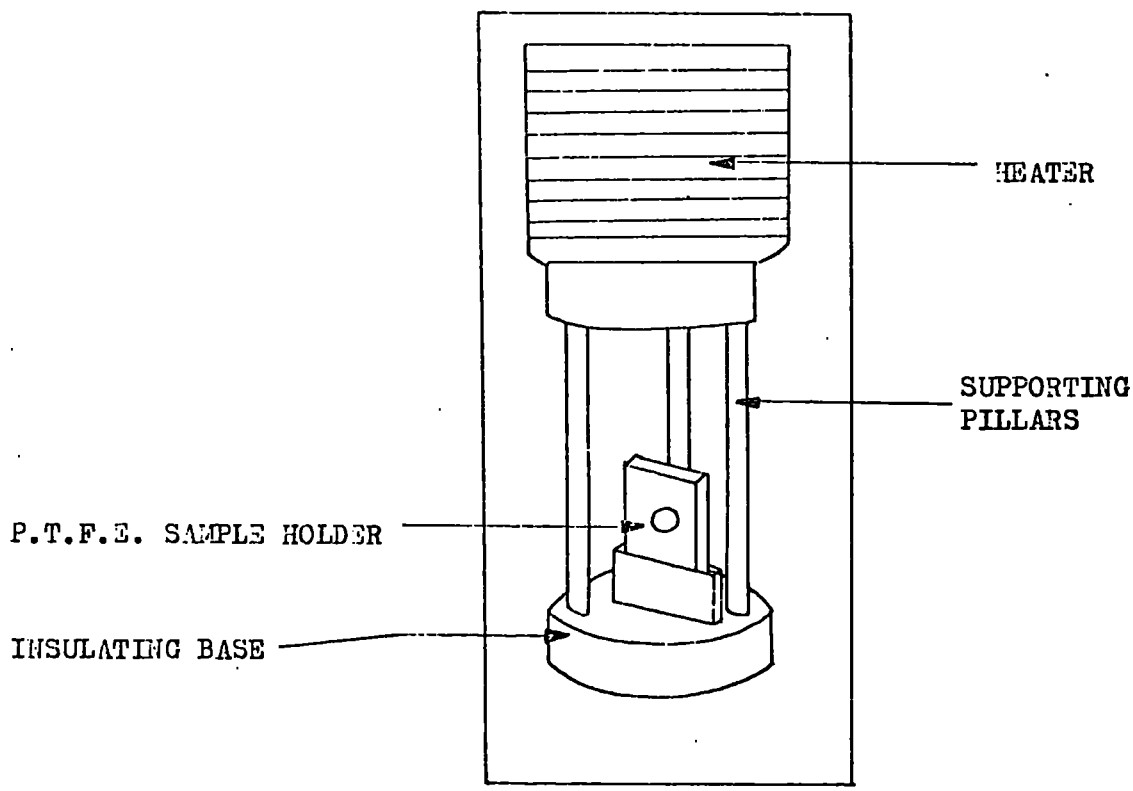

Fig. 3.8 Diagram illustrating the inside of the cryostat used for the inorganic dc. conductivity measurements.

the cryostat had a range of approximately 400 - 100K, with an accuracy of about $\pm$ 1K.

To allow easy access to the sample mount, the heater could be moved upwards along three metal pillars. The sample mount consisted of a PTFE table with an adjustable clamp. Samples were mounted on a PTFE disc to prevent leakage currents, and the disc was clamped in position. Electrical contact to the sample was made by means of fine wires taken from highly insulating lead-throughs in the wall of the cryostat, and passed along the centre of two hollow earthed pillars (those used to mount the heater). This procedure ensured good screening and reduced the electrical noise. The cryostat was securely earthed, care being taken to prevent earth loops occurring. A diagram of the inside of the cryostat is shown in Figure 3.8.

The organic materials posed special problems when it came to making electrical contacts to them. This topic will be dealt with in detail in chapter six, so it will suffice to state here that it was found convenient to use a specially modified Oxford Instruments DN 704 exchange gas cryostat for the dc. and ac. conductivity measurements on these materials. A diagram showing the main features of this cryostat is shown in Figure 3.9. It consisted of two chambers, an inner chamber in which the sample was mounted and an outside insulating jacket. The outside jacket was evacuated to a pressure of 10^{-3} torr by an Edwards ES 330 rotary pump. On cooling the pressure was reduced still further due to the inclusion of a charcoal sorb in this chamber, which cryopumped at low temperatures. The inner chamber was evacuated to a pressure of 10^{-3}torr and helium exchange gas admitted to provide thermal contact between a liquid nitrogen reservoir and the sample. A 30 watt heater was attached to a heat exchanger block through which liquid nitrogen from the reservoir could be passed. The temperature of the sample was controlled by varying the flow of nitrogen through the heater block by means of a valve, and by adjusting the power applied

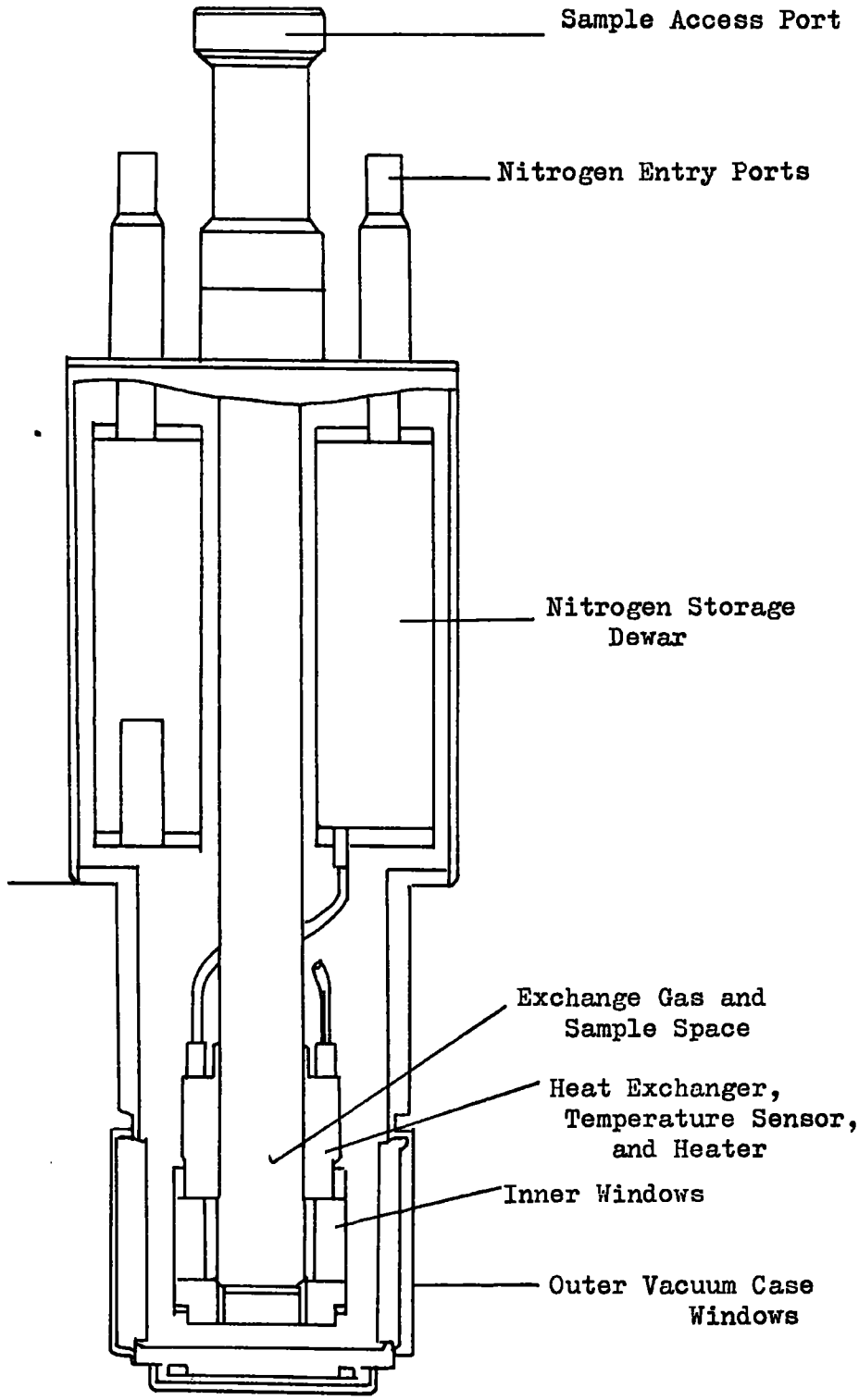

Fig. 3.9 Main features of the inside of the DN704 cryostat.

to the heater. The temperature was measured using a platinum resistance thermometer. Automatic control of the temperature was obtained by using an Oxford Instruments DTC 2 digital temperature controller, similar to that mentioned in section 3.2.2. Using this instrument temperature stability of ± 0.1K could be obtained. The operating range of the cryostat was 77K to 450K.

The sample was mounted at the end of a metal rod, which could be removed vertically from the sample chamber. This is illustrated in Figure 3.10. An O-ring seal enabled a good vacuum to be obtained before admission of the helium gas. The sample chamber was reasonably large, so that the mount at the end of the sample rod was capable of holding a 3" X 1" glass microscope slide. The sample mount was fitted with a minature positioner, which could be delicately adjusted to position a gold contacting ball on the surface of the sample's electrode. Contact was formed by carefully applying slight pressure to the gold ball, which was attached to the positioner by a fine flexible gold wire. Too much pressure invariably damaged the sample in question. Electrical contacts from the positioner were taken up the hollow central tube of the sample rod and out through two highly insulating lead-throughs.

Voltages were applied to the samples in either cryostat from a Keithley 241 high voltage stabilized supply. This equipment had a range of 0.01 to 1000V, in unit steps. The current was measured by means of a Keithley 410 A picoammeter, with a range of 10^{-14} - 10^{-2}A. This meter has an imput impedance of less than 3 X 10^{9} ohms on the 3 X 10^{-13} amp. scale, decreasing to 1 ohm on the 10^{-3} amp. scale, and was thus quite suitable for our purpose. The picoammeter produced a full scale deflection output of 1 volt, and was connected to a Bryan's 28000 x/t recorder.

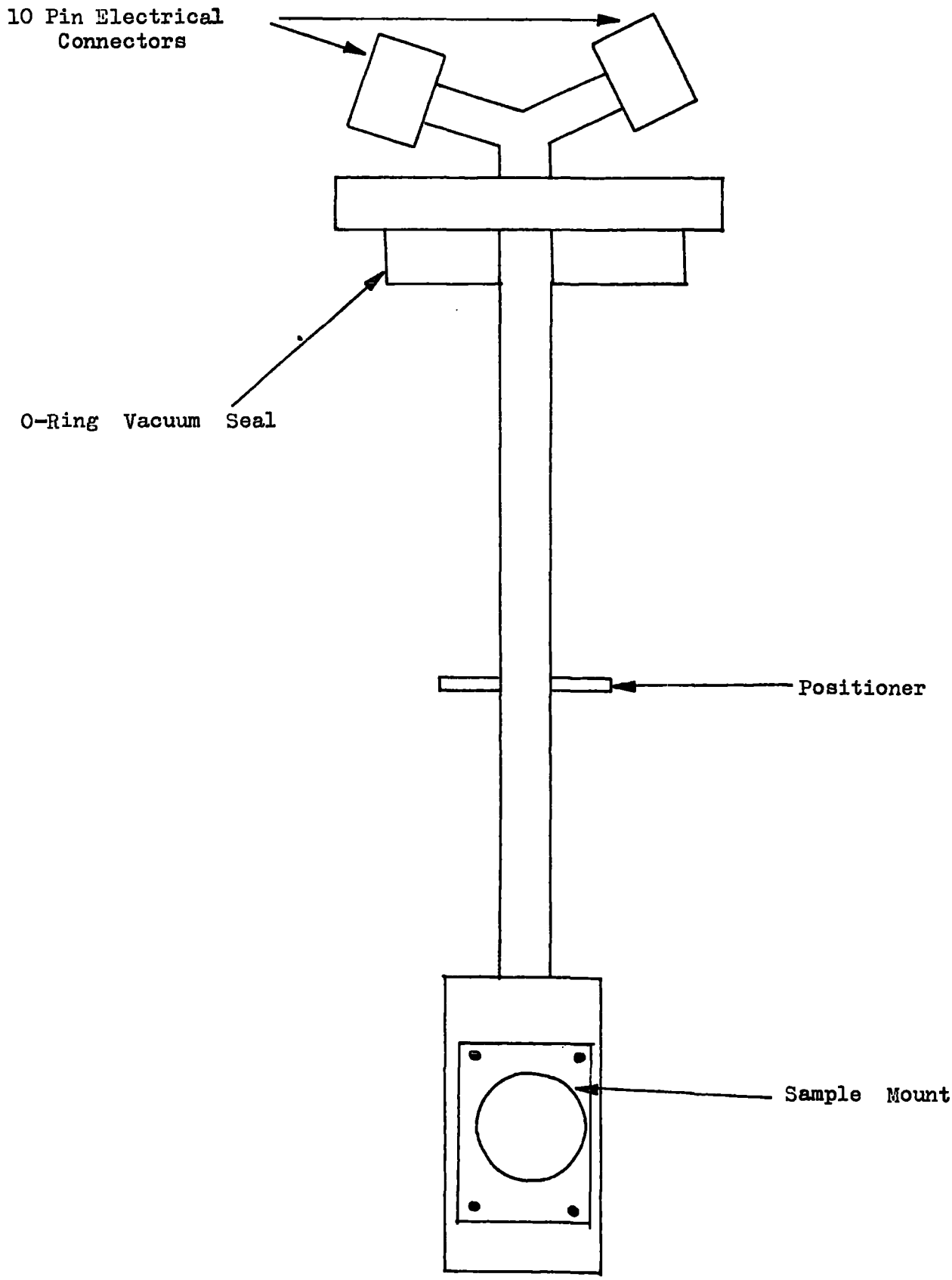

Fig. 3.10 Sample holder for the DN704 cryostat.

3.4.1 Experimental Procedure

To obtain reproducible results, the following procedure was adopted for the dc. conductivity measurements. The sample was first taken to the highest voltage which was to be applied to it in order to "form" the contact. In order to remove any space charge injected by this procedure the sample was then heated to a high temperature at a low voltage. For the inorganic materials this was usually 100°C. However, the organic materials investigated could not withstand temperatures greater than 60°C, and this was thus the maximum temperature to which they were taken. Subsequently, the sample was cooled to the desired temperature and current-voltage plots taken for increasing voltage. The current was plotted out on the Bryan's x/t chart recorder and a reading was taken when the trace was constant with time, for a particular voltage and temperature. Before reversing the voltage the sample was again heated with a small bias to drive out any remaining space charge.

For the activation energy plots, care was taken to ensure that the current did not change from ohmic to space charge limited during a run. This was accomplished by measuring the I-V curves at several temperatures before the activation energy run was performed.

A further aid to the attainment of reproducible results was to adopt the procedure of taking a room temperature reference voltage and current. In this procedure a small voltage was applied to the sample at the start of the measurements and the current recorded. On each subsequent occasion when a measurement was to be taken, the same voltage was applied at room temperature, and the current checked. This procedure ensured that any space charge injected into the sample was always removed before the next measurement was commenced. Furthermore, it enabled any permanent change in characteristic, due to degradation of the contacts, to be discovered.

In addition to the above procedure, activation energy plots were always made for decreasing temperature.

3.5 AC. Conductivity Measurements

In addition to the dc. conductivity measurements, ac. conductivity and capacitance measurements were also performed. The use of standard bridge techniques to make such measurements on insulating or semi-insulating materials is usually impractical, since for these materials the conductance component is in general very much smaller than the capacitive term. This leads to the phase angle becoming very large, and hence, bridge techniques breakdown.

Accordingly we have based our measuring circuit on phase-sensitive techniques. The principle may be understood as follows. The device may, to a first approximation, be regarded as a capacitance C_x, in series with a resistor R_x, leading to a total impedance, at a frequency ω, equal to

$$Z_x = \frac{1}{G_x + i\, C_x \omega} \tag{3}$$

where $G_x = {}^{1}/_{R_x}$

If a small ac. voltage V_1 at a frequency ω is applied to the sample in series with a standard capacitor C_o, then the output voltage V_o across C_o may be considered to have two components, one in phase with V_1 and one in quadrature with V_1. Simple ac. theory leads to the following expression for these component:-

$$V_o \text{ (in phase)} = \frac{\omega^2 C_x(C_o+C_x) + G_x^2}{\omega^2(C_o+C_x) + G_x^2} \tag{4}$$

$$V_o \text{ (out of phase)} = \frac{\omega(C_o+C_x)G_x - \omega G_x C_x}{\omega^2(C_o+C_x) + G_x^2} \tag{5}$$

The ratio of these two terms is

$$\frac{V_o \text{ (in phase)}}{V_o \text{ (out of phase)}} = \frac{\omega^2 C_x(C_o+C_x) + G_x^2}{\omega(C_o+C_x)G_x - G_x C_x \omega} \qquad (6)$$

Since $G_x = {}^1/_{R_x}$ we have

$$\frac{V_o \text{ (in phase)}}{V_o \text{ (out of phase)}} = \frac{\omega^2 C_x(C_o+C_x)R_x^2 + 1}{\omega C_o R_x} \qquad (7)$$

If however, we choose $C_o \gg C_x$ but maintain

$$G_x \ll C_o \omega$$

then we can reduce the above equation to

$$\frac{V_o \text{ (in phase)}}{V_o \text{ (out of phase)}} = C_x R_x \omega \qquad (8)$$

By a suitable choice of C_o, we were able to use this formula to obtain values of G_x and C_x over a frequency range of 10-10^6 Hz.

The actual measuring circuit is shown in Figure 3.11. The voltage V_1 applied to the device, was taken from an Advance low frequency oscillator. The magnitude of this voltage was kept as low as possible to avoid non-linear effects, and was usually less than 100 millivolts. The output voltage V_o across the capacitor C_o was fed into a Brookdeal low noise amplifier, model 450, and thence into two Brookdeal 411 phase-sensitive detectors. A reference signal was derived from the low frequency oscillator. This signal was taken to a Brookdeal reference unit, type 421. This reference unit fulfilled two purposes. Firstly, it provided two subsidiary reference outputs with a phase difference of 90^o between them, which were then

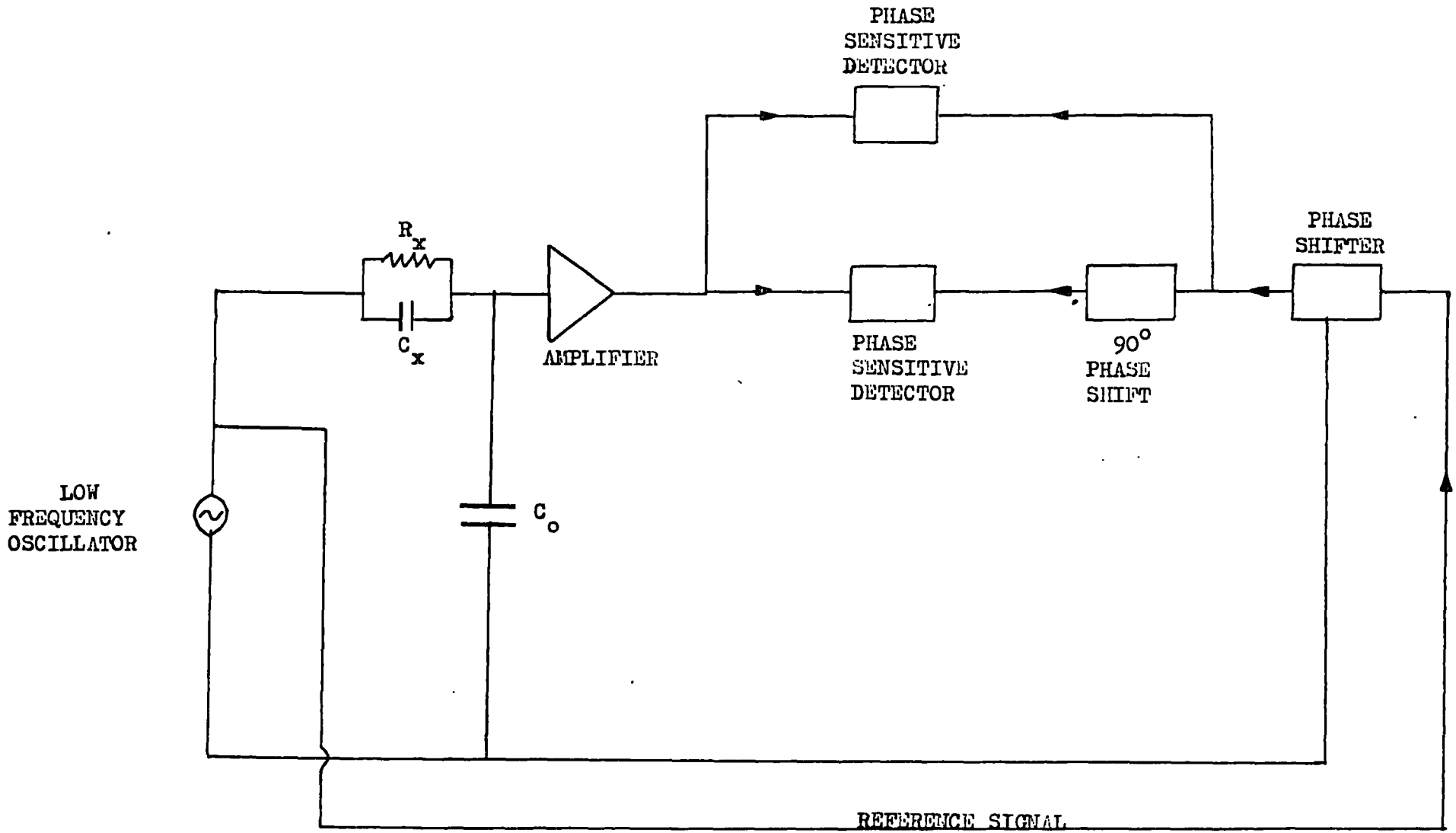

Fig. 3.11 Circuit diagram for the ac. conductivity measurements.

applied to the reference inputs of the phase-sensitive detectors. However, the reference unit also had the facility to shift the phase of its outputs with respect to its input. The facility was used to correct for any stray phase shifts of the ac. signals, such as that caused by the capacitance of the leads.

Since the two phase-sensitive detectors were referenced with a 90° phase difference between them, they could thus be used to detect the two components of V_o, that is the "in phase", and "out of phase" components. The "in phase" component is directly related to the capacitance C_x, while the "out of phase" component is related to the conductance G_x by equation (8). The output from the phase-sensitive detector which measures the conductance was usually quite small since our samples were semi-insulating, and was thus fed into a digital voltmeter for greater accuracy.

3.5.1 Experimental Procedure

The procedure for obtaining the conductance and capacitance measurements was as follows.

The sample to be investigated was initially replaced by a known resistor R_s, and a known capacitor C_s. A large range of resistors and capacitors was available, and the valves of C_s and R_s were chosen to be as close as possible to those expected for the actual sample. Care was taken to ensure that C_o was at least ten times greater than C_s. With the small voltage V_1 applied, the ratio of the outputs from the phase-sensitive detectors was given by equation (8). Since C_x, R_x, and ω were all known, the measured voltage could be checked against the calculated value. Small discrepancies occasionally occurred and were corrected by adjusting the phase of the reference unit. The standard capacitor C_s and resistor R_s could be replaced by others to ensure that the measured voltage outputs from the detectors scaled in the correct proportion. When that condition was satisfied, the system was

said to be balanced and the sample inserted. The sample's capacitance was then calculated by direct comparison with C_s, while its conductance was obtained from equation (8). The procedure of "balancing" the system was performed for each individual frequency.

For the purpose of these measurements the samples were mounted in the cryostats described in section 3.4.

3.6 Photoconductivity Measurements

Measurements of the photoconductive response of both the inorganic and organic materials were carried out using the Oxford Instruments CF 104 cryostat and the optical system described in sections 3.2.2 and 3.2.1 respectively. Gratings blazed at 0.5 and 1.0 μm were interchanged into the Hilger/Watt monochromator as required. Spectral purity was ensured using the Optics and Technology bandpass filters described earlier. The same source, an Atlas 250 watt projector bulb, was also used throughout the measurements. Temperature control of the sample was accomplished using the method described in section 3.2.2. For these measurements however, a dc. voltage was applied to the samples directly from the Keithley 240 stabilized voltage source. The photocurrent was measured on a Keithley 410A picoammeter, whose output was connected to a Bryan's 28000 x/t chart recorder.

The measured photocurrents were corrected for the spectral response of the source-filter-grating combination, using either a Gamma Scientific digital photometer, model 2400 or a United Technology Inc. photodiode. The Gamma Scientific photometer has a calibrated response from 400 nm to 700 nm. This response is shown in Figure 3.12. The photodiode on the other hand, had a calibrated response from 350 nm to 1160 nm, which is also shown in Figure 3.12. It was found more convenient to use the Gamma Scientific detector in the region below 700 nm, with the photodiode used above this wavelength. For wavelengths greater than 1.2 μm, a thermopile was used for calibration purposes.

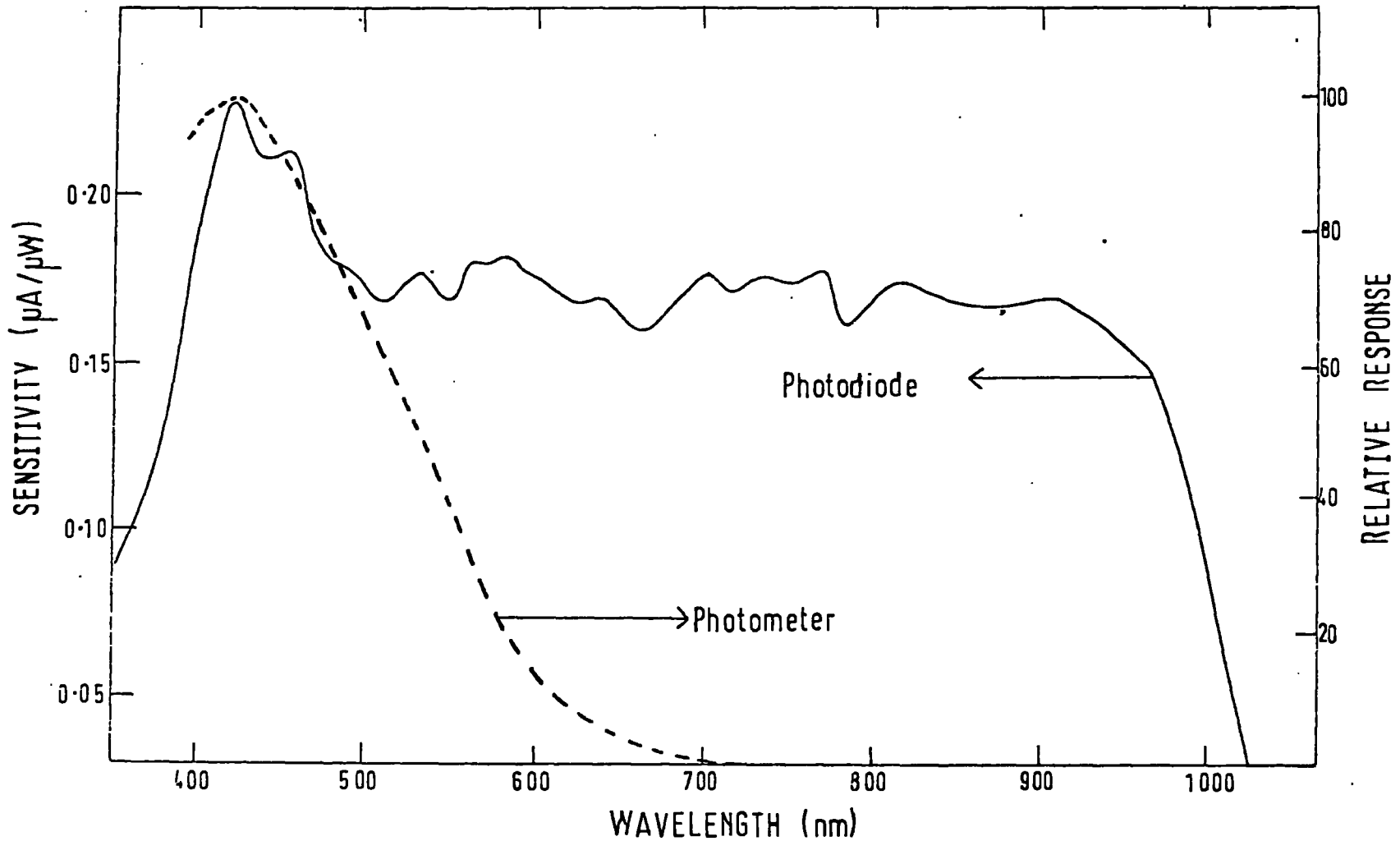

Fig. 3.12 Spectral responses of the Gamma Scientific photodetector and the United Detector photodiode.

CHAPTER IV

INTRODUCTION TO GALLIUM ARSENIDE AND INDIUM PHOSPHIDE

4.1 Introduction

The interest in binary compounds between groups III and V of the periodic table has grown extremely rapidly ever since Welker [1] demonstrated in 1952 that these materials were semiconducting. Although Welker's first paper suggested these compounds had interesting properties, it would have been difficult to imagine the rate at which our knowledge of these materials would expand, and our growth technology improve. These two factors have led to the increasing use of III-V materials in a large number of physical devices, such as microwave oscillators, infrared detectors and injection lasers.

Our interest in these materials is confined to two specific compounds, namely gallium arsenide and indium phosphide. The growth and properties of gallium arsenide have received a greater degree of attention than those of indium phosphide. GaAs is now an extremely important material for the manufacture of microwave oscillators, high frequency field effect transistors, and IMPATT diodes. It has been shown however, that InP microwave oscillators have a greater theoretical conversion efficiency than GaAs devices [2] and that it is a more suitable material for solar cell and light emitting diodes [3,4]. Accordingly, greater attention has been focussed on it in recent years with the result that high quality single crystals of both GaAs and InP can now be routinely prepared.

4.2 Growth Of Gallium Arsenide Single Crystals

A number of techniques have been used to grow gallium arsenide single crystals. These include floating zone refining, the horizontal

Bridgman method and liquid encapsulated Czochralski pulling. The main difficulty in the growth of gallium arsenide crystals arises from the dissociation pressure of arsenic at the melting point of the compounds.

The GaAs crystals studied in this work were prepared using the liquid encapsulation technique. The method depends on the use of an inert liquid to prevent the loss of volatile components from the melt. An inert gas is used to exert a pressure on the surface of the liquid. The loss of material from the melt is prevented, provided the pressure of the gas is in excess of the equilibrium vapour pressure of the most volatile components of the melt. It is essential that the liquid encapsulant is less dense than the melt, optically transparent and chemically stable in its surroundings. In addition, it is desirable that the volatile constituents of the melt should be insoluble in the liquid encapsulant.

Mullin et al [5] have reported the growth of high purity gallium arsenide crystals by the liquid encapsulation method using a standard germanium puller. These authors used B_2O_3 to contain the melt but also found $BaCl_2$ and $CaCl_2$ to be quite suitable.

Epitaxial gallium arsenide crystals have been grown by both liquid phase epitaxy (LPE) [6] and vapour phase epitaxy (VPE) [7].

4.3 Crystal And Band Structure Of Gallium Arsenide

GaAs, like most of the III-V compounds, has the zinc-blende crystal structure and space group symmetry $F\bar{4}3m$. It has a lattice parameter of 5.64 $\mathring{A}$ [8], a value which is much larger than the sum of the covalent radii of Ga and As. The density of the material is 5.31 g/cm^3. Many of the properties of the crystal depend on the lower symmetry of the zinc-blende structure compared with the diamond structure. Figure 4.1 illustrates the zinc-blende crystal

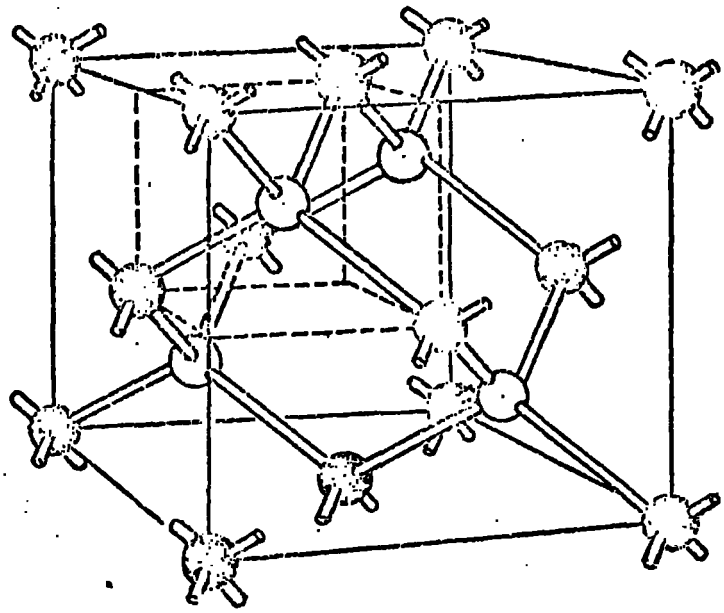

Fig. 4.1 The zinc-blende crystal structure.

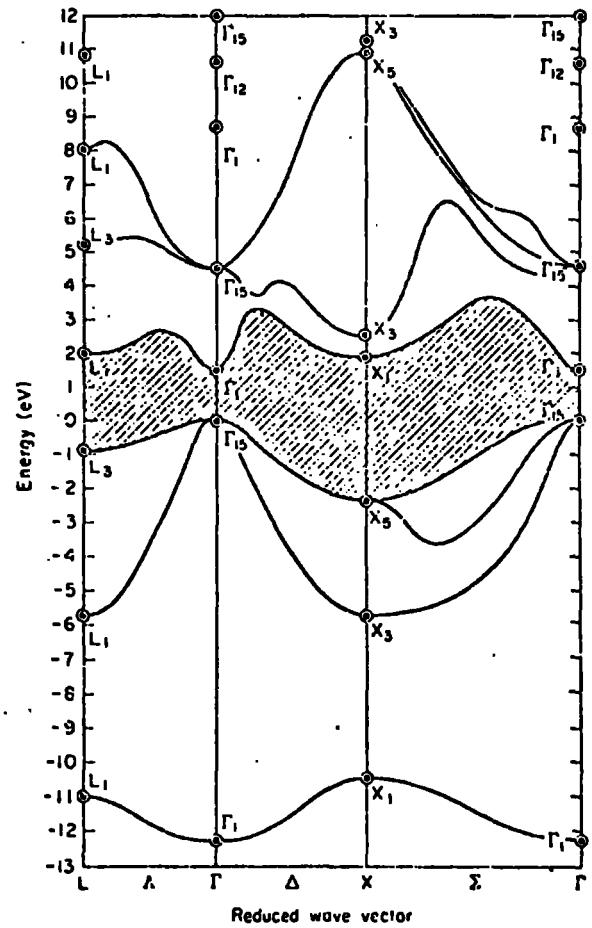

Fig. 4.2 Energy band diagram of GaAs. (15)

structure. Both the zinc-blende and diamond structures allow the lattice the 24 symmetry operations of the tetrahedral point group Td, about any lattice site, but the zinc-blende lattice does not possess the additional symmetry of inversion about a point midway between two adjacent atoms. This absence of a centre of symmetry gives rise to many of the special properties of III-V compounds.

The band structure of GaAs has been calculated by Callaway [9], among others [10], who concluded that the lowest minimum of the conduction band lies at the centre of the zone. Subsidiary minima are found to occur on the [111] and [100] directions in k-space. The valence band of GaAs is similar to that of Ge, with a heavy hole band, a light hole band, and a spin-orbit band. However, due to the absence of inversion symmetry, the heavy hole bands are split, and the maxima do not lie exactly at the centre of the zone. Experimental confirmation of the valence band structure has been found in absorption [11]. A variety of optical methods has been used to establish the direct ($k = 0$) energy gap as 1.517 eV at 20^{o}k and 1.435 eV at 295 k [12][13]. The energy separation of the two minima in the conduction band, ΔE_{12} ($X_1 - \Gamma_1$) has been found by Aukerman and Willardson [14] to be 0.38 eV, while the spacing ΔE_{13} ($L_1 - \Gamma_1$) has been determined as 0.5 eV [15]. These energy spacings, as computed by Herman et al [15] are illustrated in Figure 4.2.

4.3.1 Electrical Properties Of Gallium Arsenide

The resistivity of GaAs single crystals may be controlled from 10^{-1} to $10^{8}\Omega$cm by introducing impurities during growth. In this thesis, we are concerned exclusively with semi-insulating GaAs, that is, with material which has been deliberately compensated by doping with chromium to produce resistivities greater than $10^{6}\Omega$cm, and typically $10^{8}\Omega$cm, at room temperature. While measurements on pure GaAs have indicated a Hall mobility for electrons of 8500 $cm^{2}V^{-}sec^{-1}$ [16], the introduction of impurities leads to a lowering of the mobility. Recent reports by Lin and Bube [17] suggest a Hall mobility

Ec-Er ev	Resistivity Ωcm	Mobility $cm^2v^{-1}s^{-1}$	Method	Reference
0.70	-	5000	-	Sze & Irvin [23]
0.80	10^8	-	Photocond.	Tretyak [25]
0.81	10^8-10^9	-	Temp. dep. of impurity photolum.	Gorenlenok et al [22]
0.90	-	-	Photocond.	Bois & Pinard [24]
0.80	-	1000	Temp. dep. of Hall effect	Inoue & Okyama [18]
0.72	-	1000	Temp. dep. of Hall coeff.	Brodovoi & Derikot [19]
0.86	10^9	1600 - 2300	Photo-electronic	Lin & Bube [17]
0.98	10^8	-	S.C.L.C.	Ashby & Roberts [79]
0.70	10^9	4000 approx.	Hall effect	Look [80]

Table 4.1 Chromium level and mobility values in GaAs:Cr.

between 1600 and 2300 $cm^2V^{-1}sec^{-1}$ for electrons in semi-insulating GaAs:Cr at room temperature. Values lower than this have also been reported [18, 19].

A number of workers have investigated the electron and hole effective masses. A value of $m_e^* = 0.0648\ m_o$ was obtained by Chamberlain and Stradling [20] in non-degenerate GaAs from cyclotron resonance measurements. From reflectivity measurements Kesamanly et al [21] have determined hole effective masses, as a function of hole concentration, for degenerate p-type GaAs. For $N_p = 4.6 \times 10^{19}$ cm^{-3} to 1.8×10^{20} cm^{-3}, their values ranged from $0.28 m_o$ to $0.44 m_o$.

The nature and position in the energy gap of the chromium impurity in GaAs is the subject of much debate. Published data indicates that Cr acts as an acceptor with a level located near the middle of the band gap. The specific value of the impurity energy level has been difficult to pin down. Values range from 0.70 eV to 0.90 eV from the conduction band. Table 4.1 summarizes some of the recently reported values both of the chromium level energy and the mobilities in GaAs:Cr.

4.3.2 Optical Properties Of Gallium Arsenide

The band structure of GaAs was discussed in section 4.3, where it was indicated that a minimum of the conduction band and a maximum of the valence band occur at the same point in k-space. One would therefore expect to observe a direct optical absorption edge. In practice, the absorption edge is found to be extremely steep, but follows an exponential dependence on photon energy. Values of the absorption coefficient in the region of the main absorption edge have been determined by Moss [26] and others [27, 28]. Figure 4.3 illustrates the data obtained by Moss. Below absorption coefficients of 10^4 cm^{-1} the edge is seen to be exponential, with a slope $\simeq 100$ eV^{-1}.

The temperature dependence of the band gap is found to be about -4.30×10^{-4} eV/K at an absorption coefficient of 10 cm^{-1} [29].

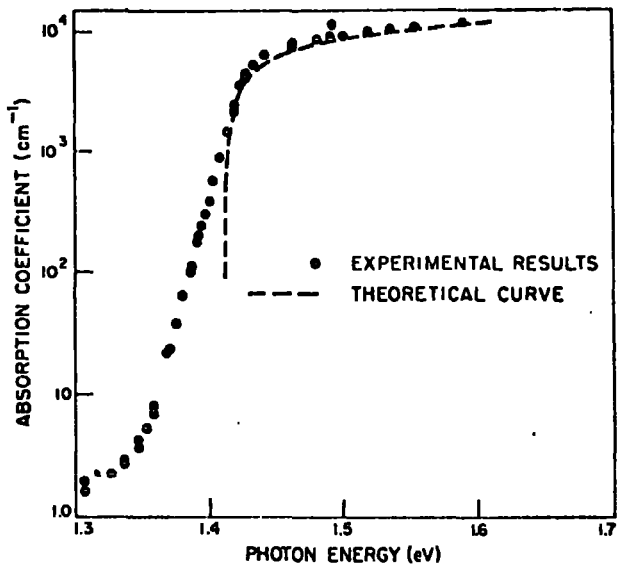

Fig. 4.3 Optical absorption coefficient of GaAs as a function of photon energy. (26)

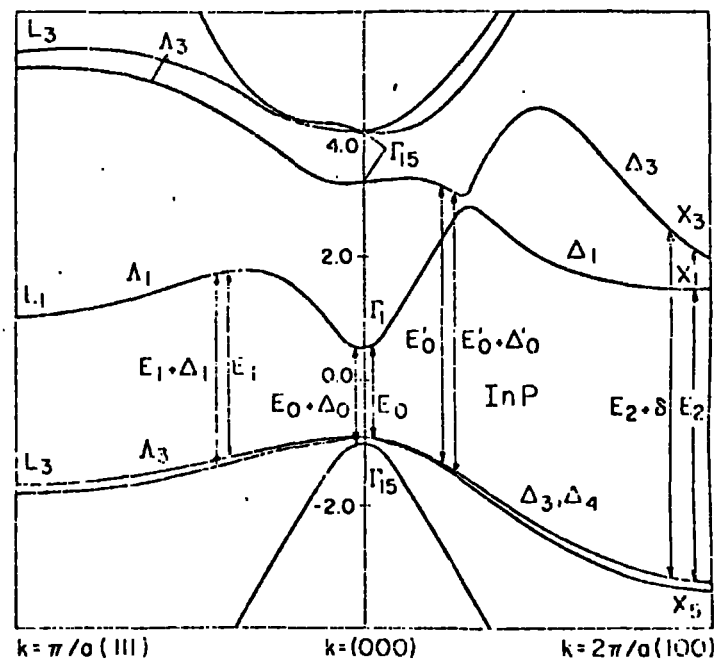

Fig. 4.4 Energy band diagram of InP including spin-orbit splittings. (34)

Zvara [30] also measured this quantity by Faraday rotation and has calculated a value of -4.26×10^{-4} eV/K between 80 and 300 K. A shift in the absorption edge due to free carriers has been recorded by Spitzer and Whelan [31] in n-type GaAs.

Typical values of the refractive index and static dielectric constant of GaAs are shown in Table 4.2 [32]. The static dielectric constant has been measured directly on high resistivity material [32].

4.4 Growth Of Indium Phosphide Single Crystals

Bulk indium phosphide crystals have been grown by four techniques, namely the gradient freeze technique, zone melting, the horizontal Bridgman method and liquid encapsulated Czochralski pulling. The chief problems encountered in the preparation of InP are its high dissociation pressure at the melting point and the reactivity of the elements at high temperatures. In the first three techniques mentioned above, the dissociation of the InP is prevented by establishing equilibrium with a phosphorous vapour atmosphere of appropriate pressure. The reactivity of the phosphorous vapour requires the use of non-metallic materials, such as fused quartz, to contain the system.

The dislocation density in crystals grown by the liquid encapsulation method is generally 1 - 2 orders of magnitude smaller than in crystals grown by the other methods. The major impurities are Si, O and C at a level of several ppm.

Mullin et al [33] have reported the growth of high quality InP crystals using the liquid encapsulation technique. The crystals grown by these workers were prepared using B_2O_3 and an inert gas at a pressure of 27 atmospheres. Typical growth rates were 2 - 3 cm per hour at 10 rpm.

4.4.1 Crystal And Band Structure Of Indium Phosphide

The crystal structure of InP is found to be extremely similar to that of GaAs, namely the zinc-blende structure. The material also exhibits an equivalent band structure with two subsidiary minima on either side of the main conduction band minimum. The band structure of InP, as calculated by Pollak et al [34] is displayed in Figure 4.4. Pitt [35] has calculated the $(X_{1c} - \Gamma_{1c})$ energy gap to be 0.70 eV, while he quotes the $(L_{1c} - \Gamma_{1c})$ gap as 0.40 eV. The spin orbit splitting factor Δ is 0.28 eV, according to Ehrenreich [36].

4.4.2 Electrical Properties Of Indium Phosphide

In view of the fact that high quality single crystals of InP have only recently been produced, there are considerable gaps in the information available concerning their electrical properties. The material can, like GaAs, be prepared with a large range of resistivities from 10^{-1} Ωcm, to 10^{8} Ωcm, simply by selective doping with impurities during growth. Doping with chromium produces crystals with resistivities of the order of 10^{4} Ω cm. This is in marked contrast to the effect of chromium in GaAs. Much higher resistivities of the order of 10^{7} - 10^{8} Ω cm may be produced in InP by doping with iron during growth. Results are presented in this thesis for both InP:Cr and InP:Fe crystals.

The mobility of InP has been investigated by Reid and Willardson [37], and Glicksman and Weiser [38]. Kovalevskaya [39] extended this work to liquid helium temperatures. Mullin et al [40] studied the variation of Hall mobility with electron concentration both in undoped InP and in semi-insulating chromium doped crystals. The maximum mobility recorded was approximately 4000 $cm^2V^{-1}s^{-1}$ at a free electron concentration of 5×10^{16} cm^{-3}. In the semi-insulating Cr doped samples this value had dropped to a maximum of 3170 $cm^2V^{-1}sec^{-1}$, for a crystal resistivity of 3.2×10^{3} Ωcm. As an illustration, Figure 4.5 reproduces a sample of Mullin's data for pure samples at room

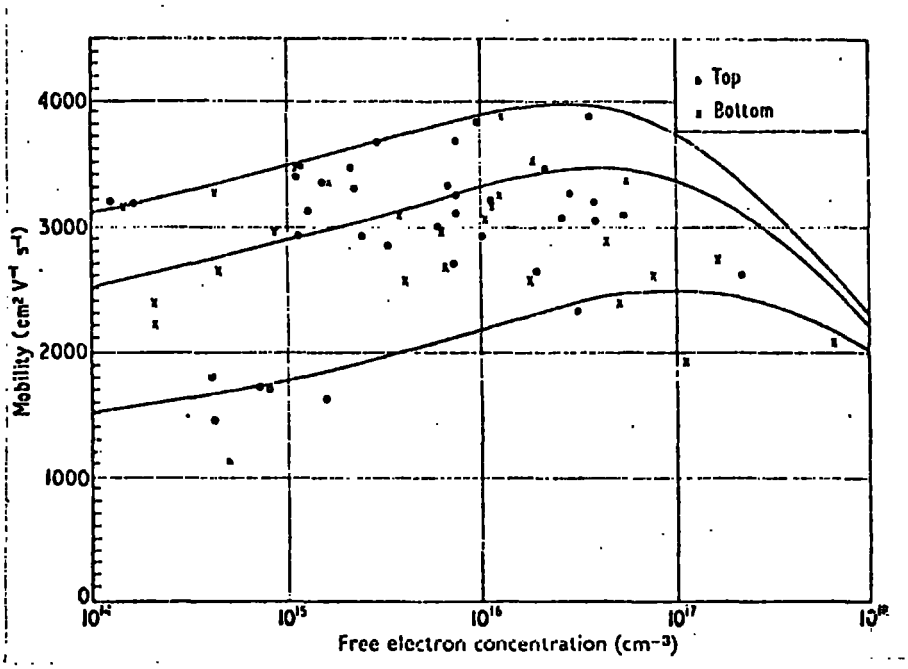

Fig. 4.5 Variation of mobility of InP crystals with free electron concentration. The full lines are theoretical curves with acceptor levels of 6.2×10^{16}, 8.8×10^{16} and 1.8×10^{17} cm^{-3}, reading from top to bottom. The curves and crosses represent measurements at the top and bottom of crystals respectively. (40)

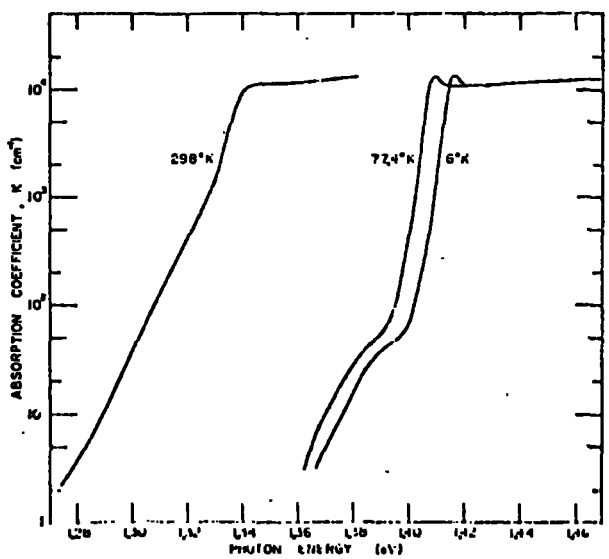

Fig. 4.6 Absorption edge of InP. (52)

temperature. In addition to the above work, Rode [41] carried out a detailed analysis of the temperature dependence of the mobility in pure InP. More recently Blood and Orton [42] have concentrated their attention on mobility studies in epitaxial InP. Apart from the work carried out by Mullin et al, practically no data are available concerning mobility in InP:Cr or InP:Fe. However, Mizuno and Watanabe [43] have made a brief report on room temperature Hall mobilities in InP:Fe. These authors obtained values ranging from 100 - 170 $cm^2V^{-1}sec^{-1}$ for samples of resistivity 10^9 Ωcm.

There is a much greater degree of agreement on the impurity energy levels in InP than in GaAs. It is generally agreed that doping the material with chromium produces a level at 0.54 eV below the conduction band [44], while doping with iron produces a deep acceptor level at 0.66 eV [45].

The reduced effective mass for electrons in pure InP was calculated by Moss and Walton [46] to be .075 m_o for a sample with $N = 1.07 \times 10^{16}$ cm^{-3}. Palik and Wallis [47] found a value of .077 m_o from cyclotron resonance experiments. The most recent value is due to Eaves et al [48], who estimated a value of $.0765\,\hat{m_o}$ at 300 K and $.0803\,\hat{m_o}$ at 77K. The value for the effective mass for holes is approximately 0.4 m_o [49].

4.4.3 Optical Properties Of Indium Phosphide

The absorption edge of InP is equally steep to that of GaAs but occurs at a slightly lower energy namely 1.42 eV at 0 K, compared to 1.52 eV for GaAs [50]. The edge also follows a similar exponential shape between values of absorption coefficient of 10 cm^{-1} and 10^4 cm^{-1}. The absorption coefficient of InP has been determined by Newman [51], Turner, Rees and Pettit [52] and others [50, 53]. Their results are displayed in Figure 4.6.

Values for the temperature dependence of the absorption coefficient range from -4.5×10^{-4} eV/K to -2.9×10^{-4} eV/K [54, 52].

The discrepancy is probably due to the fact that the slope of the absorption curve varies with temperature and it is thus necessary to quote the temperature dependence for a particular absorption coefficient.

The effects of free carriers upon the absorption edge have been studied by Dumke, Lorenz and Pettit [55] as well as by Newman [57]. In n-type InP free carrier absorption is proportional to λ^{2-5}, for samples with over 10^{17} donors per cm^3. The material exhibits a static dielectric constant of 13.10 and a high frequency dielectric constant of 9.55 [56]. The refractive index was measured by Pettit and Turner [57] and is quoted in Table 4.2 for comparison with GaAs.

Increasing interest is currently being generated as to the effect of various impurities on the electrical properties of InP. The most popular methods for the detection of deep levels in the forbidden band gap of a semiconductor are those based on optical, photoelectric or luminescent effects. Kovalevskaya et al [58] have investigated the photoconductivity spectrum of InP, while White et al [59] have examined the photoluminescence spectra of group II acceptors. Further photoluminescence work was carried out by Mullin et al [60]. More recently Bubyarskii et al [61] have studied the thermal ionization of deep centres in Au - InP:Fe barriers, while Koshel, Kaufmann and Bishop [62] have investigated the Fe acceptor in InP by means of E.S.R.

4.5 Previous Electroabsorption Work On Gallium Arsenide And Indium Phosphide

The first recorded study of electroabsorption in GaAs was carried out by Moss [26] in 1961. An example of Moss's data is reproduced in Figure 4.7. Using the data obtained in his experiments, Moss calculated the effective mass for electrons in GaAs to be $0.065\, m_o \pm 10\%$. However, some doubt surrounds the analysis used by Moss in reaching this result. As will become evident in

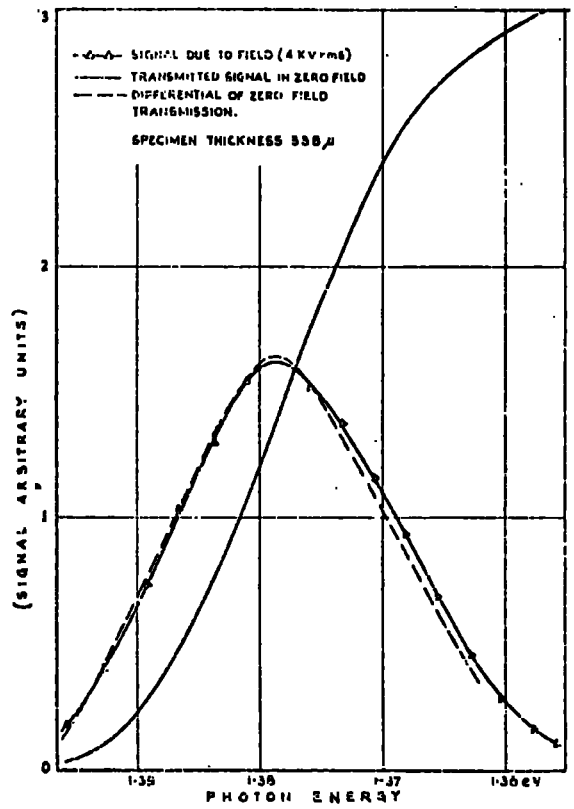

Fig. 4.7 Electroabsorption in GaAs at room temperature for a field of 4×10^3 V/cm. (26)

	GaAs	InP
n_o	3.32	3.09
ε_o	13.1	12.4

Table 4.2 Refractive index and static dielectric constant of InP and GaAs.

Chapter V, it is essential that a number of auxiliary measurements are performed along with the electroabsorption experiment before a definitive analysis of electroabsorption data may be carried out. These extra measurements include tests to ensure the absence of space-charge effects or photoconductivity within the crystal under consideration. In his paper, Moss fails to mention any such experiments, but does report that the measurements were performed at a frequency of 400 Hz. It is worth noting that in our experiments, photoconductive effects were clearly observable at that frequency in our GaAs crystals. Unfortunately, it is difficult to make an exact comparison between our data and those of Moss, since the diagrams presented by him were plotted in arbitrary units. A final point concerning the work of Moss is that it is reasonable to assume that the specimens under consideration by him in 1961 were of a much poorer quality than those currently available.

A number of other studies have been made concerning the effects of electric fields on the absorption properties of GaAs. Gutkin and Nasledov [63] studied the long wavelength threshold of the photoeffect in GaAs p-n junctions and obtained reasonable agreement between the theory of Franz and Keldysh and their experimental data. Lambert[64] compared the results of studies on semi-insulating GaAs with the theory due to Callaway and found agreement in the region below the energy gap. Above the energy gap the observed electric field effects were greater than those predicted by theory. Lambert however, carried out his experiments using blocking contacts, a procedure which raises grave doubts about the uniformity and magnitude of the field in the sample. Penchina, Frova and Handler [65], studied electroabsorption in GaAs p-n junctions. Paige and Rees [66] in 1966 were the first to observe the oscillations above the energy gap, as predicted by Callaway. These authors proposed that a detailed interpretation of their results was impossible due to the lack of a theory incorporating the Coulombic effect, at that time. In addition, the results of Paige and Rees were found to be strongly specimen dependent. Ashar and Anderson [67] examined the differential photocurrent response in p-n junctions of GaAs, and found qualitative agreement with Lambert's data at 85 K.

At room temperature, the results were closer to those obtained by Moss. Rees in 1967 [68] compared the results of an investigation with a theory developed by himself in which the effects due to the electric field can be described as a broadening of the absorption edge. Using this theory, Rees found the reduced effective mass to be $.065 \pm .005\ m_o$.

French [69] investigated electric field induced effects upon optical transmission in the region 1.4 - 2.0 eV. Field dependent oscillatory structure was observed, but the author did not attribute this to the Wannier levels predicted by Callaway. Kushev et al [70] also studied the electroabsorption in GaAs at 80 K in the region between 1.40 and 1.50 eV. These workers found that the experimental values of electroabsorption significantly exceeded those deduced from the Franz/Keldysh theory. They also found that although the exciton electroabsorption theory gave better agreement, the discrepancies were still significant. In contrast to the above paper, Bobylev et al [71] found good agreement with the one electron Franz/Keldysh theory in their electroabsorption experiments on GaAs Schottky barriers, provided allowance was made for the inhomogeneity of the electric field in the space-charge region. Using their data, the authors calculated the effective mass in the spin-orbit split band.

A number of authors have carried out studies of impurity electroabsorption in semi-insulating GaAs. Jonath et al [72] investigated GaAs:O and found significant fundamental and first harmonic structure between 0.52 and 1.39 eV, at 300 and 80 K. A further paper attempted to correlate the electroabsorption measurements with independent observations of photoconductivity, optical quenching, thermally stimulated currents and space-charge injection [73]. Burgiel and Brown [74] studied the electroabsorption spectrum of substitutional copper in GaAs. Nishino et al [75] found impurity electroabsorption peaks due to silicon and chromium in GaAs.

Several interesting papers have examined the presence of odd

harmonics in the electroabsorption spectrum. As explained in Appendix I, if an alternating field E_1 is applied to a sample, with a zero static field, then the presence of odd harmonics in the spectrum, at the fundamental absorption edge, can be attributed to a non-zero internal microfield. Such effects have been investigated by Berozashvili et al in a number of papers. These spontaneous effects are discussed in Appendix I.

While Kovalyauskas and Shileika [76], and Evangelisti et al [77] have examined electroreflection in InP, there is only one short report of electroabsorption in InP. Kovalevskaya et al [78], in a brief letter, have reported electric field effects upon the photosensitivity spectra of InP p-i-n diodes and concluded that their results were in agreement with the theory due to Callaway. The present work is the first detailed analysis of electroabsorption in InP.

4.6 Preparation Of Indium Phosphide and Gallium Arsenide For Electroabsorption And Related Measurements

The samples investigated in this work were kindly supplied by the Royal Signals and Radar Establishment at Malvern. All the specimens were single crystals formed by pulling from the melt by the liquid encapsulation technique. The crystals were made semi-insulating by doping their melts with controlled quantities of chromium or iron. In a particular sample, the actual impurity concentration was dependent on the position in the boule from which the appropriate crystal had been cut. In general, the crystals were received in the form of unpolished discs, with a diameter of about 2 cm, and thickness of approximately 1 mm.

Each sample investigated was prepared in a systematic manner as follows. The specimen was first mechanically polished down to the required thickness, usually about 350 μm, with the final grade of paste being 0.1 μm standard. It was subsequently washed in acetone and then etch polished for about one minute. For the GaAs samples a

1% (by volume) Bromine/Methanol solution was employed, and was in general, found to be satisfactory. The InP samples were chemically polished using a 1:1 solution of $HCl:HNO_3$. This etch was found to produce a superior optical finish to the samples than the Bromine/Methanol etch. After this stage, the sample was washed in Propan-2-ol, then in de-ionized water. In order to remove any oxide layer present, the sample was subsequently dipped in concentrated HF acid, for about two minutes. On removal, it was again washed in de-ionized water, and then immersed in Propan-2-ol.

Samples required for straightforward optical absorption measurements were ready at this stage for mounting in the optical crystal, since no electrical contacts were required. However, measurements such as electroabsorption and dc. conductivity necessitated the deposition of electrical contacts on the surface of the semiconductor. An Edwards E 306 evaporator was used for this purpose. This instrument was capable of reaching a vacuum of 10^{-6} torr, although in general, contacts were evaporated at a pressure of $5x10^{-6}$ torr.

In order to be able to calculate the electric field in a sample during an electroabsorption experiment, it is convenient to form good ohmic contacts to the specimen. To achieve this, investigations were carried out on samples with a number of different contacts such as indium/tin, gold or gold/germanium. As a result of these experiments, it was found that semi-transparent ohmic contacts could be routinely prepared using an alloy of 12% germanium/88% gold (by weight). This alloy was prepared prior to evaporation. All the samples examined were contacted using this alloy. For electroabsorption measurements, the evaporated contacts were about 150 $\mathring{A}$ thick, whereas greater thicknesses were used for dc. and ac. conductivity experiments.

CHAPTER V

EXPERIMENTAL RESULTS OBTAINED FOR GALLIUM ARSENIDE AND INDIUM PHOSPHIDE

5.1 Introduction

The results of an investigation concerning the effects of an electric field upon the optical properties of indium phosphide and gallium arsenide are now presented. Before doing so, however, some data obtained in auxiliary experiments are presented.

5.2 DC. Conductivity Measurements

In order to check the ohmicity of the contacts before the electroabsorption measurements were performed, the dc. conductivity was measured. An example of the data obtained is shown in Figure 5.1 for a GaAs:Cr sample at 30°C. The graph indicates good ohmic behaviour, leading to a calculated resistivity for this particular sample of 1.22×10^9 Ω cm. The evaporated contacts were an alloy of Au/Ge as discussed previously. Figure 5.2 shows a similar curve for an InP:Fe sample at the same temperature. Once again the curve shows an ohmic dependence of current on voltage. For this sample, the resistivity is calculated to be 5.33×10^7 Ω cm.

The possibility of space charge limited currents occurring in the chromium doped InP samples is demonstrated in Figure 5.3. This curve shows dc. conductivity data for an InP:Cr sample at 150 K. The graph displays ohmic behaviour below fields of 6×10^3 V/cm. Above that applied field the current rises more quickly with applied voltage, and in fact a log-log J-V plot displays a slope of 2. The rapid rise in current is certainly not due to a Joule heating effect, since the power dissipated is only approximately 6×10^{-5} W/cm^2. Pande and Roberts [1] have reported space charge limited currents in InP:Cr. It is probable that the change in slope of the J-V curve is

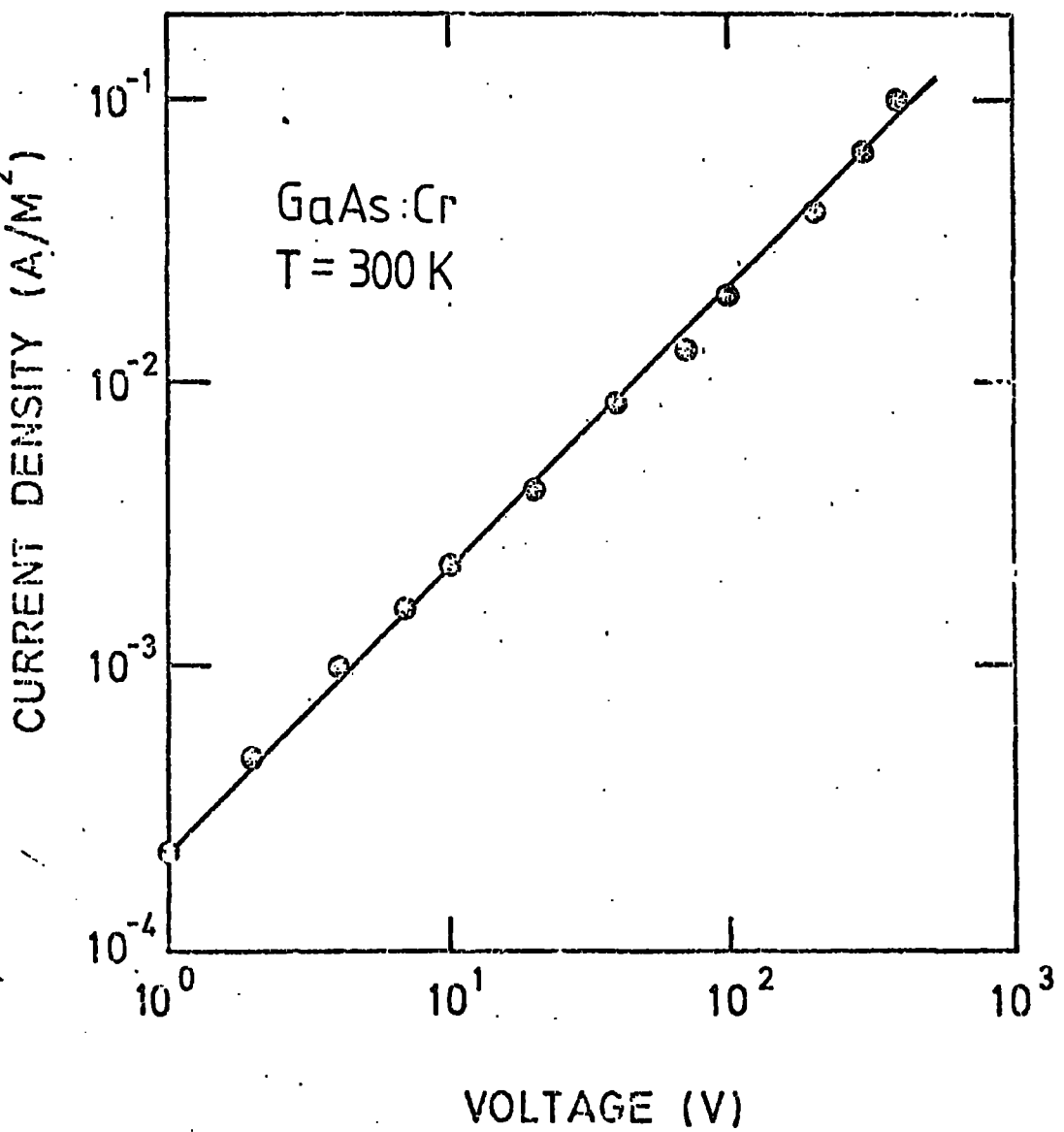

Fig. 5.1 Current-voltage relationship for a 364 μm thick GaAs specimen at 300 K.

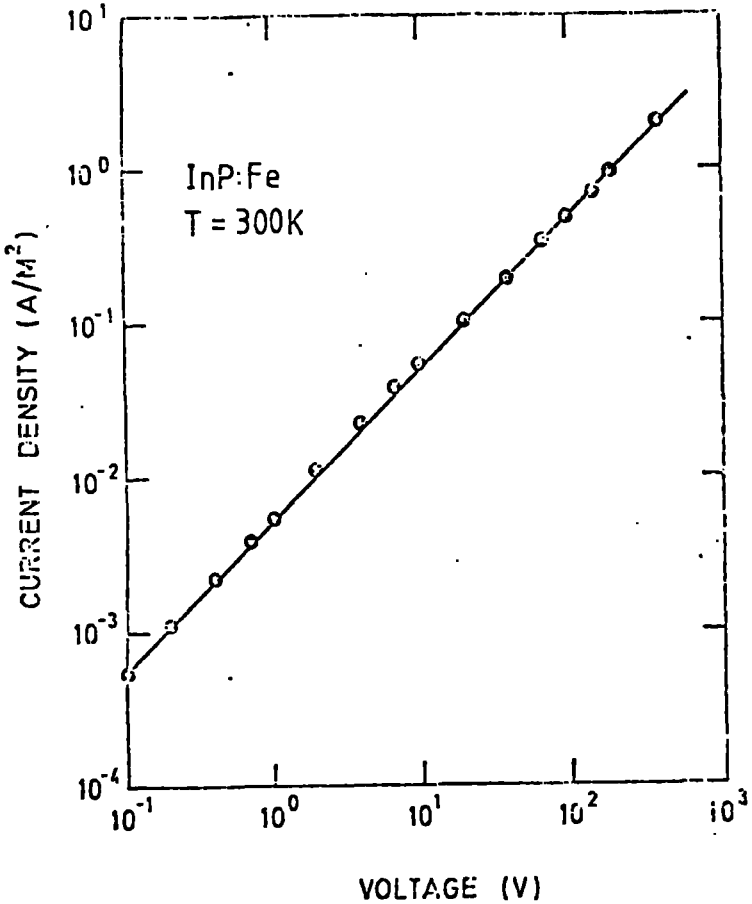

Fig. 5.2 Current-voltage relationship for a 340 μm thick InP:Fe specimen at 300 K.

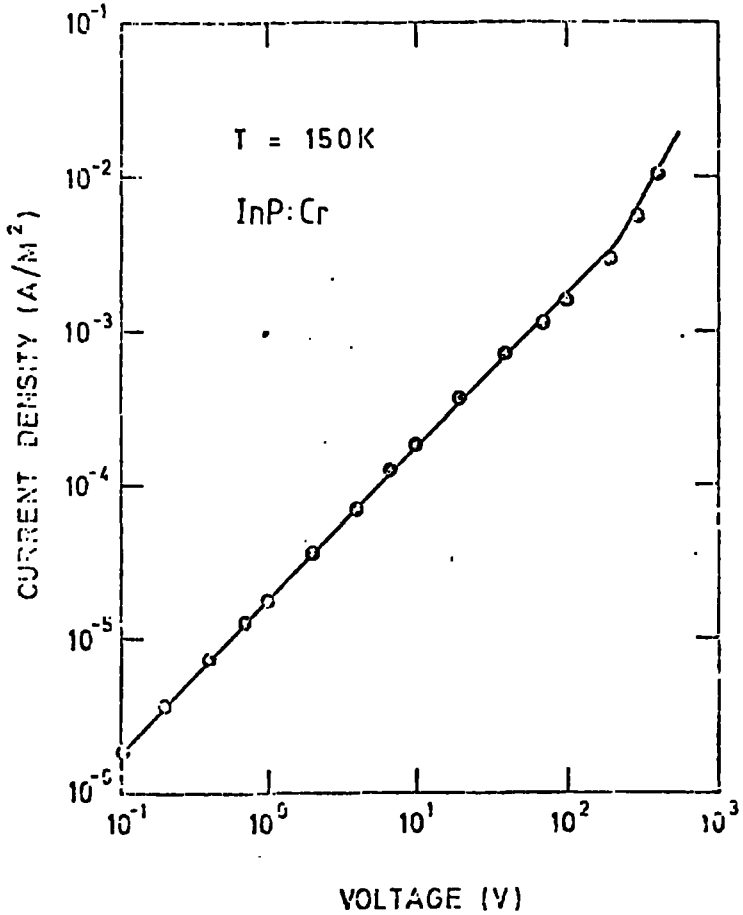

Fig. 5.3 Current-voltage graph for an InP:Cr sample at 150 K. Thickness = 340 μm.

related to that mechanism. In the experiments on electroabsorption, the electric fields applied were kept lower than the voltage required to produce charge injection, since this process leads to non-uniform fields within the sample.

The variation of current density with a temperature for typical InP:Fe and InP:Cr samples is shown in Figure 5.4. Both samples exhibit a strong temperature dependence, leading to activation energies of 0.57 eV and 0.39 eV for the iron and chromium doped samples respectively. This quantity is of greater importance for the Cr doped samples as regards electroabsorption measurements. Since the room temperature resistivity of the Cr doped samples is typically 10^3 - 10^5 Ωcm, the power dissipated in an electroabsorption experiment would be sufficient to produce a small shift in the absorption edge by Joule heating, irrespective of any change due to the Franz/Keldysh effect. However, since the Cr doped samples exhibit such a large temperature dependent resistivity, electroabsorption experiments performed below room temperature would not encounter such a problem. Figure 5.4 illustrates this point effectively. The room temperature resistivity is 4.2×10^5 Ωcm, while at 150 K, it has increased to 1.73×10^{12} Ωcm. For fields of 10^3 - 10^5 V/cm, the Joule heating in a sample with this resistivity is negligible. Accordingly, it was found possible to carry out electroabsorption experiments on the InP:Cr samples at temperatures below 200 K. No such limitation was necessary for the InP:Fe or GaAs:Cr crystals.

5.3 A.C. Conductivity And Capacitance Results

The ac. conductivity and capacitance measurements carried out on the III-V semiconductor samples were also primarily performed as a check on the ohmicity of the evaporated contacts, prior to the main electroabsorption measurements being performed. The equipment used for these measurements has already been described in some detail in Chapter III. The principle behind these measurements is that, over a certain range, a bulk single crystal semiconductor with two ohmic contacts should exhibit a frequency independent capacitance. The type

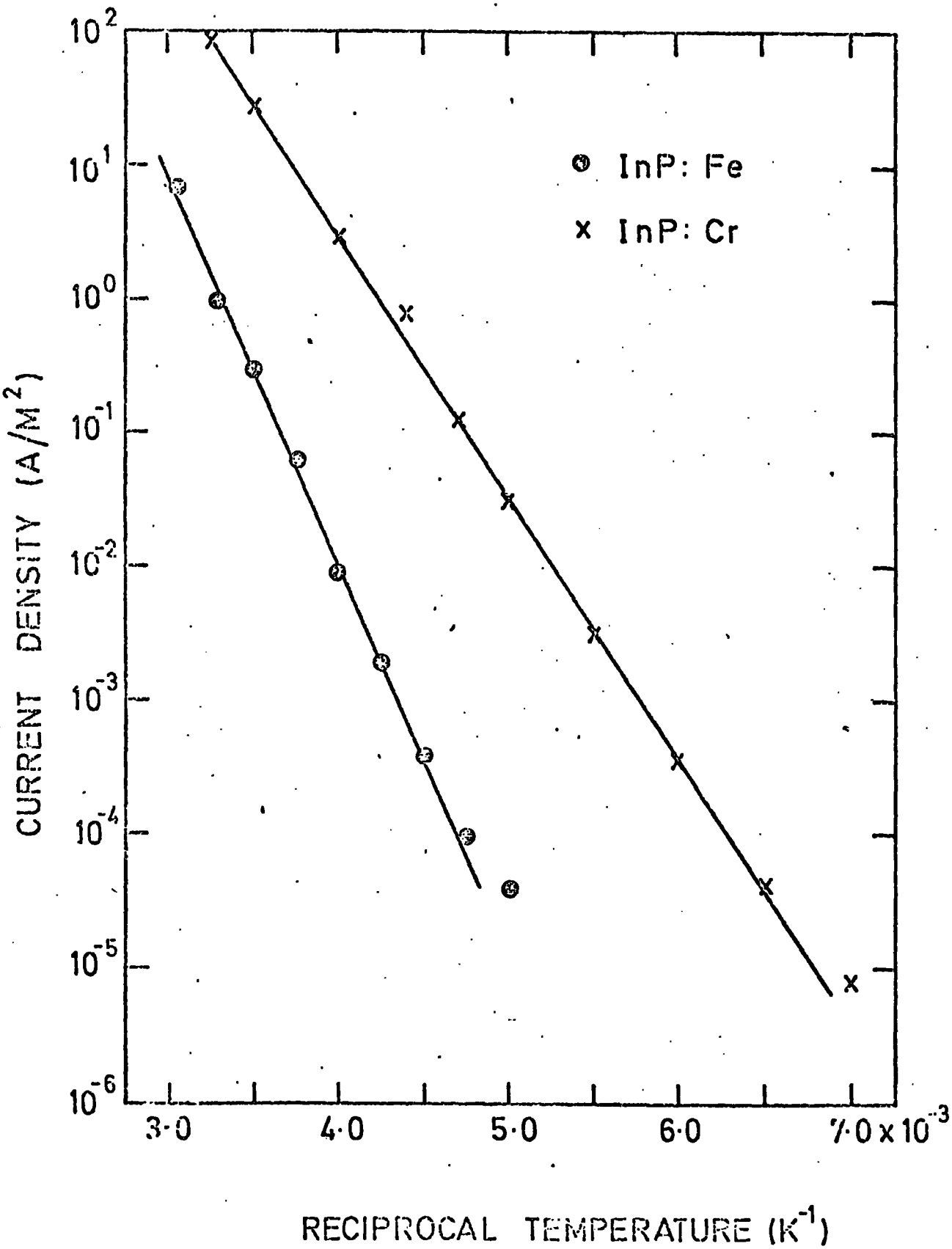

Fig. 5.4 Graph of current density versus reciprocal temperature for an InP:Fe and an InP:Cr specimen. In both cases the sample thickness is 340 μm, with a dc. bias of 100 V.

of behaviour expected is illustrated in Figure 5.5, where the capacitance and ac. conductance of an InP:Fe crystal at 300 K are illustrated (1 and 2 respectively). However, if one or both of the contacts to the specimen are non-ohmic a depletion layer is formed at the surface, leading to an increased capacitance which is frequency dependent. This behaviour is also illustrated in Figure 5.5 (3) for the same InP:Fe sample. The non-ohmic contacts were achieved by omitting the HF acid stage during sample preparation. As a result, a thin oxide layer, formed during or immediately after the etching process, was left on the surface of the sample. This was sufficient to produce the results described. It is worth noting that dc. conductivity results on the same sample did not exhibit any non-ohmic behaviour. It is evident that the ac. capacitance and conductance measurements are a much more sensitive method of checking the nature of evaporated contacts. The effect of non-ohmic contacts on the frequency dependence of the electroabsorption data is discussed in a later section.

Thus several criteria had to be satisfied before any electroabsorption measurements were performed. These were that the crystal should exhibit an ohmic dc. conductivity curve for both polarities, that it should produce the expected frequency independent capacitance, and that it should have a frequency independent ac. conductivity, over the range of interest. Knowing the static dielectric constant, the bulk capacitance could be simply calculated from:-

$$C = \frac{\varepsilon \varepsilon_0 A}{d}$$

where d is the thickness and ε is the static dielectric constant.

5.4 Results Of Electroabsorption Measurements On Gallium Arsenide And Indium Phosphide

The electroabsorption results obtained on GaAs and InP are now presented. Figure 5.6 shows typical data obtained on a GaAs:Cr sample

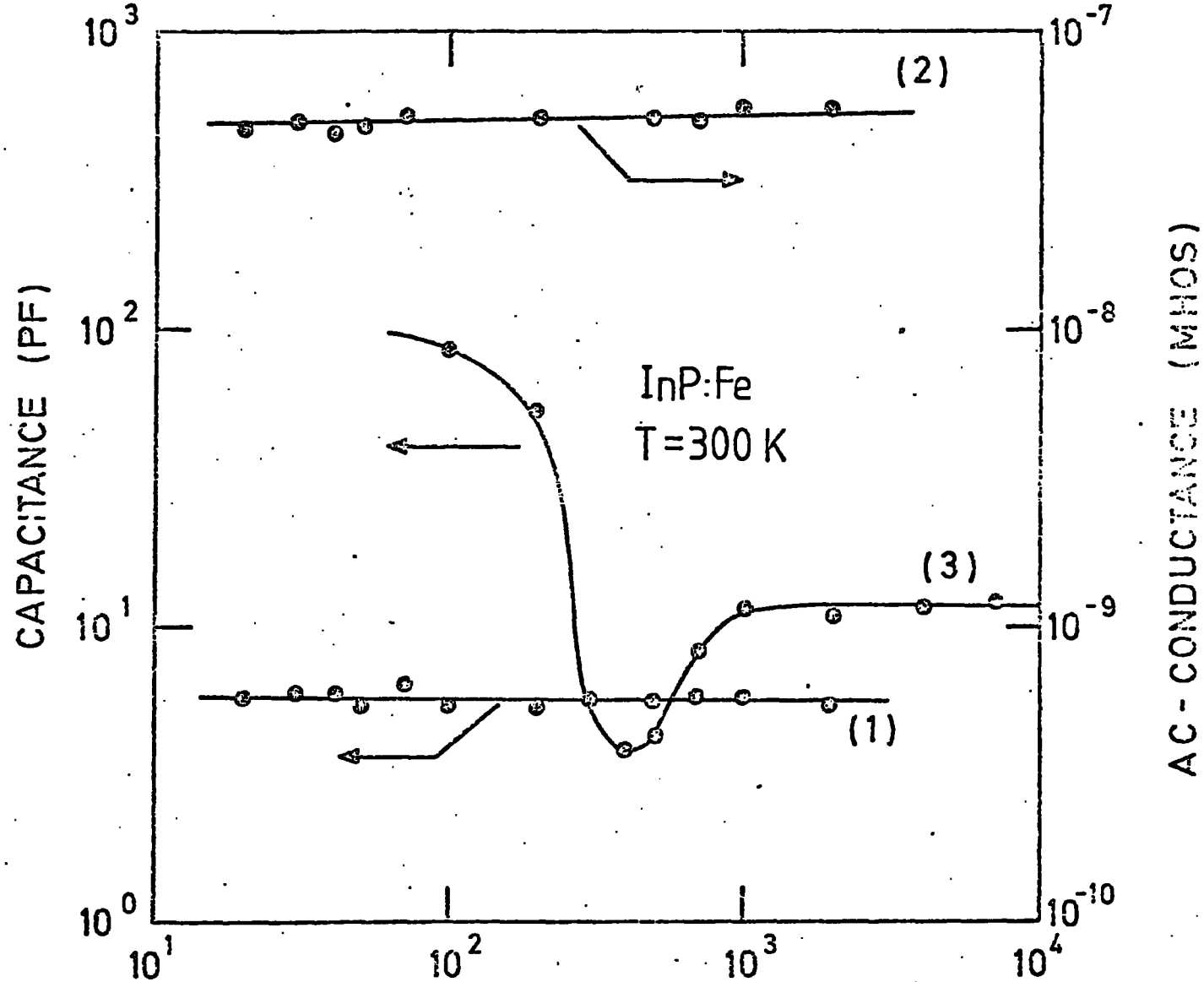

Fig. 5.5 Capacitance and conductance data for an InP:Fe specimen, at 300 K, as a function of frequency.

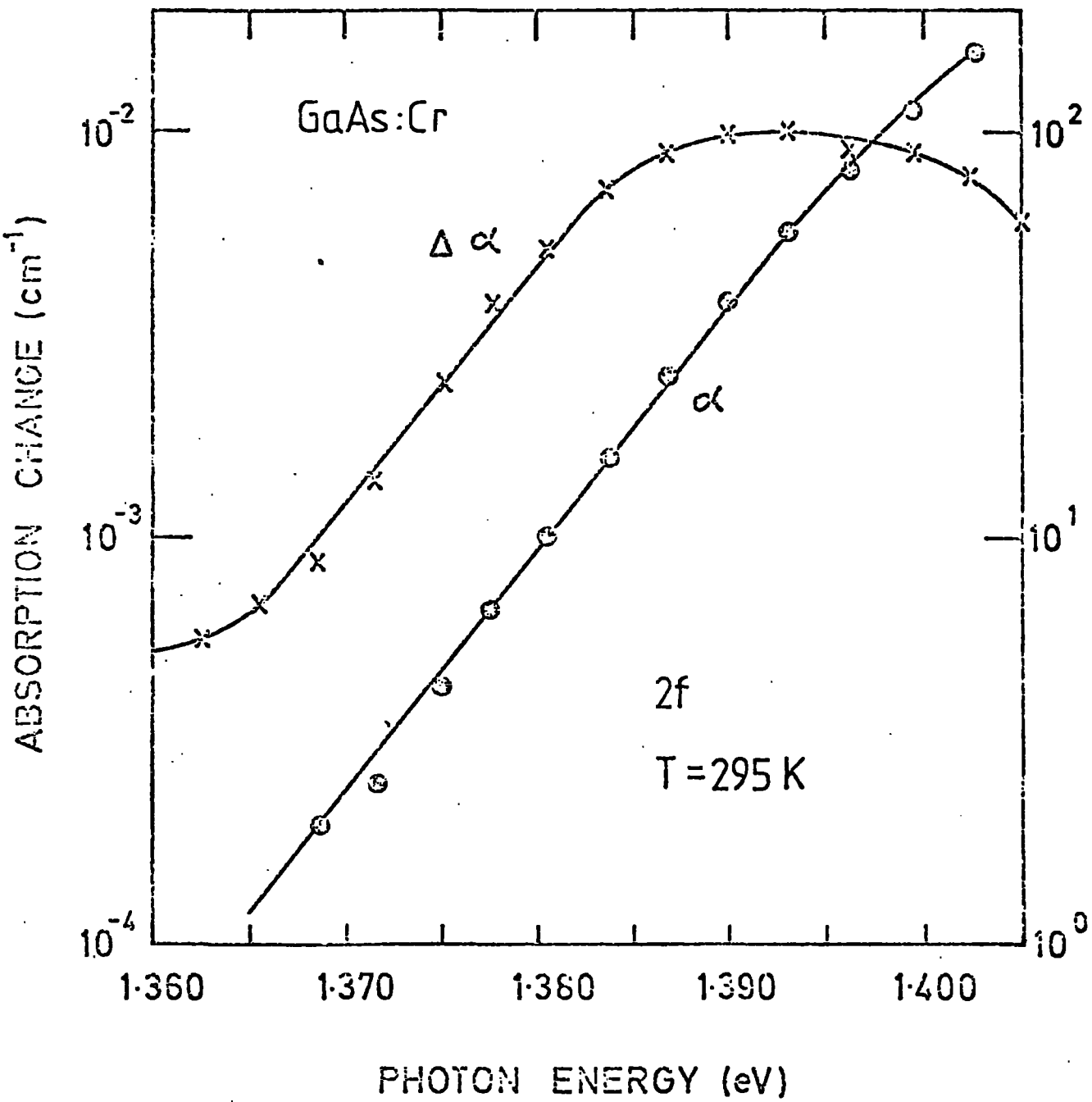

Fig. 5.6 Graph of the absorption change $\Delta\alpha$ due to an applied field of 9.6×10^4 V/m for a GaAs:Cr specimen at 295 K. In addition the zero field absorption curve is shown.

at 295 K. The graph shows the variation of both the absorption change $\Delta\alpha$, and the zero field absorption coefficient α with photon energy. The applied voltage pulse had the shape indicated in Figure 3.5 (a) and involved a peak-to-peak field of 9.61×10^4 V/m. The data shown corresponds to a shift of the zero-field absorption edge towards the long wavelength region. Due to the existence of an exponential absorption edge in GaAs, only a single peak is observed in the electroabsorption spectrum. To enable any higher energy electroabsorption peaks to be observed requires the use of samples less than 3 μm thick. Such samples pose special problems with regard to preparation, handling and mounting. Accordingly, in this thesis, we have concentrated entirely on the long wavelength area of the electroabsorption curves, both for GaAs and InP.

In agreement with the simple one-electron Franz/Keldysh theory, the slopes of the zero field absorption curve and the electro-absorption curve in Figure 5.6 are equal.

Figure 5.7 displays similar data for an InP:Fe sample, again at 295 K. In this case, two electroabsorption curves are shown, corresponding to electric fields of 8.8×10^5 V/m and 1.2×10^6 V/m respectively. Once again, only a single peak is observed in the electroabsorption curves. It is clear from the data presented that the shift of the absorption edge observed increases with increasing electric field. Figure 5.7 also shows zero field absorption data for the same sample, corresponding to absorption coefficients below 200 cm^{-1}. The slopes of the zero field absorption curve and the electroabsorption curves are equal in this case as well.

Typical data obtained for an InP:Fe sample at 77.3 K are displayed in Figure 5.8. In addition to the zero field absorption curve (a), electroabsorption curves are presented for three different electric fields, namely 1.2×10^6 V/m, 8.8×10^5 V/m and 5.88×10^5 V/m respectively. The data presented are similar to the higher temperature curves previously illustrated, except that the area at the top of the peak could not be measured with sufficient accuracy, due to noise, and

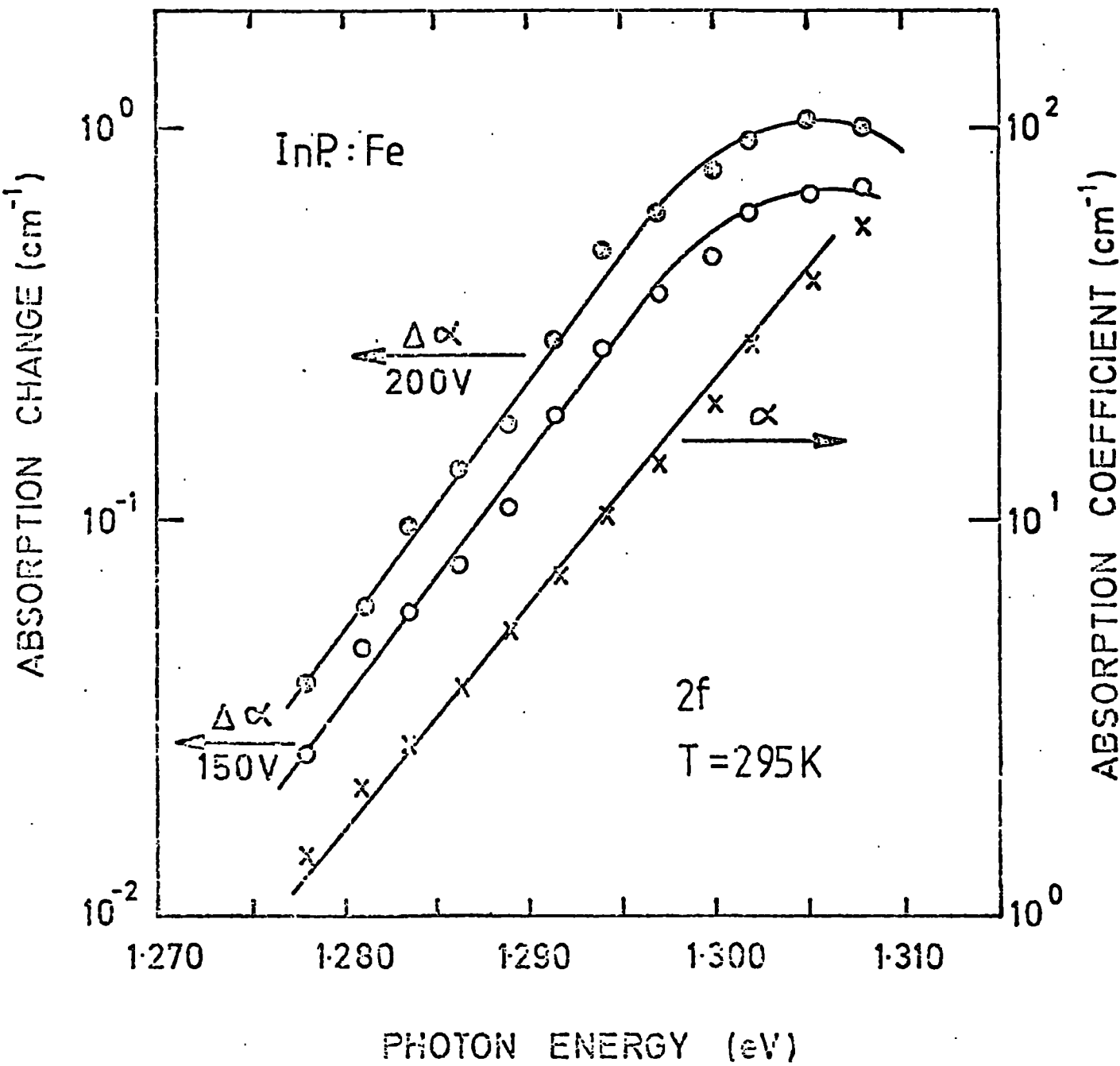

Fig. 5.7 Graph of the absorption coefficient α and the absorption change $\Delta\alpha$ as a function of photon energy for an InP:Fe sample at 295 K. The absorption change is plotted for two values of the applied field, namely 8.8×10^5 V/m and 1.2×10^6 V/m.

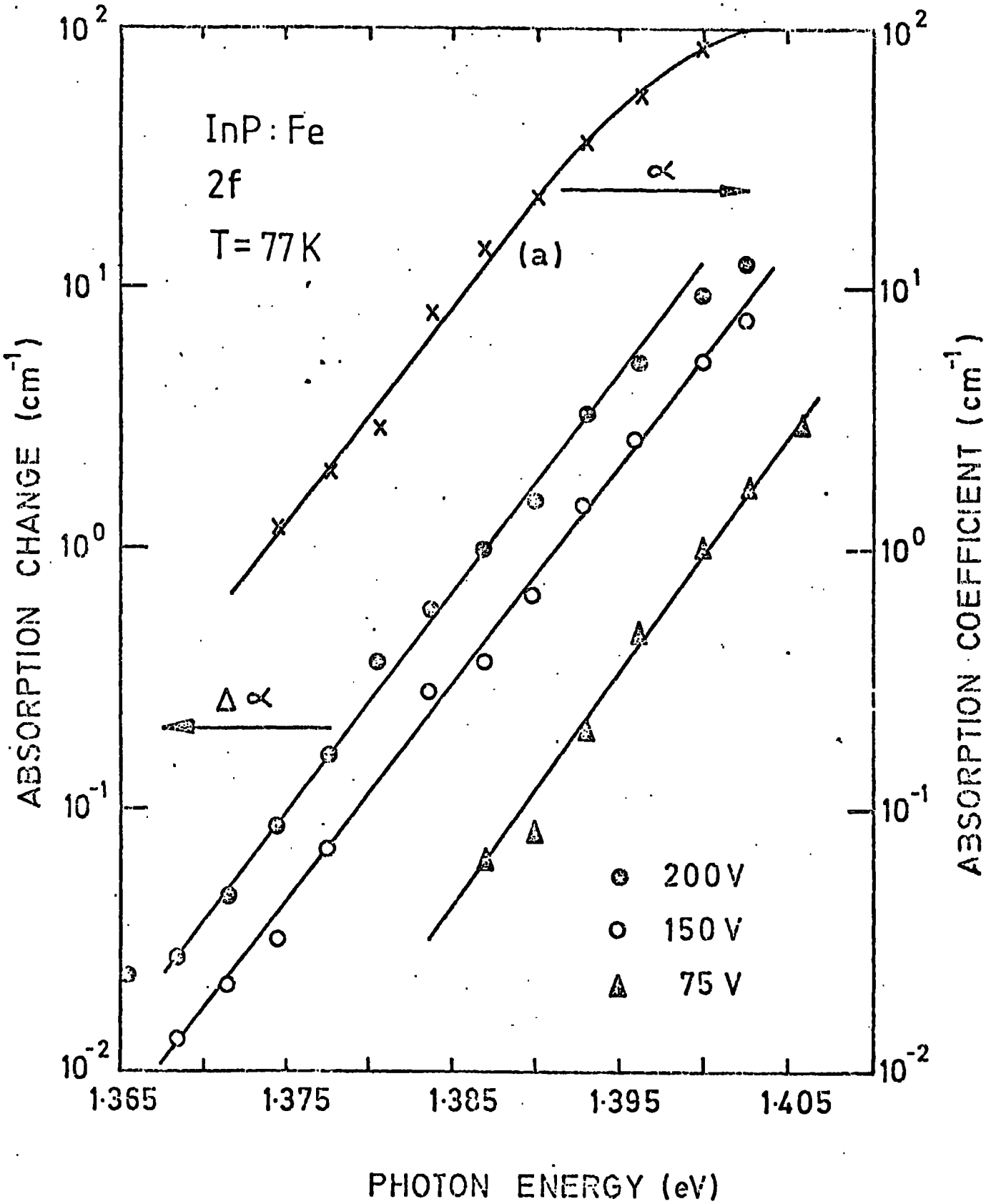

Fig. 5.8 Graph of the absorption coefficient α and the absorption change $\Delta\alpha$ as a function of photon energy, for a 340 μm thick InP:Fe crystal, at a temperature of 77 K.

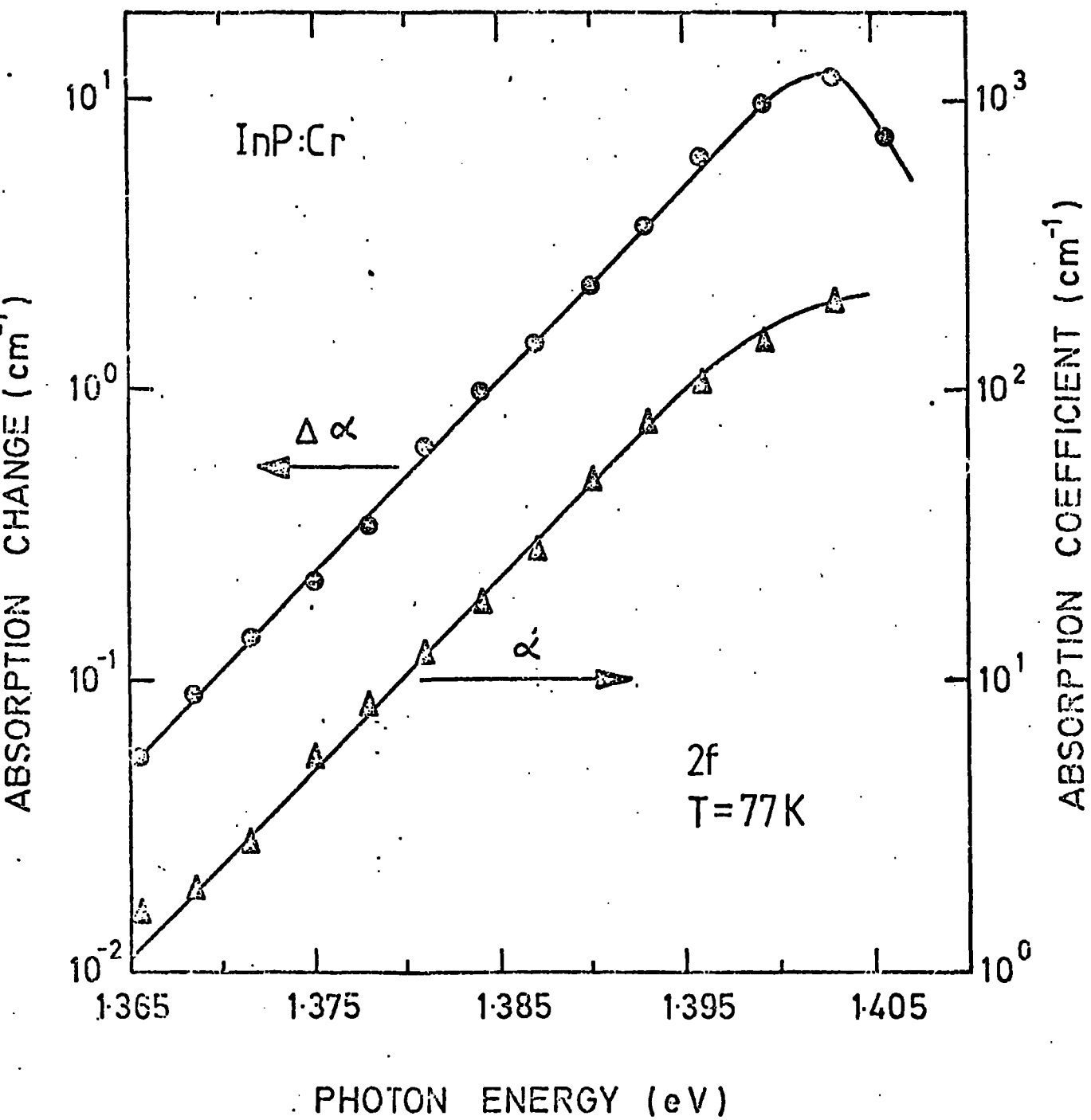

Fig. 5.9 Absorption coefficient and absorption change for an InP:Cr crystal at 77 K, as a function of photon energy. Sample thickness = 325 μm.

is not included. Again the slopes of the three electroabsorption curves and their corresponding absorption curves are all equal.

Finally, the results of electroabsorption experiments on InP:Cr are summarized in Figure 5.9. The data are similar to the InP:Fe and GaAs:Cr samples displayed earlier and previously discussed. These curves were recorded at a temperature of 77 K.

5.5 Electric Field Dependence Of The Electroabsorption Signal

In the previous section, the fact that the change in absorption was a function of applied field was briefly mentioned. Detailed investigations were carried out on a number of samples to determine the exact field dependence since, as discussed in Chapter II, the dependence of the absorption change on applied field is indicative of the absorption mechanism involved. The results of these experiments are illustrated in Figures 5.10 to 5.13.

The dependence of the absorption change on applied field in a GaAs:Cr sample at 295 K and at a wavelength equal to 9000 Å is shown in Figure 5.10. In this graph, the absorption change is plotted versus the square of the applied voltage, for the specimen whose electroabsorption spectra are illustrated in Figure 5.6. A good straight line is obtained over a wide range of voltage, indicating that the observed changes in absorption are indeed proportional to the square of the electric field. In addition, the fact that the graph extrapolates to the origin is a good indication of the absence of any space-charge injection complications in our experiments.

Similar data, on log/log plots, are shown in Figures 5.11 and 5.12 for InP:Fe crystals at 295 K and 77 K respectively. The results shown in Figure 5.12 correspond to the specimen whose electroabsorption spectra were illustrated previously in Figures 5.7 and 5.8. Finally, Figure 5.13 displays equivalent data for an InP:Cr crystal. In each case, a slope of 2 is obtained on a log/log plot.

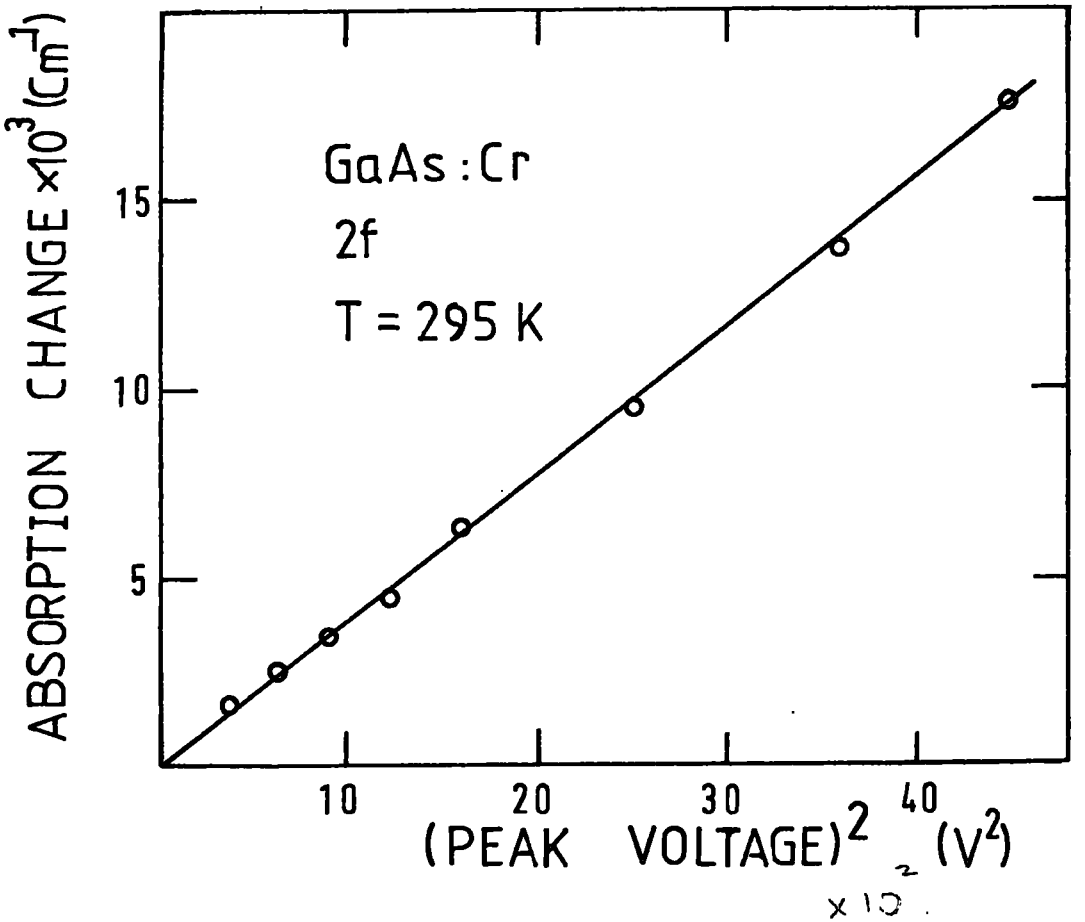

Fig. 5.10 Dependence of the absorption change of a GaAs:Cr specimen on the magnitude of the applied field.

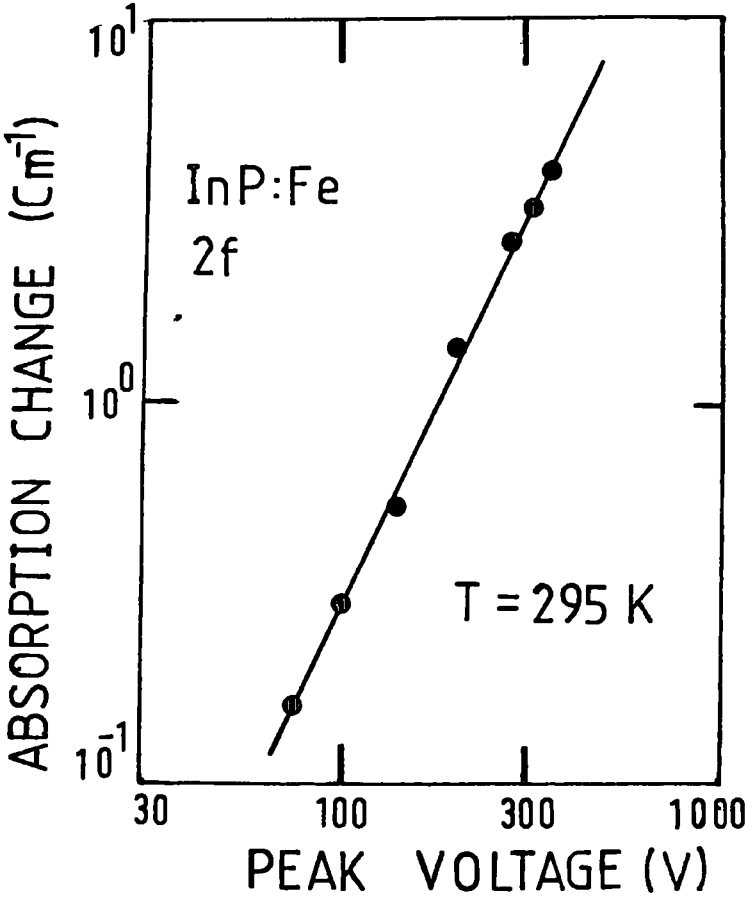

Fig. 5.11 Dependence of the absorption change of an InP:Fe crystal at 295 K on the magnitude of the applied field.

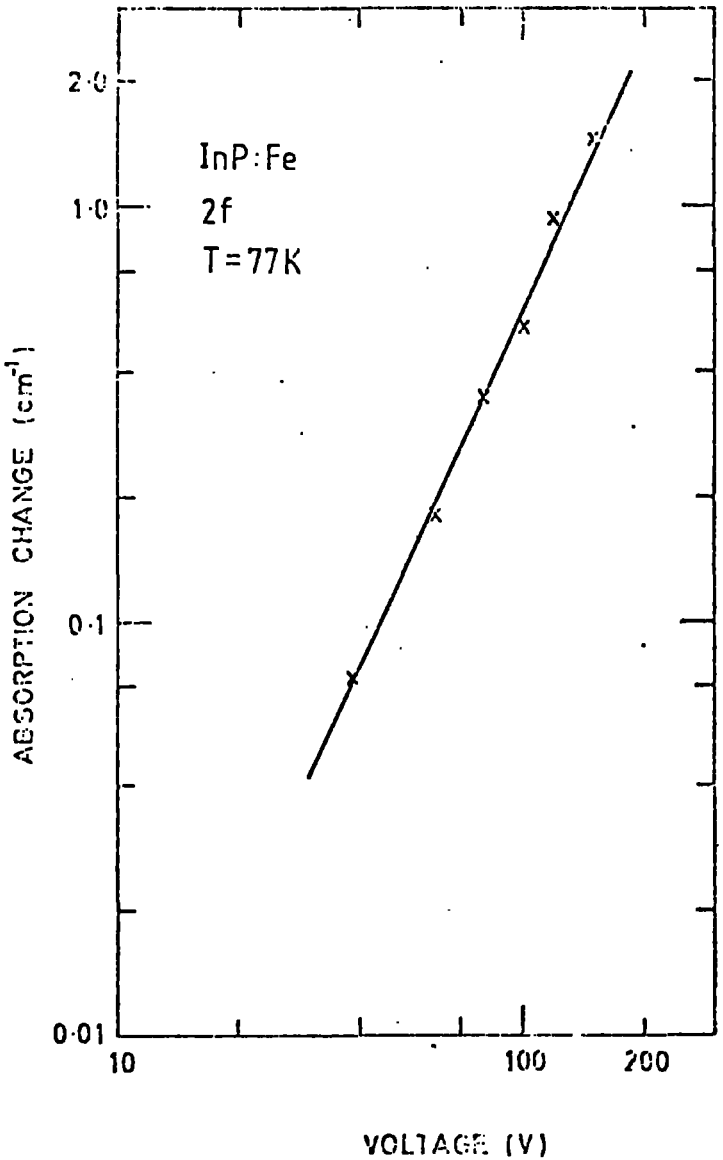

Fig. 5.12 Dependence of the absorption change of an InP:Fe crystal at 77 K on the magnitude of the electric field.

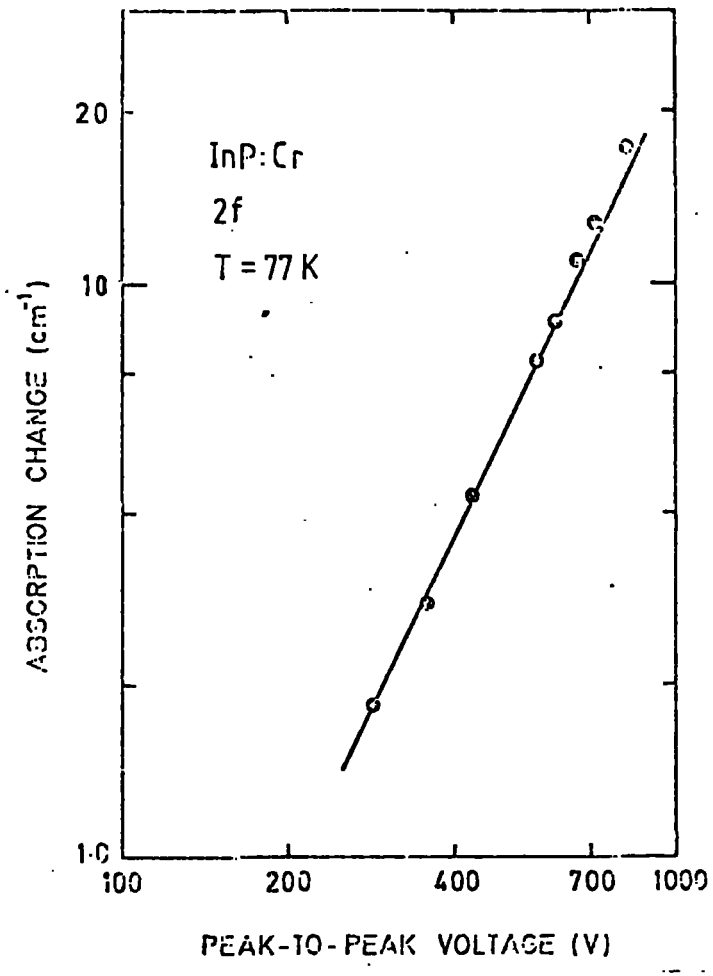

Fig. 5.13 Dependence of the absorption change of an InP:Cr specimen at 77 K upon the size of the applied field.

5.6 Dependence Of Electroabsorption Response On The Frequency Of The Applied Field

The theory of electroabsorption developed by Franz and Keldysh proposes that the observed changes in absorption should be independent of the frequency of the modulating field. In addition, it is accepted that a positive electric field is equivalent to a negative electric field in so far as the effects produced should be the same. Accordingly, if a sinusoidal electric field is applied to a specimen each half of the cycle is equivalent and the electroabsorption spectra should be detected at twice the frequency of the applied field, that is, at the first harmonic (2f). This point is discussed further in Appendix I. However, deviations from this idealized situation are often encountered, though not often explained.

Our electroabsorption results on both GaAs and InP were found to fall into the latter category, insofar as the magnitude of the electroabsorption response was dependent on frequency and in addition, a signal existed at the fundamental frequency (f). These two points will now be discussed in turn.

5.6.1 Frequency Dependence Of The Magnitude Of The Electroabsorption Signal

The type of behaviour observed is illustrated in Figure 5.14 for an InP:Cr sample at a temperature of 77 K. The change in absorption is plotted as a function of frequency. It is obvious that the absorption change is strongly dependent upon the frequency of the modulating field. This type of behaviour was found for all the III-V samples examined although the InP:Fe samples exhibited the effect to a greater degree at low temperatures.

One explanation of the above behaviour is that the contacts to the crystals were non-ohmic, a condition which would produce a non-uniform field within the sample. A variation in frequency would alter the resultant field distribution, producing a change in the electro-

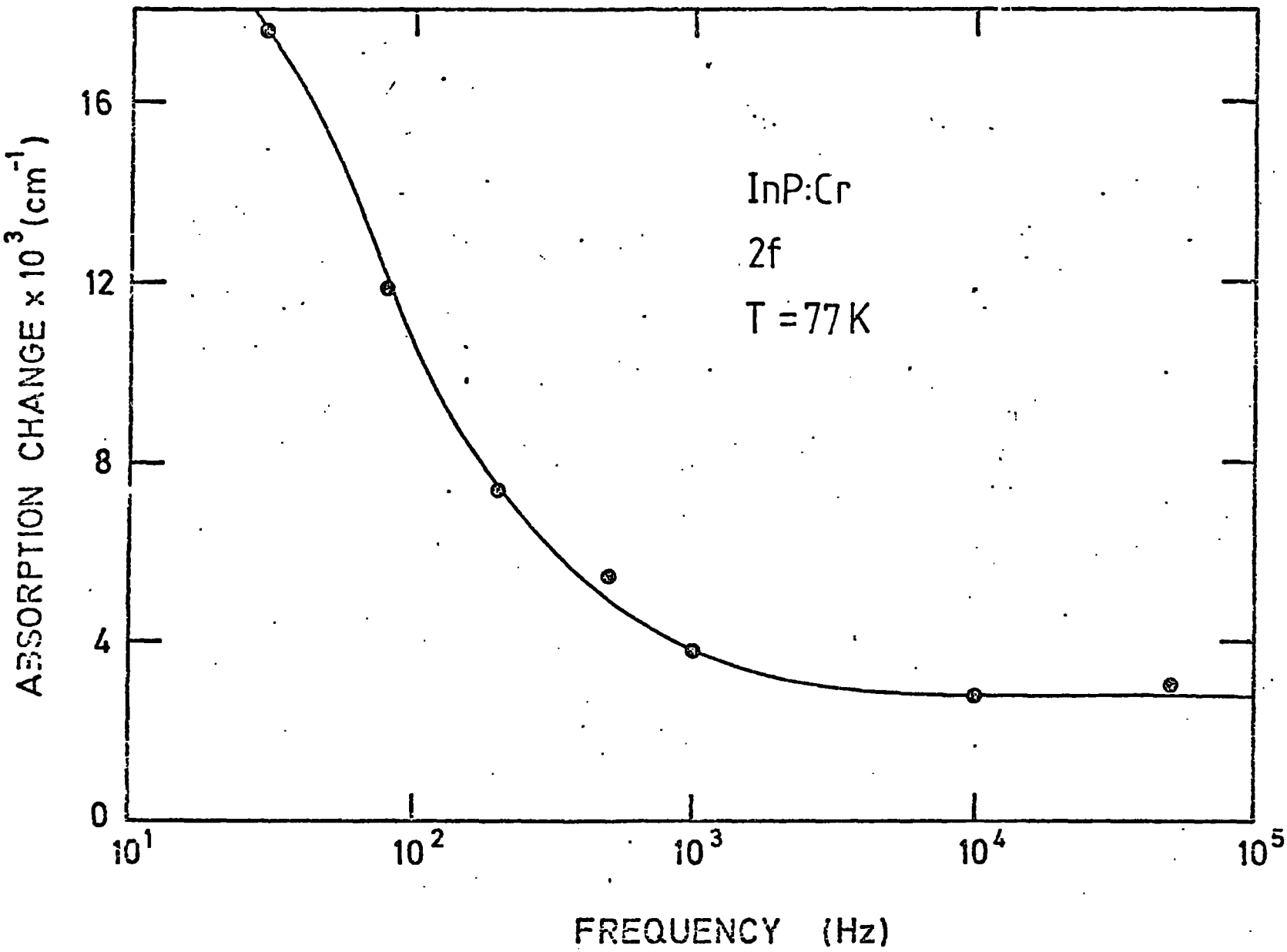

Fig. 5.14 Effect of a variation of the frequency of the applied electric field upon the absorption change for an InP:Cr specimen at 77 K. Wavelength = 896 nm.

-absorption signal. However, this explanation can be rejected due to the extensive tests discussed in sections 5.2 and 5.3 to ensure ohmic contacts to the specimens.

In order to try to explain this unexpected behaviour, a detailed series of experiments was performed. It was finally concluded that the effect was connected with photogenerated carrier effects within the samples. The III-V crystals examined were all semi-insulating, and as such were found to be strongly photoconductive. As an illustration, Figure 5.15 shows the normalised photocurrent of an InP:Fe sample versus photon energy at two different temperatures. A large photocurrent was found to flow at energies very close to the bandgap energy in agreement with the absorption spectra. Since the electroabsorption experiments are also performed at energies close to the bandgap, one might expect some correlation.

The relationship between the sample's photoconductivity and the observed absorption changes is demonstrated in Figure 5.16 for a GaAs:Cr sample at 295 K. In the figure, the recorded absorption changes due to the applied electric field are shown as a function of the frequency of the field, but for three different incident light intensities. In agreement with figure 5.14, larger absorption changes are recorded at frequencies below 10^3 Hz. The interesting point is that for the lower frequencies the magnitude of the absorption change is critically dependent upon the intensity of the incident radiation. At higher frequencies, a variation in the incident radiation intensity has zero effect upon the observed absorption changes.

One possible explanation is that the above effects arise due to polarization of the crystal under illumination in the presence of an alternating field. An alternative explanation is that the sample's photoconductivity results in an area at the surface of the specimen which is electrically less resistive than the bulk. Accordingly, the applied voltage is effectively dropped across a smaller region of the crystal, resulting in a larger electric field, which in turn leads to larger field dependent changes. However, every photoconductive pro-

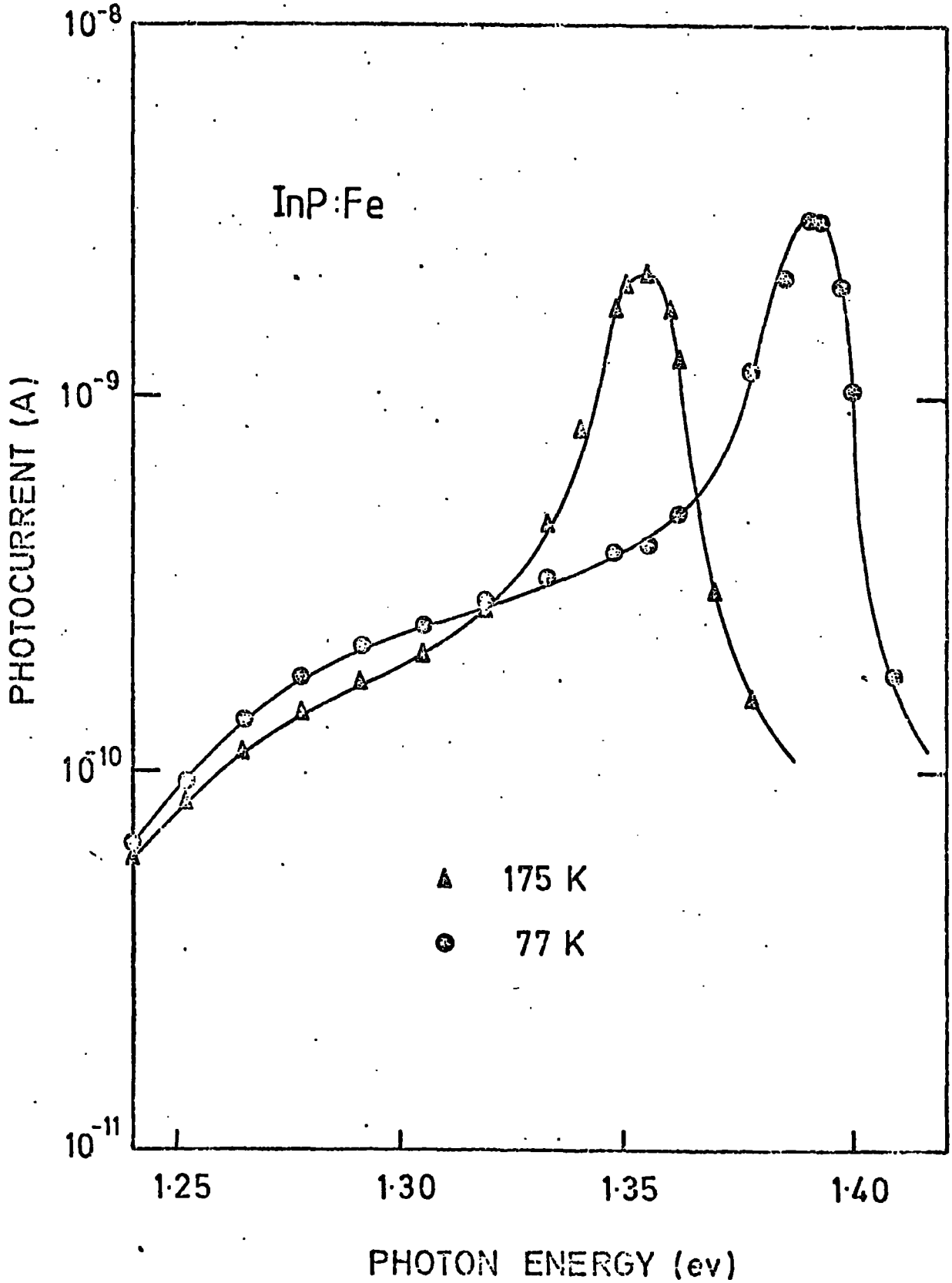

Fig. 5.15 Photocurrent of an InP:Fe crystal at 77 K and 175 K.

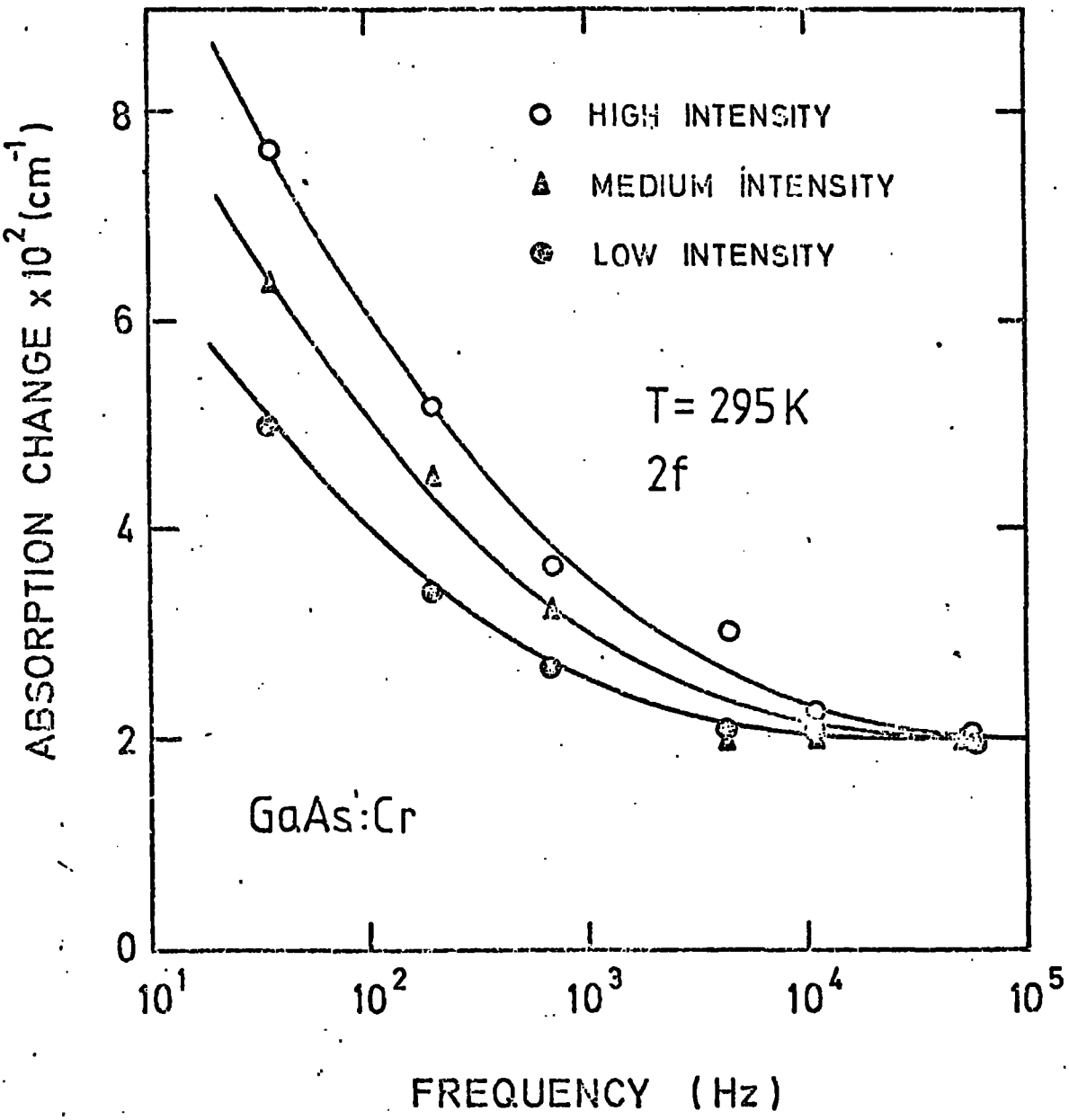

Fig. 5.16 Absorption change of a GaAs:Cr specimen at 295 K as a function of the frequency of the applied electric field, for three different incident light intensities. Sample thickness = 364 μm.

cess has particular time constants associated with it. At frequencies larger than the inverse of these time constants the effect of the photoconductivity would be expected to be reduced, since the sample could not respond fast enough. Thus, the electric field induced absorption changes at higher frequencies should be almost independent of incident light intensity. This is exactly what is observed in practice.

From the above discussion, one would expect that a simple measurement of photocurnent versus applied electric field frequency would show decreasing photocurrent for increasing frequency, in the frequency range in which the electroabsorption data are frequency dependent. Figure 5.17 illustrates the results of such a measurement upon a GaAs:Cr sample. A large photocurrent is observed to flow at low frequencies, but this decreases practically to zero at about 10^4 Hz. It is worth noting that the electric field induced absorption changes recorded in Figure 5.16 become frequency independent at about 10^4 Hz.

5.6.2 Analysis Of The Presence Of Fundamental And First Harmonic Absorption Changes

In the presence of an external electric field of the form $E_o \cos \omega_1 t$, the resultant absorption changes should be detected at a frequency of $2\omega_1$. As explained in Appendix I, the presence of a signal at the fundamental, namely ω_1, can only occur due to the presence of either an external static electric field E_1, or an effective internal static field.

The form of the electric fields applied to our samples was illustrated in Figure 3.5. None of the applied fields contained any external dc. component. One would therefore have expected our samples to exhibit a zero signal at 1f (fundamental) and to produce a signal proportional to the absorption changes at 2f (first harmonic).

In practice, however, it was generally found that a signal did exist at the fundamental. Since contact effects have previously been rejected, the foregoing discussion would lead to the conclusion that an

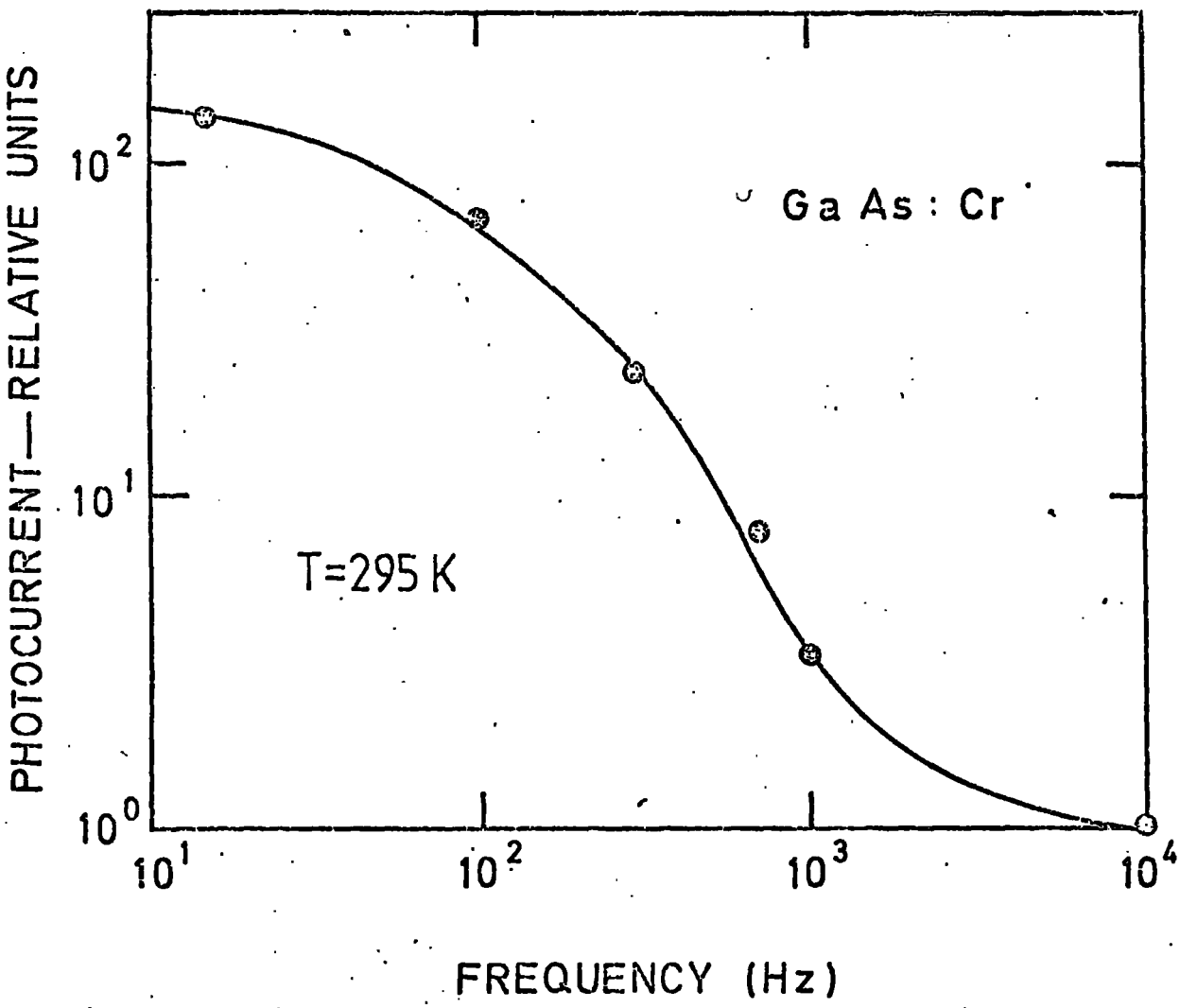

Fig. 5.17 Photoconductivity of a GaAs:Cr crystal as a function of the electric field frequency, at a temperature of 295 K.

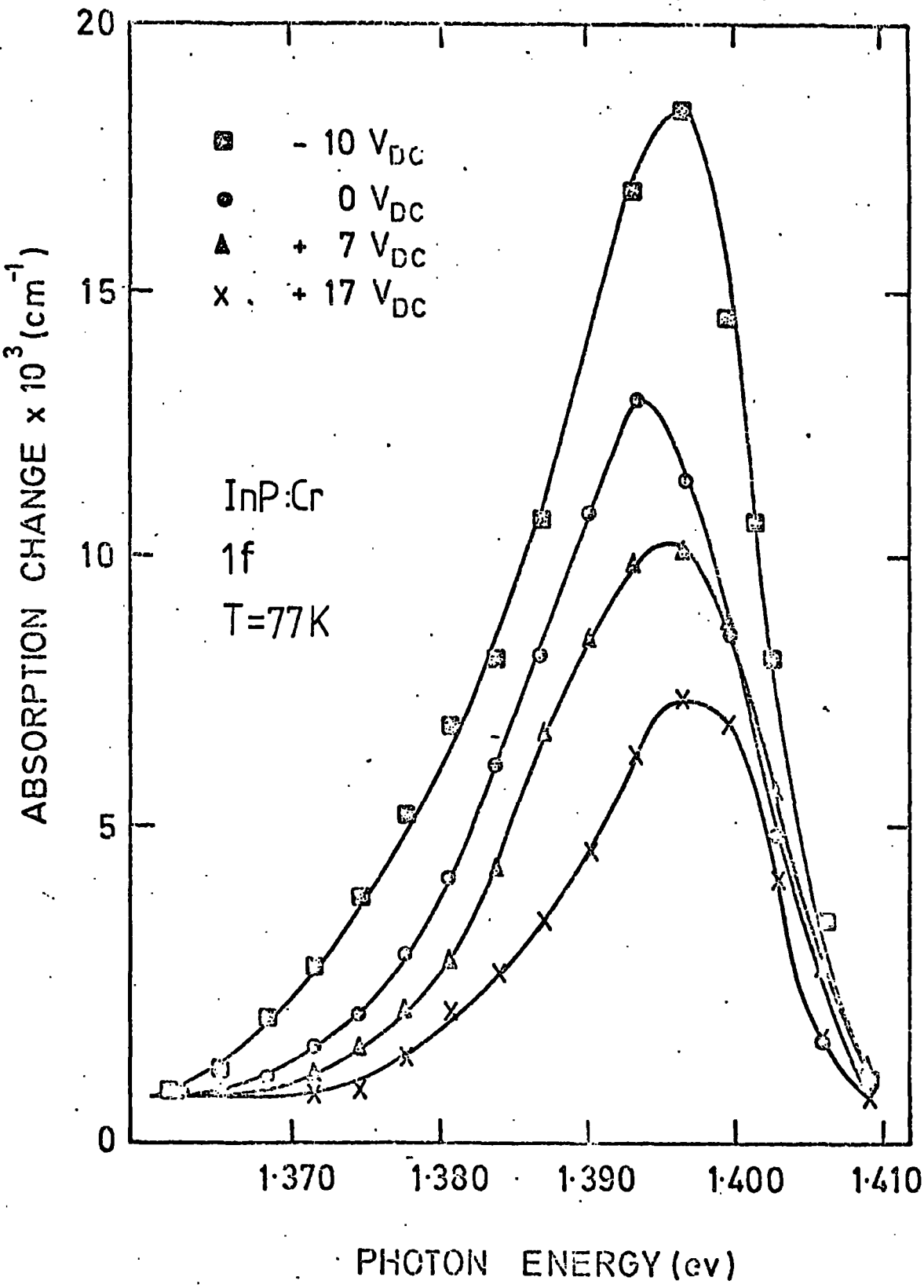

Fig. 5.18 Absorption change of an InP:Cr specimen as a function of photon energy, for electric fields of the form $E_1 + E_o \cos \omega t$. E_1 is allowed to take the values -10, 0, +7, +17 volts in turn. The data were recorded at 1f.

effective internal static electric field was present in the crystals. This was considered rather surprising, in view of the high quality of the samples under investigation. In order to clarify this position a series of experiments were performed to elucidate the true situation.

In Appendix I, it is shown that by applying a combination of a static external electric field and an alternating external electric field, one should be able to reduce or increase the effect of any internal static electric field upon the electroabsorption signal. Figure 5.18 displays the results of such an experiment on an InP:Cr sample at 77 K. The figure shows a graph of the absorption change at 1f versus photon energy for electric fields of the form $E_1 + E_o \cos \omega t$. E_1 is allowed to take the values -10, 0, +7 and +17 volts in turn. It is clear from the figure that the magnitude of the signal recorded at the fundamental is distinctly dependent on the size and polarity of the external static field, with the signal greatly increasing for negative voltages.

Figure 5.19 shows equivalent data obtained on the same sample, but recorded at the first harmonic frequency 2f. Once again, the diagram shows the values of the absorption change versus photon energy for electric fields of the form $E_1 + E_o \cos \omega t$. In this case, however, it is clear that a variation in the value of E_1 has, within experimental error, zero effect on the recorded signal. That is, the signal is independent of any dc. bias, external or internal, and is totally due to the alternating field component.

It is of interest to study in what manner an external dc. bias, superimposed on the ac. voltage, affects the recorded electroabsorption signal. Figure 5.20 shows the results of such an analysis on a GaAs:Cr sample at 295 K. An alternating electric field of magnitude 1.46×10^3 V/cm was applied to the sample, together with a dc. bias which was varied between -6 and +12 volts. The figure records, for a fixed wavelength, the absorption change as a function of the external dc. voltage. Two points are evident from a study of the graph. First a remarkably straight line is obtained showing that the observed change in absorption

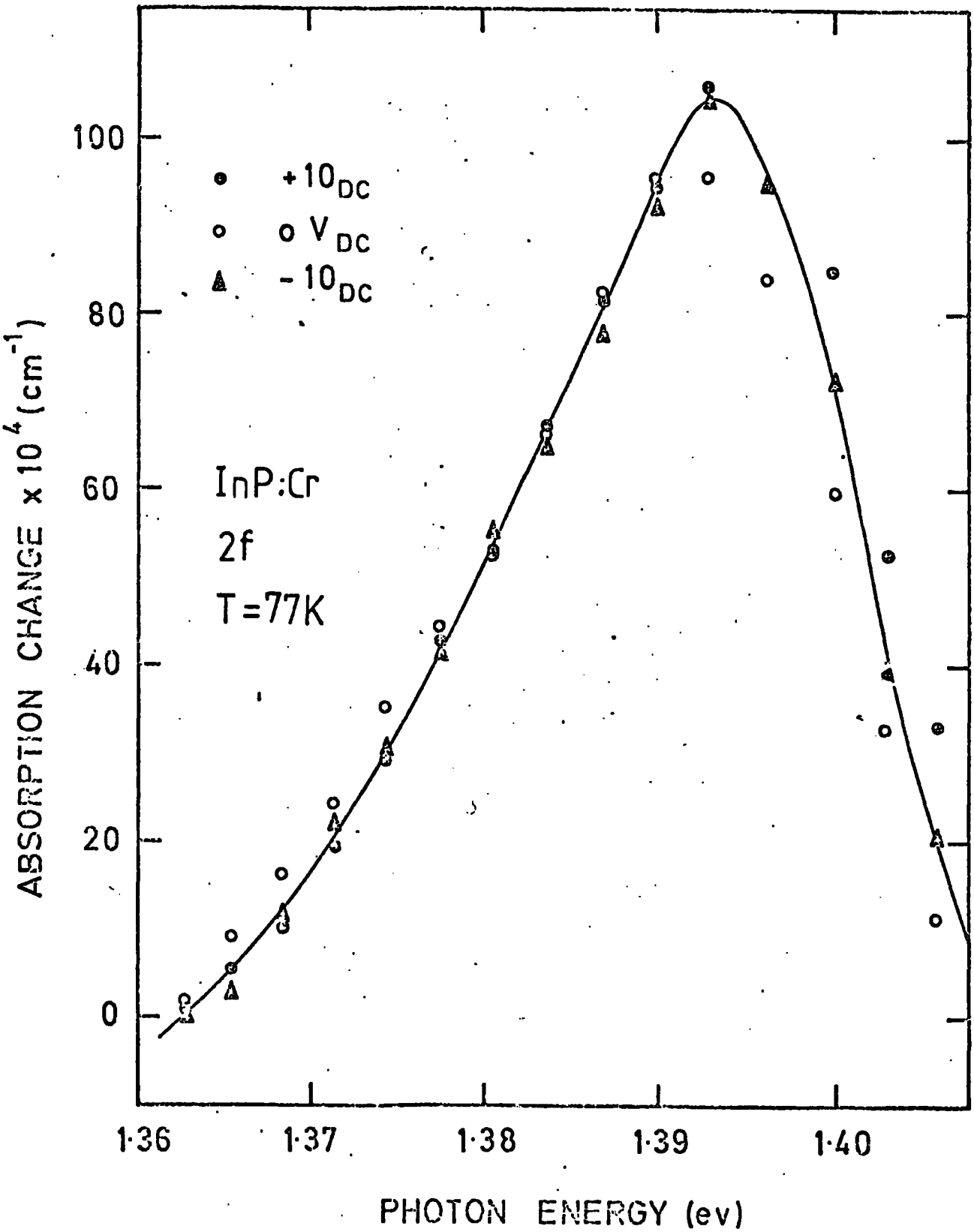

Fig. 5.19 Absorption change of the same specimen as for Fig. 5.18 due to fields of the form $E_1 + E_o \cos \omega t$. E_1 = -10, 0, 10 volts in turn. Data recorded at 2f.

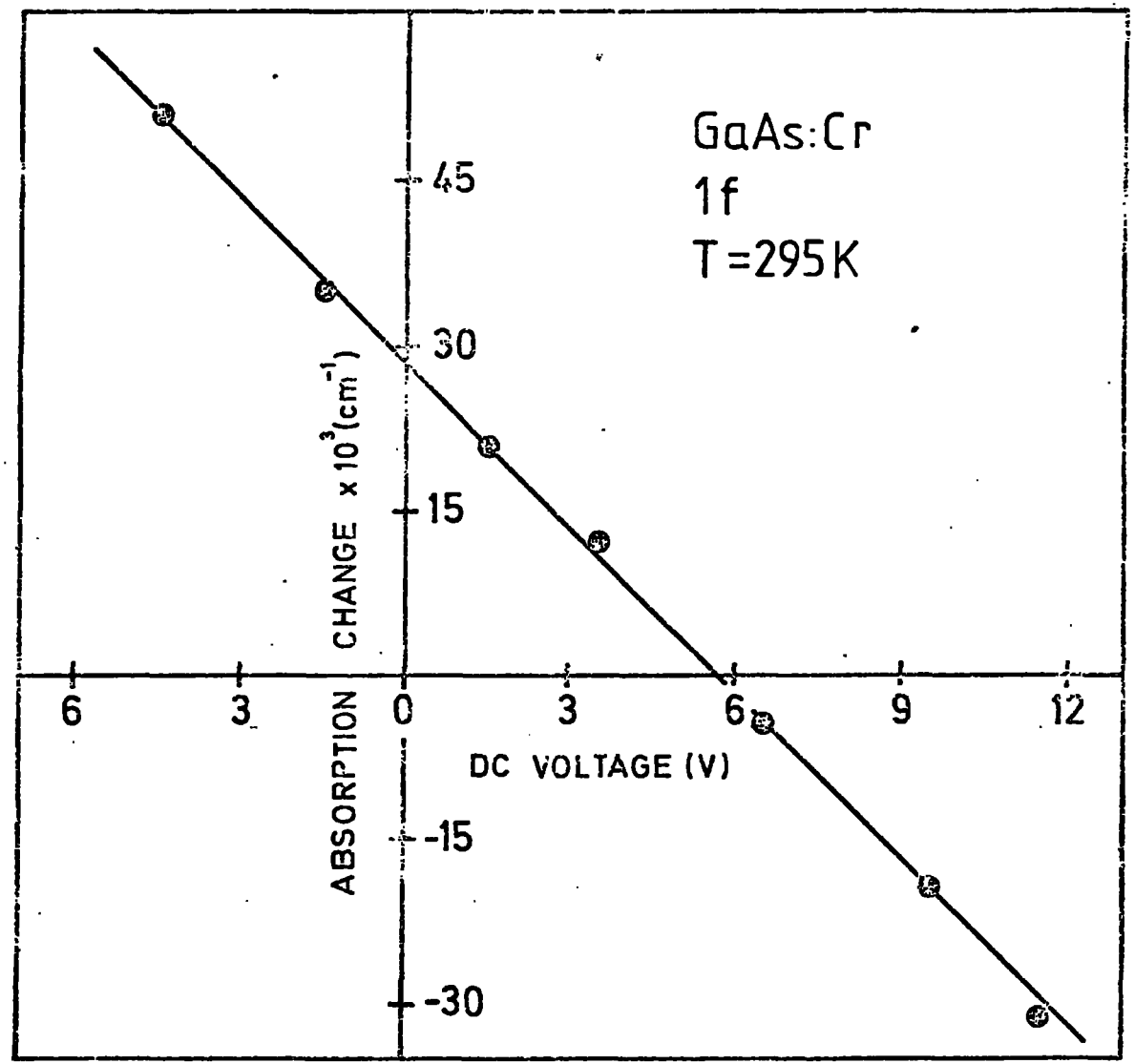

Fig. 5.20 Variation of the absorption change as a function of the dc. bias, superimposed on an ac. voltage, for a GaAs:Cr specimen at 295 K. F_{ac} = 1.46 x 10^3 V/cm.

is linearly dependent on applied dc. voltage. Of greater interest, however, is the fact that at a particular value of external dc. bias, in this case 6V, the absorption change falls to zero and thus assumes the theoretical value. An increase in the dc. voltage above 6V leads to a 180^{o} reversal of the phase at which the signal is recorded on the phase sensitive detector. This is shown as a "negative" absorption change for clarity.

Figures 5.21 and 5.22 show similar graphs for an undoped GaAs sample and an InP:Cr sample respectively. The undoped GaAs sample was received from the Naval Research Laboratory in Washington, and was interesting in that it had semi-insulating electrical properties despite being undoped. It was examined since an absence of a fundamental signal in this crystal would have pointed to the presence of the impurity (Cr) as the cause of the apparent internal static field, in agreement with a theory developed by Redfield [2, 3], and expanded by Yacobi [4]. However, it is clear from figure 5.21 that the sample behaved exactly the same as the chromium doped crystals, with the electroabsorption signal tending to zero for an applied static voltage of 5.5 V, for a 260 μm thick sample.

The data displayed in Figure 5.22 follow a similar form as the previous two diagrams but is exceptional for the large value of applied dc. voltage required to null the fundamental signal. It must be remembered, however, that these data are for an InP:Cr sample at 77 K. The relevance of the temperature to the data will become evident later.

5.6.3 Source Of The 1f Electroabsorption Signal

While the foregoing results and discussion have shed some light on the effects of the apparent internal electric field, little information has been presented concerning the reason for the field's existence. Figure 5.23 gives the nucleus of an explanation. The diagram is similar to the previous three in that it presents a graph of absorption change versus the superimposed dc. bias, in this case for an InP:Fe sample at 77 K. Two sets of data are presented, one for the sample oriented with

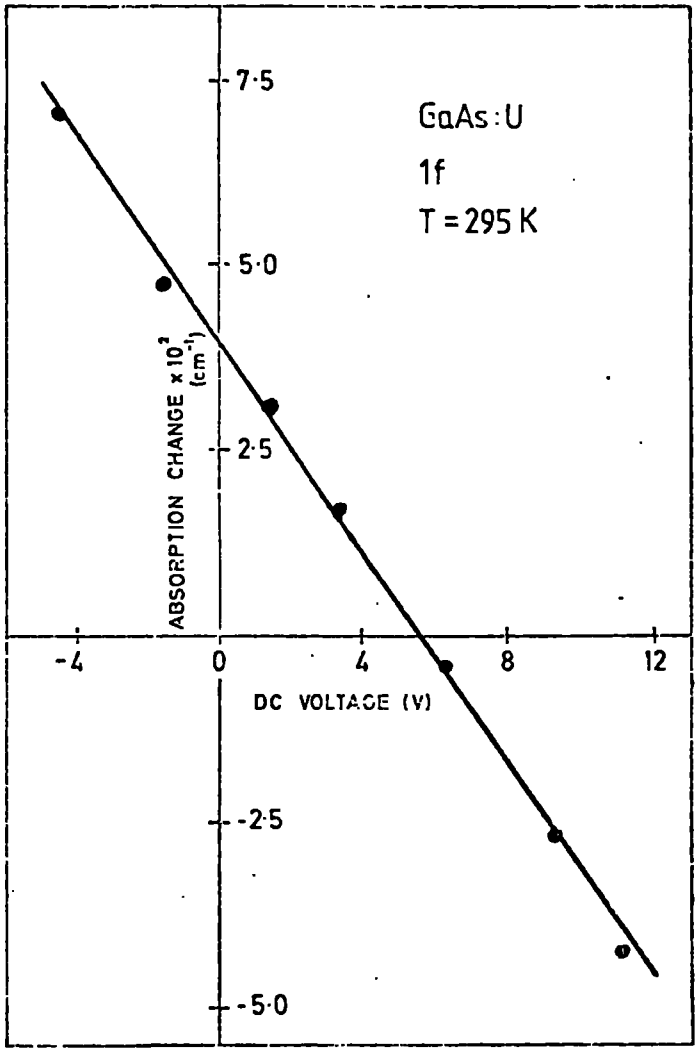

Fig. 5.21 Absorption change versus superimposed dc. bias for an undoped GaAs specimen. AC. bias = 2.83 x 10^3 V/cm. Sample thickness = 260 μm.

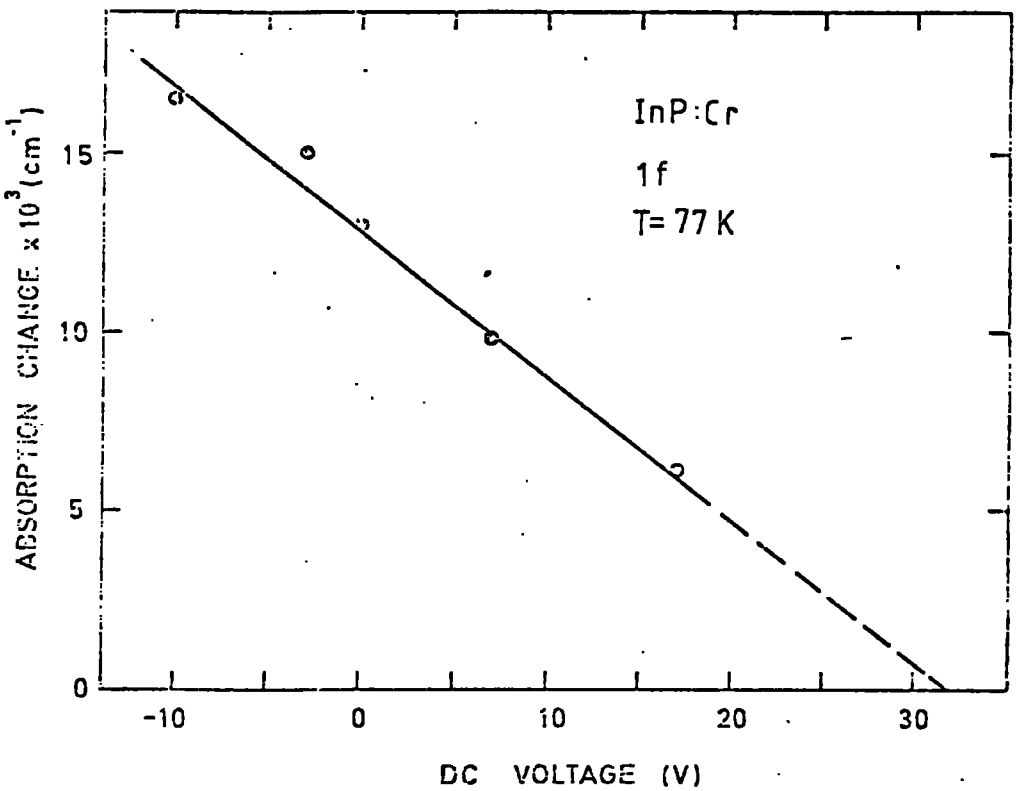

Fig. 5.22 Variation of the absorption change of an InP:Cr specimen at 77 K as a function of the superimposed dc. bias. Wavelength = 890 nm.

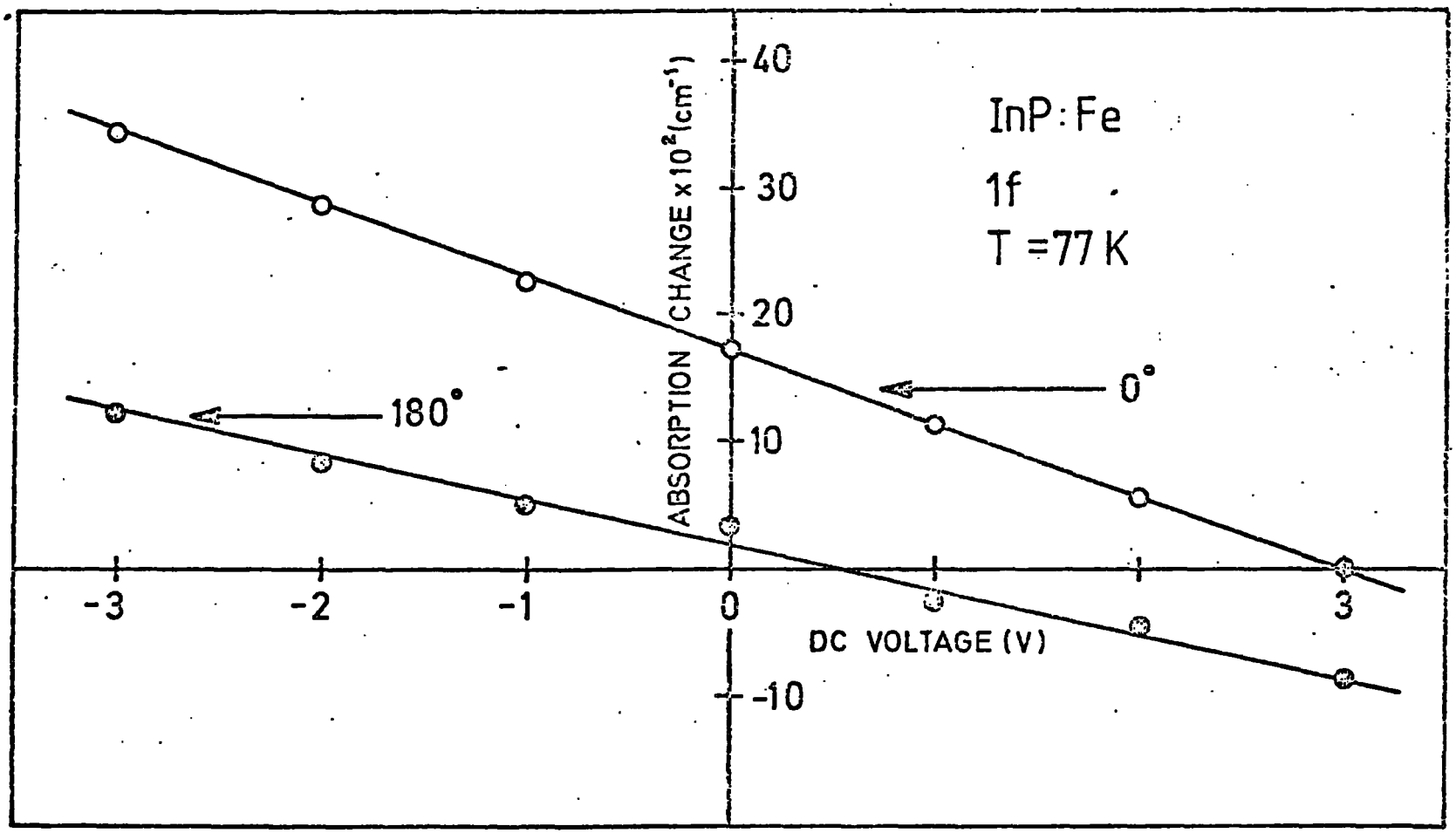

Fig. 5.23 Absorption change of an InP:Fe crystal as a function of the dc. component of the electric field, for a particular face of the crystal both towards and then away from the incident light. Wavelength = 878 nm. Sample thickness = 276 μm.

a particular face towards the incident radiation, the other for the sample with the same face rotated by 180°. An analysis of the graphs illustrates that the voltage required to null the electroabsorption signal is positive in both cases, and the slopes of the lines are practically equal and definitely of the same sign. It appears, therefore, that although the sample has been rotated by 180°, the internal field has not changed direction. An obvious conclusion is that the apparent internal field is not an inherent property of the crystal but is externally generated.

Figure 5.24 suggests that the static field is due to a photovoltage. In the figure, the absorption change due to the applied alternating external field (with zero dc. external bias) is displayed as a function of incident light intensity, both for the fundamental and 1st harmonic signals, for a fixed wavelength. It is evident that while the first harmonic curve is apparently independent of incident light intensity, the fundamental signal is strongly dependent. Up until a relative intensity of 4, the 1f signal is increasing extremely rapidly but begins to saturate above that value.

Somewhat similar photocarrier effects have been observed by McClelland [5] in his study of electromodulation spectra in TiCl and TiBr crystals, although he did not investigate any frequency dependence. Shimizee and Koda [6] have also noted photocarrier effects in electroabsorption.

From the data presented, one would conclude that in the samples investigated, the presence of a fundamental electroabsorption signal is indeed due to the existence of an apparent internal electric field, but that this field is generated by the incident radiation. The generation of a photovoltage at the surface of a semiconductor is now well understood [7]. While these voltages may be quite large in thin films, they are generally of the order of a few volts in single crystals [8]. Dahlberg [9][10] has studied transient photovoltaic effects in InP single crystals and has found them to be dependent not only on light energy and intensity, but also on surface conditions. Photovoltages

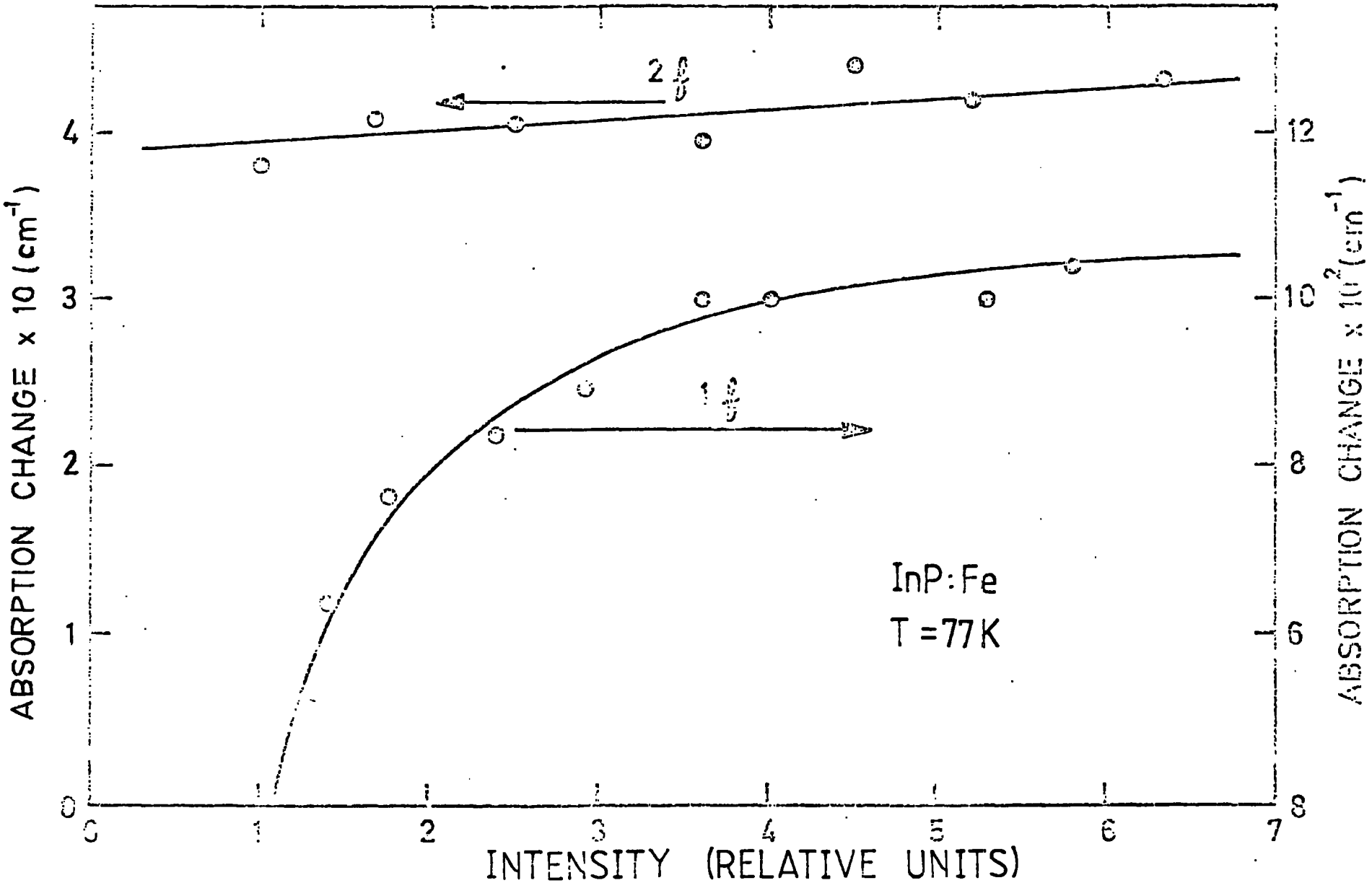

Fig. 5.24 Effect of a variation in incident light intensity on the 1f and 2f electroabsorption signals, at a frequency of 5 KHz for an InP:Fe specimen at 77 K.

have also been recorded in InP thin films [11]. Our results would appear to indicate that the existence of a photovoltage at the surface of a crystal can have drastic effects upon electroabsorption signals due to much larger external applied fields.

A verification that the fundamental (1ℓ) electroabsorption signal is due to the presence of a photo e.m.f. is that some of the InP:Fe samples which exhibited only weak photoconductivity at room temperature did not display a measurable 1f response until the temperature had fallen below about 200 K. By that temperature, the crystals have become strongly photoconductive. The InP:Cr samples also became strongly photoconducting at low temperatures, which explains the rather large nulling voltage obtained from Figure 5.22.

5.7 Observation Of Impurity Peaks In Electroabsorption

In Chapters I and II it was noted that the absorption of radiation could be due not only to the fundamental absorption edge but also to the presence of impurities and defects in crystals. Shallow impurity states can produce an extended long wavelength response in the absorption spectrum, as illustrated in Figure 1.20 in Chapter I. The presence of these absorption mechanisms is quite often hidden by the existence of an exponential absorption edge.

The zero field absorption studies performed on GaAs and InP in this work yielded no clearly defined impurity or defect structure within 0.2 eV of the absorption edge. However, a number of InP samples displayed extra structure in the electroabsorption spectrum, particularly at low fields and low temperatures. An example of such structure is shown in Figure 5.25 for an InP:Cr crystal at 77 K. The diagram displays the change in absorption due to the applied field as a function of photon energy. A number of curves are presented, each for a different value of applied field. For the lowest field, clearly defined structure is obtained at a photon energy below the main electroabsorption peak. As the magnitude of the field increases, the structure is gradually washed out. At a field of 6.2×10^3 V/cm the extra peak

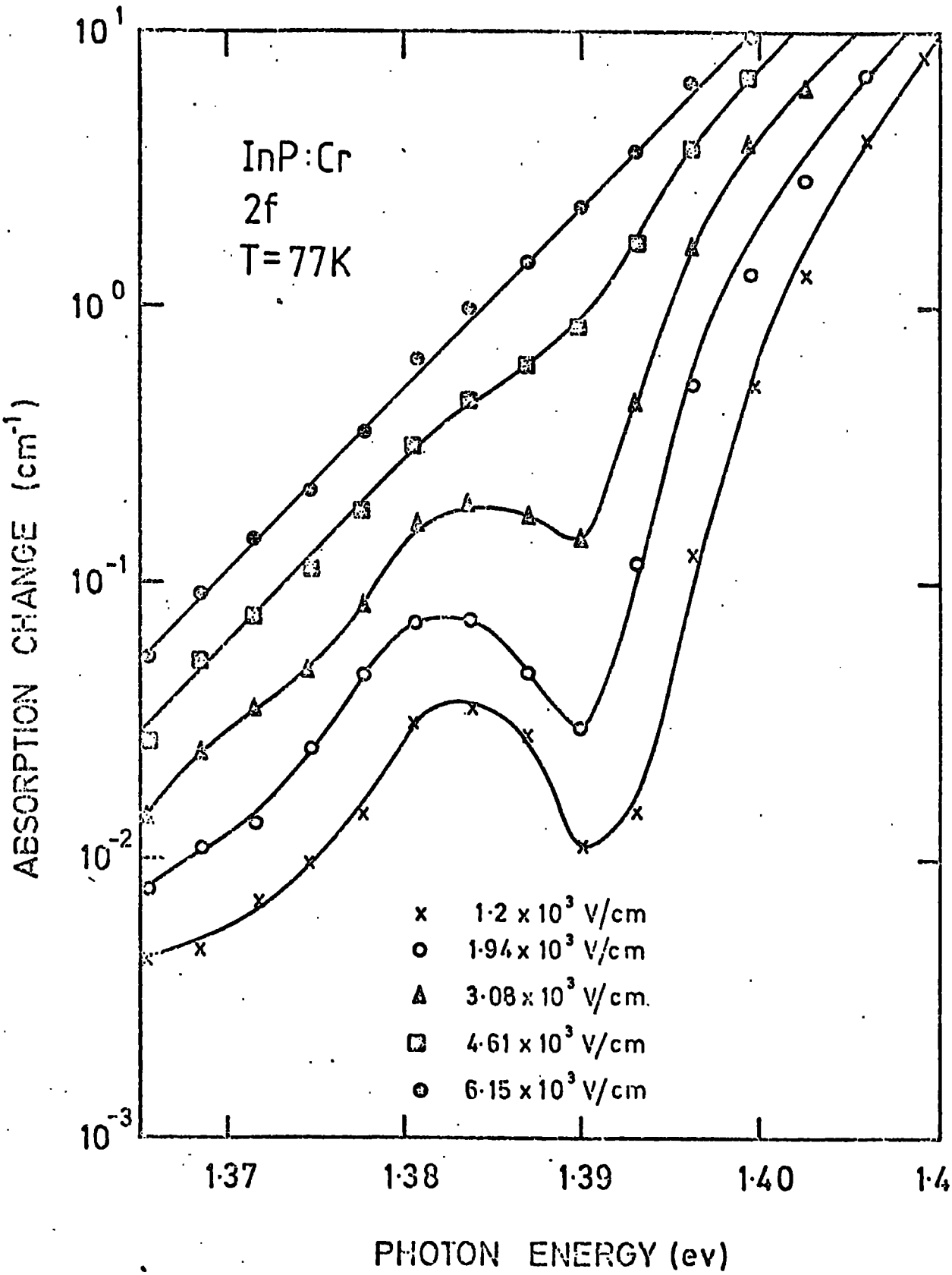

Fig. 5.25 Impurity electroabsorption in InP:Cr at 77 K, for a number of values of the applied electric field.

is completely quenched.

The electroabsorption curve for the same sample at 175 K is displayed in Figure 5.26. In this case, the peak has been considerably broadened, but surprisingly is still there, at a field of 6.2×10^3 V/cm, in marked contrast to the 77 K case. The centre of the peak occurs at a lower energy, in agreement with the temperature dependence of the bandgap.

Similar structure is observed in some InP:Fe crystals. Data for a typical crystal are shown in Figure 5.27 (a) for a temperature of 175 K, and fields of 5.9×10^3 V/cm, and 4.4×10^3 V/cm. By comparison to the InP:Cr sample at 175 K, this crystal exhibits a more clearly defined peak. The energy at which the maximum of the peak occurs may be more clearly located if the background absorption change due to the fundamental absorption edge is subtracted from the composite curve. This calculation has been performed and the results are shown in Figure 5.27 (b). From this graph, the maximum of the peak is found to occur at 1.347 eV, at this particular temperature.

It is reasonable to assume that the extra structure observed in the electroabsorption spectra, below the main electroabsorption peak, is due to the existence of either shallow impurity or defect states. Although these states do not appear to give rise to a detectable level of absorption in the zero-field absorption spectrum, it is quite possible that electroabsorption, being a more sensitive technique, could detect such a low level signal. With respect to the assignment of peaks in impurity electroabsorption, Ivanov et al [12] argue that the principal maximum of the spectrum should be located at the wavelength corresponding to the ionization energy of the impurity. This proposal is based on Lucovsky's [13] results that absorption by such centres resembles shoulders of typical interband transitions. Application of this argument to the above data leads to a level at 37 meV below the conduction band in InP:Cr and InP:Fe. The existence of an extended low energy photoconductive response in the InP:Fe samples was noted in section 5.6.1. Similar data for an InP:Cr specimen are displayed in

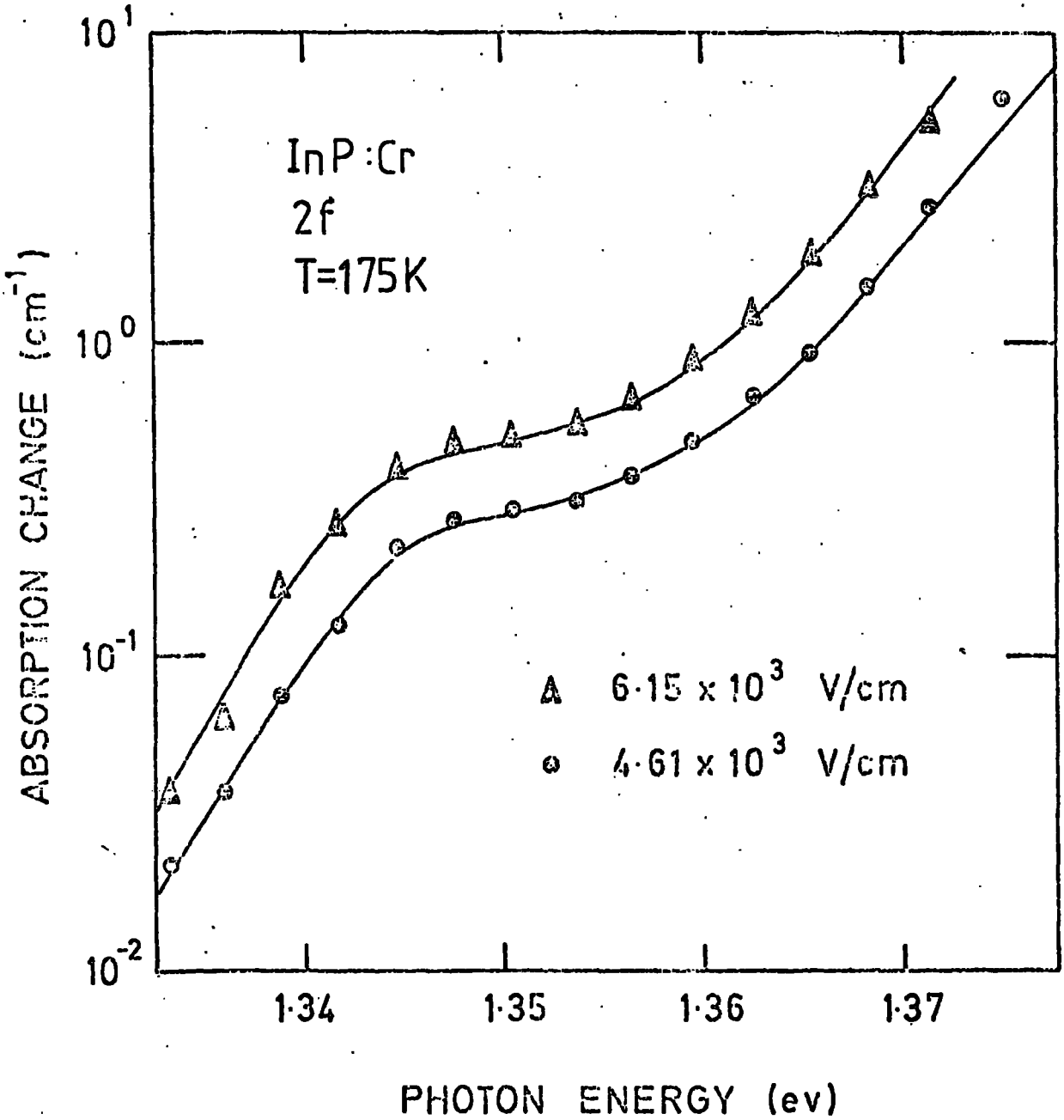

Fig. 5.26 Impurity electroabsorption spectra for the same specimen as Fig. 5.25 but at a temperature of 175 K.

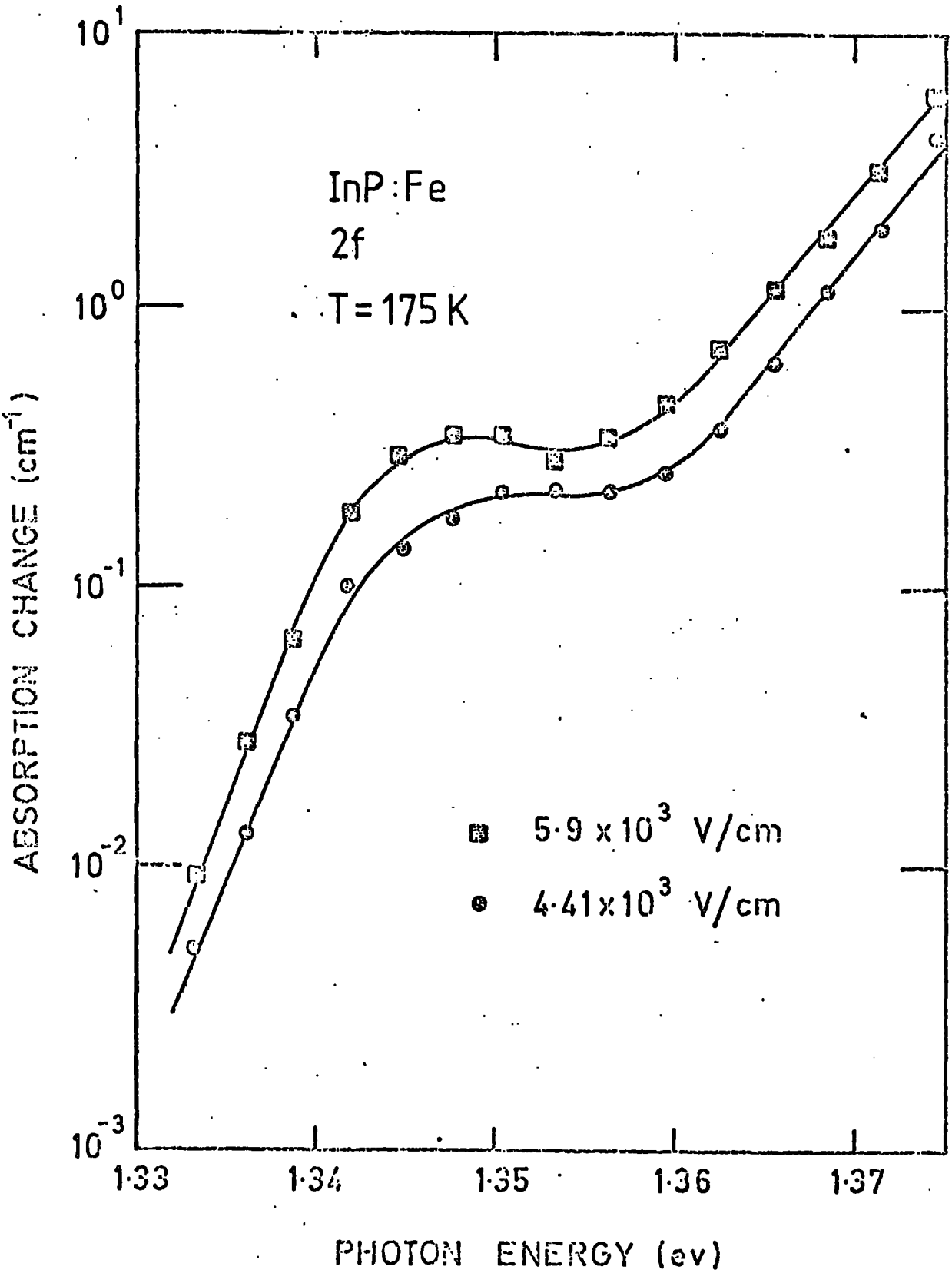

Fig. 5.27 (a) Impurity electroabsorption spectra of an InP:Fe crystal at 175 K for two values of the electric field. Sample thickness = 340 /um.

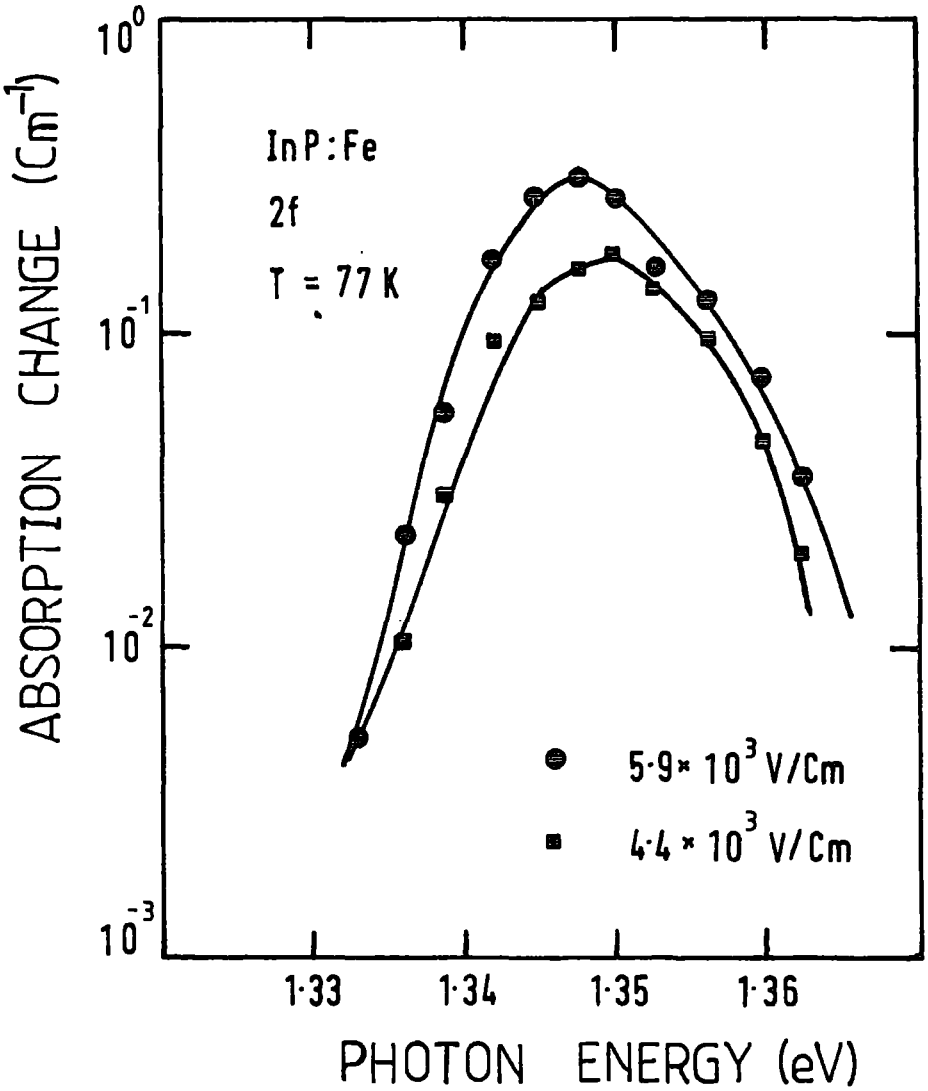

Fig. 5.27 (b) Data of Fig. 5.27 (a) redrawn with the background electroabsorption due to the fundamental absorption edge subtracted.

Figure 5.28. The photocurrents found in these specimens at energies just below the absorption edge may be attributed to shallow impurity or defect states. That conclusion would appear to be in agreement with the results presented above.

5.8 Discussion Of Results

The theory of electroabsorption was discussed extensively in Chapter II, where it was noted that two main methods of analysis had been proposed. The first method is the one-electron theory, originally developed by Franz and Keldysh and subsequently extended by Callaway, among others. The second branch of electroabsorption theory regards Coulombic effects as being critically relevant, particularly in the region of high absorption coefficients.

A careful consideration of the results presented in this chapter has led the author to the conclusion that these data may be satisfactorily analysed on the basis of the one-electron theory. The reasons for such a decision are as follows. The experiments were concerned exclusively with the region of low absorption coefficients namely $\alpha < 200\ cm^{-1}$. This is the area in which the Franz/Keldysh theory is most likely to be applicable. Furthermore, the theory predicts that for exponential absorption edges, the change in absorption coefficients should be dependent upon the square of the applied field. Both InP and GaAs exhibit an exponential absorption edge. A quadratic dependence of absorption change upon applied field was recorded for every sample examined, as demonstrated in Figures 5.10 to 5.13. Another prediction of the one-electron theory is that the slopes of the zero field absorption curve and the electroabsorption curve should be equal. Figures 5.6 to 5.9 demonstrate that this is also verified in our case.

It could be argued that it has also been clearly shown that photocarrier effects prevent a clear cut analysis of electroabsorption in semi-insulating InP and GaAs. However, Figures 5.14 and 5.16 demonstrate that above a frequency of about 2 kHz, there are no photo-

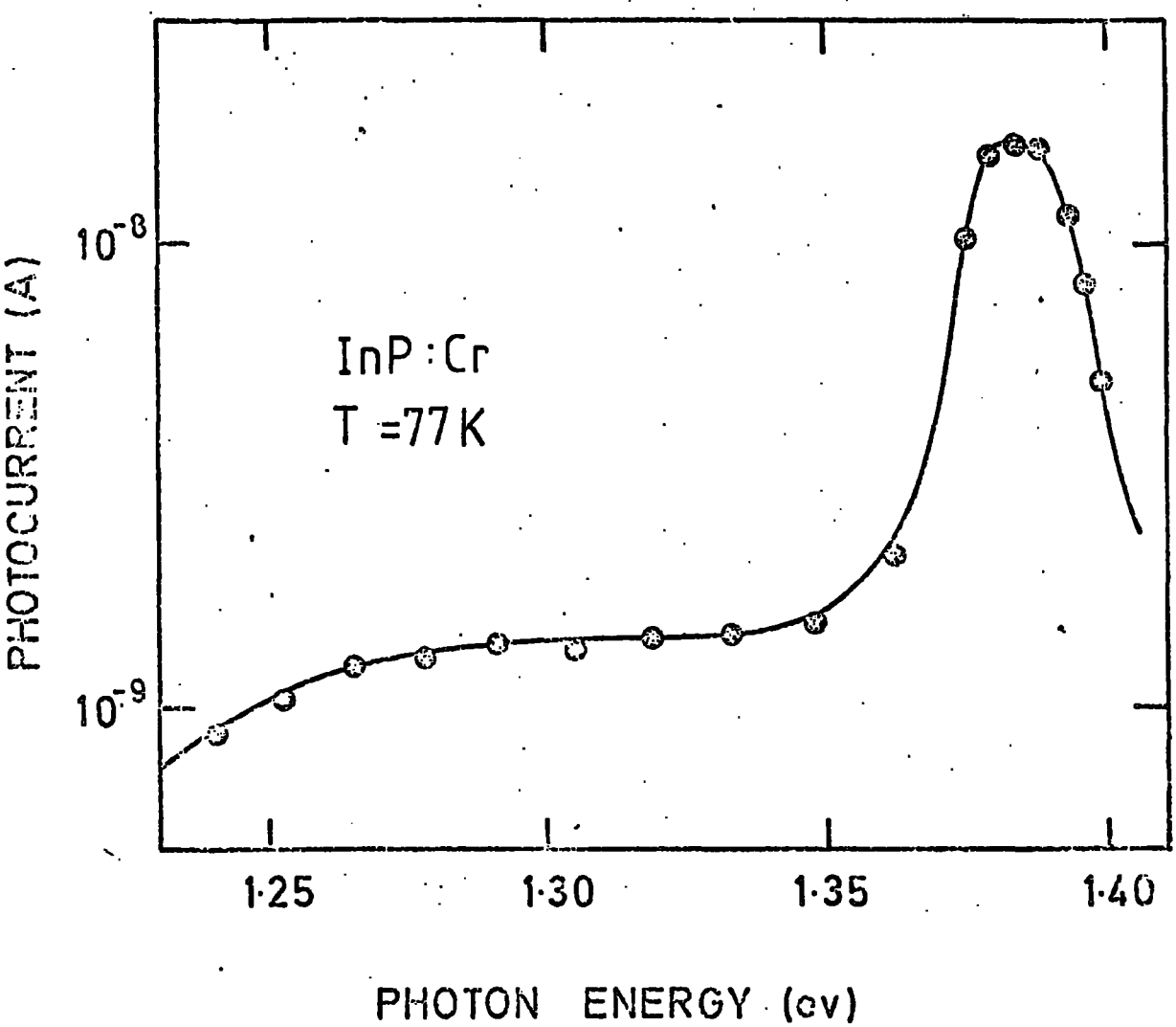

Fig. 5.28 Photoconductivity of an InP:Cr crystal at 77 K.

carrier effects upon the electroabsorption signal at 2f. Furthermore, this signal is independent of any dc. bias and is due solely to the alternating field component. In view of this one could conclude that the electroabsorption signal recorded at 2f and at a frequency above 2 KHz is the true Franz/Keldysh absorption change due only to the known external applied field.

If this is so, it is possible to fit the recorded data to equation 2.17, namely:-

$$m^* = \frac{\beta^3 \hbar^2 F^2 \alpha}{24e \Delta\alpha}$$

This equation has been used to calculate the effective mass m^* for the InP:Cr, InP:Fe and GaAs:Cr specimens. The results of such an analysis are shown in Table 5.1 for the various temperatures at which the data were recorded. During the course of the study a total of eight InP:Fe, four InP:Cr and four GaAs crystals were investigated, to varying degrees. In Table 5.1 the data of Eaves et al [14] on pure InP and Chamberlain and Stradling on pure GaAs [15], are also shown for comparison purposes. The overall accuracy of the values of m^* from our electroabsorption experiments is approximately $\pm 10\%$. In some cases, however, we believe the accuracy may be as good as $\pm 5\%$ in view of the quality of the data obtained. One of the factors limiting the accuracy was the difficulty in obtaining reproducible values of the absorption coefficient α. This is because only a single beam monochromator was available for the spectral area of interest. However this problem did not affect the determination of $\Delta\alpha$, since the measurements of the incident light intensity I_o is not necessary for a calculation of the absorption change. Accordingly, bearing in mind the complexity of the technique, the results quoted in Table 5.1 appear quite satisfactory.

Material	Dopant	m^*/m_o	Temperature	Published Value For Pure Material
GaAs	Cr	.070	295 K	.067
InP	Fe	.076	295 K	.078
InP	Fe	.084	77 K	.080
InP	Cr	.079	77 K	.080

Table 5.1 Calculated values of the reduced effective masses of InP:Cr, InP:Fe and GaAs:Cr from the electroabsorption data.

5.9 Conclusion

In this chapter results have been presented demonstrating the effect of large electric fields upon the optical absorption properties of both GaAs and InP in the region of small absorption ($\alpha < 200\ cm^{-1}$). The preparation and characterization of electrical contacts to the specimens have also been discussed. A detailed examination of photo-carrier effects upon the frequency dependence and harmonic content of the electroabsorption spectra has also been made. Data have been presented illustrating the presence of impurity states in the InP samples. Finally the data have been analysed within the framework of the one-electron Franz/Keldysh theory and found to give reasonable values of reduced effective mass.

CHAPTER VI

ELECTRICAL AND OPTICAL PROPERTIES OF ANTHRACENE LANGMUIR FILMS

6.1 Introduction

The preparation and properties of Langmuir/Blodgett "built-up" organic multilayers have recently attracted an increasing degree of interest. These thin films consist of a series of monolayers of a suitable organic material, with each monolayer being deposited upon the previous layer until the required thickness is reached. Provided certain conditions are carefully controlled, a film of great perfection may be obtained, whose electrical and optical properties may be extremely useful.

Organic thin films could in principle be used for a number of practical devices. It has been suggested [1], that if anthracene could be formed into high-quality films approximately 0.1 - 1.0 μm thick, it would probably be an efficient large-area electroluminescer. A proposal has been made [2] that organic layers could be suitable for use in rectifiers and memory devices. The ability to prepare smooth homogeneous layers is essential for integrated optics devices [3], superlattices [4], thin film transistors [5] and M.I.S. devices [6]. There is a distinct possibility that Langmuir/Blodgett films would fulfil this requirement.

This chapter of the thesis is devoted to a detailed description both of the preparation and structure of such films, and to their electrical and optical characterization. In particular, results are presented concerning the effects of large electric fields on the optical absorption properties of these materials. The data presented here are the first detailed electroabsorption measurements on a Langmuir film. In many ways, Langmuir films present an ideal system for electroabsorption studies. For example, the thickness of each

monolayer is typically 20 Å, so that only a small voltage supply is required in order to drop large electric fields (typically 10^6 V/cm) across a film. In addition, because of their high dielectric strengths, the films are capable of withstanding such high fields, without giving rise to Joule heating.

6.2 Preparation And Structure Of Langmuir/Blodgett Films

Langmuir/Blodgett films are formed by depositing a small quantity of a solution of a suitable material on the surface of previously purified water, waiting for the solvent to evaporate and then compressing the mono-molecular layer so produced until it forms a quasi-solid one molecule thick. To remove the film from the water, a suitable substrate is dipped through the quasi-solid and then removed. One monolayer is transferred to the substrate during this process, provided certain stringent requirements have been met. If the substrate is repeatedly dipped through the water a multilayer of the organic substance is built up, with a high degree of structural perfection. The process by which the multilayers are built up is illustrated in Figure 6.1. Using this method, Langmuir/Blodgett films may be built up from an initial thickness of approximately 25 Å to depths in excess of one millimetre. The method is attractively simple in principle, but to obtain deposited layers which are well-ordered and structurally stable requires meticulous attention to experimental detail. Furthermore, only a limited range of organic materials can be formed into Langmuir/Blodgett multilayers. Both these points are discussed in detail in the following sections.

6.2.1 Suitable Materials For Langmuir/Blodgett Films

In general, molecules to be deposited using the Langmuir/Blodgett technique must possess both a hydrophobic and a hydrophilic component [7]. Furthermore, to obtain multilayers as opposed to monolayers, the hydrophilic group must normally be quite strong. An aliphatic side-chain is normally used as the hydrophobic part of the molecule. In order to avoid excessive water-solubility, the aliphatic component must

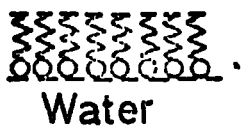

(a) Monolayer on the surface of the water.

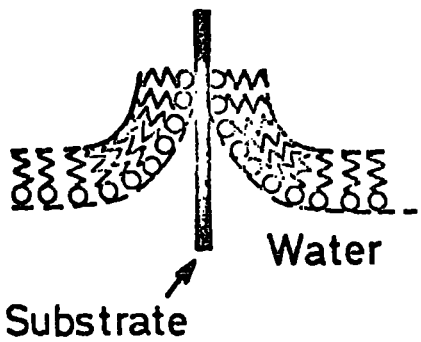

(b) First layer on withdrawal.

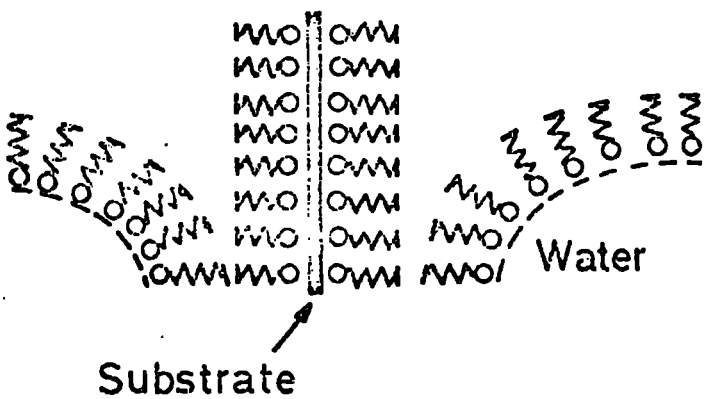

(c) Second layer (2nd Insertion)

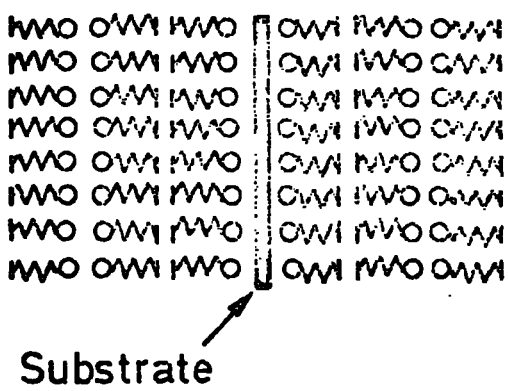

(d) Slide with three layers (after 2nd Removal)

Fig. 6.1 Illustration of the build-up of a multilayer film from a Langmuir trough.

also be quite large. Accordingly, suitable molecules generally contain one or more long ($\approx$18 carbon) aliphatic hydrocarbon chains. Materials which immediately suggest themselves are the long-chain fatty acids [7], whose structure is illustrated in Figure 6.2.

Recently a number of authors, including Handy and Scala [8], Horiuchi et al [9], Nathoo and Jonscher [10], Mann and Kuhn [11] and Sugi et al [12] have investigated the electrical properties of such fatty acid monomolecular layers. The most common materials examined were the Cd salts, cadmium arachidate, cadmium stearate and cadmium palmitate. These films were studied either sandwiched between evaporated metal electrodes (MIM) or deposited on a semiconducting surface (MIS). The general conclusion of these workers was that fatty acid Langmuir films are good insulators with dielectric strengths greater than 10^6 V/cm. Roberts et al [13] have reported the electrical conduction properties of cadmium arachidate films deposited on InP substrates. These authors obtained an unusual log J vs. $V^{\frac{1}{4}}$ relationship between current and voltage in single monolayer films but the expected log J vs. $V^{\frac{1}{2}}$ relationship for multilayer films. For a review of the characterization of long-chain fatty acid Langmuir films, the reader is referred to Agarwal [14] or Srivastava [15].

The discussion at the start of this section leads to the conclusion that it is in general not possible to form Langmuir/Blodgett multilayers from conjugated molecules, unless their aromaticity is very heavily diluted with aliphatic molecular substituents. Up to the present this has indeed been the case, so that almost all Langmuir/Blodgett multilayer work using conjugated molecules has included the use of one or more C18, or sometimes C12, aliphatic chains. The stability of such monolayers is often improved by mixing the aliphatic chains with an excess of long-chain fatty acid molecules. As a result, the films so produced bear little resemblance in many ways to the original conjugated material. Since conjugated systems, with their extended π-electronic orbitals, are likely to show more interesting and useful electrical properties, this is a significant drawback. The greater thermal stability

FATTY ACID SALTS

$$[CH_3(CH_2)_{n-2}COO^-]_2 Cd^{2+}$$

n = 18 CADMIUM STEARATE

n = 20 CADMIUM ARACHIDATE

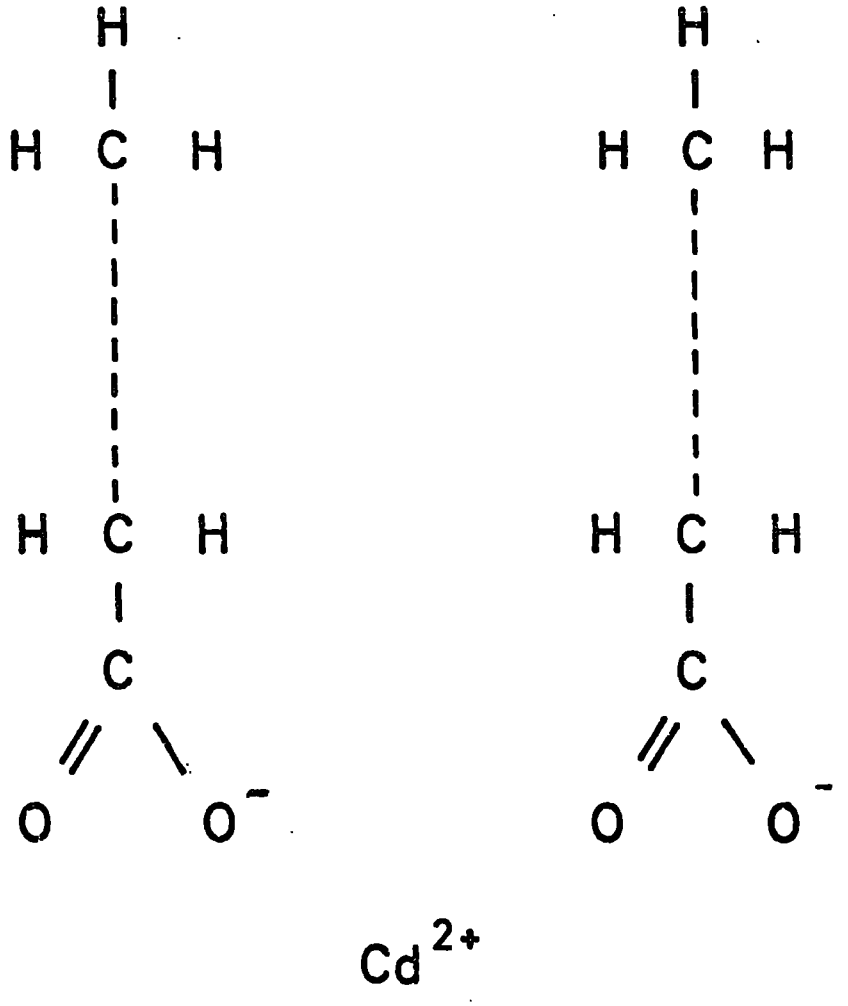

Fig. 6.2 Structure of long-chain fatty acid salts.

exhibited by conjugated systems over their aliphatic counterparts is also important, particularly for integrated optics and electronic device applications.

Recently, however, Vincett, Barlow, Boyle and Roberts [16] have reported the successful deposition of high-quality multilayers of lightly-substituted anthracene derivatives, with aliphatic side-chains as short as 4 CH_2 units. This present study is exclusively concerned with such novel films and has been undertaken in collaboration with the above authors [17, 18].

A description of the preparation of lightly-substituted anthracene Langmuir films is now presented.

6.2.2 Preparation Of Lightly-Substituted Anthracene Langmuir/Blodgett Films

The anthracene derivatives were normally prepared in a 3×10^{-3} M chloroform solution. This solution was spread on the surface of water in a glass trough, at a temperature of approximately 20°C. The layout of the trough is illustrated schematically in Figure 6.3. Little effect was produced by substitution of the chloroform by methylene chloride, or by adjusting the solution strength. The solvent usually evaporated in a few minutes, after which the surface area of the monolayer was varied by means of motor-driver PTFE-coated glass fibre barriers. In order to investigate the structure of the monolayer, and to establish optimum dipping conditions, surface pressure-area isotherms were recorded. These were achieved by compressing the monolayer at a constant rate, typically 3 $Å^2$ per molecule per minute. In addition, the surface area and surface pressure were recorded. A suitable method of determining the latter quantity was to insert a piece of filter paper of known dimensions vertically in the monolayer and attach it to a sensitive microbalance.

High purity water for the trough was prepared using a millipore "Milli-Q" purification system. The pH of the water sub-phase was

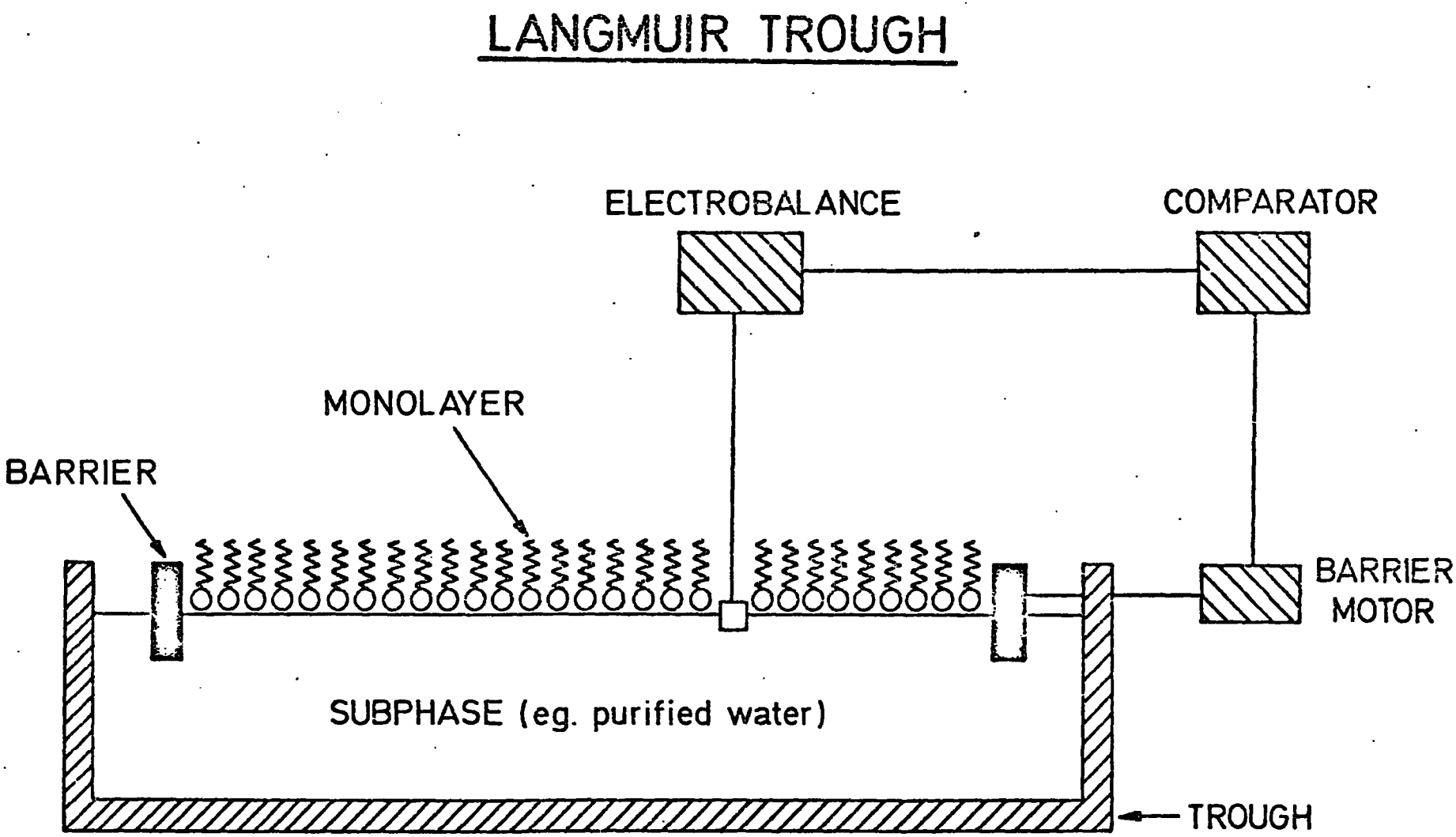

Fig. 6.3 Schematic diagram showing the main components of the Langmuir trough.

adjusted by the addition of HCl. All chemicals used in the entire process were of the best available commerical grade.

While some multilayer films were deposited on semiconducting substrates, most of the experiments were performed on samples prepared on glass slides. These Chance-Select slides were carefully cleaned by ultrasonic agitation in chloroform, then in "Decon 90", followed immediately by a thorough rinse with water. Finally, the slides were blown dry with filtered compressed air.

In order to facilitate the deposition of the multilayers, it was found necessary to coat both sides of the glass slide with aluminium. Typical aluminium thicknesses were 500 $\mathring{A}$. However, for the electroabsorption experiments it was necessary to transmit light through the aluminium, so for these specimens the thickness was about 150 $\mathring{A}$. To deposit the multilayers upon the substrate, the slides were gently lowered into the water at a speed of 2.5 to 5 mm per minute, using a smooth motorized system. During this process, a suitable surface pressure was automatically maintained by means of a proportional feedback system. Under the proper conditions, a monolayer was deposited onto the slide during each passage through the water except the first.

An opaque box with U.V. - opaque windows was used to surround the trough, to prevent both dust contamination and photo-oxidation of the anthracene. Prior to use, the anthracene derivatives were kept in the dark. As far as possible, clean-room conditions were maintained in the room in which the trough was contained.

6.2.3 Attainment Of Suitable Surface Pressure-Area Isotherms

As previously explained, it is relatively easy to study anthracene derivatives on the Langmuir trough provided R contains 12 or more CH_2 groups (See Figure 6.4). The difficulty arises when R is much shorter than $C_{12}H_{25}$. Figure 6.5 compares an isotherm obtained for 9-dodecyl-10-anthryl propionic acid, R = $C_{12}H_{25}$, R' = C_2H_4COOH, at pH 4.0 with one

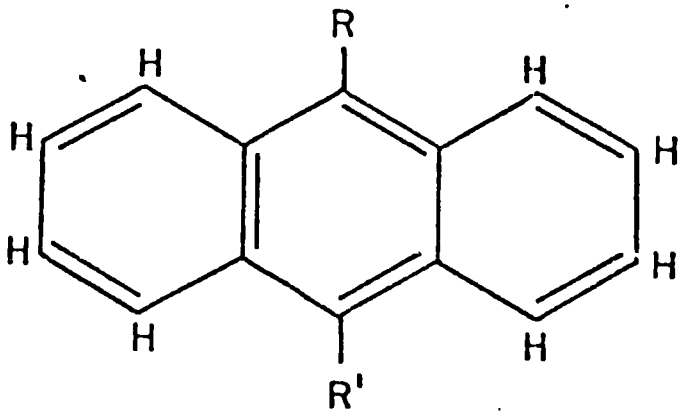

Fig. 6.4 Structure of the anthracene derivatives.

obtained using R = C_4H_9 and R' = CH_2OH. While the long chain derivative (a) is stable up to a surface pressure of approximately 30 dynes cm^{-1}, the short chain derivative (b) showed only a very small upswing in surface pressure. Furthermore, in the case of the lightly substituted derivative, if the compression was stopped once a finite surface pressure was reached, the pressure rapidly decreased to zero. These observations explain the generally held belief that chain lengths of this kind are too short for useful aromatic work.

The solution to the above problem was reported in reference [16]. These authors, having traced the instability effects to solubility of the anthracene derivatives in water, bypassed the effects by repeatedly compressing many monolayers of the anthracene derivative on the same water. The effectiveness of this procedure, which presumably works by saturating the water surface with the compound, may be seen from Figure 6.5 (c). In this diagram, the isotherm (c) was obtained after repeatedly compressing the film, at a similar speed to that used for curve (b). It is obvious that the procedure has converted a very poor quality isotherm into one very similar to the C12 case.

Several other techniques were also employed to improve the situation further. These included the addition of 2.5×10^{-4} M $CdCl_2$ to the water to assist the cohesion of the film, and a reduction of the pH level to 4.5. Figure 6.5 (d) shows the effect of reducing the sub-phase pH to 4.0, without using any saturation techniques. R in this case is again C_4H_9, with R' = C_2H_4COOH. Presumably, reduction of the pH leads to a suppression of monolayer ionization and thus a drop in its degree of solubility. However, it was found [16] that if the pH value was too low, the films lacked cohesion during deposition. A further improvement in isotherm could be obtained by faster compression.

Using the above techniques, it was found possible to produce conditions under which the deposition of short chain Langmuir films of anthracene could be contemplated.

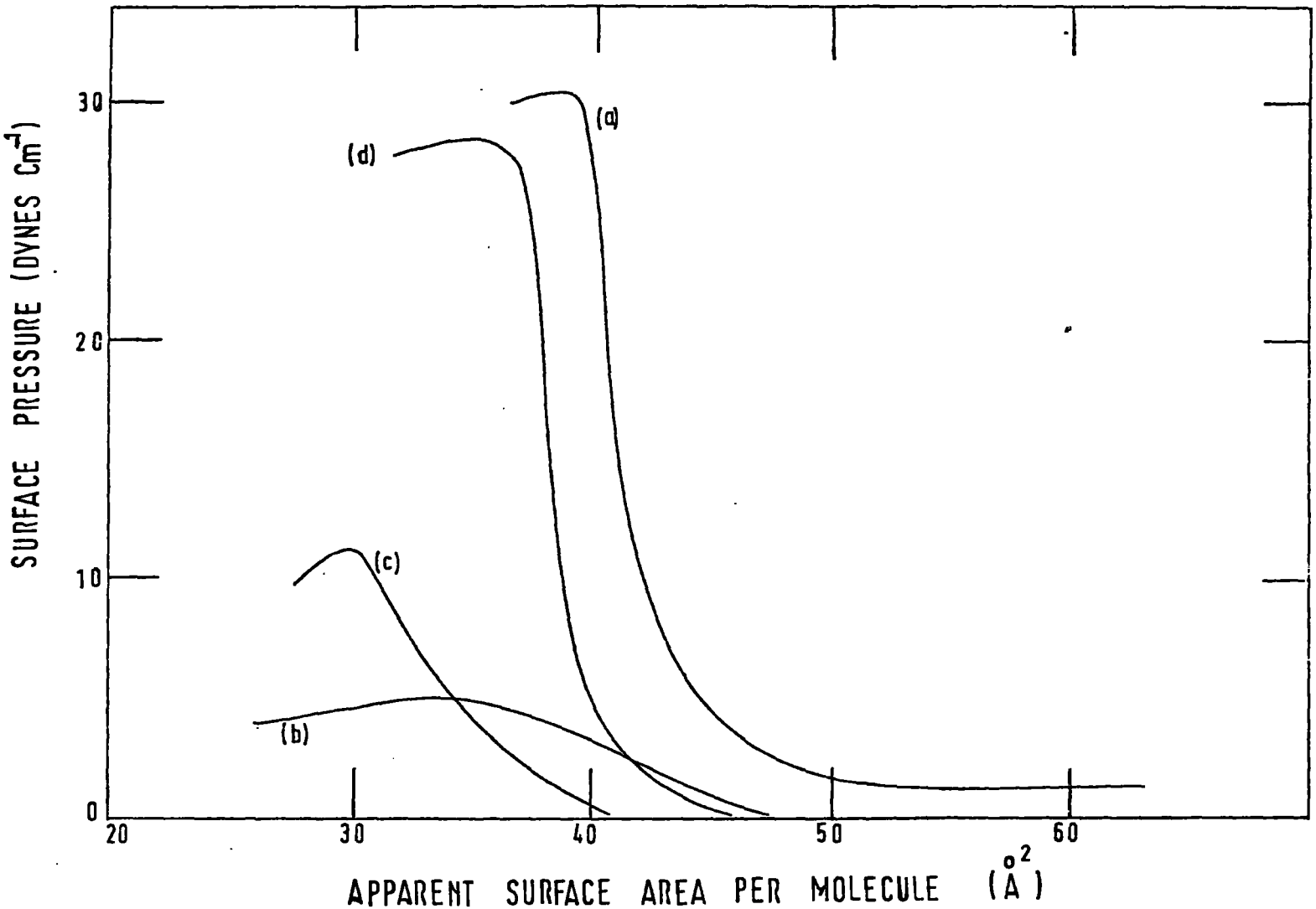

Fig. 6.5 Surface pressure–area isotherms obtained on anthracene derivatives; (a) R = $C_{12}H_{25}$, (b) R = C_4H_9 (c) R = C_4H_9, after a number of compressions; (d) C_4H_9 at a pH = 4.0.

6.2.4 Deposition Of Multilayers Of Anthracene Derivatives

Multilayer deposition was carried out using the derivatives with R = C_4H_9, C_8H_{17}, C_6H_{13} and $C_{12}H_{25}$, and R' = C_2H_4COOH, since it was found that an -OH termination on the polar substituent did not permit adequate Langmuir/Blodgett deposition beyond the first monolayer. Figure 6.6 displays the structure of these unique Langmuir films for the C4 case. For the C4 and C8 compounds the surface pressure for deposition was 15 dynes cm^{-1} rising to 20 dynes cm^{-1} for the C12 material. These pressures were close enough to the compressed state to ensure a coherent film but yet not high enough to collapse the film. In general, the deposition was Y type, that is, transfer of a monolayer on each passage through the water surface. As the thickness of the multilayer increased an occasional change to Z type deposition(transfer on upstroke only) was observed. The ratio of the area of the multilayer to the monolayer area lost on each deposition stroke was within about 5% of unity. After emerging from the water the film was almost dry, although less so at large thicknesses of the multilayer.

The molecular arrangement of the deposited films consisted of layers of tilted anthracene nuclei, separated alternately by layers of polar head groups and interleaving aliphatic chains. This unusual structure, without the tilt, is sketched in Figure 6.7. For the C4 anthracene the separation of the π-electron systems of neighbouring molecules is approximately 6 Å, in a direction normal to the plane of the film. The packing density of the C4 anthracene nucleus is nearly half its value in crystals of unsubstituted anthracene. The thickness of a C4 monolayer has been determined to be approximately 12.5 Å, from x-ray measurements.

6.2.5 Deposition Of Electrical Contacts To The Multilayers

The evaporation of a base aluminium electrode to the glass substrate has already been mentioned. For the electroabsorption experiments, this layer was kept to a thickness of about 150 Å, so that it would be

NOVEL LANGMUIR FILMS

B —	C —	L
HYDROPHOBIC GROUP	CYCLIC STRUCTURE (planar delocalized system of π electrons)	HYDROPHILIC GROUP
eg. hydrocarbon chain	eg. anthracene	eg. COOH

9-BUTYL-10 ANTHRYL PROPIONIC ACID OR C4 ANTHRACENE

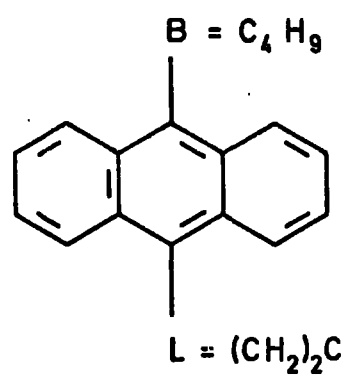

Fig. 6.6 Structure of the lightly substituted anthracene derivatives.

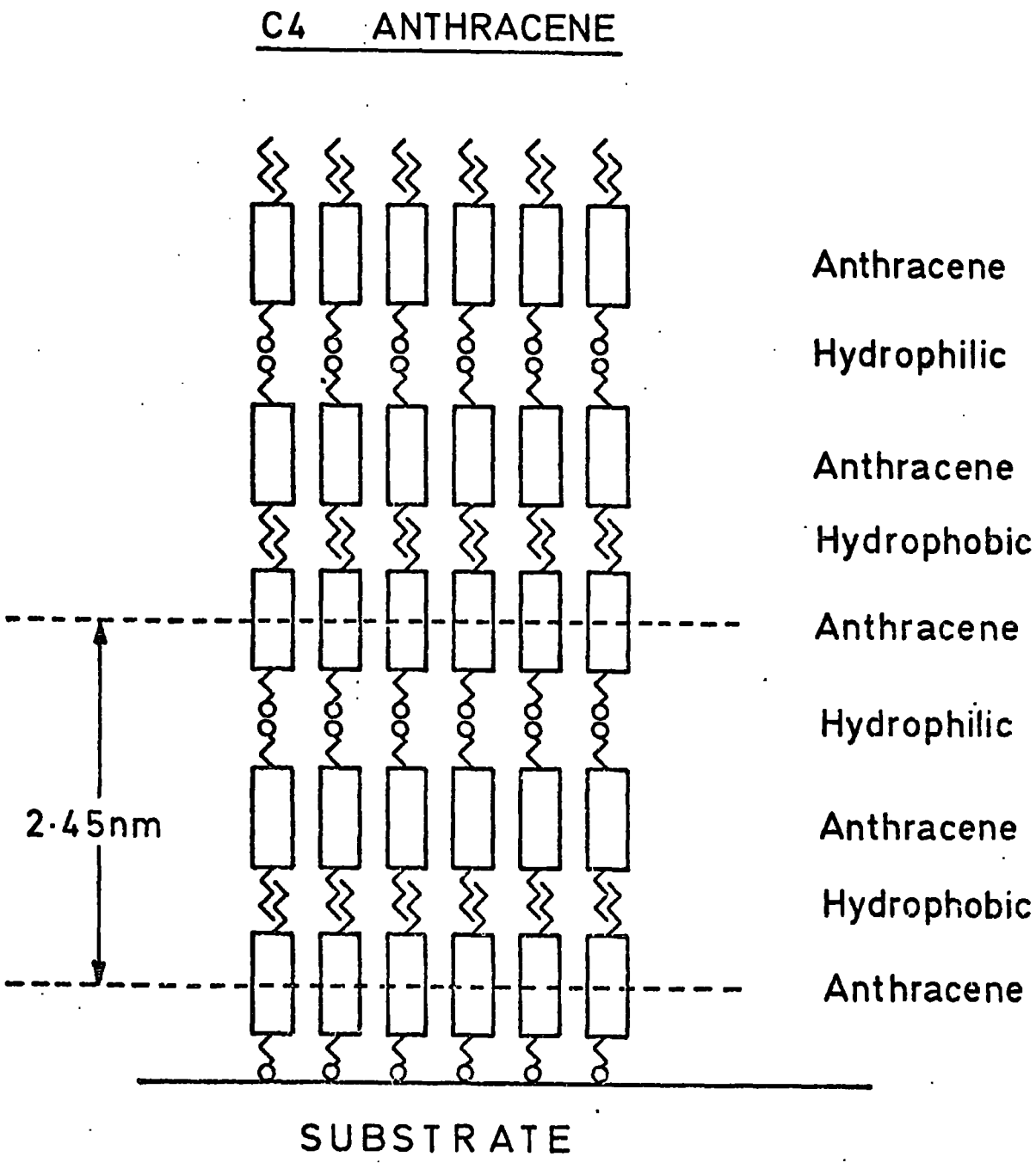

Fig. 6.7 Interleaving of the C4 anthracene multilayer films.

possible to transmit radiation through the structure. For the ac. and dc. conductivity experiments the thickness of this electrode was not so critical. Later in this chapter, results are presented concerning electroluminescence in the anthracene films. It is probable that the thickness of the base electrode is important for efficient light emission from these specimens, since presumably the oxide controls the electron injection. However, no detailed measurements were performed to verify this.

The top electrode used was generally gold, evaporated at a pressure of approximately 10^{-5} torr. During this evaporation the film was maintained at around $-40^{\circ}C$, by means of a liquid nitrogen cold finger within the evaporator. To prevent any condensation of water vapour on the sample, the system was flushed out several times with dry N_2 gas prior to pump down. Once again, this electrode was kept to a thickness of about 150 Å for electroabsorption and electroluminescence experiments. For other experiments, this electrode was usually 300 Å thick.

6.3 Experimental Results

The results of a series of experiments performed on Langmuir films of anthracene are now presented.

6.3.1 Capacitance Data

The capacitance of the films, as a function of the number of layers, was determined using the equipment described in Chapter III. Typical data for a C6 specimen are displayed in Figure 6.8. This film was deposited at $18^{\circ}C$ with a subphase pH of 4.67. The graph indicates a linear dependence of reciprocal capacitance on the number of layers, N, and suggests an almost ideal build-up of the film. For comparison, Figure 6.9 illustrates equivalent data for a C4 film obtained by Vincett et al [16]. Both curves indicate the reproducibility of the monolayer capacitance, and hence thickness.

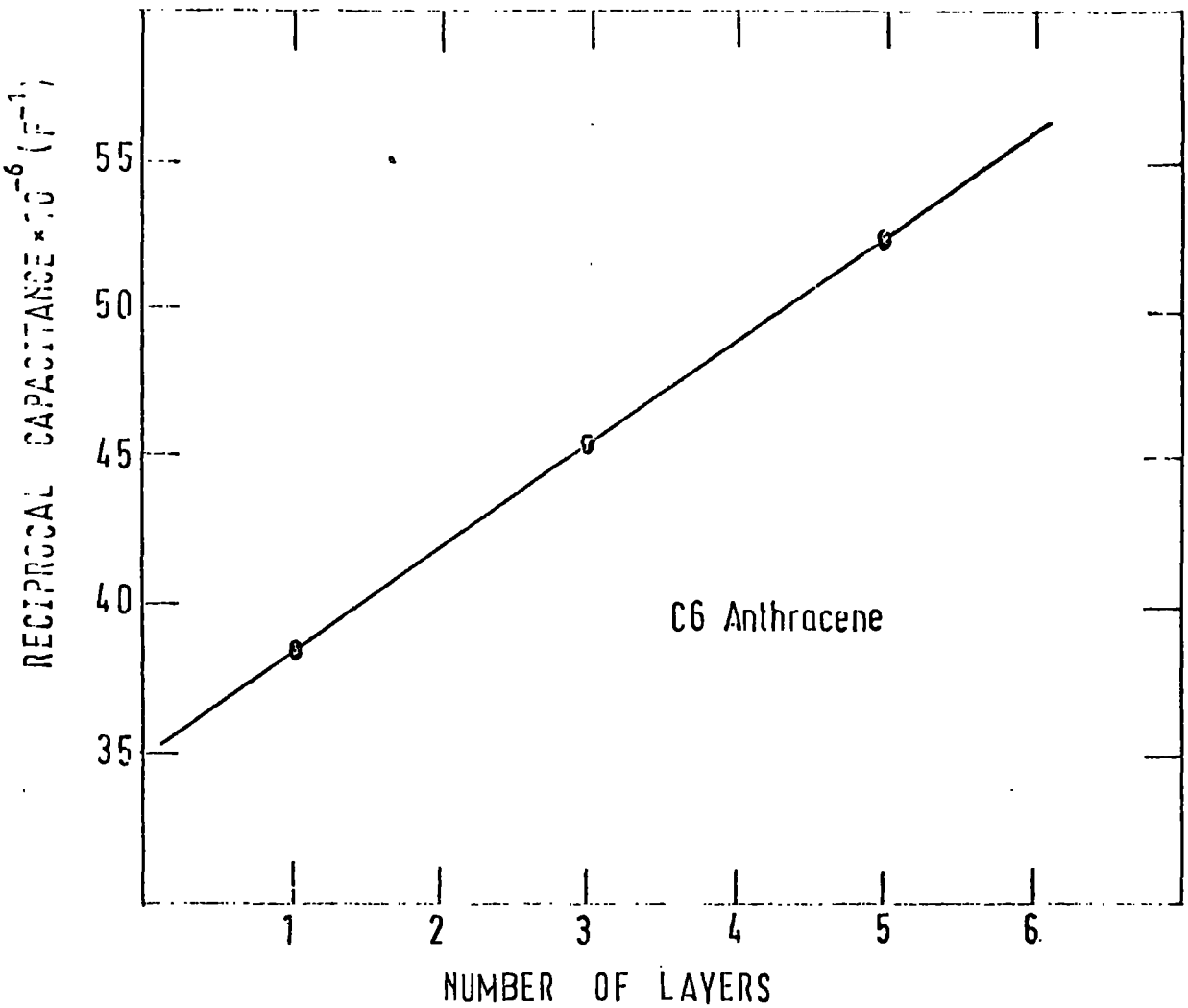

Fig. 6.8 Plot of reciprocal capacitance versus the number of monolayers for a C6 anthracene film at 295 K.

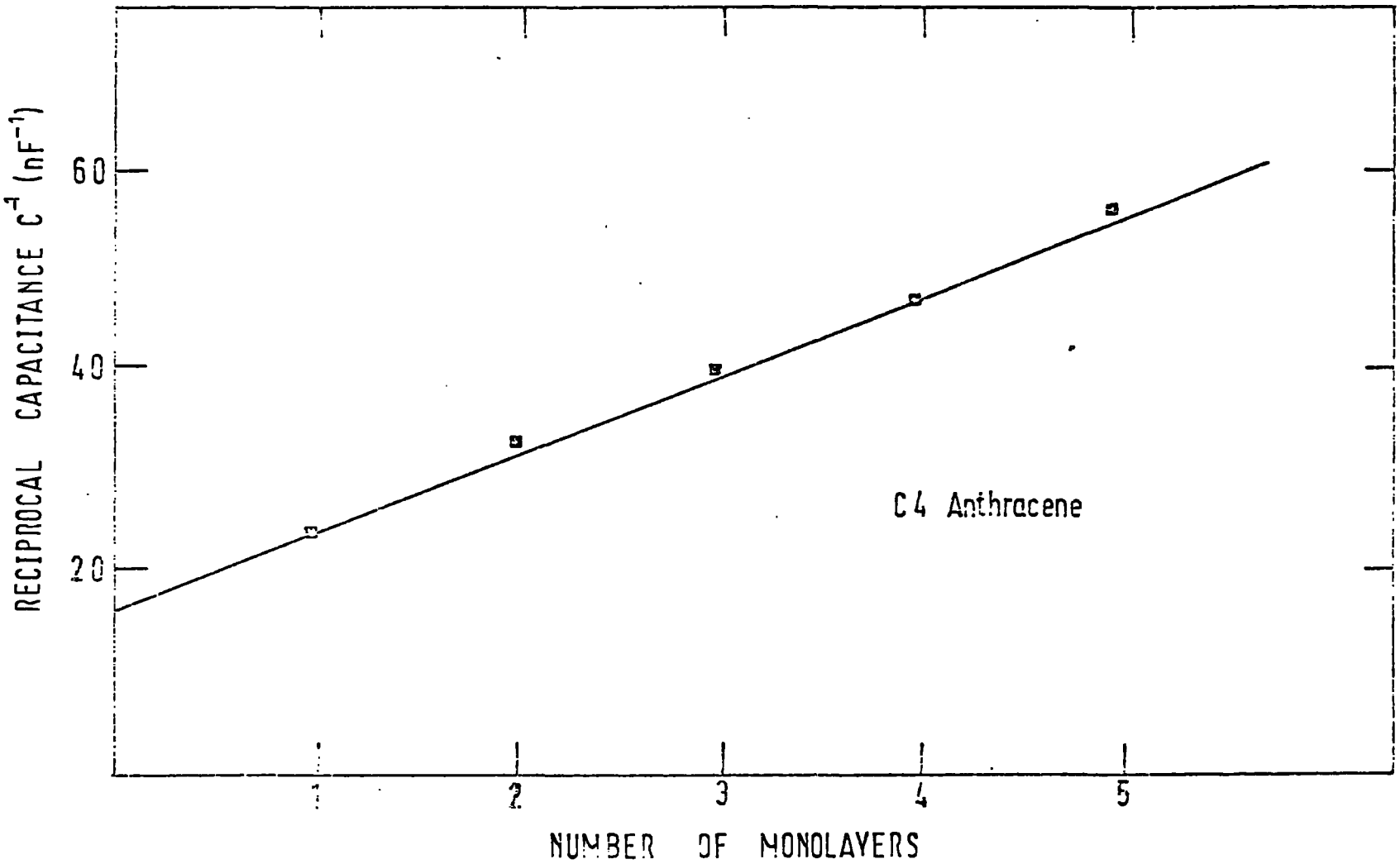

Fig. 6.9 Graph of reciprocal capacitance versus the number of monolayers for a C4 anthracene film. (16)

The non-zero intercept on the capacitance axis suggests the existence of an extra capacitance in the structure. Since the films were deposited on an aluminium-coated substrate, it is reasonable to assume that this extra capacitance is due to aluminium oxide. When this capacitance is included, the total capacitance per unit area may be expressed as;

$$C^{-1} = (\varepsilon_o)^{-1} \quad \frac{d_{ox}}{\varepsilon_{ox}} + \frac{Nd}{\varepsilon} \qquad (1)$$

where N is the number of layers and ε the dielectric constant of each layer.

Measurements were also performed to check the variation of capacitance as a function of frequency. A typical set of results, again for a C6 anthracene film, is displayed in Figure 6.10, from which it may be seen that the capacitance is almost independent of frequency in the range 40 - 10,000 Hz. This behaviour is indicative of a good contact to the specimen.

6.3.2 Conductance Data

Typical ac. conductivity data for a C6 anthracene film are displayed in Figure 6.11. The film exhibits a frequency dependent conductivity with $G \propto \omega^n$. Below 10 KHz, n is approximately equal to 0.8, whereas above that frequency, it takes on a value in the region of 2.0. Street et al [19] have attributed the latter dependence to a series resistance associated with the electrodes. According to these authors, the conductance depends on the various parameters such that;

$$G \propto \omega^2 C_x^2 R_o \qquad (2)$$

where G is the conductance of the specimen, C_x the sample's capacitance and R_o the series resistance. Thus provided the specimen's capacitance and the series resistance are frequency independent, the

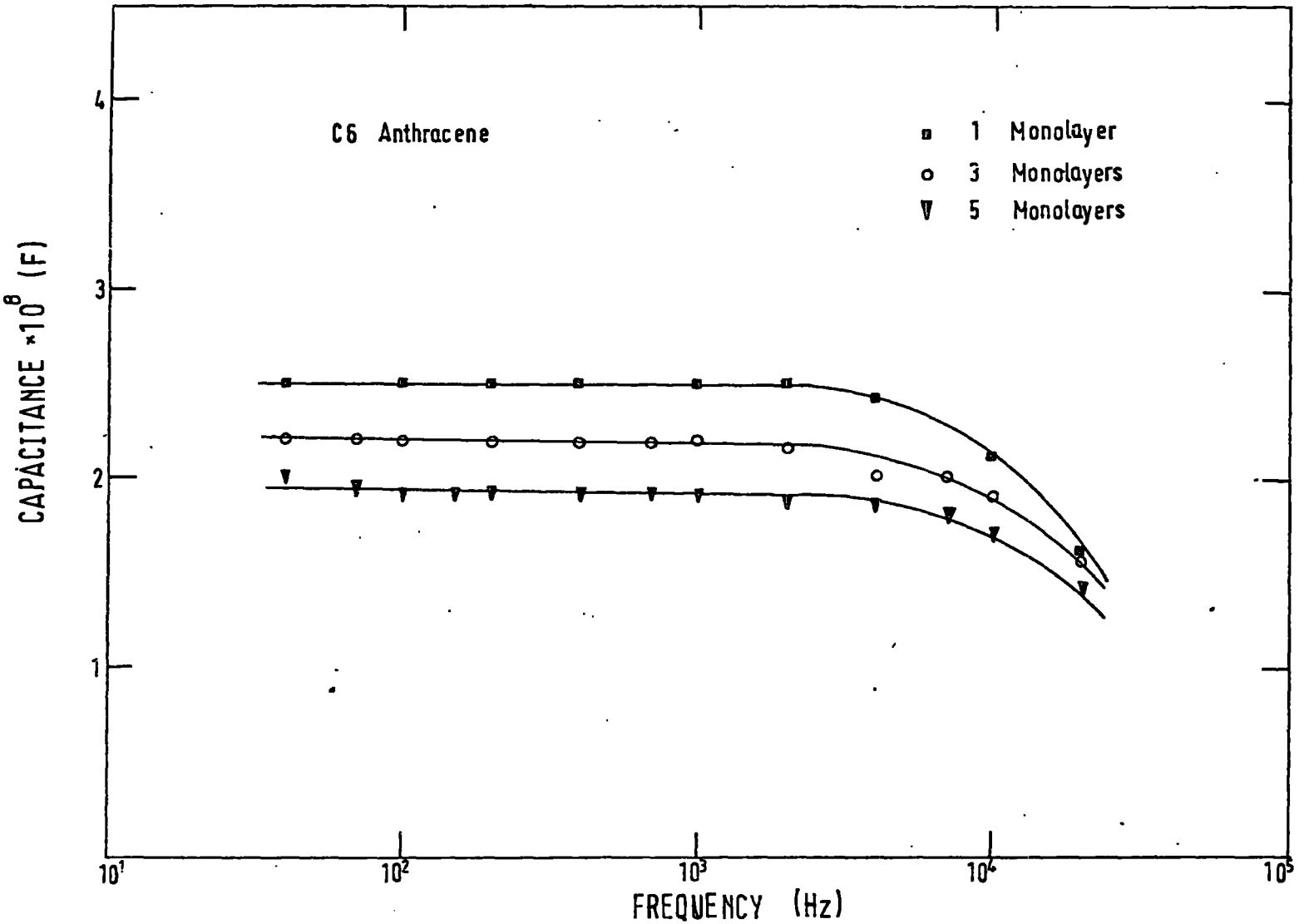

Fig. 6.10 Frequency dependence of the capacitance of a C6 anthracene specimen for several film thicknesses.

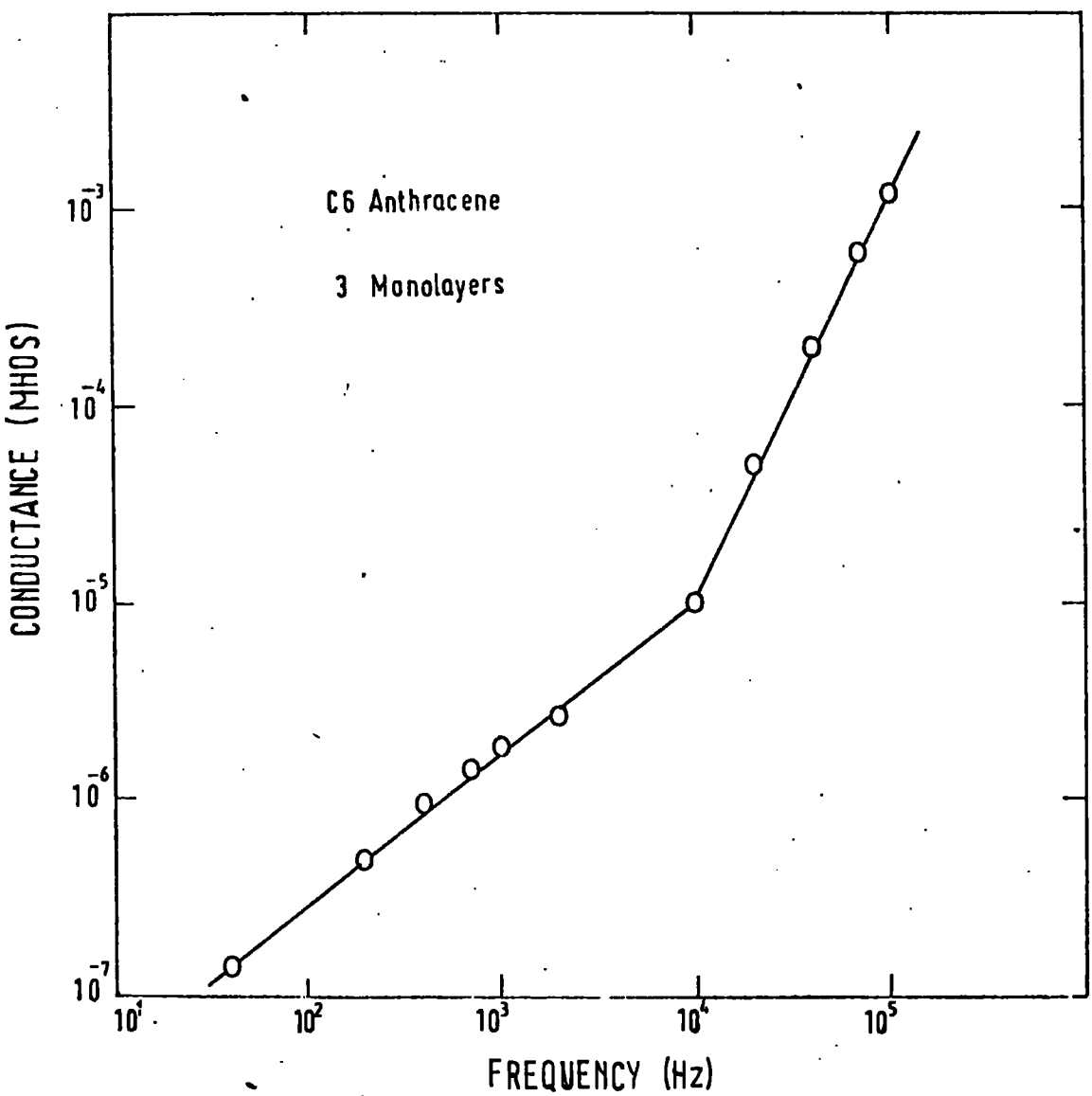

Fig. 6.11 Conductance of a 3 layer C6 anthracene film as a function of frequency at room temperature.

conductance is proportional to ω^2. A close inspection of Figure 6.11 however, shows that it is possible to draw another line of slightly lower slope through the high frequency points. This could be explained if the specimen's capacitance was slightly frequency dependent. A more detailed inspection of Figure 6.10 shows that the capacitance of the films does indeed decrease slightly as the frequency is increased.

The almost linear power law dependence in the low frequency region has previously been reported by several authors, including Nathoo and Jonscher [10] and Roberts et al [13]. This type of behaviour is usually associated with disordered materials. The above results confirm the conclusion of Nathoo and Jonscher that frequency dependent conduction is a general feature of low mobility hopping-type systems and is not confined to disordered solids. Recently, Carcem and Jonscher [20] have attributed the observed frequency dependence in Langmuir films to phase transitions arising from the dipolar COOH groups.

6.3.3 DC. Conductivity Results And Discussion

The dc. conductivities of the lightly substituted anthracene films were studied extensively before any electroabsorption measurements were performed. While some experiments were carried out on C8 and C12 specimens, the study concentrated on the C6 and C4 samples, since these films were expected to exhibit more interesting properties.

Figure 6.12 displays conductivity data for a 51 layer C4 anthracene film, for the case of conduction through the sample. The data were recorded at room temperature. The specimen exhibits a linear current-voltage relationship up to a field of approximately 1.8×10^8 V/m. This is believed to be the first time an Ohmic ($J \propto V$) curve has been observed in Langmuir films, and is in marked contrast to the conduction process in fatty acid films. These films, such as cadmium arachidate or cadmium stearate, usually display a bulk barrier limited conduction mechanism, with $J \propto V^{\frac{1}{2}}$ [13].

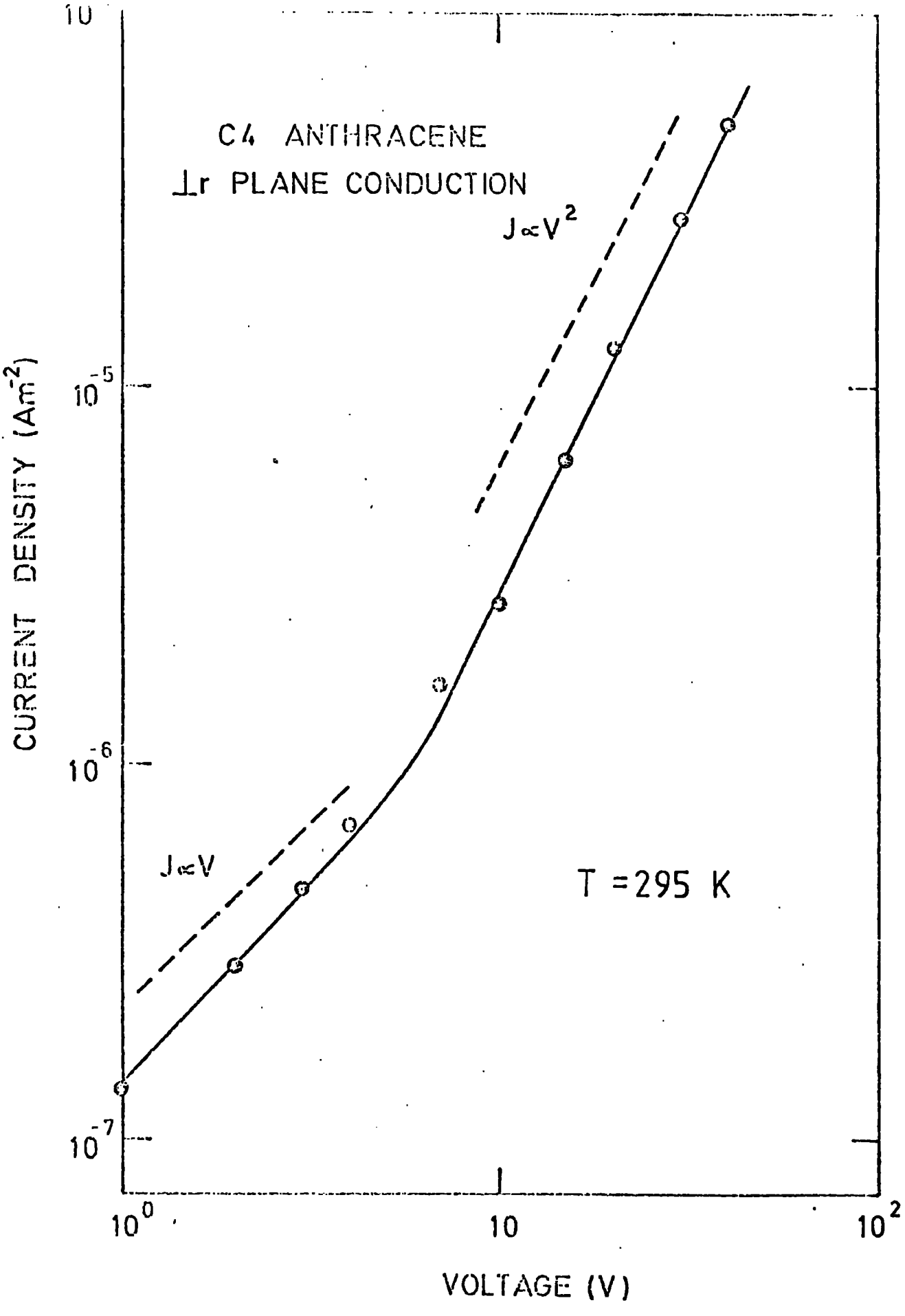

Fig. 6.12

Current-voltage relationship for a 51 layer C4 anthracene film at room temperature.

Above a field of about 10^8 V/m charge injection may occur, as shown in Figure 6.12. In this case, a quadratic dependence of current on voltage is obtained. Some specimens, however, exhibited a conduction process with $J \propto V^3$ as shown in Figure 6.13. This behaviour is characteristic of a double injection process.

As one might expect, each conduction mechanism was found to have a particular activation energy associated with it. An accurate value for the temperature dependence of the conductivity in the linear region may be obtained from Figure 6.14, where an activation energy for a 51 layer C4 film is displayed. An analysis of this data leads to a value of $\Delta E = 0.73$ eV. Similar data for the $J \propto V^2$ and $J \propto V^3$ regions are shown in Figure 6.15. For these regions $\Delta E = 0.43$ eV and 0.17 eV respectively. It is thus clear that the activation energies recorded in the space-charge injection regions are less than for the ohmic region, in agreement with the theory of Roberts and Schmidlin [21].

The information presented to date has been concerned with electrical conduction through the multilayer films. However, in view of the structure of the films, one might expect an anisotropy in the multilayers' conductivities. This is indeed observed and is remarkably high. Evidence for this is displayed in Figure 6.16 where data are presented for conduction along the plane of a 20 layer C4 anthracene film. The electrode configuration used in these measurements is illustrated in Figure 6.17. Considerable care was taken to ensure that the current recorded during the measurement of this curve was a true in-plane current, as opposed to a current through the film and along the base. The principal precaution taken was to deposit the C4 anthracene on top of about 3 monolayers of cadmium arachidate, which were previously deposited on an aluminium-coated glass slide. Since the cadmium arachidate presented an extremely resistive path along the base of the film, this ensured that the measured current was due to a true in-plane conduction mechanism. An additional precaution was to carry out measurements with different electrode spacings and confirm that the current was inversely proportional to

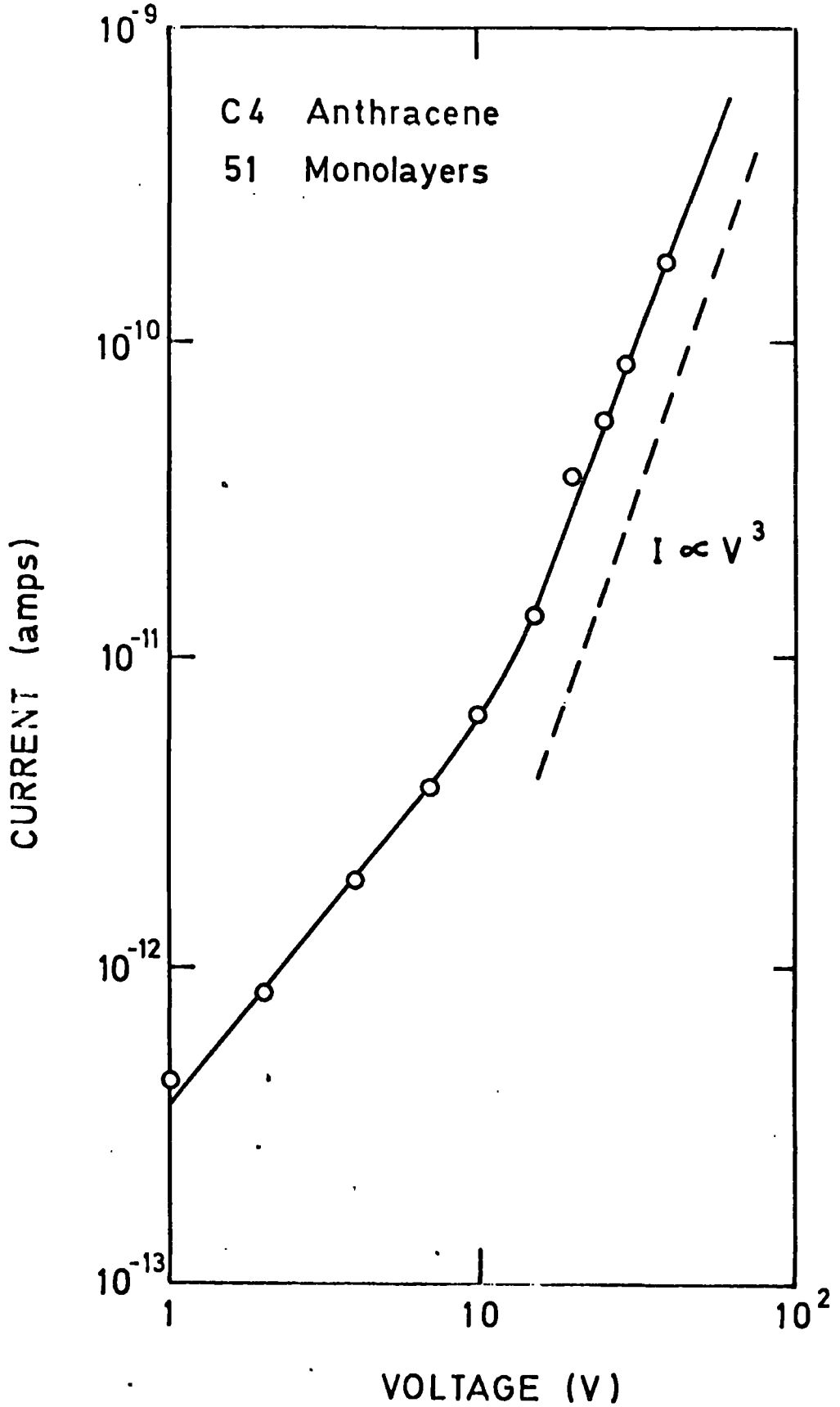

Fig. 6.13 Current-voltage graph for a 51 layer C4 anthracene film showing a $J \propto V$ to $J \propto V^3$ transition.

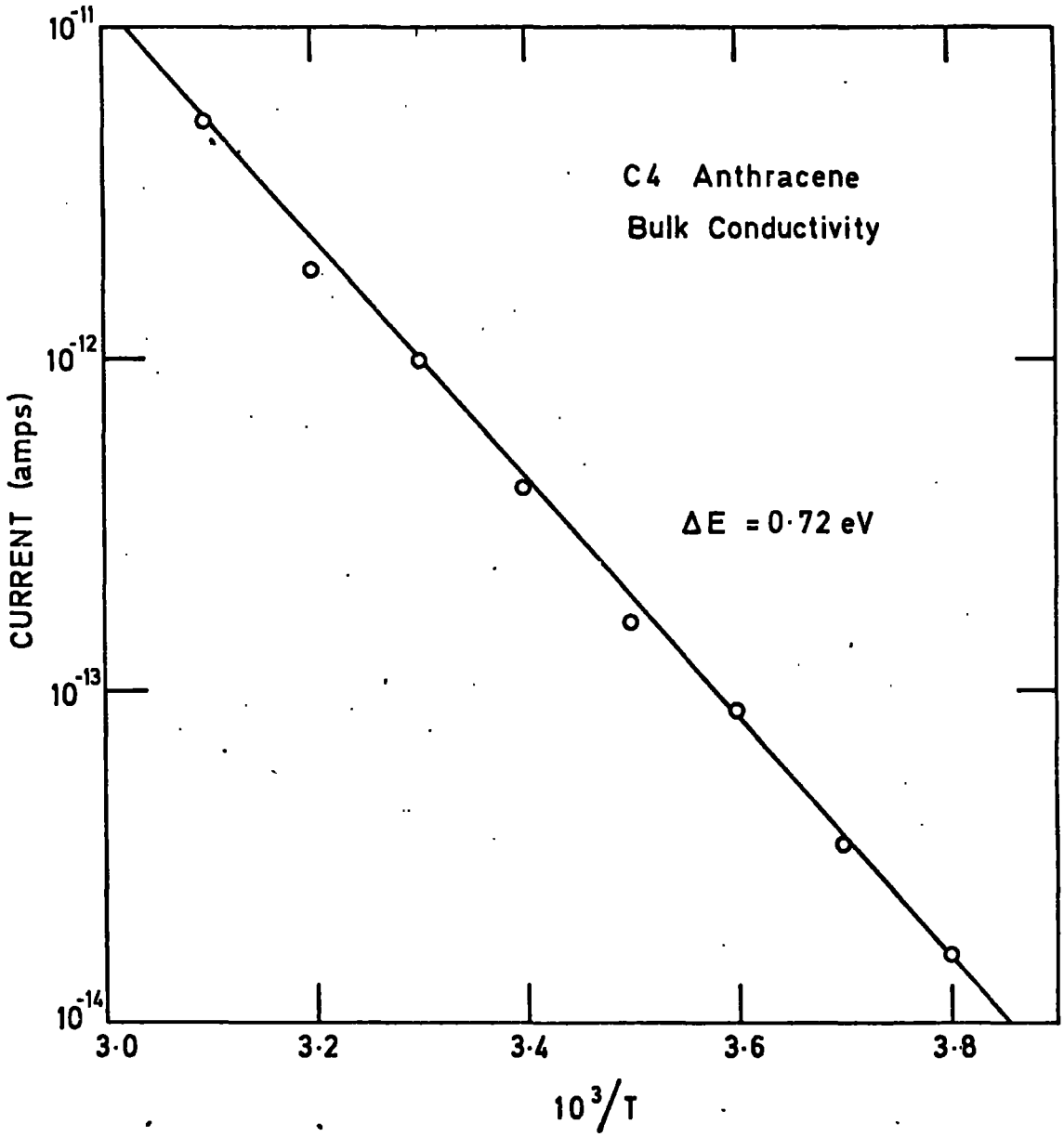

Fig. 6.14 Ohmic activation energy for a C4 anthracene specimen for the case of conduction perpendicular to the plane of the film.

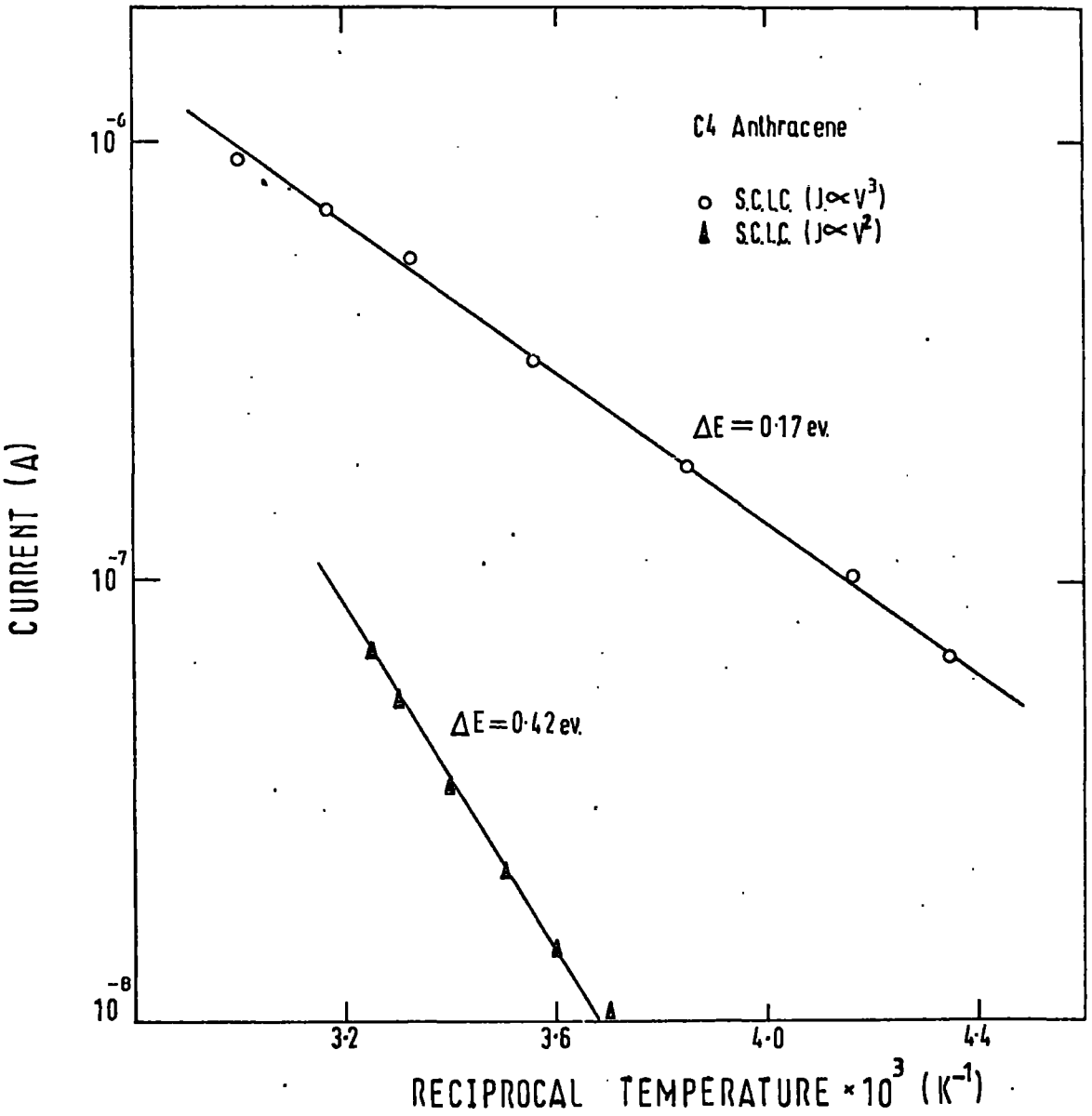

Fig. 6.15 Activation energies for a C4 anthracene specimen in the $J \propto V^2$ and $J \propto V^3$ regions.

the distance between the electrodes.

An analysis of the data presented in Figure 6.16, in conjunction with the results shown in Figure 6.12, leads to the conclusion that the in-plane conductivity is approximately 10^8 times greater than the through-plane conductivity. However, despite this large anisotropy the activation energy for in-plane conduction is similar to that for bulk (through-plane) conduction as shown in Figure 6.18. This graph leads to a value of $\Delta E = 0.72$ eV for the in-plane activation energy, in clear agreement with the value obtained from Figure 6.14 for the through-plane case. The dc. conductivity results for the C4 specimens are summarized in the insert of Figure 6.16.

In addition to the measurements performed on the C4 films, data were recorded on some C8 and C12 anthracene specimens. The results of these experiments are summarized in Figures 6.19 and 6.20 for a 59 layer C8 and 20 layer C12 film respectively. The main result of these measurements was to confirm the extremely highly insulating behaviour of these materials.

As previously mentioned, the existence of an Ohmic conduction mechanism in Langmuir films is quite unusual in that practically all Langmuir film studies to date have recorded a $J \propto V^{\frac{1}{2}}$ current-voltage relationship. The C4 dc. conductivity data may be explained in terms of a model proposed by Eley and Parfitt [22]. The theory assumes that charge transfer between one molecule and its neighbour occurs by tunnelling. The model is based on the potential box description of an organic semiconductor, and may be understood with reference to Figure 6.21. In this diagram, three adjacent similar molecules are depicted:- (a) in the absence of an applied voltage gradient and (b) after application of a voltage V and after excitation of an electron in the central molecule. On excitation of the electron, both the electron and the hole can tunnel from one molecule to another, as shown in Figure 6.21 (b).

The drift velocity of the electron is proportional to the product

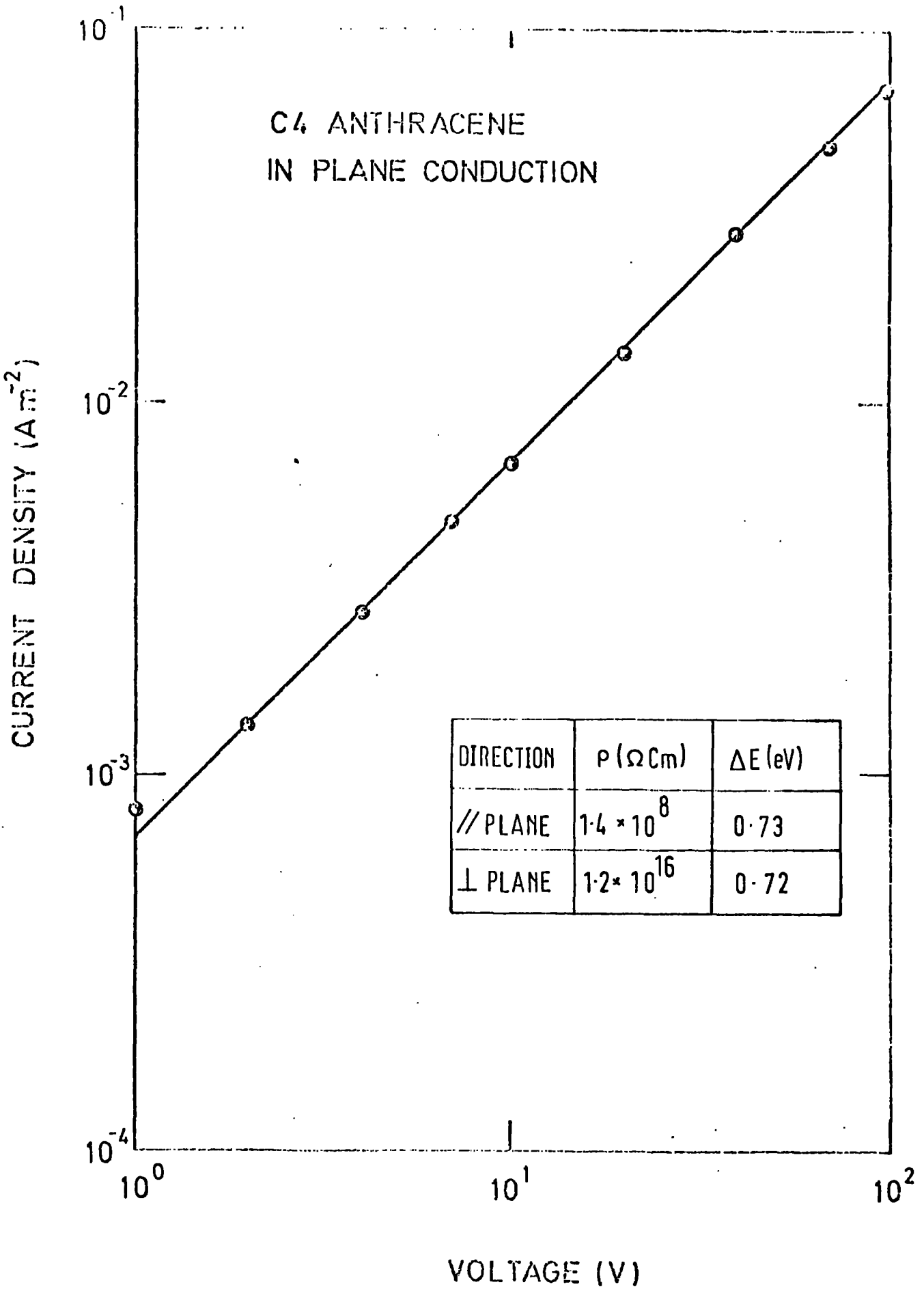

Fig. 6.16 Graph of current density versus voltage for a C4 anthracene film, for the case of conduction in the plane of the specimen. The insert summarizes the dc. conductivity results obtained on the C4 anthracene samples.

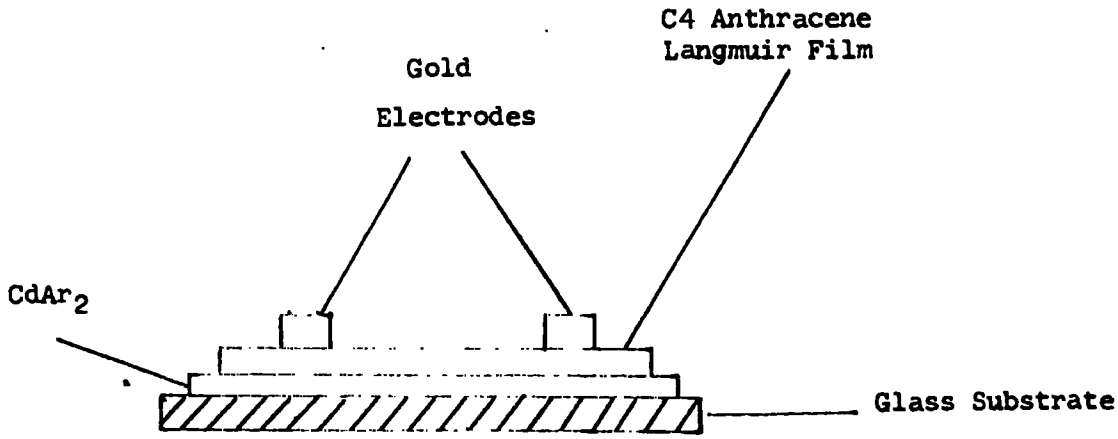

Fig. 6.17
Illustration of the sample configuration for the data of Fig. 6.16 and 6.18.

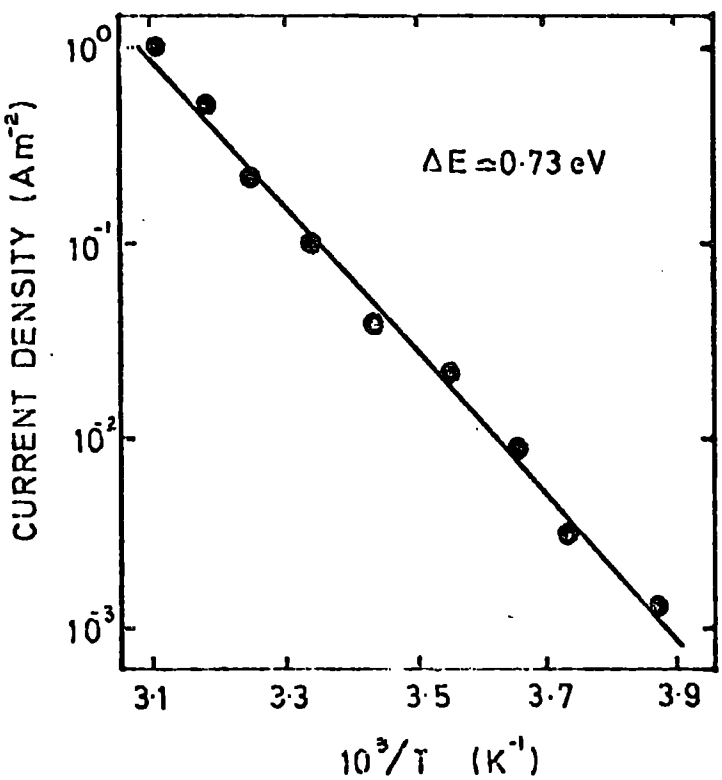

Fig. 6.18
Ohmic activation energy due to in-plane conduction for a C4 anthracene multilayer.

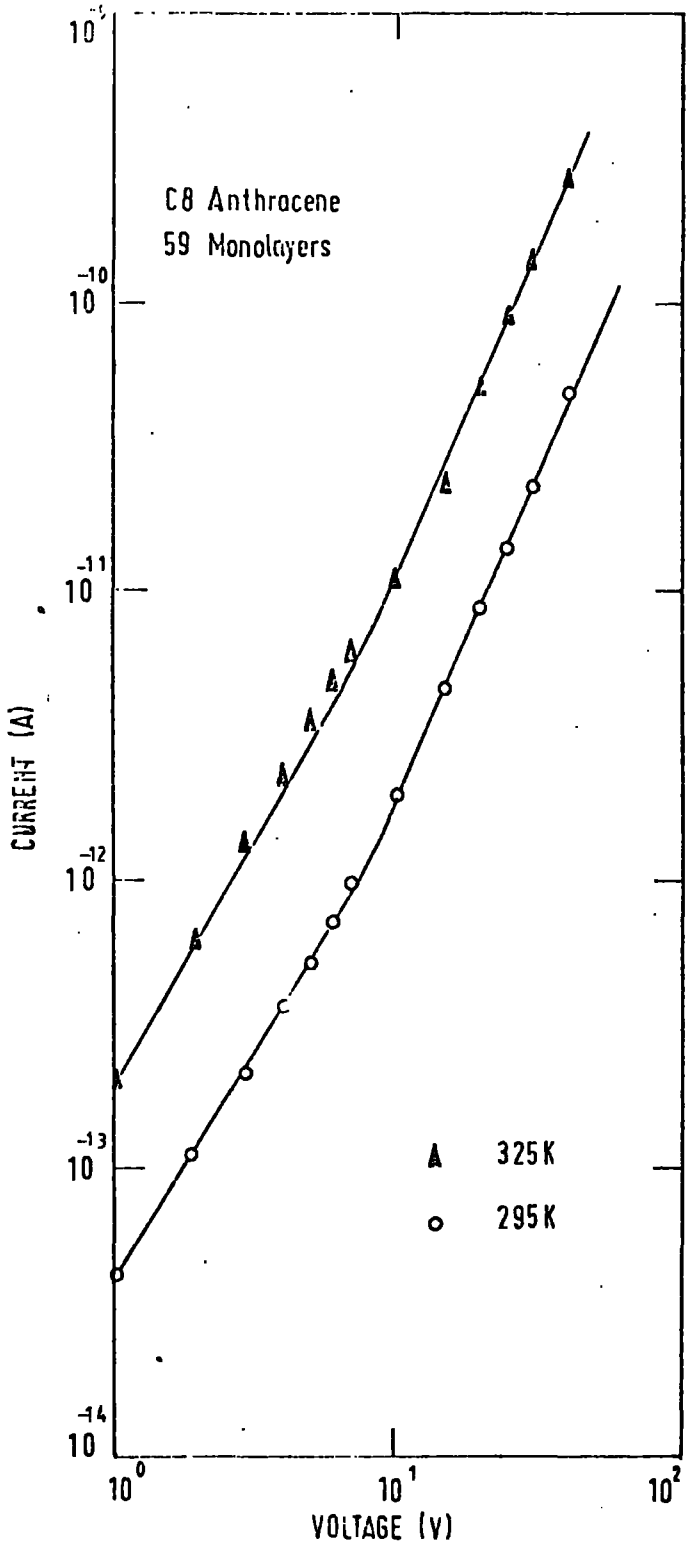

Fig. 6.19 Current-voltage data for a 59 layer C8 anthracene specimen at two different temperatures.

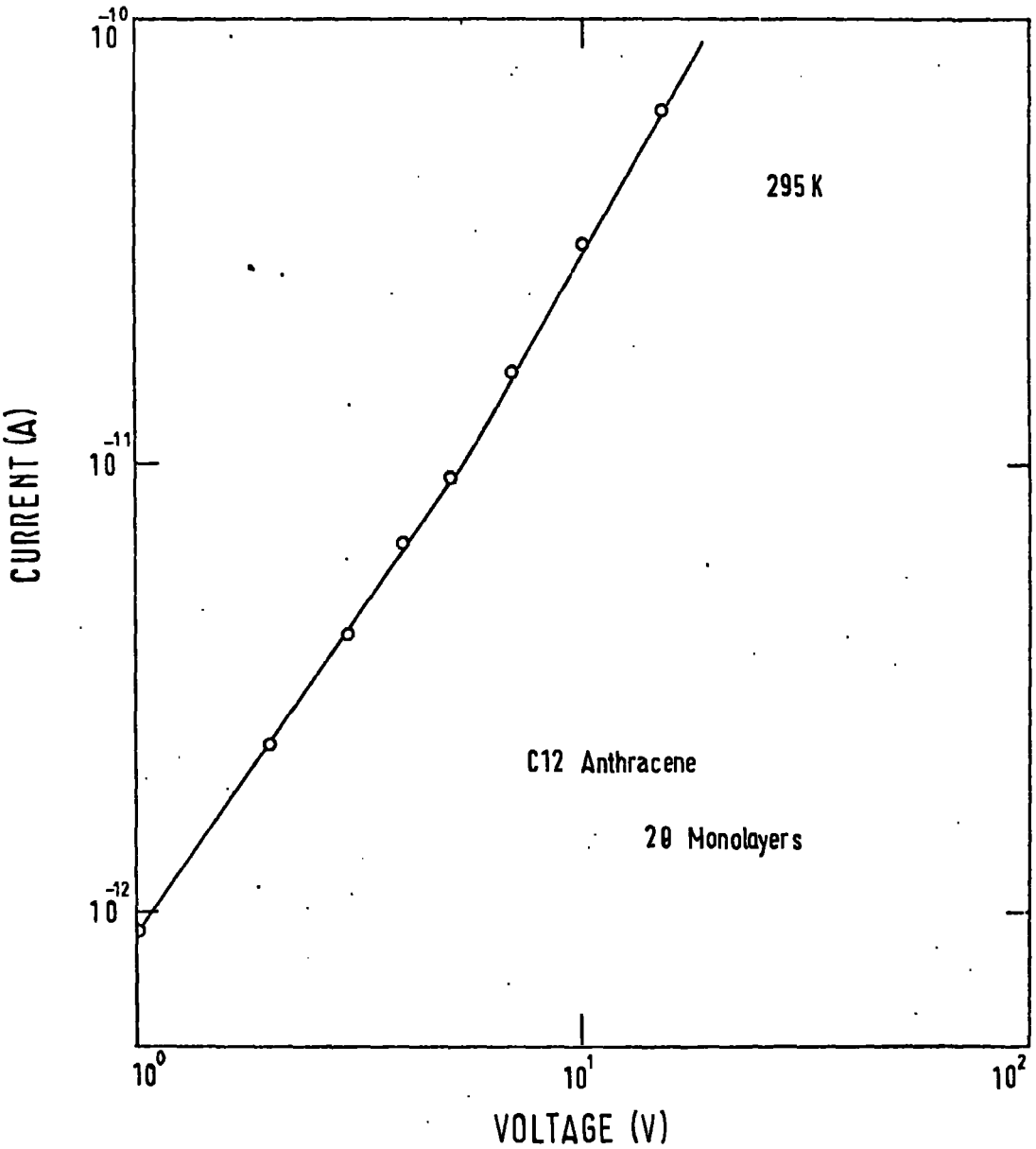

Fig. 6.20 DC. conductivity data for a 20 layer C12 anthracene film.

of the number of times it strikes the barrier and the probability of penetration. It may be expressed as:

$$v_{de} = (v_e/2l)(a + 1)(P_f - P_r) \qquad (3)$$

where

v_e is the electron velocity between the potential walls;

l is the distance across the well;

a is the barrier width;

P_f is the probability of penetrating the barrier in the direction of the field;

and

P_r is the probability of penetrating the barrier in the direction opposite to the field.

The current density is given by:

$$i = n\, e\, v_{de} \qquad (4)$$

Eley and Willis [23] introduced the following expression, from conventional band theory, for n, the concentration of excited electrons;

$$n = \left[2(2\pi kT)^{3/2} / h^3\right].(m_e^* m_h^*)^{3/4}. \exp(-E/2kT) \qquad (5)$$

where

m_e^* is the effective mass of electrons

m_h^* is the effective mass of holes

Using this expression, one may write:

$$i = \left[2(2\pi m_e^* kT)^{3/2} / h^3\right]\left[\exp(-E/2kT)\right] \times (N/2 + 1)h(a+1)(P_f - P_r)4l^2 m_e^* \quad (6)$$

where N is the number of conjugated π-electrons in a molecule.

This equation is of the form:

$$i = \sigma_o V \exp(-E/2kT) \quad (7)$$

For square barriers, Eley and Willis, utilizing the results of Kauzmann [24], predicted that Ohm's law should be obeyed to within about 1% for fields up to about 5×10^7 V/cm.

A consideration of the structure of the C4 anthracene multilayers leads to the conclusion that the above model is applicable to them. The multilayers consist of a series of semiconducting layers, separated by regions of high resistivity, approximately 0.6 nm. thick. Accordingly even in the low voltage region, electric fields of the order of 10^6 V/cm are applied across each insulating section and under these conditions tunnelling currents may occur.

If one assumes the Eley/Parfitt model is applicable, it is not surprising that a similar activation energy is recorded for both in-plane and through-plane conduction. This quantity is then related only to the thermal generation of carriers within the semiconducting region, since the tunnelling mechanism is only weakly temperature dependent. A similar (ΔE = 0.73 eV) activation energy has been recorded for single crystal anthracene and has been attributed to hole conduction.

The super-ohmic current-voltage curves, displayed in Figures 6.12 and 6.13, may be interpreted in terms of injection from one or both

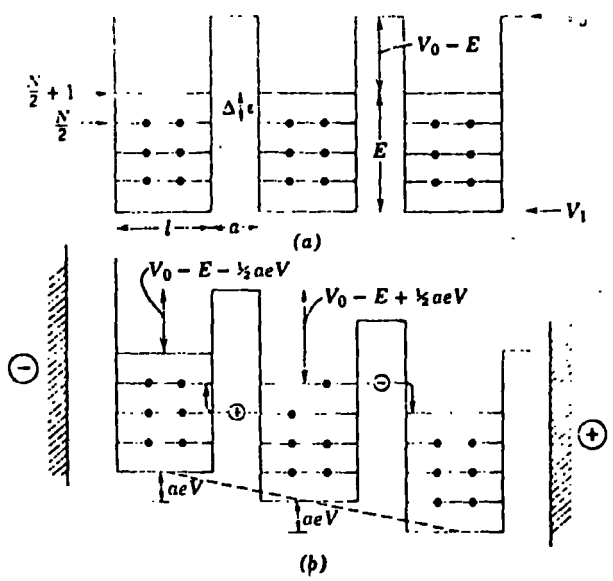

Fig. 6.21 Potential box model of an organic semiconductor.

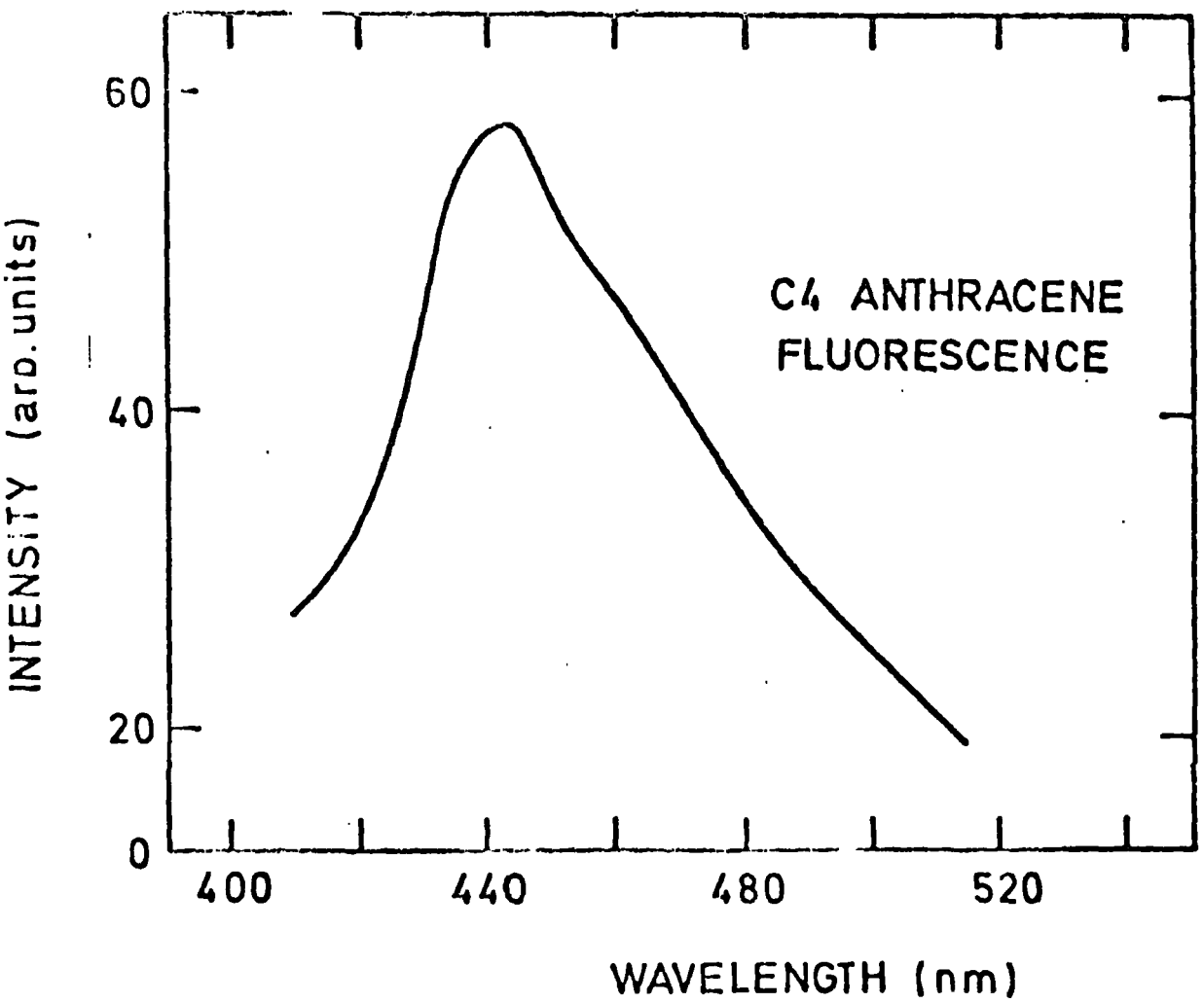

Fig. 6.22 Room temperature fluorescence spectrum of a C4 film.

electrodes. Previous work on tetracene [25] and pentacene [26] evaporated thin films, as well as on anthracene single crystals have verified that hole injection occurs from the Au contact. It is reasonable to assume this is happening in our case as well. The $J \propto V^3$ curve is indicative of a double injection mechanism, and accordingly points to the injection of minority carriers from the Al contact. In this case, however, the electrons must be injected through the Al_2O_3 film and so this process is likely to be much less efficient than the hole injection process. Thus, depending on the nature and thickness of the Al_2O_3 film one might expect to observe either a $J \propto V^2$ or $J \propto V^3$ current-voltage curve.

6.3.4 Fluorescence Results

The room temperature fluorescence spectrum of a C4 anthracene multilayer film is shown in Figure 6.22. The data were obtained using exciting light of wavelength 364 nm. The curve is interpreted in terms of an excimeric fluorescence mechanism in view of the distinctly structureless emission peak. It is interesting to note that conventional crystalline anthracene displays "monomer" fluorescence. It has been suggested [27], that the discrepancy is due to differing degrees of $\pi - \pi$ interaction. In crystalline anthracene $\pi - \pi$ interaction between nearest neighbours is minimal, due to the lack of symmetry. This position is different in C4 anthracene multilayers where the nuclei are encouraged to align themselves parallel to each other, resulting in a greater level of π– electron overlap. Accordingly, the C4 anthracene films are closely related to a material such as perylene, which exhibits excimeric emission. In contrast, a solution of substituted anthracene displays sharply defined peaks, a situation which one might expect from the above argument.

6.3.5 Electroluminescence Results

It is well known that single crystals and evaporated films of anthracene may emit light under the application of large electric fields. Indeed, it has long been recognised that anthracene, in view of its high

fluorescence efficiency, may possibly have applications in the area of large scale electroluminescence panels. Electroluminescence from evaporated films of anthracene is often found when the current-voltage relationship takes on the form shown in Figure 6.23. An analysis of this curve shows that it is composed of a low field $J \propto V^2$ region, a region in which the current rises extremely rapidly, and a high field $J \propto V^3$ region. The onset of electroluminescence is found to occur at the point where the current rises fastest, that is, at the onset of double injection.

For comparison, a current-voltage relationship occasionally found on our C4 anthracene films is also plotted in Figure 6.23. This curve is extremely similar to the evaporated film graph. Accordingly, it was not altogether unexpected when light emission was observed from our C4 anthracene multilayer films. Figure 6.24 illustrates the spectral dependence of the observed electroluminescence. A shoulder in the curve is observed where the fluorescence spectrum peaks. In addition, a rapid decrease in electroluminescence intensity occurs as the photon energy is increased. This behaviour has been recorded previously for a number of other materials and has been explained in terms of shallow trapping. The increase in emission intensity beyond 460 nm is possibly related to influences from the Al_2O_3. For example, electroluminescence in aluminium oxide has been observed by Pong et al [28] and has a somewhat similar long wavelength spectral dependence.

While no attempt was made to determine the conversion efficiency of the process, the emission was visible in a darkened room using a power input of 10^{-1} W m^{-2}. The intensity of the electroluminescence was found to decay rapidly with time, if a dc. field was used as the exciting medium. This is similar, as is the J-V curve, to the results obtained for both evaporated films and single crystals of anthracene. The observed electroluminescence decay for a 69 layer C4 film is also illustrated in Figure 6.24. In agreement with previous work on evaporated films of anthracene, it was found that the lifetime of the emission could be extended by the application of an ac. field of suitable frequency, which is thought to reduce the polarization within the sample.

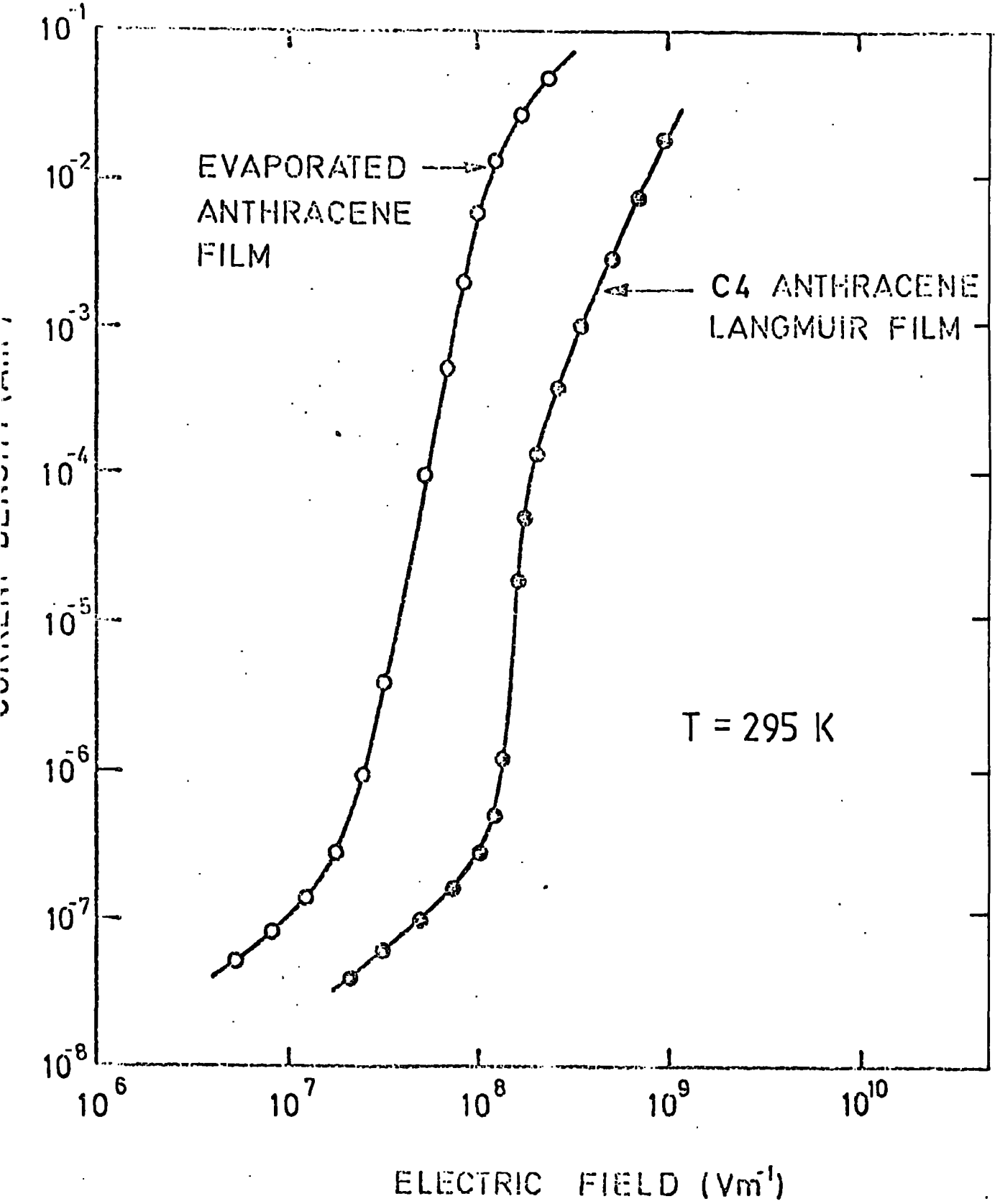

Fig. 6.23 Comparison of the current-voltage relationship obtained for an evaporated anthracene film with one occasionally found for the C4 anthracene specimens.

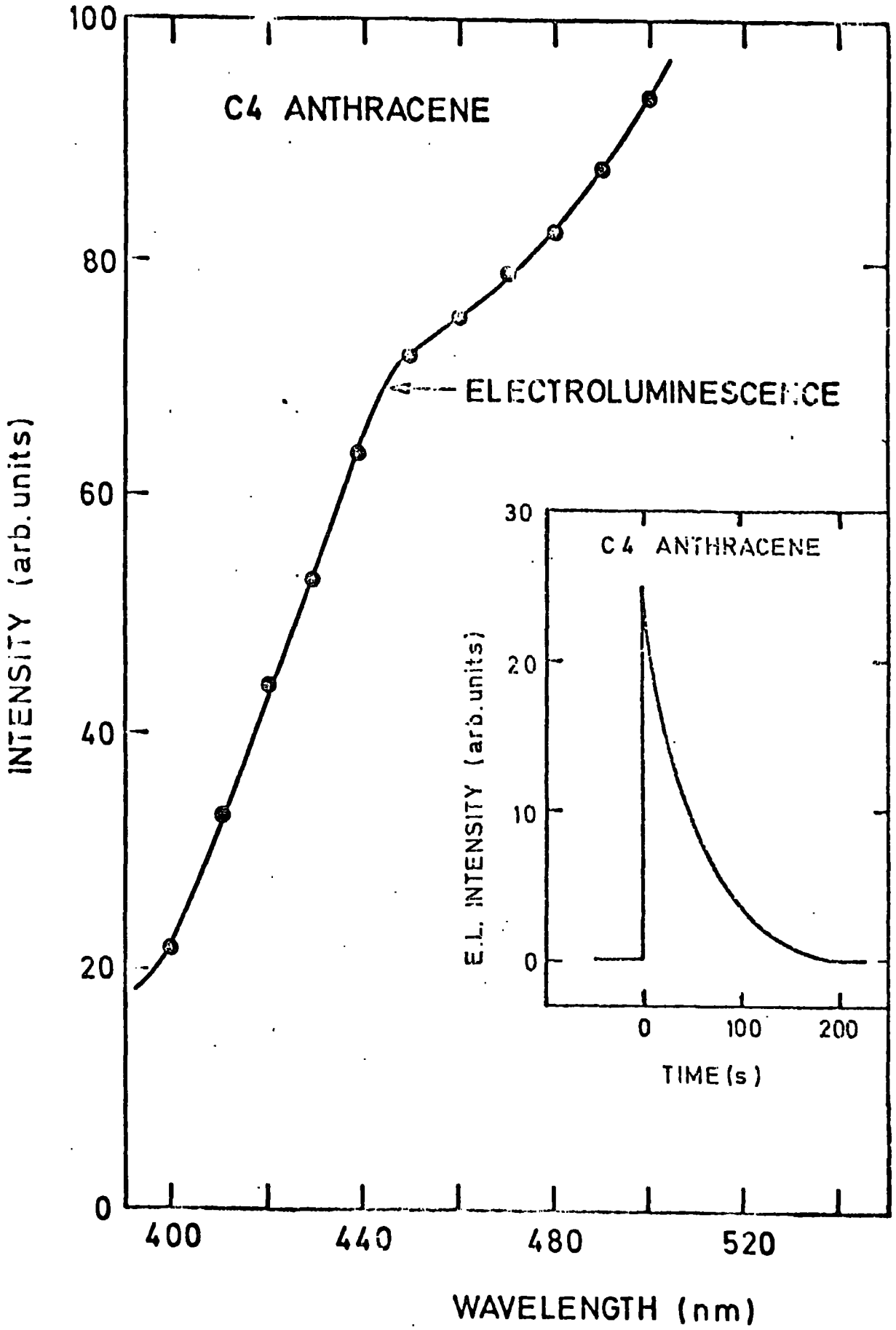

Fig. 6.24 Spectral dependence of the electroluminescence obtained from a C4 anthracene film under an alternating electric field of 1.6×10^6 V/cm. The insert shows the decay of the electroluminescence when excited with a dc. electric field.

Light emission was only observed from the C4 multilayer films which exhibited an almost vertical rise in the current-voltage plots. The electroluminescence is assumed to be due to recombination of charge carriers injected from the electrodes. In the discussion concerning dc. conductivity given previously, it was decided that holes were being injected from the gold electrodes, with electrons being injected from the aluminium. While the efficiency of the electroluminescence from the multilayer films is estimated to be much higher than for evaporated anthracene films, the limiting factor is almost certainly the injection of minority carriers from the aluminium electrode. The current-voltage data previously discussed have shown that the $J \propto V^2$ currents are quite high, thus demonstrating that the gold electrodes are efficient hole injectors. Accordingly, the overall efficiency of the electroluminescence is probably dependent upon the nature of the Al_2O_3 film. In particular, the thickness of this film is likely to be critical. A program of research on this topic would prove very useful.

No electroluminescence was found from the C8 or C12 multilayer films.

6.3.6 Optical Absorption And Photo-Conductivity Results

The optical absorption spectrum of a C4 anthracene multilayer film in the region of the first absorption band is illustrated in Figure 6.25 (a). These data were recorded at room temperature on a 69 layer sample deposited upon a glass substrate. The spectrum is similar to that of a solution of the derivative and thus demonstrates that a multilayer film of the anthracene derivative has indeed been deposited. The weak nature of the inter-molecular interactions in the molecular crystals is also evident from this result.

It is of interest to compare the optical absorption of the C4 anthracene with that of an evaporated anthracene film (Figure 6.25 (b)). It is clear that a shift in each of the vibronic bands of the substituted anthracene occurs in the direction of longer wavelengths. The

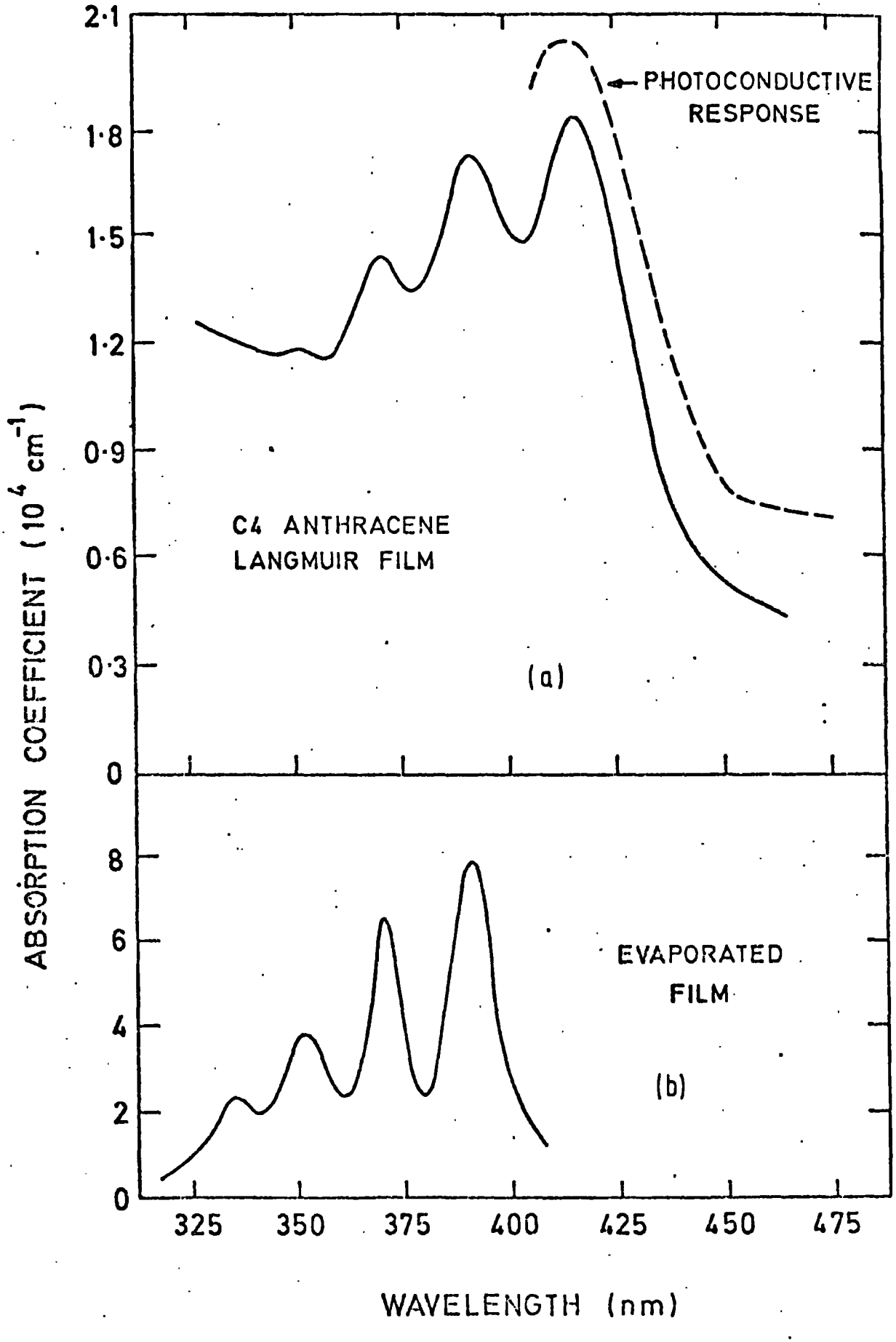

Fig. 6.25 Optical absorption of a C4 anthracene film and an evaporated anthracene film as a function of photon energy. The spectral dependence of the photoconductivity is also illustrated.

magnitude of the wavelength shift is approximately 25 nm. This occurs due to a disturbance of the anthracene nuclei's environment. The C6, C8 and C12 films all exhibit the same vibronic peak pattern and are similarly shifted to lower energies.

The absorption spectrum is due to the $A_{1g} \longrightarrow B_{2u}$ transition, along the shorter in-plane molecular axis. The existence of appreciable optical absorption in the C4 anthracene films indicate further that the anthracene nuclei in the multilayers are tilted away from the direction normal to the film, instead of being stacked vertically. This fact has previously been deduced from x-ray analysis.

The increase in the conductivity of the C4 multilayers upon illumination with suitable radiation is also shown in Figure 6.25. This is believed to be the first observation of photoconductivity in any Langmuir film. The data were recorded at room temperature using a sandwich configuration. Illumination was through the aluminium electrode. The magnitude of the photocurrent has been corrected to allow for the spectral response of the source-grating combination. The curve indicates that the photoconductive response follows the shape of the long wavelength absorption curve namely, the transitions from the ground state to the first singlet state. A resemblance between the spectral response of the photocurrent and the absorption spectrum has previously been recorded for single crystal anthracene, using a surface cell configuration [29].

6.3.7 Electroabsorption Results And Discussion

The principal objective of the work recorded in this chapter was to measure the effects of large electric fields upon the optical absorption properties of the anthracene multilayer films. All the experimental data presented to date were collected with the aim of providing background information concerning the materials under investigation. In particular, these supplementary data were recorded in order to be aware of, and if possible avoid, certain pitfalls, such as space-charge effects, which would lead to an incorrect analysis of the electroabsorption

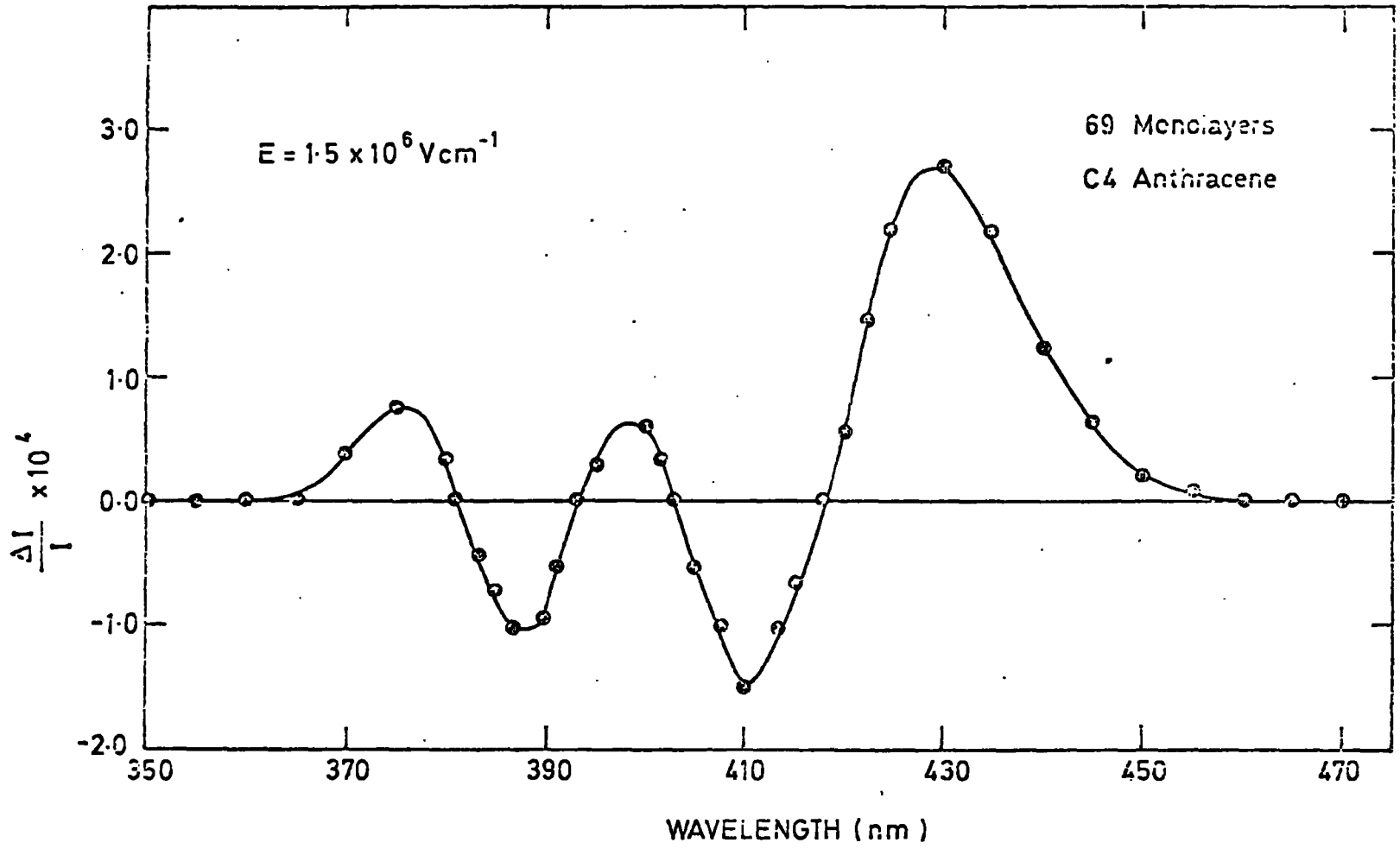

Fig. 6.26 Fractional change in transmitted light intensity of a 69 layer C4 anthracene film due to an electric field of 1.6 x 10^6 V/cm, at a frequency of 3 kHz.

results.

As previously discussed in Chapter II, the Stark effect is expected to be the dominant electroabsorption mechanism in these organic materials, in view of their large effective masses. Stark effect studies have previously been performed on anthracene molecules dispersed in an inert polystyrene matrix [30]. However, this procedure raises doubts concerning the field distribution within the specimen. This is believed to be the first report of an electroabsorption study in any Langmuir film.

A few minor changes were made to the experimental equipment in order to make the measurements possible. The 1.0 /um grating used for the III-V samples was replaced with one blazed at 0.5 /um. In addition, the optical filters were changed to those appropriate for the spectral range 300-600 nm. Apart from these alterations the equipment was essentially unchanged.

Electroabsorption data obtained at room temperature on a 69 layer C4 film are displayed in Figure 6.26. The graph shows the change in absorption of the film as a function of photon energy, for an electric field of 1.6×10^8 V/m. The frequency of the sinusoidal field was 3 KHz, with the results being recorded at the first harmonic. This frequency was chosen to eliminate any effects due to polarization of the specimen, as previously discussed in Chapter V for indium phosphide and gallium arsenide. The electric field produces a uniform shift of the entire vibronic spectra to longer wavelengths. As a result, the electroabsorption spectra is an exact first derivative of the zero-field absorption curve. These data are extremely similar to those recorded by Blinov et al for evaporated tetracene films, as illustrated previously in Figure 2.18. The spectra may thus be interpreted in terms of the quadratic Stark effect of localized excitations in the anthracene molecule. Confirmation of this conclusion is presented in Figure 6.27, where the field dependence of the absorption change is shown to be quadratic in nature.

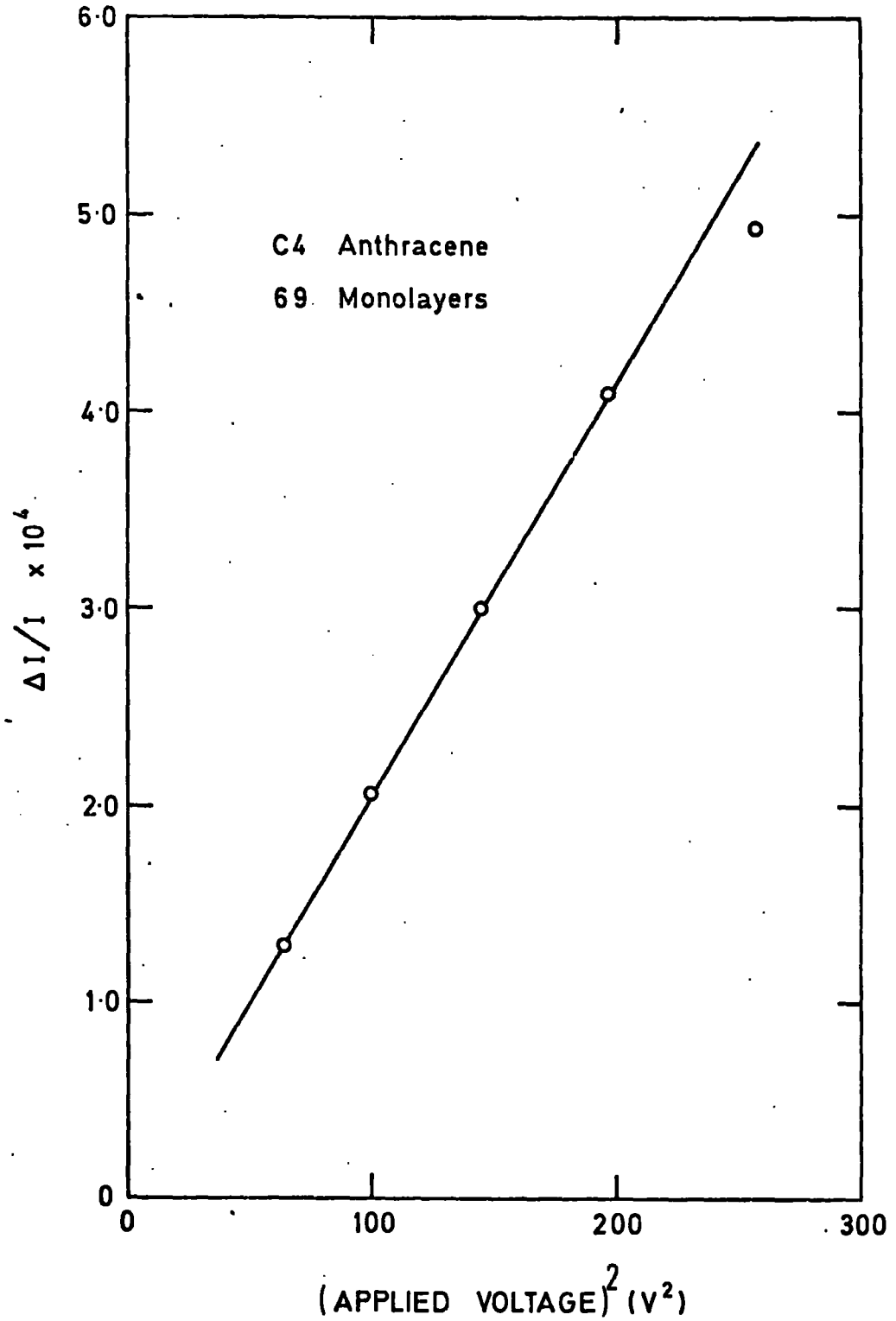

Fig. 6.27 Dependence of the fractional change in transmitted light intensity of a C4 film upon the square of the electric field.

An investigation was performed to determine if the magnitude of the absorption change depended on the frequency of the applied electric field. Figure 6.28 shows electroabsorption data recorded at a frequency of 300 Hz on the same specimen as discussed above. It is evident, by comparison with Figure 6.26, that a reduction in the magnitude of each peak has occurred, except the one at 388 nm which has increased. However, the information concerning this last peak is not believed to be very accurate since electrical noise at the 300 Hz frequency was substantial in this spectral area, and indeed prevented the extension of the measurements beyond 375 nm. In view of this fact, and the information previously obtained on the III-V materials, all subsequent electroabsorption measurements were performed at frequencies around 3 kHz.

Using the data recorded above, it is possible to calculate the difference in static polarizability between the excited and ground states of the anthracene molecule. This calculation may be performed by the application of equation (49) quoted in Chapter II, namely;

$$\frac{\Delta I}{I} = \frac{1.15}{hc}\left[\frac{\varepsilon+2}{3}\right]^2\left[\lambda D + \lambda^2 \frac{dD}{d\lambda}\right]\Delta a\left[\frac{V^2}{d\sqrt{2}}\right] \qquad (8)$$

where d is the sample thickness, ε the dielectric constant, D the optical density and $\frac{V}{d}$ the applied electric field. As explained in Chapter II, this expression is only approximate, in view of the Lorentz correction. However, using parameters appropriate for C4 anthracene, the above expression leads to a value of $\Delta a = 36\ \text{Å}^3$ for the polarizability change in the region of the first singlet absorption. An identical result to this has previously been obtained by Kurzmach and Malley [30] for a number of substituted anthracenes dispersed in an inert matrix. Our results support the analysis of these authors who conclude that the static polarizability change, upon transition to the first excited singlet state, was independent of substitution at the 9, 10 position.

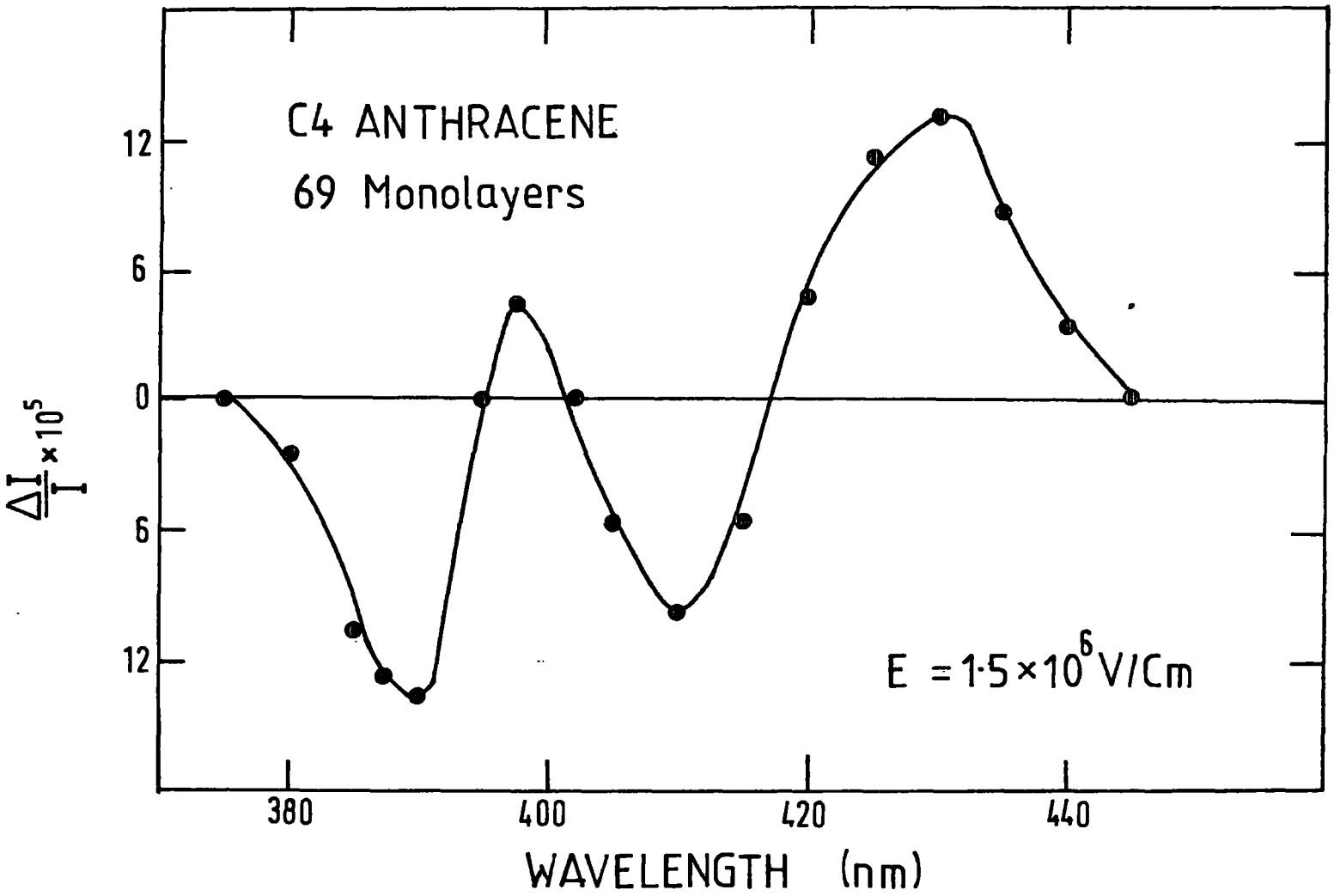

Fig. 6.28 Fractional change in the transmitted light intensity of the same C4 film as Fig. 6.26 but at a frequency of 300 Hz.

The conductivity studies performed on the C4 anthracene films were extremely useful in that the field at which space-charge injection was expected to occur could be calculated prior to the recording of any electroabsorption data. In all the electroabsorption experiments performed on these materials, attempts were made to remain in the linear region of the current-voltage curve, and thus avoid injection effects. The fact that the graph of absorption change versus the square of the applied electric field (Figure 6.27) extrapolates to zero, is an indication that space-charge effects were indeed avoided. Nevertheless if the Eley/Parfitt model of conduction in the C4 multilayers (discussed in section 6.3.3) is correct one might expect the field distribution within the specimens to take on a complicated form, since this model assumes regions of high and low resistivity. However, the fact that the polarizability value obtained from these experiments is in good agreement with the figure obtained from a completely different structure is a good indication that the field within the films is not too seriously distorted.

The electroluminescence effects reported earlier did not interfere with the accuracy of the electroabsorption measurements since the electroabsorption experiments were performed over long periods of time compared to the lifetime of the electroluminescence emission. The measurements previously performed to determine the photoconducting properties of the films also indicated that photocarrier effects were sufficiently negligible as to be ignored in the electroabsorption studies.

Attempts were made to determine the effects of polarized light upon the electroabsorption spectra. Preliminary data are displayed in Figure 6.29 where the fractional change in transmitted light intensity of a 69 layer C4 anthracene film is plotted as a function of photon energy for two orthogonal directions of polarized light. The resulting spectra are similar in shape to the data reported in Figure 6.26, but the magnitude of the peak at 430 nm in curve (b) appears to have decreased while the peak at 388 nm in curve (a) appears to have been enhanced. However, no definitive analysis of the results could be

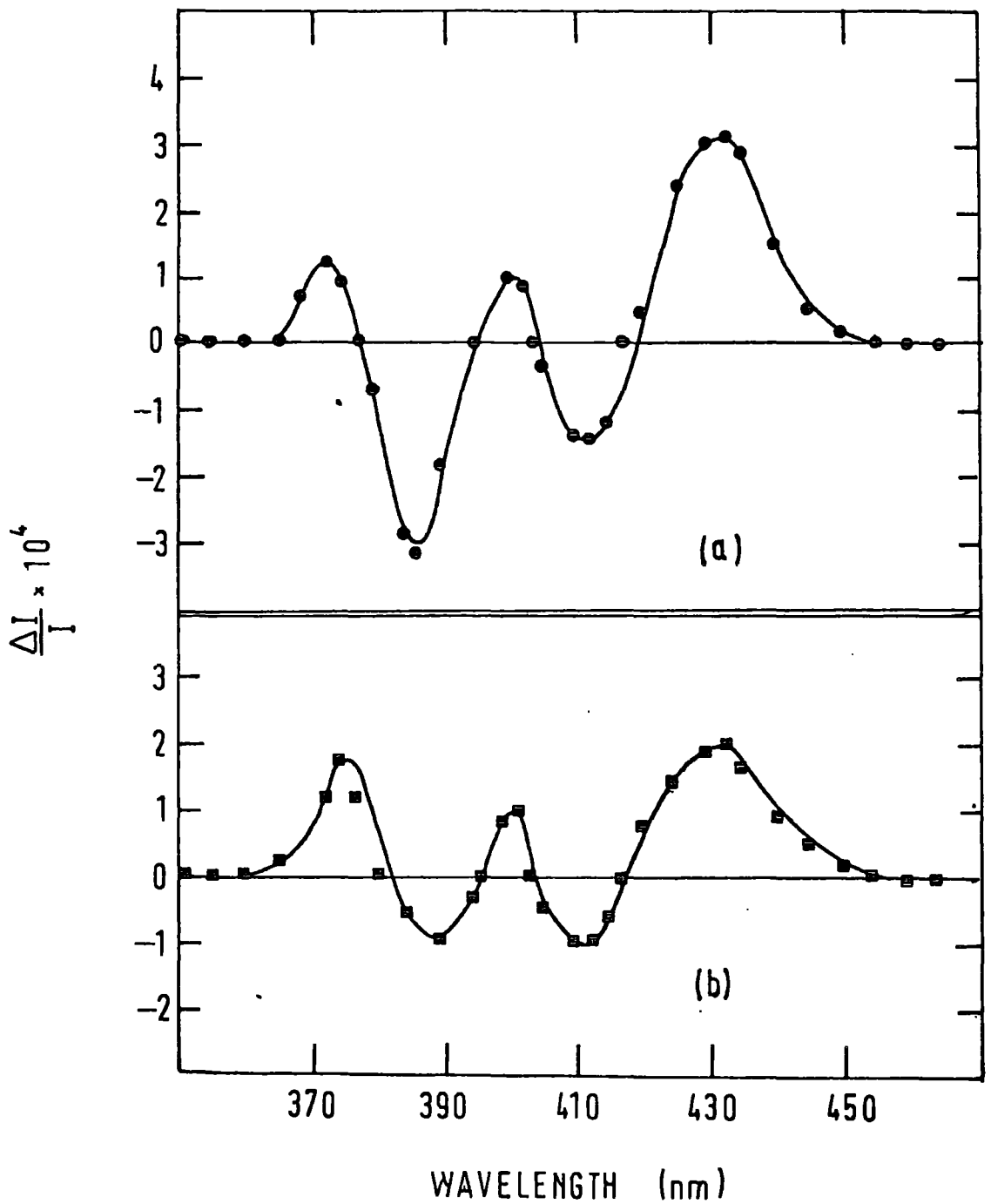

Fig. 6.29 Results of a preliminary experiment to determine the effects of polarized light upon the electroabsorption spectra:- (a) Vertical polarization (b) Horizontal polarization.

contemplated without additional experiments being performed.

6.4 Conclusion

The results discussed in this chapter are the fruit of a preliminary investigation into the electrical and optical properties of a novel new material, namely C4 anthracene. Data have been presented concerning the ac. and dc. conductivities of these multilayer films. An analysis of the dc. conductivity data indicate that the material is a highly anisotropic conductor, with a factor of 10^8 difference between the in-plane and through-plane resistivities. Single and double injection currents have also been reported. The latter are assumed to be related to the emission of light from some of the films.

In addition, optical absorption and electroabsorption results have been presented for the C4 multilayers. The optical absorption is similar to that of unsubstituted anthracene but shifted to longer wavelengths by approximately 25 nm. The electroabsorption spectra have been analysed in terms of the quadratic Stark effect, leading to an approximate value of the static polarizability change of $36 {}^{o}A^{3}$.

CHAPTER VII

CONCLUSION AND SUGGESTIONS FOR FURTHER WORK

7.1 Introduction

This chapter is devoted to an examination of what has been achieved in this study, and to identifying the areas in which the work could be usefully extended. These topics are now discussed in turn.

7.2 Summary Of Objects Achieved

The aims of this study were to investigate the effects of large electric fields upon the optical absorption properties of some semi-insulating materials. The specimens under investigation were related in that they all possessed semi-insulating electrical properties, but may be conveniently divided into two groups namely (a) the III-V compounds GaAs and InP and (b) Anthracene Langmuir/Blodgett multilayer films.

7.2.1 Gallium Arsenide And Indium Phosphide

The principal aim of the electroabsorption study was to determine the reduced effective masses of these materials. While information was available concerning the effective masses of pure GaAs and InP, no such data were available for crystals which had been deliberately doped during growth. The reduced effective mass of GaAs had previously been calculated from electroabsorption measurements [1]. However, the specimens used in that study are believed to have been both poorly characterized and of inferior quality. The study of electroabsorption described in this thesis is believed to be the first detailed report of electroabsorption in InP.

The procedures adopted to achieve the results were to carefully control the conditions under which the experiments were performed and by means of extensive supporting experiments, to specify problems which would lead to errors in the numerical analysis. The experiments performed may be summarized as follows:-

(a) DC. conductivity: These experiments produced information concerning the nature of the evaporated contacts, the resistivity of the specimens, and the ohmic activation energies.

(b) AC. conductivity: An analysis of the ac. conductivity and capacitance data, in conjunction with the dc. data, enabled a more definitive identification of the contact type to be achieved.

(c) Electroabsorption as a function of frequency: As a result of these measurements it was found that the magnitude of the electroabsorption response varied within a certain range of frequency. An extensive series of experiments, including photoconductivity studies, led to the identification of photogenerated carriers as the source of this effect.

(d) Harmonic analysis of the electroabsorption signal: In addition to a signal at the first harmonic, an electroabsorption signal was found to exist at the fundamental frequency of the applied field. This signal was attributed to an effective dc. field within the specimens due to the crystals' photoconductivity. However, further work proved that the magnitude of the true first harmonic signal was independent of this static field.

(e) Electroabsorption as a function of electric field strength: In agreement with the one-electron electroabsorption theory, a quadratic field dependence was found for all the III-V crystals examined.

A careful analysis of the above experiments led to a calculation of the effective masses in InP:Cr, InP:Fe and GaAs:Cr. In

conclusion therefore, the objectives of this part of the study were clearly achieved.

7.2.2 Anthracene Langmuir Films

The objective of the work carried out on the anthracene Langmuir films was primarily to determine whether the Stark effect could be detected in these materials, and if so, to calculate the static polarizability change. As for the III-V specimens, it was necessary to perform additional experiments on the anthracene multilayers, in order to discover whether other effects were distorting the data and threatening correct analysis of the results. The measurements carried out may be summarized as follows:-

(a) DC. conductivity: These measurements were performed, as for the III-V specimens, to determine the in-plane and through-plane conductivities, the onset of super-ohmic conduction, the breakdown field within the crystals and the space charge and ohmic activation energies.

(b) AC. capacitance and conductivity: The aim of these experiments was similar to those carried out on InP and GaAs, but with the additional objective of comparing the ac. conductivity with the model proposed by Jonscher et al.

(c) Photoconductivity: The magnitude and spectral dependence of the photoconductivity was recorded to check whether it was sufficiently intense to interfere with the electroabsorption results.

(d) Electroluminescence: In view of the known electroluminescent properties of evaporated anthracene films, measurements were performed to determine whether light was emitted from our films at the voltages which were to be applied during the electroabsorption studies. While significant electroluminescence was detected, it was found to have a relatively short lifetime and thus presented no obstacle with regard to the electroabsorption measurements.

(e) Electroabsorption: An electroabsorption signal, though extremely small, was successfully detected and recorded.

(f) Electric field dependence of the electroabsorption signal: A quadratic dependence of the absorption change upon the electric field strength was found.

An analysis of the above mentioned experiments allowed an identification of the electroabsorption spectra in terms of the quadratic Stark effect of localised excitations in the anthracene molecule. Upon application of the theory, the static polarizability change was calculated. It may thus be concluded that the objectives set out for this part of the study were also obtained.

7.3 Proposals For Further Study

At the conclusion of a thesis, it is customary to suggest areas in which the work of the thesis might be usefully extended. Three such areas, related to the present study, in which the electroabsorption technique could be usefully employed, have been identified. These are (a) an investigation of ternary and quaternary alloys, (b) a study of impurity electroabsorption and (c) an examination of space-charge effects in electroabsorption.

7.3.1 Investigation Of Alloy Systems

In recent years, ternary and quaternary alloys of II-VI and III-V materials have received a considerable degree of attention, due to their possible applications in the field of opto-electronics. In principle these alloys could provide sources, detectors and opto-electronic components over a wide wavelength range. In both the ternary and quaternary systems, the bandgap is found to be a function of composition. In addition, however, the quaternary alloys possess an extra degree of freedom, thus allowing the independent control of energy bandgap and lattice constant. Accordingly, it is possible to arrange that an epitaxial quaternary compound is lattice matched to a binary

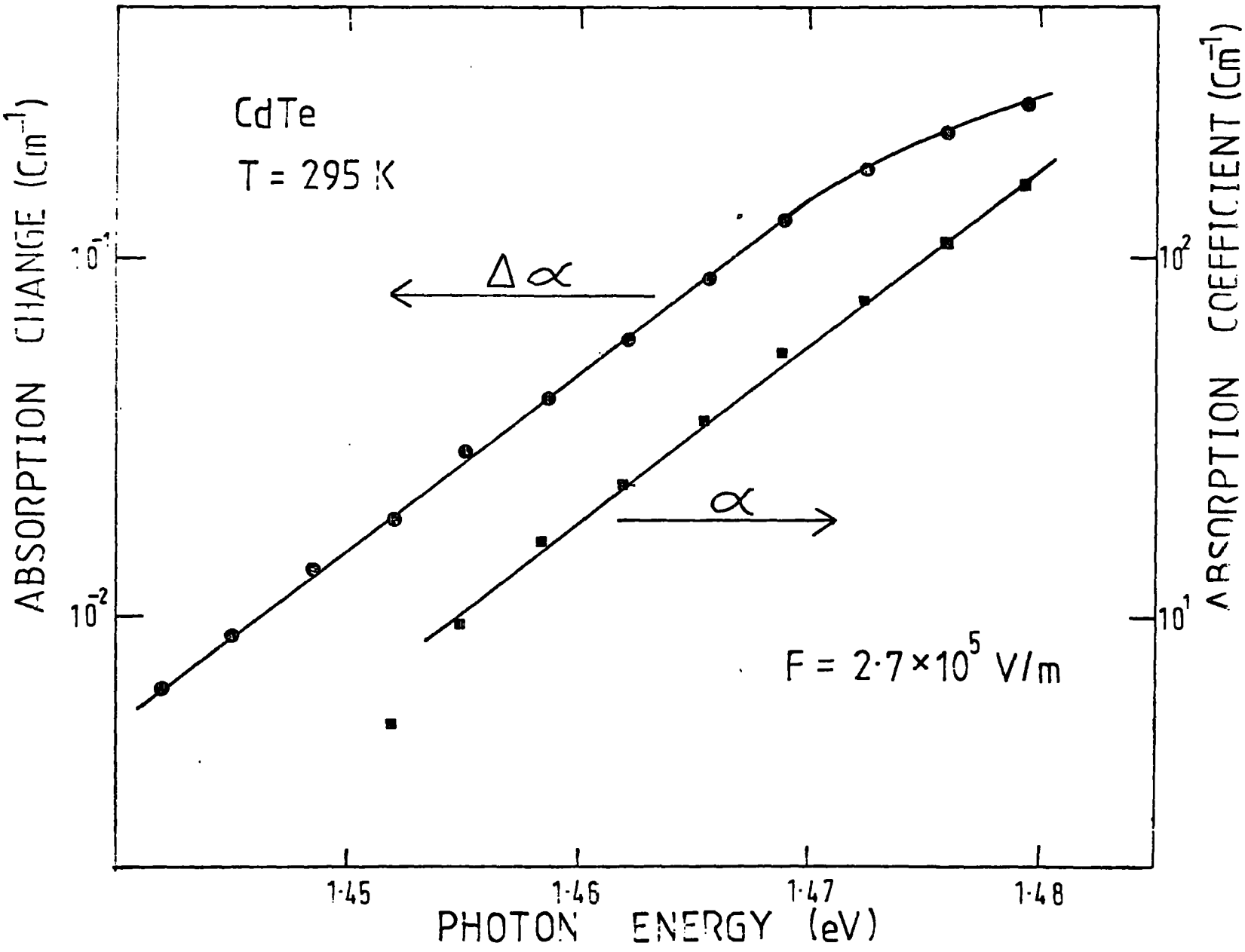

Fig. 7.1 Absorption change of a CdTe specimen at room temperature, due to a field of 2.7×10^5 V/m. Also shown is the zero field absorption spectrum.

substrate, with consequent improved device performance.

In view of the variation of energy bandgap with composition, it would be both interesting and useful to determine the effective masses of the ternary and quaternary alloys as the bandgap is varied. Provided the compounds could be made sufficiently resistive to withstand the high fields, it may be possible to achieve this by means of the electroabsorption technique, at least over a limited range of composition.

One system worth investigating is the $Cd_xHg_{1-x}Te$ ternary alloy system. In this material, the energy bandgap can be varied between -0.02 eV, for HgTe, and 1.5 eV, for CdTe. In connection with the proposed study, we have carried out a preliminary investigation of a semi-insulating CdTe specimen. The results are displayed in Figure 7.1 where both the zero-field absorption and the absorption change are plotted as a function of photon energy. The data are encouraging in view of the agreement between the slopes of the two curves. Application of the theory to these preliminary data leads to a value of 0.125 m_o for the reduced effective mass of CdTe, in fair agreement with published results for pure material.

A quaternary system which could also be investigated in this way is the $Ga_xIn_{1-x}As_yP_{1-y}$ alloy. These compounds have only recently become available. We have performed a preliminary examination of electroabsorption on a crystal of this system. The specimen had a room temperature bandgap of 1.23 eV, with a lattice constant of 5.869 Å and a thickness of 8 μm. It was deposited on a conducting InP substrate, so that in the electroabsorption experiment practically all the field was dropped across the quaternary. Figure 7.2 displays the results of the study. The zero-field absorption curve and the electroabsorption curve have equal slopes, as predicted by theory for an exponential absorption edge.

There are, of course, a number of problems. The main difficulty is that in electroabsorption experiments, one is dealing with extremely low level signals buried in noise. It is essential therefore, that a

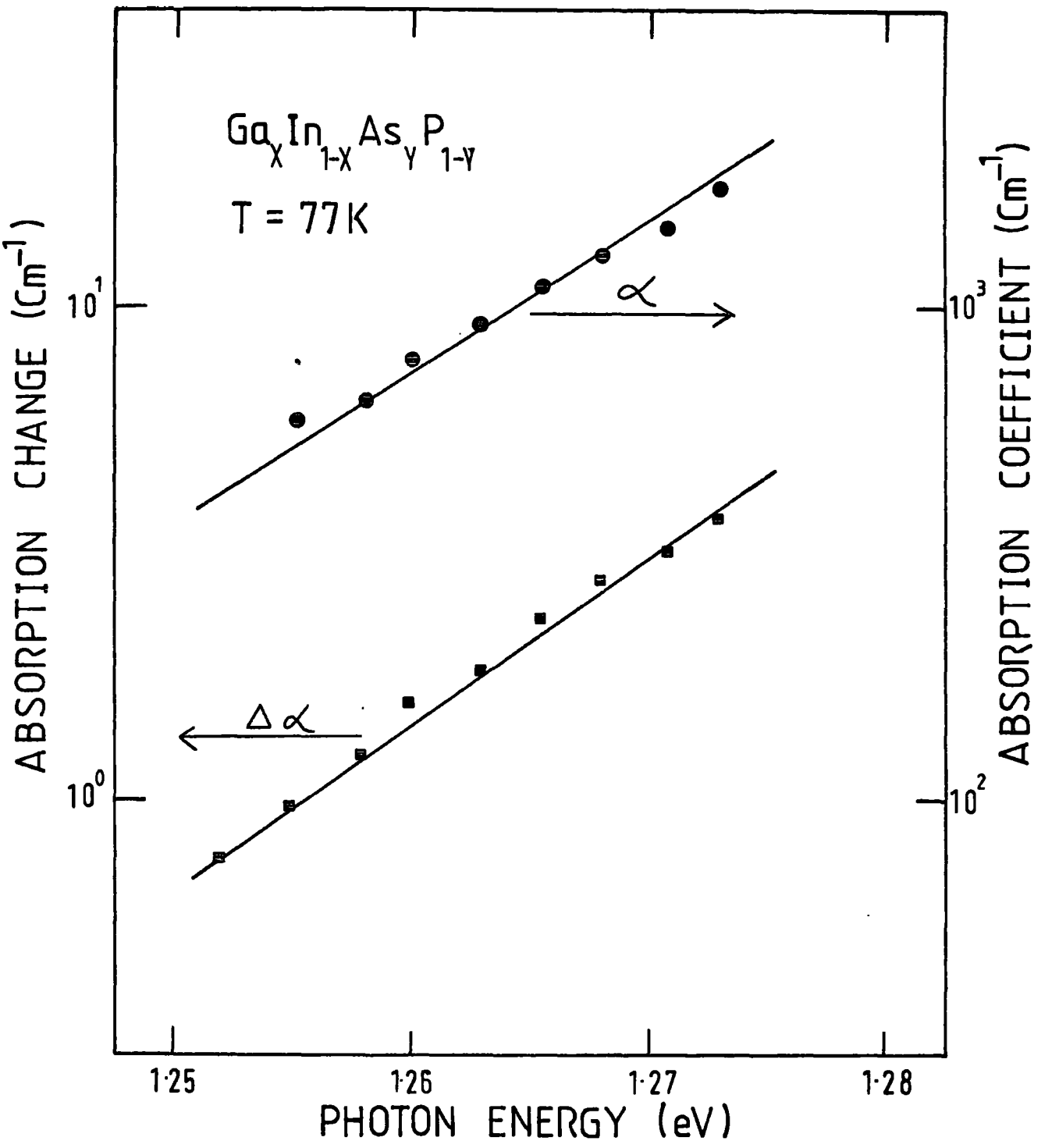

Fig. 7.2 Electroabsorption and absorption spectra of a $Ga_xIn_{1-x}As_yP_{1-y}$ alloy at 77 K.

suitable radiation detector is available. Unfortunately, the infrared detectors such as InSb, available for the spectral region above 1.0 μm suffer from severe noise limitations. These cells would need to be used in both the above-mentioned studies. The problem might be overcome by mounting the detector within about 1 mm from the specimen, a procedure adopted by Jonath et al [2].

7.3.2 Impurity Electroabsorption

The detection of impurity electroabsorption in semi-insulating or insulating materials is a useful tool for analyzing impurity state symmetry. The principle of the method depends on the analysis of electroabsorption data obtained for several field directions. In these studies, a transverse sample configuration is most suitable, in that it allows for light polarized either parallel or perpendicular to the field direction. Jonath et al [2] demonstrated with GaAs:O that richly detailed extrinsic spectra can thereby be obtained and correlated with other experimental results. In this study, impurity electroabsorption was detected in InP:Fe, as discussed in Chapter V.

A suitable material in which impurity electroabsorption could be investigated is magnesium oxide. This material is an insulator and thus can withstand large electric fields. Furthermore, it is possible that the impurity or defect absorption may occur in the spectral area between 300 nm and 1000 nm. This area is very suitable for electroabsorption work since a photomultiplier may be used to detect the transmitted light, with consequent noise reduction.

Preliminary data obtained for electroabsorption in an $MgO:C_o$ specimen are shown in Figure 7.3. The graph shows the absorption change for a field of 1.25×10^4 V/cm. Structure was observed at an energy of 3.20 eV. The figure illustrates the feasibility of the project, but further data are required before any analysis may be attempted.

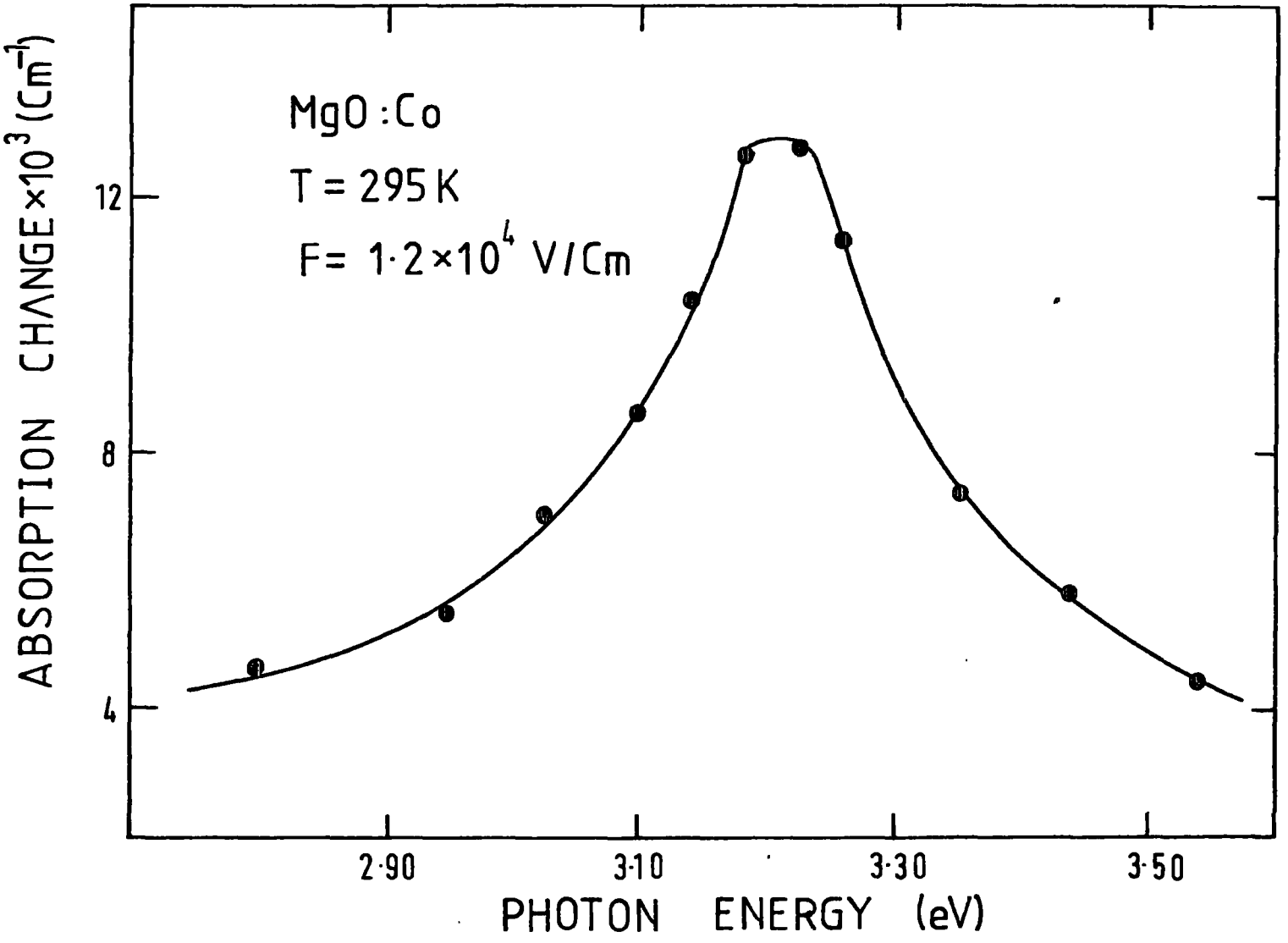

Fig. 7.3 Impurity electroabsorption in an MgO:Co sample at 295 K.

7.3.3 Space-Charge Effects In Electroabsorption

At frequent intervals during the course of this thesis, the problems caused by the injection of space-charge into specimens under investigation, in electroabsorption experiments, have been discussed. In the present study these difficulties have been overcome by maintaining the electric fields so low that space-charge effects could be neglected. However, in materials where injection occurs at very small electric field strengths, it may be impossible to follow this procedure. Accordingly, it would be extremely useful if an investigation were performed with the aim of determining what corrections are necessary to electroabsorption data recorded in the space-charge limited currents region of the current-voltage curve.

A suitable approach to the problem would be to initially perform electroabsorption experiments in the absence of injection currents, and subsequently, on the same specimens, to repeat the measurements under space-charge conditions. A comparison of the shapes of the electroabsorption spectra, the field dependences of the peaks, and the magnitude of the observed absorption changes should provide a basis for understanding the electric field distribution under injection conditions. A concurrent theoretical approach to the problem would also be advantageous.

The range of materials suitable for electroabsorption experiments were such a study successful is quite large. For example, if space-charge limited current effects could be eliminated it would be possible to study the electroabsorption properties of powders dispersed in an inert plastic matrix.

7.4 Applications Of The Electroabsorption Technique

To conclude this thesis, some of the principal benefits of the electroabsorption technique are summarized. These may be listed as follows:

(a) The technique is useful for the determination of the effective masses in some semi-insulating single crystals and alloy systems.

(b) It may be applied to an examination of the Stark effect in molecular crystals, with a consequent evaluation of polarizability changes.

(c) It is an extremely sensitive method of studying the reproducibility of thin films as discussed by Roberts et al [3].

(d) The technique may be applied to an investigation of band-tailing effects in inorganic solids.

(e) The identification and study of impurities in semiconductors and insulators may be conveniently performed by the electroabsorption technique, as discussed in Chapter II.

(f) In addition to the applications mentioned above, the precise determination of an energy bandgap is possible from electroabsorption data.

APPENDIX I

In electroabsorption theory, it is accepted that a positive electric field is equivalent to a negative electric field in so far as the effects produced should be the same. Accordingly, if a sinusoidal electric field is applied to a sample, each half of the cycle is equivalent and the electroabsorption result should be detected at twice the frequency of the applied field, that is, at the first harmonic (2f). Despite this, a situation is sometimes encountered in electroabsorption experiments where a signal is recorded at the fundamental frequency (f). A model to explain such harmonic effects has been presented by Bordas [1] and is briefly summarized here.

If we define the symbols:

F_a = applied alternating field
F_A = peak-to-peak value of F_a
F_b = any applied dc. bias
F_e = the effective field in the sample
F_i = any internal field present in the absence of any external field
f = frequency of applied field
$2f$ = the frequency of the first harmonic
S_f = signal at f
S_{2f} = signal at 2f
$\Delta\alpha = \alpha(F_1) - \alpha(F_2)$ is the absorption change

then a number of situations may be considered.

1. When the applied field F_a is sinusoidal about zero, and both the internal and external static fields are also zero, then the field seen by the sample is that shown in Figure A1(b). In this case, F_e has no Fourier component at 1f and the response will be detected at 2f.

FIG. A1

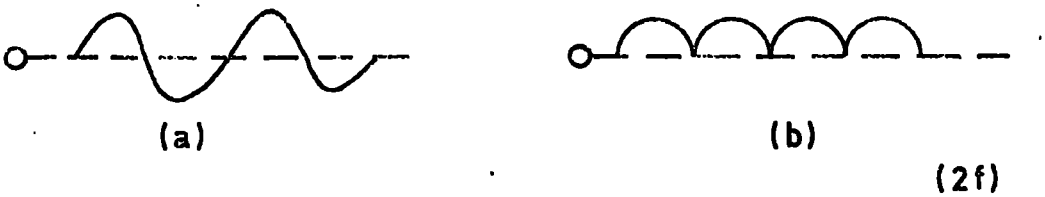

FIG. A2

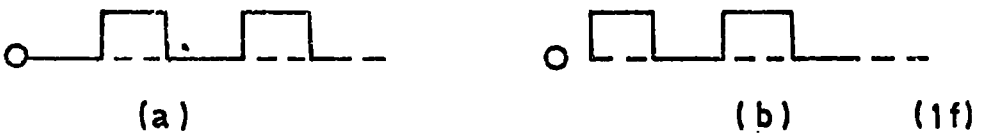

FIG. A3

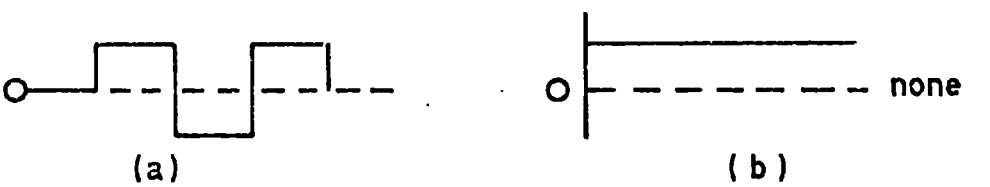

FIG. A4

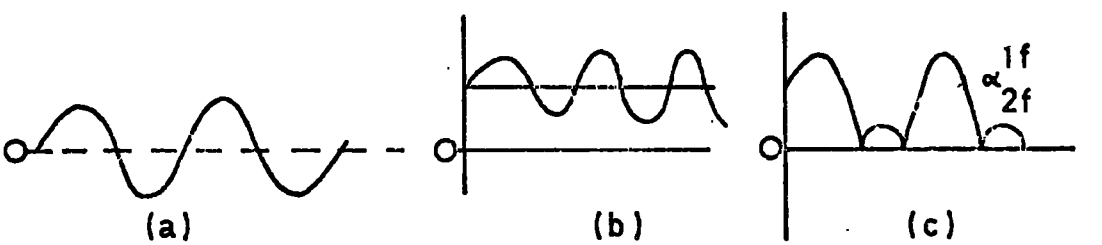

FIG. A5

FIG. A6

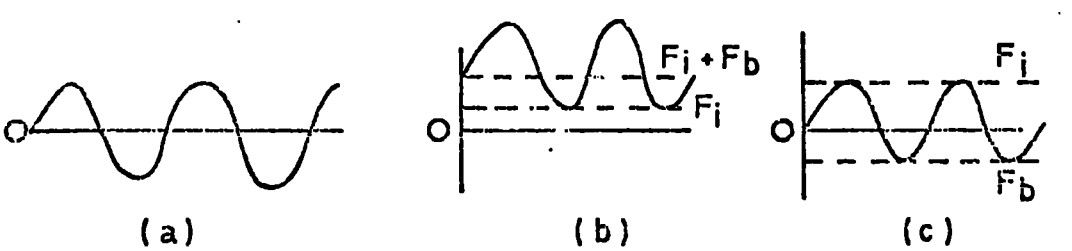

Figs. A1-6 Electric field distributions in electroabsorption studies. (see text for details)

2. If a square wave alternating from 0 to a positive value is used, and again F_i, $F_b = 0$, the resultant waveform seen by the sample is as shown at Figure A2(b) provided the sample and lead capacitance have not resulted in deformation of the square wave. Since the resultant is a square wave, which has no first harmonic, the signal should be detected at f, the fundamental frequency.

3. If a symmetrical square wave about zero is applied, F_e is effectively constant, and no modulated response should be obtained. This is an idealized situation since it assumes very fast rise and fall times of the square wave, rarely achieved in practice.

4. This case assumes the existence of an internal static field F_i within the crystal. The source of the static field is of no immediate relevance. Suppose a sinusoidal field is applied as in 1; then F_e takes the form shown in Figure A4(b).

   Provided $F_i \geqslant F_A$, F_e does not possess a first harmonic, and the signal is detected at f. However, if $F_A \geqslant F_i$ the resultant waveform is as shown in Figure A4(c). This situation is more complicated and a signal is detected at both f and 2f, as is evident from a Fourier analysis.

5. Suppose a modulating field is a square wave, operating from zero to a positive value, and there is a built-in field F_i. In this case, the square wave is superimposed on F_i, and takes the form illustrated in Figure A5(b). As a result, the modulation is from a positive to a non-zero value of field. The response is however, detected at f. If the square wave operates in a negative direction and F_i is positive and equal to F_A, then both S_f and $S_{2f} = 0$.

6. Finally, suppose a sinusoidal field F_a is applied in the presence of a built-in field F_i. If in addition, an external static field F_b is superimposed, two possible situations could arise, as shown in Figures A6(b) and (c).

If F_i and F_b are of equal sign, say positive, then $\Delta\alpha$ equals $\alpha(F_A + F_i + F_b) - \alpha(F_i + F_b)$ and a signal is recorded at f. If, however, F_b and F_i are of opposite sign, a situation may arise where with $F_i = F_b$, the modulated response at f would fall to zero, and instead the signal would be recorded at 2f, as in 1.

The above analysis completely ignores the source cause of any internal static field. In Chapter I, a series of papers by Redfield [2] was mentioned proposing that the electric fields of charged impurities could produce an "internal" Franz/Keldysh effect. In addition, Berozashvili et al [3, 4, 5] have carried out a series of experiments concerning the presence of odd harmonics in electroabsorption signals of GaAs and CdTe. These authors attribute the presence of an electroabsorption signal at the fundamental frequency to the existence of oriented microfields which they believe should occur in crystals without a centre of symmetry. In addition, to the above work Lorentz et al [6] have investigated internal fields in CdTe films by electroabsorption. A signal at the fundamental frequency was observed in these films, but this response could be reduced to zero by the application of a static external field of the correct polarity. A correlation between the internal static field and a photovoltage was also discussed.

REFERENCES TO CHAPTER I

1. G. W. Gobeli and H. Y. Fan, Phys. Rev. 119, 613 (1960)
2. E. O. Kane, J. Phys. & Chem. Solids 1, 249 (1957)
3. J. R. Dixon and J. M. Ellis, Phys. Rev. 123, 1560 (1961)
4. W. G. Spitzer and H. Y. Fan, Phys. Rev. 106, 882 (1957)
5. A. H. Kahn, Phys. Rev. 97, 1647 (1955)
6. F. Matossi and F. Stern, Phys. Rev. 111, 472 (1958)
7. R. Braunstein and E. O. Kane, J. Phys. & Chem. Solids 23, 1423 (1962)
8. R. Braunstein, J. Phys. & Chem. Solids 8, 280 (1959)
9. T. S. Moss, G. J. Burrell and B. Ellis, "Semiconductor Opto-Electronics", London Butterworths (1973)
10. W. C. Dash and R. Newman, Phys. Rev. 99, 1151 (1955)
11. P. J. Dean and D. G. Thomas, Phys. Rev. 150, 690 (1966)
12. J. Frenkel, Phys. Rev. 37, 1276 (1931)
13. G. Wannier, Phys. Rev. 52, 191 (1937)
14. R. Elliott, Phys. Rev. 108, 1384 (1957)
15. R. S. Knox, "Theory of Excitons", Solid State Physics, Suppl. 5 (1963)
16. J. O. Dimmock, "Semiconductors and Semimetals" 3, 259 (1967)
17. M. D. Sturge, Phys. Rev. 127, 768 (1962)
18. W. Turner, W. E. Reese and G. Pettit, Phys. Rev. 136, A1467 (1964)
19. E. J. Johnson and H. Y. Fan, Phys. Rev. 139, A1991 (1965)
20. A. Terenin in H. Kallman and M. Silver (Ed.), "Sympos. on Electrical Conductivity in Organic Solids", Durham, N. C., (Interscience, N. Y., 1961) P39
21. A. S. Davydov, Sov. Phys. Uspeki, 7, 145 (1964)
22. A. S. Davydov, "Theory of Molecular Excitons", McGraw-Hill, N. Y. (1962)
23. D. S. McClure, Solid State Physics, 8, 1 (1959)
24. H. C. Wolf, Solid State Physics, 9, 1 (1959)
25. D. C. Craig and S. H. Walmsley, "Phys. and Chem. of the Organic Solid State", 1 (1963)
26. T. S. Moss and T. D. F. Hawkins, Infrared Phys. 1, 111 (1961)
27. F. Stern and J. Dixon, J. Appl. Phys. 30, 268 (1959)
28. J. I. Pankove, Phys. Rev. 140, A2059 (1965)

29. D. Redfield, Phys. Rev. 130, 916 (1963); 140, A2056 (1965)
30. W. Franz, Z. Naturforsch, 13a, 484 (1958)
31. L. W. Keldysh, Sov. Phys. JETP, 7, 788 (1958)
32. J. Tauc, Materials. Res. Bull., 5, 721 (1970)
33. R. Zallen, Phys. Rev. 173, 824 (1968)
34. J. Dow and D. Redfield, Phys. Rev. B, 5, 594 (1972)
35. D. L. Dexter, Phys. Rev. Letters, 19, 383 (1967)
36. F. Urbach, Phys. Rev. 92, 1324 (1953)
37. G. G. Roberts, S. Tutihasi and R. C. Keezer, Phys. Rev. 166, 637 (1968)
38. D. Dutton, Phys. Rev. 112, 785 (1958)
39. C. Hilsum and A. C. Rose-Innes, "Semiconducting III-V Compounds", Pergamon Press, London (1961)
40. J. Bardeen and W. Shockley, Phys. Rev. 80, 72 (1950)
41. W. Shockley, "Electrons and Holes in Semiconductors", Van Nostrand, N. Y. (1950)
42. Y. P. Varshni, Physica, 34, 149 (1967)
43. M. B. Panish and H. C. Casey, J. Appl. Phys. 40, 163 (1969)
44. G. G. Macfarlane, T. P. McLean, J. F. Quarrington, and V. Roberts, Phys. Rev. 108, 1377 (1957)
45. E. Burnstein, G. S. Picus and N. Sclar, Proc. Photoconductivity Conference, Atlantic City, Wiley (1956), P353
46. D. Eagles, J. Phys. and Chem. Solids, 16, 76 (1960)
47. J. Callaway, J. Phys. and Chem. Solids 24, 1063 (1963)
48. W. P. Dumke, Phys. Rev. 132, 1998 (1963)

REFERENCES TO CHAPTER II

1. W. Franz, Z. Naturforsch, 13a, 484 (1958)
2. L. W. Keldysh, Sov. Phys. JEPT, 7, 788 (1958)
3. C. Zener, Hippel Z. Physik,
   (a) 67, 707 (1931)
   (b) 68, 39 (1931)
4. J. Callaway, Phys. Rev. 130, 549 (1963)
5. E. N. Adams, J. Chem. Phys. 21, 2013 (1953)
6. E. O. Kane, J. Phys. Chem. Solids 12, 181 (1959)
7. P. W. Argyres, Phys. Rev. 126, 1386 (1962)
8. W. V. Houston, Phys. Rev. 57, 184 (1940)
9. K. Tharmalingham, Phys. Rev. 130, 2204 (1963)
10. G. Dresselhaus, Phys. Chem. Solids 1, 14 (1956)
11. R. J. Elliott, Phys. Rev. 108, 1384 (1957)
12. J. Callaway, Phys. Rev. 134, A998 (1964)
13. G. H. Wannier, Phys. Rev. 117, 432 (1960)
14. D. E. Aspnes, Phys. Rev. 147, 554 (1966)
15. D. E. Aspnes, Phys. Rev. 153, 972 (1967)
16. J. C. Philips, B. O. Seraphin, Phys. Rev. Letts, 15, No 3 (1965)
17. D. E. Aspnes, P. Handler and D. F. Blossey, Phys. Rev. 166, 921 (1968)
18. C. M. Penchina, Phys. Rev. 138, A924 (1965)
19. L. Fritsche, Phys. Stat. Sol., 11, 381 (1965)
20. M. Chester and L. Fritsche, Phys. Rev. 139, A518 (1965)
21. Y. Yacoby, Phys. Rev. 140, A263 (1965)
22. A. Frova, P. Handler, F. A. Germano and D. E. Aspnes,
    Phys. Rev. 145, 575 (1966)
23. E. Gutsche and H. Lange, Paris Semiconductor Conference, (1964)
24. R. Williams, Phys. Rev. 117, 1487 (1960)
25. T. S. Moss, J. Appl. Phys. 32, 2136 (1962)
26. M. Chester and P. H. Wendland, Phys. Rev. Letts. 13, 193 (1964)
27. A. Frova and P. Handler, Appl. Phys. Letts. 5, 11 (1964)
28. A. Frova and P. Handler, Phys. Rev. 137, A1857 (1965)
29. H. D. Rees, Solid State Comm. 5, 365 (1967)

30. B. B. Snavely, Solid State Comm. 4, 561 (1966)
31. Y. Yacoby, Phys. Rev. 142, 445 (1966)
32. L. N. Strel'tsov and L. I. Verbitskaya, Izvestiya Akademii Nauk SSSR, Neorganicheskie Materialy, 4, 618 (1968)
33. G. A. Chalikyan and V. K. Subashiev, Sov. Phys. - Solid State, 10, No. 2 (1968)
34. R. E. Drews, Appl. Phys. Letts. 9, 347 (1966)
35. R. Williams, Phys. Rev. 126, 442 (1962)
36. Y. Hamakawa, F. A. Germano and P. Handler, Proc. Int. Conf. Phys. Semiconductors, Kyoto (1966); J. Phys. Soc. Japan, Suppl. 21, 111 (1966)
37. Y. Hamakawa, F. A. Germano and P. Handler, Phys. Rev. 167, 703 (1968)
38. B. B. Snavely, Phys. Rev. 167, 730 (1968)
39. J. Frenkel, Phys. Rev. 37, 17 (1931)
40. G. H. Wannier, Phys. Rev. 52, 191 (1937)
41. G. Dresselhaus, Phys. Chem. Solids 1, 14 (1956)
42. R. J. Elliott, Phys. Rev. 108, 1384 (1957)
43. C. Lancos, Z. Phys. 62, 518 (1930)
44. C. B. Duke and M. E. Alferieff, Phys. Rev. 145, 583 (1966)
45. H. I. Ralph, J. Phys. C 1, 378 (1968)
46. J. D. Dow and D. Redfield, Phys. Rev. B 1, 3358 (1970)
47. J. D. Dow, Phys. Stat. Sol. 34, K71 (1969)
48. R. Enderlein, Phys. Stat. Sol. 26, 509 (1968)
49. D. F. Blossey, Ph.D. Thesis, Univ. of Illinois (1969); Phys. Rev. B2, 3976 (1970); Phys. Rev. B3, 1382 (1971)
50. M. R. Tubbs and A. J. Forty, J. Phys. Chem. Solids 26, 711 (1965)
51. G. Baldini and S. Franchi, Phys. Rev. Lett. 26, 503 (1971)
52. P. I. Perov, Sov. Phys. - Solid State 11, 438 (1969)
53. J. Bordas in "Optical and Electrical Prop. of Layer Materials", Ed. by P. A. Lee (1977)
54. P. Handler, Phys. Rev. Letts. 23, 1387 (1969)
55. J. Stark, Ann. d. Phys. 43, 965 (1919)
56. A. Lo Surdo, Accad. Lincei Atti 22, 665 (1913)
57. L. Pauling and E. Wilson "Introd. to Quantum Mechanics", McGraw-Hill, N. Y. (1935)

58. L. I. Schiff, "Quantum Mechanics", McGraw-Hill
59. P. S. Epstein, Phys. Rev. 28, 695 (1926)
60. J. H. Van Fleck, "Theory of Electric and Magnetic Susceptibilities", Oxford Univ. Press 1965 (reprint of 1932 edition)
61. E. Schrodinger, Ann. d. Phys. 80, 437 (1926)
62. W. Liptay, Z. Naturforsch, 26A, 2020 (1971)
63. Y. Udagawa and D. M. Hanson, J. Chem. Phys. 65, 5367 (1977)
64. F. P. Chen and D. M. Hanson, J. Chem. Phys. 63, 3879 (1975)
65. F. P. Chen and D. M. Hanson, J. Chem. Phys. 66, 4950 (1977)
66. D. A. Dunmur and R. W. Munn, Chem. Phys. 11, 297 (1975)
67. R. M. Hochstrasser and L. J. Noe, J. Mol. Spectrosc. 38, 175 (1971)
68. J. R. Platt, J. Chem. Phys. 34, 862 (1961)
69. J. C. Powers and J. Kumamato, J. Chem. Phys. 36, 2893 (1962)
70. J. C. Powers Jr, W. R. Heller, J. Kumamato and W. E. Donath, J. Am. Chem. Soc. 86, 1004 (1964)
71. R. Hochstrasser, J. Chem. Phys. 48, 514 (1968)
72. L. M. Blinov, Sov. Phys. - Solid State 12, 1246 (1970)
73. R. Mathies and A. Albrecht, Chem. Phys. Letts. 16, 231 (1972)
74. R. Hochstrasser, Acc. Chem. Res. 6, 263 (1973)
75. H. Veenuliet, Chem. Phys. 2, 69 (1973)
76. J. H. Meyling and D. A. Wiersma, Chem. Phys. Letts. 20, 383 (1973)
77. M. A. Kurzmack and M. M. Malley, Chem. Phys. Letts. 21, 385 (1973)
78. L. M. Blinov and N. A. Kirichenko, Opt. Spectrosc. 37, 513 (1974)
79. G. G. Roberts, B.S. Keating, P.S. Vincett and W. A. Barlow, J. Phys. C 11, 3847 (1978)
80. U. M. Grassano, G. Margaritondo and R. Rosei, Phys. Rev. B 2, 3319 (1970)
81. A. D. Jonath and R. H. Bube, Surface Science 37, 167 (1973)
82. R. Boyn and J. Gardavsky, Phys. Stat. Sol. B 68, 275 (1975)
83. J. Gardavsky and R. Boyn, Phys. Stat. Sol. B 68, 575 (1975)
84. R. S. Bauer, Phys. Rev. Letts. 34, 1088 (1975)
85. G. Neu and Y. Marfaing, Rev. Phys. Appl. (France) 12, 263 (1977)
86. F. Luty, Surface Science 37, 120 (1973)
87. H. Veenvliet and D. A. Wiersma, Chem. Phys. 2, 69 (1973)

REFERENCES TO CHAPTER IV

1. H. Welker, Z. Naturforsch, 7a, 744 (1952)
2. C. Hilsum and H. D. Rees, Electron. Letts. 6, 277 (1970)
3. J. L. Shay, K. J. Bachmann and E. Buehler, Appl. Phys. Letts. 24, 192 (1974)
4. G. M. Blom and J.M. Woodall, Appl. Phys. Letts. 17, 373 (1970)
5. J. B. Mullin, J. Phys. Chem. Solids 26, 782 (1964)
6. M. Otsubo and M. Miki, Jap. J. Appl. Phys. 13, 1655 (1974)
7. C. M. Wolfe, G. E. Stillman and E. B. Owens, J. Electrochem. Soc. 117, 129 (1970)
8. G. Giesecke and H. Lister, Acta Cryst. 11, 369 (1958)
9. J. Callaway, J. Electronics 2, 330 (1957)
10. B. O. Seraphin, J. Appl. Phys. 37, 721 (1966)
11. R. Braunstein, J. Phys. Chem. Solids 8, 280 (1959)
12. M. V. Hobden, Phys. Letts. 16, 107 (1965)
13. M. D. Sturge, Phys. Rev. 127, 768 (1962)
14. L. W. Aukerman and R. K. Willardson, J. Appl. Phys. 31, 293 (1960)
15. F. Herman and W. E. Spicer, Phys. Rev. 174, 906 (1968)
16. H. Ehrenreich, Phys. Rev. 120, 1951 (1960)
17. A. L. Lin and R. H. Bube, J. Appl. Phys. 47, 1859 (1976)
18. T. Inoue and M. Okyama, Solid State Comm. 8, 1309 (1970)
19. V. A. Brodovoi and Z. A. Derikot, Sov. Phys. - Semicond. 7, 958 (1974)
20. J. M. Chamberlain and R. A. Stradling, Solid State Comm. 7, 1275 (1969)
21. F. P. Kesamanly, O. V. Emel'yanenko and D. N. Nasledov, Sov. Phys. - Solid State 4, 397 (1962)
22. A. T. Gorelenok, B. V. Tsarenkov and N. G. Chiabrishvili, Sov. Phys. - Semicond. 5, 95 (1971)
23. S. M. Sze and J. C. Irvin, Solid State Elect. 11, 599 (1968)
24. D. Bois and P. Pinard, Jap. J. Appl. Phys. 12, 936 (1973)
25. O. V. Tretyak, Sov. Phys. - Semicond. 4, 517 (1970)
26. T. S. Moss, J. Appl. Phys. Suppl. to V32, 2139 (1961)
27. M. D. Sturge, Phys. Rev. 127, 768 (1962)
28. D. Redfield and M. A. Afromowitz, Appl. Phys. Letts. 11, 138 (1967)

29. C. Hilsum and Rose-Innes, "Semiconducting III-V Compounds", Pergamon Press, London (1961)
30. M. Zvara, Phys. Status Sol. 36, 785 (1969)
31. W. G. Spitzer and J. M. Whelan, Phys. Rev. 114, 59 (1959)
32. K. G. Hambleton, C. Hilsum and B. R. Holeman, Proc. Phys. Soc. 77, 1147 (1961)
33. J. B. Mullin, A. Royle and B. Straughan, Proc. 3rd Int. Symp. on GaAs (1970), Aachen (London IPPS), P41-9
34. F. H. Pollak, C. W. Higginbotham and M. Cardona, J. Phys. Soc. Japan, Suppl. to V21, 20 (1966)
35. G. D. Pitt, Solid State Comm. 8, 1119 (1970)
36. H. Ehrenreich, J. Appl. Phys. Suppl. 32, 2155 (1961)
37. F. J. Reid and R. K. Willardson, J. Electron. 5, 54 (1958)
38. M. Glicksman and K. Weiser, J. Electrochem. Soc. 105, 728 (1958)
39. G. C. Kovalevskaya, Yu. G. Popov and N. V. Siukaev, Sov. Phys. - Semicond. 1, 178 (1967)
40. J. B. Mullin, A. Royle and B. W. Straughan, Proc. 3rd Int. Symp. on GaAs and Rel. Comp. (Aachen 1970) London, IPPS P41-9
41. D. Rode, Phys. Rev. B 3, 3287 (1971)
42. P. Blood and J. W. Orton, J. Phys. C 7, 893 (1974)
43. O. Mizuno and H. Watanabe, Elect. Letts. 11, No. 5 (1975)
44. K. P. Pande and G. G. Roberts, J. Phys. C 9, 2899 (1976)
45. G. K. Ippolitova, Sov. Phys. - Semicond. 11, No. 7 (1977)
46. T. S. Moss and Walton, Physica 25, 1142 (1959)
47. E. D. Palik and R. F. Wallis, Phys. Rev. 123, 131 (1961)
48. L. Eaves, R. A. Stradling, S. Askenazy, J. Leotin, J. C. Portal and J. P. Ulmet, J. Phys. C 4, L42 (1971)
49. M. Glicksman and K. Weiser, J. Phys. Chem. Solids 10, 337 (1959)
50. K. Losch and J. U. Fischbach, Phys. Stat. Sol. A 33, 473 (1976)
51. R. Newman, Phys. Rev. 111, 1518 (1958)
52. W. J. Turner, W. E. Rees and G. D. Pettit, Phys. Rev. 136, A1467 (1964)
53. T. R. Baroev, P. G. Eliseev, P. G. Siukaev and M. K. Khadikov, Sov. Phys. - Semicond. 5, 854 (1971)
54. F. Oswald, Z. Naturforsch 10a, 927 (1955)
55. W. P. Dumke, M. R. Lorentz and G. D. Pettit, Phys. Rev. B 1, 4668 (1970)

56. C. Hilsum, S. Fray and C. Smith, Solid State Comm. 7, 1057 (1969)
57. G. D. Pettit and W. J. Turner, J. Appl. Phys. 36, 2081 (1965)
58. G. G. Kovalevskaya, E. E. Klotyn'sh, D. N. Nasledov and S. V. Slobodchikov, Sov. Phys. - Solid State 8, 1922 (1967)
59. A. M. White, P. J. Dean, K. M. Fairhurst, W. Bardsley, E. W. Williams and B. Day, Solid State Comm. 11, 1099 (1972)
60. J. B. Mullin, A. Royle, B. W. Straughan, P. J. Tufton and E. W. Williams, 1972 Symp. on GaAs, Paper 13
61. S. V. Bulyarskii, N. S. Grushko, A. A. Gutkin and D. N. Nasledov, Sov. Phys. - Semicond. 9, 187 (1975)
62. W. H. Koschel, U. Kaufman and S. G. Bishop, Solid State Comm. 21, 1069 (1977)
63. A. A. Gutkin and D. N. Nasledov, Sov. Phys. - Solid State 4, 999 (1962)
64. L. M. Lambert, Phys. Rev. 138, A1569 (1965)
65. C. Penchina, A. Frova and P. Handler, Bull. Am. Phys. Soc. 9, 714 (1964)
66. E. G. Paige and H. D. Rees, Phys. Rev. Letts. 16, 444 (1966)
67. K. G. Askar and R. L. Anderson, Phys. Rev. 154, 721 (1967)
68. H. D. Rees, Solid State Comm. 5, 365 (1967)
69. B. T. French, Phys. Rev. 174, 991 (1968)
70. D. B. Kushev, V. I. Sokolov and V. K. Subashiev, Sov. Phys. - Solid State 13, 2488 (1972)
71. B. A. Bobylev, A. F. Kravchenko and A. S. Terekhov, Sov. Phys. - Semicond. 6, 1635 (1973)
72. A. D. Jonath and R. H. Bube, Surf. Sci. 37, 167 (1973)
73. A. D. Jonath, E. Voronkov and R. H. Bube, J. Appl. Phys. 46, 1755 (1975)
74. J. C. Burgiel and H. J. Braun, J. Appl. Phys. 40, 2583 (1969)
75. T. Nishino, T. Yanagida and Y. Hamakawa, Jap. J. Appl. Phys. 11, 1221 (1972)
76. Y. U. Kavalyauskas and A. U. Shileika, Sov. Phys. - Solid State 14, 915 (1972)
77. F. Evangelisti, J. U. Fischback and A. Frova, Phys. Rev. B 9, 1516 (1974)
78. G. G. Kovalevskaya, V. I. Alyushina, S. G. Metreveli and S. V. Slobodchikov, Sov. Phys. - Semicond. 10, 1306 (1976)
79. A. Ashby, G. G. Roberts, D. J. Ashen and J. B. Mullin, Solid State Comm. 20, 61 (1976)
80. D. C. Look, J. Appl. Phys. 48, 5141 (1977)

REFERENCES TO CHAPTER V

1. K. P. Pande and G. G. Roberts, J. Phys. C 9, 2899 (1976)
2. D. Redfield, Phys. Rev. 130, 914 (1963)
3. D. Redfield, Phys. Rev. 140, A2056 (1965)
4. B. G. Yacobi, Phys. Letts. 55A, 313 (1975)
5. T. McClelland, Ph.D. Thesis, Iowa State Univ. (1976)
6. R. Shimizee and T. Koda, J. Phys. Soc. Japan 38, 1550 (1975)
7. J. I. Pankove in "Optical Processes in Semiconductors" 1971 (Eagle Cliffs, N. J., Prentice-Hall)
8. H. R. Johnston, R. H. Williams and C. H. B. Mee, J. Phys. D 8, 1530 (1975)
9. S. C. Dahlberg, Surface Science 60, 231 (1976)
10. S. C. Dahlberg and W. A. Orr, Surface Science 67, 226 (1977)
11. M. D. Uspenskii, N. G. Ivanova and I. E. Malkis, Sov. Phys. - Semicond. 7, 427 (1968)
12. V. S. Ivanov, Sov. Phys. - Semicond. 5, 101 (1971)
13. G. Lucovsky, Solid State Comm. 3, 299 (1965)
14. L. Eaves, R. A. Stradling, S. Askenazy, J. Leotin, J. C. Portal and J. P. Ulmet, J. Phys. C 4, L42 (1971)
15. J. M. Chamberlain and R. A. Stradling, Solid State Comm. 7, 1275 (1969)

REFERENCES TO CHAPTER VI

1. (a) J. Dresner, R.C.A. Review 30, 322 (1969)
   (b) J. Dresner and A. M. Goodman, Proc. IEEE 58, 1868 (1970)
2. A. Aviran and M. A. Ratner, Chem. Phys. Letts. 29, 277 (1974)
3. C. W. Pitt and L. M. Walpita, Electron. Letts. 12, 479 (1976)
4. L. Esaki and R. Tsu, I.B.M. J. Res. Dev. 14, 61 (1970)
5. P. K. Weimer, Proc. I.R.E. 50, 1462 (1962)
6. G. G. Roberts, K. P. Pande and W. A. Barlow, Electron. Letts. 13, 581 (1977)
7. G. L. Gaines Jr. "Insoluble Monolayers at Liquid-Gas Interfaces", Interscience, N. Y. (1966)

   or

   G. L. Gaines Jr. "Surface Chemistry and Colloids", V7, ed. by M. Kerker, Butterworths, London (1972)
8. R. M. Handy and L. C. Scala, J. Electrochem. Soc. 113, 109 (1966)
9. S. Horiuchi, J. Yamaguchi and K. Naito, J. Electrochem. Soc. 115, 634 (1968)
10. M. H. Nathoo and A. K. Jonscher, J. Phys. C 4, L301 (1971)
11. B. Mann and H. Kuhn, J. Appl. Phys. 42, 4398 (1971)
12. M. Sugi, K. Nembach and D. Mobius, Thin Solid Films 27, 205 (1975)
13. G. G. Roberts, P. S. Vincett and W. A. Barlow, J. Phys. C 11, 2077 (1978)
14. V. K. Agarival, Electrocomponent Sci. Technol. 2, 1 (1975); 2, 75 (1975)
15. V. K. Srivastava, Phys. Thin Films, 7, 311 (1974)
16. P. S. Vincett, W. A. Barlow, F. T. Boyle and G. G. Roberts, Thin Solid Films, to be published.
17. W. A. Barlow, J. A. Finney, M. McGinnity, G. G. Roberts and P. S. Vincett, Proc. Edinburgh Semiconduct. Conf. 1978, to be published.
18. M. McGinnity, G. G. Roberts and W. A. Barlow, Solid State Comm. to be published.
19. R. A. Street, G. Davies and A. D. Yoffe, J. Non-Cryst. Solids 5, 276 (1971)
20. M. Careem and A. K. Jonscher, Phil. Mag. 35, 1489 (1977)
21. G. G. Roberts and F. W. Schmidlin, Phys. Rev. 180, 785 (1969)

22. D. D. Eley and G. D. Parfitt, Trans. Faraday Soc. 51, 1529 (1955)
23. D. D. Eley and M. R. Willis in "Semiconductivity of organic substances, part 5". H. Kallmann and M. Silver eds. "Sympos. on Elect. Conduct. in Organic Solids", Interscience N. Y. (1961) P257
24. W. Kauzmann "Quantum Chemistry" Acad. Press N. Y. (1957) P197
25. A. K. Ghosh and T. Feng, J. Appl. Phys. 44, 2781 (1973)
26. K. O. Lee and T. T. Gan, Phys. Stat. Sol. (a) 43, 565 (1977
27. B. Stevens, Spectrochim Acta 18, 439 (1962)
28. W. Pong, C. Inouye, F. Matsunaga and M. Morwaki, J. Appl. Phys. 46, 2310 (1975)
29. See for example K. Hasegawa and W. G. Schneider, J. Chem. Phys. 40, 2533 (1964)

REFERENCES TO CHAPTER VII

1. T. S. Moss, J. Appl. Phys. 32, 2136 (1961)
2. A. D. Jonath and R. H. Bube, Surface Science 37, 167 (1973)
3. G. G. Roberts, B. S. Keating, P. S. Vincett and W. A. Barlow, J. Phys. C 11, 3847 (1978)

REFERENCES TO APPENDIX I

1. J. Bordas in "Optical and Electrical Properties of Layer Materials", ed. P. A. Lee (1977)
2. D. Redfield, Phys. Rev. 130, 914 (1963); Phys. Rev. 140, A2056 (1965)
3. Y. N. Berozashvili, A. V. Dundua and D. Sh. Lordkipanidze, Sov. Phys. - Solid State 15, 616 (1973)
4. R. M. Akopyan, Y. N. Berozashvili, A. V. Dundua and D. Sh. Lordkipanidze, Sov. Phys. - JETP 38, 1003 (1974)
5. Y. N. Berozashvili, A. V. Dundua and V. I. Imnaishvili, Sov. Phys. - Semicond. 9, 256 (1975)
6. E. Lorentz, F. T. Novik and O. A. Trafimov, Sov. Phys. - Semicond. 10, 328 (1976)